Improved sub-µs gating analysis indicates conformational changes as caused by ion/pore interactions in the MaxiK channel

vorgelegt von
Indra Schröder

Kiel, Dezember 2007

Referent: Prof. Dr. U.P. Hansen ....

Korreferenten: Prof. Dr. Axel Scheidig und Prof. Dr. Gerhard Thiel.............

Tag der mündlichen Prüfung: 31.1.2008...

Zum Druck genehmigt: Kiel, den ....

....
Der Dekan

Vorbemerkung

Teilergebnisse dieser Dissertation sind bereits wie folgt vorab veröffentlicht worden:

1. Schröder, I., Huth, T., Suitchmezian, V., Jarosik, J., Schnell, S. and Hansen, U. P. 2004. Distributions-per-level: a means of testing level detectors and models of patch-clamp data. *J. Membrane Biol*. 197: 49-58.
2. Schröder, I., Harlfinger, P., Huth, T., Hansen, U. P. 2005. A subsequent fit of time series and amplitude histogram of patch-clamp records reveals rate constants up to 1 per microsecond. *J. Membrane Biol.* 203: 83-99.
3. Schroeder, I., Hansen, U.P. 2006. Strengths and limits of Beta distributions as a means of reconstructing the true single-channel current in patch clamp time series with fast gating. *J. Membrane Biol.* 210: 199-212
4. Huth, T., Schroeder, I., Hansen, U. P. 2006. The power of two-dimensional dwell-time analysis for model discrimination, temporal resolution, multichannel analysis and level detection. *J. Membrane Biol*. 214: 19-32
5. Schroeder, I., Hansen, U.P. 2007. Saturation and µs-gating of current indicate depletion-induced instability of the MaxiK selectivity filter. *J. Gen. Physiol*. 130: 83-97.

Eine weitere Veröffentlichung ist gerade eingereicht worden:

6. Schroeder, I., Hansen, U.P. 2008. Tl^+-induced µs-gating of current indicate instability of the MaxiK selectivity filter as caused by ion/protein interaction. (submitted)

Table of contents

1. Introduction

The adaptation of the function of ion channels to the needs of the living organism is mainly brought about by gating, i.e., by interrupting the flow of ions by pauses of different lengths. This gating originates from spontaneous or messenger-induced switching between open and closed states of the channel. Since gating is the crucial determinant of average current, the investigation of ion channel gating is a major issue in pharmacological and medical research (Lehmann-Horn and Jurkat-Rott, 1999; Ashcroft, 2000; Shieh et al., 2000).

In biophysical studies seeking to understand the molecular machinery accomplishing ion transport, the role of gating seemed to be underestimated for a long time. For instance, models like that one of Hille and Schwarz (1978) or of Wu (1991) explained the peculiar phenomenon of the AMFE (anomalous mole fraction effect) on the basis of ion/ion interactions during the translocation of individual ions. Furthermore, the snug fit hypothesis of ion selectivity (Mullins, 1959; Bezanilla and Armstrong, 1972; Doyle et al., 1998) was based on the assumption of a rigid pore whose dynamics were not influenced by the passage of ions. Opening and closing was believed to occur at the inner gate or to be brought about by the ball-and-chain mechanism (Armstrong et al., 1973) whereas little attention was paid to the selectivity filter.

The biophysics group in Kiel tried for a long time to draw the attention to gating processes. This started with the description of damped oscillations in the membrane potential of characean cells (Boels and Hansen, 1982) as caused by feedback loops controlling transport activity (Hansen, 1990). In those early models, "lazy (inactive) states" of the transport molecule were assumed (Hansen et al., 1983; Hansen, 1986). A lazy state model was also employed to explain the finding of a great dynamic membrane capacity of ca. 5 μFcm^{-2} in *Acetabularia*. Tittor et al. (1983) assumed that this lazy state belonged to the Cl^- pump in *Acetabularia,* but from a today's point of view it cannot be excluded that it was the K^+ channel.

The focus on fast gating came with the patch clamp technique, enabling the study of the gating of single channels. Draber et al. (1991) suggested an alternative model to the Hille-Schwarz model in order to explain patch clamp data of the AMFE in *Chara* obtained in the cell attached mode. This model was based on the assumption of a lazy state of the K^+ channel. However, at that time the temporal resolution was not high enough for the detection of the existence of the putative lazy states with lifetimes shorter than the available temporal resolution. This problem led to strong efforts to increase the temporal resolution of patch clamp analysis. The first success was obtained by increasing the sampling rate from 5 kHz to 100 kHz (Albertsen, 1992): The negative slope found in *Chara* at negative potentials in the presence of Cs^+ turned out to be a gating effect. The true single-channel current increased with negative potentials, but in the low-pass filter of the set-ups for patch clamp recordings averaging over undetected open and closed times reduced it to an apparent current. This pretended a negative slope at negative potentials (Draber and Hansen, 1994). Klieber and Gradmann (1993) came to this result by means of an evaluation based on beta distributions using the theory for 1st order filters, but Draber and Hansen (1994) could show the fast gating directly.

The next goal was to show that the AMFE in *Chara* in Tl^+/K^+ solutions was also a result of undetected fast gating. Finally, this could be shown by replacing dwell-time analysis by a direct fit of the time series (HMM fit) which became especially powerful as the results were tested by simulations (Farokhi et al., 2000).

Crucial for the success of the analysis of fast gating was the improvement of both the experimental set-up to reduce the noise and the software for the analysis of gating in

the time series. Enhanced temporal resolution was achieved by three major improvements:

1. Minimizing the immersion depth of the electrode, (Keunecke, 1995; Farokhi et al., 2000).
2. Coating the patch pipettes internally with sigmacote and heating them over night (Huth, 2005).
3. Improving of the analytical tools: Dwell-time analysis with an improved jump detector (Schultze and Draber, 1993), missed events correction (Draber and Schultze, 1994a), HMM fit (Albertsen and Hansen, 1994), beta distributions (Riessner, 1998; Harlfinger, 2003; results of the present thesis), 2-D dwell-time analysis (Huth, 2005; Huth et al., 2006).

However, up to recently, the immediate goal was to demonstrate that people should be more cautious, i.e., to show that the traditional Hille-Schwarz model (Hille and Schwarz, 1978) and others based on ion/ion interaction may not apply, when the observed effect is brought about by fast gating and not by ion/ion interaction during a single translocation step of an ion. Hansen et al. (2003) tried to create a mechanistic model for explaining the AMFE in *Chara* by gating effects. However, this model had still a lot of unproven assumptions. Concepts about protein dynamics were not yet included.

The new virtue of fast-gating analysis found in this thesis, i.e., to offer an approach to the study of protein dynamics came as a surprise. Actually, this started with a great disappointment. On the meeting of the European Biophysical Society in Montpellier in July 2005, we wanted to show that the IV curve of the true single-channel current at positive membrane potentials in MaxiK channels becomes linear, when the effect of gating on apparent current is eliminated. This was especially tempting as T. Huth, now working in the Institute of Physiology in Kiel, told us that they found that some MaxiK channels had linear single-channel IV curves under the influence of U73122 (PLC-inhibitor, personal communication from T. Huth). We thought that these channels had lost the ability to do fast gating and thus displayed the true single-channel current. We expected to find this current after reconstructing the true single-channel current from the apparent current by means of the analysis of beta distributions. Indeed, the first two evaluated data points were on this linear curve. However, then the disappointment came. These two points were the only ones which coincided with the extrapolated linear behavior. All other data points gave lower true single-channel currents. The average of all these points resulted in a saturation curve. Repetitive tests of the evaluation routines did not help. Finally we had to accept that the true single-channel current deviated from a linear IV curve and showed saturation at high voltages.

At that time, we were not aware of the fact that we ought to be extremely happy about this finding. However, after the data had convinced us that the true single-channel current saturated we realized that onset of saturation and of gating occurred at the same membrane potential. They seemed to be coupled. This insight was the stimulus to start thinking about a mechanistic model. The final model as described in appendix 6.5 assumes that voltage-induced ion depletion in the selectivity filter causes instability of the filter. The presence of ions is required to compensate the repulsive forces of the carbonyl groups of the filter which replace the water shell (Doyle et al., 1998).

The creation of that model came just at the right time. Following the determination of the KcsA crystal structure, there was a tremendous progress in understanding the

molecular events of ion transport. Progress came along two lines: Crystal structure analysis (Doyle et al., 1998; Zhou et al., 2001b) and Molecular Dynamics (MD) simulations.

Crystal structure analysis could reveal the channel structure with such high resolution that even single ions and water molecules could be identified. Unfortunately, crystal structure analysis delivers static pictures which do not tell very much about the protein dynamics associated with ion transport and gating. However, this is not absolutely true, since conformational changes depending on experimental conditions can be observed, e.g., the collapse of channel structure when the permeating ion is missing. This occurs when crystals were grown in low K^+ (3 mM) as shown by Zhou et al. (2001b).

Fluorescence technique and ESR in spin-labeled channels are new tools supplementing crystal structure analysis. Perozo et al. (1999) could monitor the opening of the inner gate by ESR of cysteine-labeled TM1 and TM2 helices in KcsA. Renart et al. (2006) used tryptophane fluorescence for studying changes in KcsA structure as caused by K^+ or Na^+. Fluorescence lifetime spectroscopy was used by Blunck et al. (2006) to verify the open state of KcsA.

The most powerful approach to protein dynamics, however, is a theoretical one: Molecular Dynamics simulations (MD). By means of these algorithms, the conformational changes related to the movement of an ion through the selectivity filter can be calculated for channels of known structure, e.g., KcsA (Compoint et al., 2004; Noskov et al., 2004; Berneche and Roux, 2005) or Kir6.2 (Capener et al., 2003). Other calculations deal with the role of the negative charges at the pore mouth of the viral channel Kcv (Tayefeh et al., 2007) and the related flipping of salt bridges before the ion can move. Changes in the concentrations of the permeant ions can lead to instabilities of the selectivity filter, when the repulsive forces of the carbonyl groups of the selectivity filter are no longer compensated by the electrostatic attraction of the ions (Berneche and Roux, 2005).

MD simulations can span a temporal range of some ps, if all atoms of a channel protein are taken into account. Simplifications of the algorithms can expand the range to about 30 ns (Tayefeh et al., 2007). Further improvements of the algorithms like the "coarse grain" method lead to the expectation that a considerable extension of the temporal range will occur in near future (Bond et al., 2007).

MD simulations are calculations starting from the actual state of the knowledge about channel structure. The results of these calculations have to be verified by experimental results. However, nowadays, only macroscopic quantities are available for this kind of tests, e.g., conductivity and selectivity. More desirable are experimental approaches which can monitor the calculated changes in protein structure. One hope to succeed on this way comes from fluorescence studies as mentioned above. Another access could be opened if the temporal resolution of fast gating events in the single-channel current could reach the range covered by MD simulations. The present gap has to be closed from both sides: 1. Extending the time scale of MD simulations by new algorithms and faster computers. 2. Improving the temporal resolution of the analysis of the gating of single-channel currents.

In this thesis, the tools for the analysis of gating are improved reaching the sub-microsecond range. Applying these tools to the fast gating observed in single-channel currents of MaxiK led to a model about ion/channel interactions (chapters 6 and 7) which seems to be in line with the mechanisms suggested by MD simulations. Thus, there is hope that this thesis helps to close the gap between physiology and structural biology from the physiological side.

2. Current state of research

Summary. A short introduction is given into the field of membrane transport with special emphasis on the structure of ion channels and the mechanisms underlying permeation (translocation) of ions and the interruption of the flow of ions by gating. Permeation and selectivity are explained by two different hypotheses: "snug fit" and "field strength". They are related to different concepts about the flexibility of the selectivity filter. Gating can occur at three loci: selectivity filter, inner gate and at the pore mouth (ball-and-chain). The flexibility of the selectivity filter is of great importance for ion/channel interaction and its influence on that kind of gating that is in the focus of the present thesis. The descriptions here are extended in a more specialized form in the discussions of the results in chapters 6 and 7.

2.1. Membrane transport

Membranes separate different compartments in living organisms, i.e., the plasma membrane separates the cytosol inside the cells from the outer medium, the thylakoid membrane the stroma in the chloroplasts from the inner lumen, the vacuolar membrane the cytosol from the vacuole, etc. However, life would not be possible if exchange between the compartments were completely abolished. Thus, there are many kinds of different transport proteins spanning the membrane. The following types can be distinguished by means of the transport rates (s^{-1}) with the relationship: $1.6\ pA = 10^7$ ions/s:

1. water channels: 10^9
2. ion channels: 10^7 to 10^8
3. cotransporters: 10^3 to 10^4
4. ABC-transporters 10^2 to 10^7
5. pumps: 10^2 to 10^3

Ion channels are the most intensively investigated transporters. At the beginning of electrophysiological research, this originated from the interest in nervous excitation (Cole, 1968). Nowadays, all cellular functions are investigated. Nevertheless, scientists are still attracted by the high transport rates which enable the direct measurement of single-channel currents by means of the patch clamp technique described in chapter 3. Channels can transport ions only downhill, i.e., along the gradient of the ion-motive force consisting of membrane potential and concentration difference.

Cotransporters couple the normally impossible uphill movement of an ion or of a sugar, amino acid, etc. to the downhill movement of a driver ion, usually Na^+ in animal cells (Mann et al., 2003) and H^+ in plant cells (Baker, 1978; Maathuis and Sanders, 1992). However, apart from these standard scenarios, the variety of driver ions and transportees is great, especially in kidney cells (Verrey et al., 1999). The structure of some cotransporters has been revealed recently (Abramson et al., 2003; Huang et al., 2003).

Pumps play an important role in plant membranes providing the driving force for cotransport (Sanders, 1990; Maathuis and Sanders, 1992) and in organs of animals (Apell, 2003).

H$^+$ pumps in mitochondria (Sambongi et al., 1999), chloroplasts (Junge et al., 1997) and bacteria (Stocker et al., 2007) are driven backwards by a proton-motive force generated by light- or redox-driven electron transfer chains. These pumps, often called ATPases, synthesize ATP.

ABC-transporters were neglected for a long time, even though they build up one of the largest super family of transporters (Holland and Blight, 1999). They transport all the stuff other transporters refuse to handle, like cytostatic drugs out of cancer cells or herbicides out of plant cells (Chang and Roth, 2001). TAP-transporters in the membrane of the ER (Lankat-Buttgereit and Tampe, 2002) attach peptides to the MHC (Major Histocompatibility Complex I). Failure of the CFTR is the cause of cystic fibrosis (Sheppard and Welsh, 1999). The list could be continued over many pages.

Here, K$^+$ channels are investigated. Thus, we concentrate the description on this kind of transporters.

2.2. Potassium channels

As mentioned above, electrophysiology started with the investigation of ion channels. The following list gives some of the major keystones of the history of channels:

1936: Permeation of neutral molecules in *Chara*: 4 Å
1952: Theory of the action potential with K$^+$ and Na$^+$ channels
1965: Other transporters: electrogenic pump, cotransporter, Mitchell's hypothesis
1982: Na$^+$: „mindless mill of hydrophobicity analysis" (Miller, 1991)
1987: K$^+$: cloning of the *Shaker* gene of *Drosphila*, recombinant DNA manipulation
1989: Docking of toxins showed: the P-loop lines the pore
1990: Tetramer, RNA-mixing (inactivation and toxin sensitivity, Isacoff et al., 1990; Ruppersberg et al., 1990)
1995: Cloning of KcsA from *Streptomyces lividans* over expression in E. coli, insertion into artificial membranes: Schrempf et al. (1995): **The race for determining the structure started.**
1998: Crystal structure: 3.2 Å resolution, MacKinnon-group
2003: Inner Gate, S4, Nobel price for MacKinnon and Aegre (water channel).

Collander and Bärlund (1933) realized that neutral molecules with a diameter below 4 Å could enter characean cells. Bigger ones were excluded. This led to the concept of a pore. In the 1930's and 1940's the action potential transmitting the information in the nerves was investigated in animal (Cole and Curtis, 1939) and in plant cells (Hope, 1961; Mullins, 1962). This led to the first great highlight, the mathematical description of opening and closing of the Na$^+$ and the K$^+$ channel in nerves cells by Hodgkin and Huxley (1952) who received the Nobel price in 1963. In the 1960's another large field of electrophysiology, the investigation of ion pumps in animal (Na$^+$ pump, Skou, 1965) and plant cells (H$^+$ pump, Kitasato, 1968; Sanders et al., 1981) emerged. The most important achievement was the chemiosmotic hypothesis which explains the most efficient process of converting redox energy from light (Jagendorf and Uribe, 1966; Witt, 1979) or metabolic energy (Siedow and Umbach, 1995) to the energy stored in ATP. Mitchell (1966) received the Nobel price after 15 years of fighting against the hypocrisy of chemists (Tupper and Tedeschi, 1969) disliking that one of the most important processes of life was based on a biophysical mechanism.

The understanding of channel structure started when it became possible to determine the sequence of amino acid residues of the channel protein (Fig. 2.1). The hydrophobicity of the individual residues was plotted vs. the number of the residues starting at the N-terminus (Fig. 2.1A). Doing so, it was realized that the hydrophobic residues had a tendency to build helices. This led to the generally accepted concept that ion channels consist of membrane-spanning helices connected by external loops (Fig. 2.1B). Later on, the analysis of the binding sites for blockers (e.g., TEA^+) or toxins (Miller, 1991; Aiyar et al., 1995) made the P-loop (the loop between helices S5 and S6 or between TM1 and TM2 in smaller channels) turn down from the external medium into the pore (Fig. 2.1B).
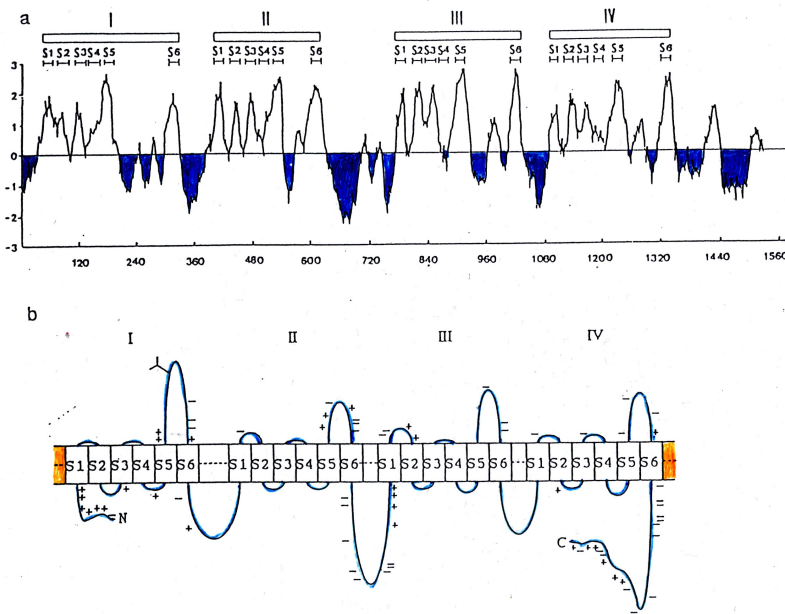
Fig. 2.1. "The mindless mill of hydrophobicity plots". (A) The hydrophobicity of the amino acids of the channel protein is plotted vs. the position of the residue in the sequence of a Na^+ channel. Striking is the finding that the hydrophobic and hydrophilic amino acid are grouped. (B) The observation that the hydrophobic residues are those which form helices formed the picture of 24 membrane spanning helices connected by external loops. (from Sato and Matsumoto, 1995)

In Fig. 2.1, a Na^+ channel is shown which consists of 24 channel grouped in 4 domains. In the case of K^+ channels, the 4 domains are separated. K^+ channels consist of 4 subunits. These tetramers can be homomers or heteromers (Beimgraben, 2007). The number of helices can be different in different K^+ channels. The small channels like Kir, KcsA and Kcv consist of 4 x 2 helices, named TM1 and TM2. Voltage-gated channels have 4 x 6 helices, named S1 to S6 similar to the Na^+ channel in Fig. 2.1. Obviously, the S1 to S4 unit with the charge carrying S4 helix (Liman et al., 1991) had been merged with channels of the 4 x 2 type to form voltage-sensitive channels. This is suggested by the finding that the S1 to S4 unit is not only found in channels, but also in a voltage-sensitive enzyme (Murata et al., 2005). The S1-S4 unit is connected to the S5/S6 channel unit very loosely via the S4-S5 linker. This was the reason that the structure of the KvAP isolated by the group of MacKinnon (Jiang et al., 2003) was not native,

because the orientation of the S1-S4 unit to the S5/S6 channel was lost when the channels were extracted from the membrane.

The MaxiK channel (also called BK channel) used in the investigations here, is a 4 x 7 helices channel. It is assigned to the voltage-sensitive class of 4 x 6 channels. However, there is one important difference: The additional helix, S0, brings the N-terminus to the luminal side. The N-terminus closes the inner pore mouth like a finger (Bentrop et al., 2001) after the channel has been opened by depolarizing membrane potential, thus causing an inactivation after excitation (ball-and-chain mechanism, Armstrong et al., 1973). The absence of this mechanism allows continuous recording of MaxiK transport activity (Meera et al., 1997).

After overexpression of channel cDNA in bacteria (Schrempf et al., 1995), it became possible to crystallize ion channels. The MacKinnon group was the first one which could successfully crystallize the bacterial KcsA channel (Doyle et al., 1998). This was a breakthrough in ion channel research.
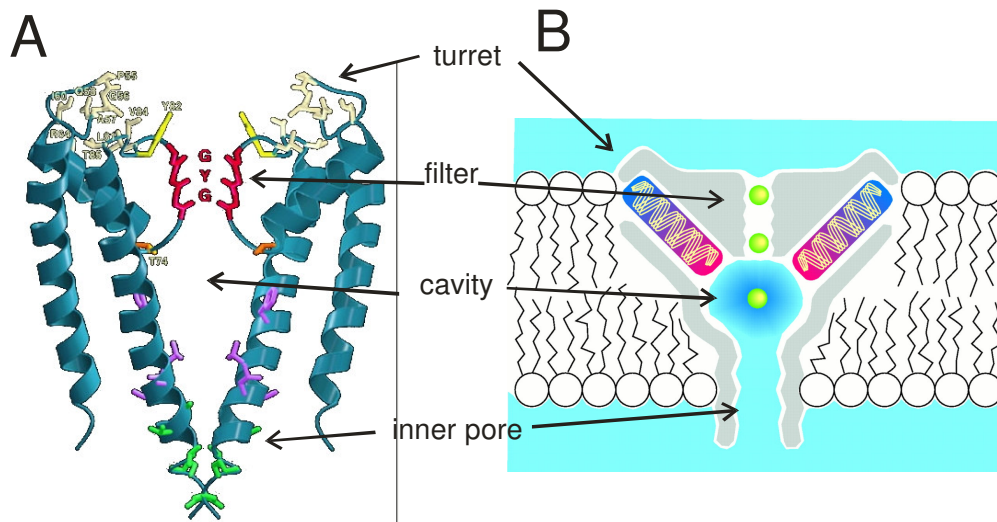
Fig. 2.2. Crystal structure of the KcsA. It is build from 4 x 2 helices, TM1 and TM2. For clearer presentation, only two subunits are shown here. The P-loop carries the signature GYG which is characteristic for all K$^+$ channels. Turret, selectivity filter (GYG), cavity and inner pore are highlighted (A) Ribbon presentation of the architecture (B) schematic presentation. The pore helices (yellow spirals) stabilize the structure and carry negative charges which coordinate the ion in the cavity (adapted from Figs. 4 and 7, Doyle et al., 1998).
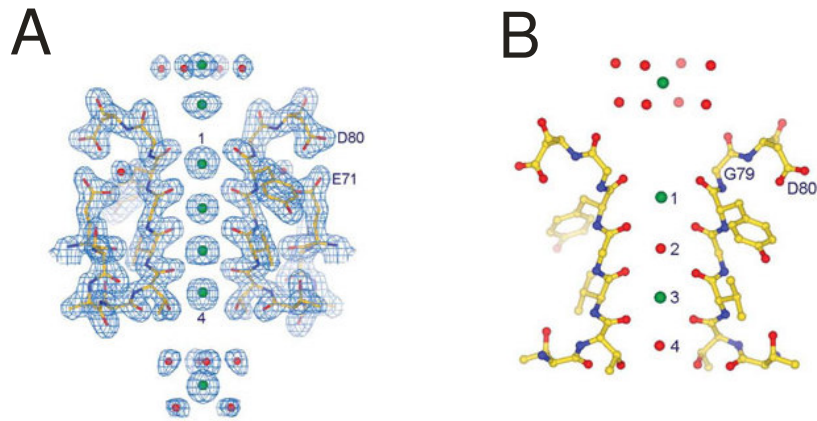
Fig. 2.3. Replacement of the water shell by the carbonyl groups of the selectivity filter of an ion channel. (A) 2-σ plot of the electron density of KcsA (X-ray structure). The oxygens of H_2O or of the carbonyl groups are shown in red. The ions are green. (B) Schematic representation showing that in the selectivity filter two ions are separated by one water molecule (adapted from Figs. 2 and 4, Zhou et al., 2001b).

The most important part of the channel is the selectivity filter with the GYG signature shown in Fig. 2.2A. It is of crucial importance for the mechanism of ion conduction and selectivity. The fundamental idea is that the channel protein has to replace the water shell of the ion. This is achieved by placing the carbonyl groups of the peptide bonds in such a distance that they can pretend a water environment for the ion (Fig. 2.3). This distance is adjusted exactly for one kind of ion, e.g., K^+. The smaller Na^+ would not feel cozy and would not penetrate the selectivity filter. This is the so-called snug fit theory, which now has been modified by insights obtained from Molecular Dynamics simulations as discussed below in section 2.4.

A still open question is the mechanism by which the S4 helix opens the inner gate (Ferrer et al., 2006). The crystal structure obtained from the bacterial KvAP channel (Jiang et al., 2003) was not native, because of the loose connection between pore unit and voltage sensor mentioned above. This led to a long controversy dealing with the paddle model suggested by the MacKinnon group and the rotating helix supported by Bezanilla (2000). Recently, the water-filled crevices focusing the field as suggested by Bezanilla seem to come back on the scene (Jogini and Roux, 2007; Sands and Sansom, 2007).

Further details of channel structure are discussed in subsequent chapters together with the results of this thesis.

2.3. Drawing the line: Differentiation between gating and permeation effects

Permeation and gating are the two mechanisms of channel function which determine the average current through a channel and thus determine its functions in the organism. The separation of these two processes is a major topic of this thesis. The mechanism of permeation determines the average time an ion requires for passing through the channel. Thus it determines the value of the true single-channel current (exact definition see section 4.1.1). The mechanisms of gating result in interruptions of the current flow.

Nowadays, the distinction between permeation and gating mechanisms may become difficult, as both processes are known to be related to conformational changes in the channel protein as discussed in more detail below.

Here the following definitions are given:
Permeation: During the passage of a single ion, the protein undergoes conformational changes. If these changes come back to the initial state during the average time for the passage of a single ion, then these conformational changes belong to the mechanism of permeation.
Gating: If the conformational changes of the protein last for a time longer than the average time of the transition of a single ion, then they are related to the mechanism of gating. These rearrangements can be brought about by voltage, ligands or any other influence of physical or chemical nature.

Maybe that in near future, the above definitions will no longer be sufficient as discussed in section 2.6.

In section 4.1.1, it will be shown that the distinction between gating and permeation is of great importance for the distinction between true single-channel current and apparent single-channel current, one of the key topics of this thesis.

The distinction between permeation and gating is of great importance for the understanding of the biophysical background of ion transport. Traditionally, anomalies of ion transport like the AMFE (anomalous mole fraction effect), negative slopes in the IV curves or discrepancies between electrical current and ion flux measurements have been described on the basis of permeation effects. For instance, the Hille-Schwarz model (Hille and Schwarz, 1978) and the Wu model (Wu, 1991) explain the AMFE by ion-ion interactions in the pore. The occurrence of the negative slope was assumed to be caused by the presence of blocking ions (e.g., Na^+: Nimigean and Miller, 2002). The concept of single-file diffusion was employed to explain that electrical impedance and tracer measurements of ion fluxes resulted in contradicting result (Hodgkin and Keynes, 1955). The Woodhull model (Woodhull, 1973) suggested the calculation of the depth of a binding site of a blocking ion from the voltage-dependence of blocking.

Improving the temporal resolution of patch clamp analysis it became possible to draw the attention to normally unresolved gating effects. Farokhi et al. (2000) and Hansen et al. (2003) found that the current reduction related to the anomalous mole fraction effect (AMFE) in the dominant K^+ channel of *Chara* is not caused by an effect on true single-channel conductance as e.g., explained by the Hille-Schwarz model (1978), but that it is an artifact resulting from averaging over open and closed states of a rapidly flickering channel. Averaging is introduced by the inevitable anti-aliasing filter of the recording set-up. Klieber and Gradmann (1993) and Draber and Hansen (1994) could show that current reduction and the occurrence of a negative slope in the IV curves of the dominant K^+ channel in *Chara* were caused by fast gating. This fast gating became obvious when the bandwidth of the recording set-up was increased from normally 5 kHz to 20 kHz (Draber and Hansen, 1994). In the case of the Cs^+ effect, also a problem of the Woodhull model became apparent, namely, that the blocking ion Cs^+ had to penetrate non-realistic 110% of the dominant K^+ channel in the *Chara* membrane to reach its binding site (Draber and Hansen, 1994).

2.4. Mechanism of ion permeation and selectivity: "snug fit" vs. "field strength"

In an electrolyte solution, the ions, such as Na^+ and K^+, are hydrated, i. e. surrounded by water molecules in a well-defined and ion-specific geometry (Wedler, 1985). When entering a channel, the ion must almost completely strip its water shell. This is only possible, when the channel provides an environment that helps to compensate for the energy barrier arising from dehydration. Selectivity arises when this compensation (relative to the hydration free energy) is better for one ion type than for another (Noskov and Roux, 2006).

The concept of snug fit came up with the suggestion of Mullins (1959) that the ion channel is a narrow pore that forces the ions to shed part of their water shell and replace it by the pore wall. The origin of selectivity was explained by means of the pore radius, which has to match exactly the hydration radius of the ion. Subsequent to the hypothesis of Mullins, two theories dominated the field: the snug-fit mechanism (Bezanilla and Armstrong, 1972) and the field strength model (Eisenman, 1962).

Bezanilla and Armstrong (1972) divided the pore into a wide non-selective vestibule (the cavity), where the ion remains fully hydrated and and a narrow section forcing the ion to dehydrate completely (the selectivity filter). The authors suggested that: "*The oxygens are fixed rigidly in positions that provide a good fit for a K^+ ion.*" Selectivity arises because the distance of the oxygen atoms provided by the protein exclusively matches the distance of the oxygens in the first water shell of a hydrated K^+ ("K^+" in Fig. 2.4A). Ions of different radius would be very unlikely to enter the channel because of the energetically unfavorable geometry inside the pore ("Na^+" in Fig. 2.4A) in comparison with the hydration shell in the bulk water (Fig. 2.4B).
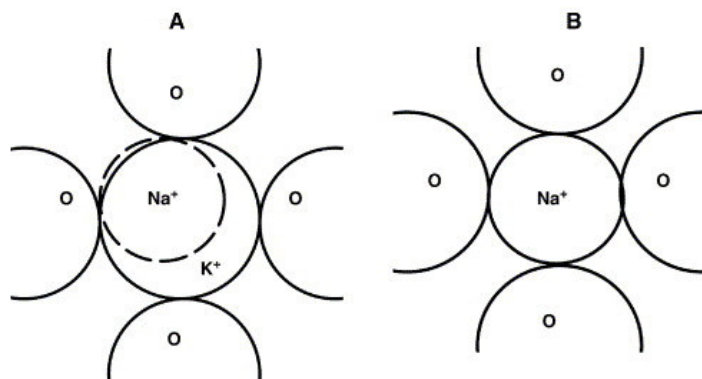
Fig. 2.4. Illustration of the snug fit theory. (A) Simplified representation of a K^+ and Na^+ ion surrounded by 4 oxygen atoms of a proposed coordination cage in the narrowest part of the K^+ pore. (B) Simplified representation of Na^+ solvation shell in water. (Fig. 5 from Noskov and Roux, 2006)

A totally different approach was chosen by Eisenman (1962), who proposed the field strength model of ion selectivity. This was originally developed for the equilibrium selectivity of glass electrodes. Eisenman calculated the electrostatic energy ΔE required for the exchange of one water molecule (from the hydration shell) for a freely movable ligand coordinating the ion:

$$\Delta E = E_{ion-ligand} - E_{ion-water} \qquad (2.1)$$

The energies for different ionic radii were estimated from experimentally obtained dipole strengths for the ligands and water molecules. In this model, the relative energy difference ΔE for different cations is the origin of ion selectivity. Fig. 2.5 shows the calculations for three different dipole strengths of the ligands. High field strength (red triangles) selects for small radii, whereas ligands with low field strength (blue squares) favor larger cations. Based on the assumption that ion channel proteins are highly dynamic structures, Eisenman and Krasne (1973) examined various solvents, coming to the conclusion that the K^+ selective sites probably are constructed by the amide carbonyl groups from the protein backbone.
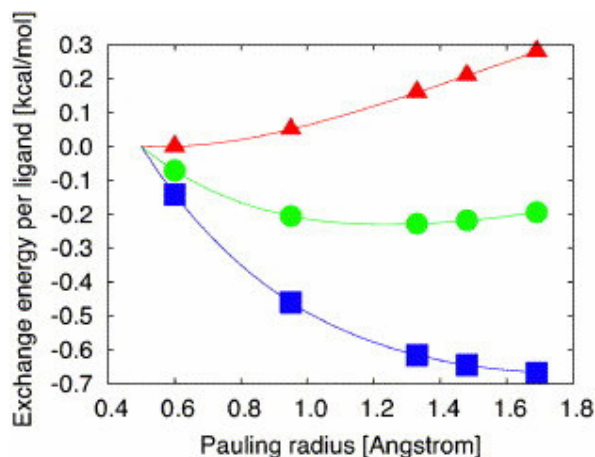
Fig. 2.5. Energy difference caused by removing one water molecule in the first hydration shell of a monovalent cation and replacing it by a carbonyl-like group. The energy is shown for different electric dipoles for the purpose of illustrating the effect of high (red triangles), medium (green circles) and low (blue squares) field strengths on ion selectivity. The circles represent Li^+, Na^+, K^+, Rb^+ and Cs^+ using classical Pauling radii for the cations (Pauling, 1960). (Fig. 4 from Noskov and Roux, 2006)

These two conflicting theories were summed up concisely by Hille (1973): The snug fit mechanism assumes that "*the narrow part of the channel is a barrier to sodium because the dipoles (carbonyl groups) of the wall are held rigidly at the diameter of a K^+ ion (2.66 Å) and cannot all approach the small Na^+ ion (diameter 1.90 Å) as closely as the dipole of water can in solution*", whereas the concept of field strength "*would be useful if the dipoles of the channel are free to move and can be pulled in by small ions and pushed back by large ones*". In the following years, no novel concepts about ion selectivity were proposed because of the lack of structural information (Noskov and Roux, 2006).

The first crystallographic structure of a potassium channel (Doyle et al., 1998) finally triggered a new (and still ongoing) wave of publications on this topic. The structure of the selectivity filter, with the carbonyl-oxygens surrounding the ions in a precisely ordered configuration seemed to prove the snug fit hypothesis. This concept of a rigid selectivity filter was adopted by many authors (Hille et al., 1999; Yellen, 2002; Armstrong, 2003; Beckstein et al., 2003; Garofoli, 2003; Ban et al., 2004).

However, proteins, as most biological macromolecules, are not rigid. Numerous X-ray-diffraction and MD-simulation studies confirmed that the fluctuations in the selectivity filter of the KcsA channel are in the order of 0.75-1.0 Å (Guidoni et al., 2000; Shrivastava et al., 2002; Compoint et al., 2004; Noskov et al., 2004). These

findings clearly contradict the snug fit theory. Moreover, Allen et al. (2004) found that in some places the channel diameter is too small for water molecules and ions. Therefore, some structural flexibility is essential for ion conduction.

Slowly, the analysis of crystal structure and MD simulations led to a convergence of both models. Varma and Rempe (2007) found a narrow window of flexibility within which the selectivity filter achieves selective K^+ ion partitioning. If the filter were too rigid K^+ ions could never physically partition from one binding site to another. If the filter were too flexible like a liquid, K^+/Na^+ selectivity could not occur. Similarly, MD simulations done by Roux show that the design of the selectivity filter is a compromise between high selectivity (rigid structure, snug fit) and mobility (Noskov et al., 2004; Noskov and Roux, 2006). The simulations have shown that only K^+ occupies the well-ordered S0 to S4 positions in the filter. Na^+ (Kast et al., 2008) and also Rb^+ (Morais-Cabral et al., 2001) coordinate at intermediate sites leading to different activation energies of permeation.

An experimental access to different structural changes induced by K^+ and Na^+ was obtained from intrinsic tryptophane fluorescence (Renart et al., 2006). Together with the MD simulations mentioned above, these results indicate that the snug fit concept of almost absolute maintenance of the protein structure as found by Zhou and MacKinnon (2003) in KcsA crystals does not hold and that the flexibility of the protein is higher than suggested by crystal structure analysis.

The state of research regarding flexibility of the channel as a putative source of gating will be discussed in more detail in chapter 6 and 7 together with the results of this thesis. Flexibility is of great importance for the investigations here which seek to understand gating and its relationship to ion-channel interactions. It is the basis for the gating models in chapters 6 and 7 (Schroeder and Hansen, 2007; Schroeder and Hansen, 2008).

2.5. Ion channel gating

Gating is the major determinant of the physiological function of channels. Drugs and cellular messengers do not influence single-channel conductivity, but gating. Failure of channel function which leads to channelopathies (Lehmann-Horn and Jurkat-Rott, 1999; Ashcroft, 2000; Shieh et al., 2000) is related to defects in channel insertion into the membrane (e.g., SUR-KATP: Partridge et al., 2001) or to modifications in gating behavior (examples in Lehmann-Horn and Jurkatt-Rott, 1999; Ashcroft, 2000). Thus, the investigation of gating is a major field in medical research. The role of gating for the understanding of physical mechanisms is a major topic of the investigations presented in chapters 6 to 8.

2.5.1. Three gates

Until now, there are three known gates in K^+ channels which contribute to the modulation of average current:
1. N-terminal ball-and-chain mechanism,
2. Inner gate,
3. Selectivity filter.
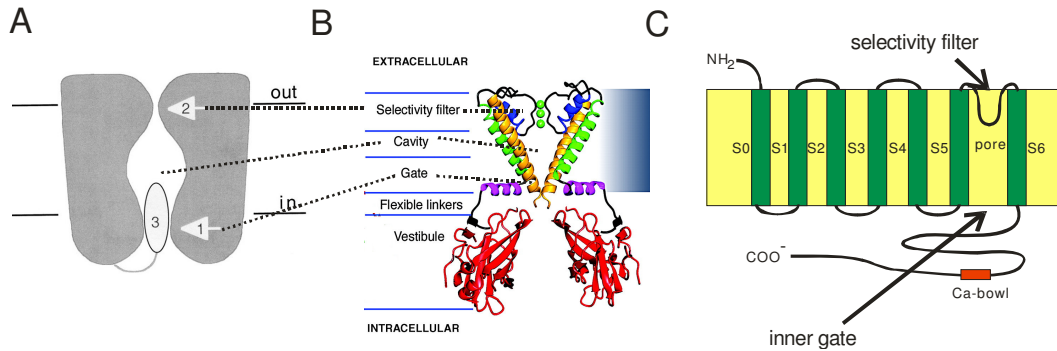
Fig. 2.6. (A) Schematic presentation of the gates in an ion channel (Zheng et al., 2001). 1: Inner gate, closing the inner pore. It can be operated via the flexible linkers in (B); 2: Selectivity filter (section 2.5.2) which is of major importance in this thesis; 3: "ball-and-chain", which is a finger in K⁺ channels (N-terminus, Bentrop et al., 2001) or a hinged lid in Na⁺ channels (Catterall, 2000). This gate is not present in KirBac1.1 (B, Kuo et al., 2003) or MaxiK (C).

The term "**ball-and-chain mechanism**" was coined by Armstrong et al. (1973). It plays an important role in inactivation processes especially during action potentials of nerves (Catterall, 2000). The suggestion of Armstrong et al. (1973) was correct with respect to the fact that the inner mouth of the channel was closed by a movable part (Hoshi et al., 1990; Zhou et al., 2001a). Structure analysis revealed that it is actually a finger-like structure in K⁺ channels (Bentrop et al., 2001) or a hinged lid (the loop between domain III and IV) in Na⁺ channels (Catterall, 2000). This gate does not play a role in the investigations here because MaxiK channels have 7 helices per subunit (Fig. 2.6C), thus locating the N-terminus at the luminal side (Koval et al., 2007).

The **inner gate**, too, is located at the cytosolic mouth of the channel. It can fluctuate spontaneously, pH controlled (Blunck et al., 2006) or, in the case of voltage-gated channels, its opening is coupled to the movement of the voltage sensor S4 (Papazian, 2004). So far, 4 different mechanisms have been identified to operate the inner gate. Best-known is "bundle crossing" caused by the bending of the inner helices (S6 or TM2) at a glycine hinge (Zhao et al., 2004). Bundle crossing is found in most ion channels like KcsA (Perozo et al., 1999), NaChBac (Zhao et al., 2004), MthK, (Jiang et al., 2002b) and *Shaker* (del Camino and Yellen, 2001). A different version of this mechanism is found in the virus-encoded Kcv. Here, Molecular Dynamics simulations suggest that the N-terminal segment attached to TM1/S6 forms the inner gate (Tayefeh et al., 2007). The TM2 helices furnish also the gate of the nicotinic ACh receptor from Torpedo ray, but here the TM2 helices are rotated (Unwin, 1995; Miyazawa et al., 2003; Doyle, 2004). In contrast, the bacterial MscL tilts the TM1 helices (Sukharev et al., 2001; Perozo et al., 2002; Doyle, 2004).

An experimental benefit of the inner gate is that its open state can directly be monitored by TMRM (Tetramethylrhodamine maleimide) fluorescence lifetime measurements (Blunck et al., 2006) or by ESR after cysteine labelling (Perozo et al., 1999; Perozo et al., 2001). The long-living states of the "full" Markov model (chapter 8) of gating are probably related to the inner gate.

Gating by the **selectivity filter** was clearly shown in experiments where gating was observed even though the inner gate was locked in the open state by acidic pH. Blunck et al. (2006) employed fluorescence measurements to prove that KcsA was really open when patch clamp records definitely showed gating. In GIRK channels,

gating of the selectivity filter became obvious when the inner gate was locked in the open state by mutations (V188G, Yi et al., 2001).

There are several types of gating associated with the selectivity filter. The best-known one is C-inactivation (Choi et al., 1991; Lopez-Barneo et al., 1993; Starkus et al., 1997; Kurata and Fedida, 2006) which closes the channel after prolonged depolarization. It is promoted by low K^+, and thus is also called a foot-in-the-door effect (Gibor et al., 2007).

In the LQT mutant L273F of KCNQ1, two types of selectivity filter-mediated inactivation mechanism were found (Gibor et al., 2007). The fast one also occurring in WT was voltage-independent and had little effect on current. It became obvious only in the tail currents. The slow one was voltage-dependent. In contrast to C-inactivation, this kind of gating was promoted by elevated concentrations of external K^+. This acceleration of inactivation by external K^+ was also found in Kv4 channels (Jerng and Covarrubias, 1997; Jerng et al., 1999; Bahring et al., 2001) and in Kv2.1 (Immke et al., 1999).

Involvement of the selectivity filter in very fast gating as postulated by Schroeder and Hansen (2007; 2008) and in chapters 6 and 7 was found in Kir channels (Proks et al., 2001; Claydon et al., 2003; Xie et al., 2004). Furthermore, the occurrence of subconductance levels during channel opening and deactivation in the T442S mutant of *Shaker* (Zheng and Sigworth, 1998; Zheng et al., 2001) was considered to be related to fast structural changes in the selectivity filter.

In this thesis, the selectivity filter is in the focus of the research. Thus, the present state of research regarding selectivity filter gating is described in more detail in the next section and in chapters 6 and 7.

2.5.2. Selectivity filter gating

2.5.2.1. Foot in the door – interaction of permeant ion and selectivity filter

Early hints to the interaction between permeant ion and channel structure came from the effect of the permeant ion on gating. Almers and Armstrong (1980) observed in squid axons "that a K^+ channel is normally occupied by one or more small cations, and becomes non-functional when these cations are removed". This so-called "foot-in-the-door-effect" (Yeh and Armstrong, 1978) or "modulation of gating by a site inside the pore" (Matteson and Swenson, 1986) has been verified by a plethora of papers up to now in different kinds of channel (e.g., K^+ channel in squid: Swenson and Armstrong (1981); delayed rectifier: Spruce et al. (1989); MaxiK: Demo and Yellen (1992); *Shaker*: Melishchuk et al. (1998); KcsA: LeMasurier et al. (2001); *Shaker* and Shab: Ambriz-Rivas et al. (2005); Kv2.1: Immke et al. (1999); Wood and Korn (2000); Kv1.5: Wang et al. (2000)). Constriction of the filter is indicated by the conduction of Na^+ in the absence of K^+ (Immke et al., 1999).

2.5.2.2. Molecular moieties of the selectivity filter involved in gating

As mentioned in the previous section, there are several mechanisms of gating which involve structural changes of the selectivity filter. Even though this work concentrates on fast gating, also the structural background of the other mechanisms will be

mentioned here. It cannot be excluded that structural changes in one place of the filter will not influence the gating of another moiety. Furthermore, the investigations show what kinds of methods are available to reveal the involved molecular mechanisms.

Several interesting features are known from C-inactivation. Kiss et al. (1999) showed that during C-inactivation the selectivity of the channel changed from K^+ to Na^+ selectivity. In line with the snug fit hypothesis (see section 2.4), this is caused by narrowing the tryptophane ring supporting the selectivity filter (Larsson and Elinder, 2000; Loots and Isacoff, 2000). Here, the concept of filter-backbone interaction comes into play. The change in gating behavior was brought about by S4-induced shifting of hydrogen bonds from E418 on S5 to V541 or V453 on the pore loop causing the contraction of the aromatic cuff. Another indication of backbone-pore interaction was found by Ogielska and Aldrich (1998; 1999): A bridge between V443 neighboring the GYG motif and T469 on the S6 helix of *Shaker* influences C-Inactivation as well as Na^+ conductivity at K^+ depletion. Interactions between helix S6 and the permeation path are also known from other channels, e.g., in CFTR (Tabcharani et al., 1993).

Gibor et al. (2007) employed mutational studies and MD simulations to reveal the mechanism of the slow inactivation in the LQT mutant L273F of KCNQ. They found that the oxygens of the carbonyl groups of the S1 position in the selectivity filter come closer. The resulting tighter coordination of K^+ (or Ba^{2+} used as an indicator) in position S1 hinders dehydration/resolvation, thus trapping the ions in the S1 position. Interesting is the inspection of the kurtosis, the 4th moment of the distribution function of carbonyl-carbonyl distances. Its value is small in inactivating mutants, thus providing a too small number of events in the tail of the distribution. This reduced flexibility causes a decrease in "breathing motions" of the filter and leads to an increase of the time K^+ resides in the filter. Also in the investigations of Gibor et al. (2007), the importance of bridges (H-bonds or carboxy-carboxylate) to different parts of the protein backbone (e.g., indicated by the mutations E295A in the turret (Fig.2.2)), D371A in the outer pore vestibule, V310G in the pore helix) becomes obvious.

The role of the "cuff" and the S1 position for C-inactivation seems also be indicated in studies of Somodi et al. (2004) in Kv1.3 dealing with protonation of His399 located 3 residues upstream of GYG. The same position in a *Shaker* mutant (T449C) slows down C-inactivation when binding to Cd^{2+} (Yellen et al., 1994).

In the case of fast gating the interaction between permeant ion and pore structure has to be investigated. Searching for a mechanism mediating the influence of the ionic milieu on filter stability, it is tempting to assume a mechanism similar to the collapse of the selectivity filter of KcsA channels crystallized at very low K^+ concentrations (3 mM, Zhou et al., 2001b). This structure with flipped backbone carbonyl groups is similar to that predicted in molecular dynamics simulations of V127T mutations of Kir6.2 (Capener et al., 2003). Bernèche and Roux (2005) found in free energy molecular dynamics simulations of the filter of KcsA that the occupation of the S2 position by a K^+ ion is important for preventing the 180°-turn of a single V76 - G77 amide plane followed by reorientation of the plane T75 - V76. Relaxation from this stable non-conducting state of broken symmetry is expected to be in the range of 0.1 ms, far too slow for the events observed here. In our paper Schroeder and Hansen (2007 and chapter 6) we found it tempting to assign the fast flickering at positive membrane potentials to the metastable reorientation of the V76-G77 amide plane. However, further experimental work is required to prove whether this or other mechanisms are the origin of the fast flickering.

A snapshot of the postulated induction of flickering in dependence on ion concentration seems to have been found in KcsA crystals grown in Tl^+ solutions around

a midpoint concentration of 80 mM. The selectivity filter is poorly defined in these structures, but ion occupancy measurements indicate that about half the channels in the crystal are in the conductive and half in the collapsed state (Zhou and MacKinnon, 2003). However structural data from the filter in K^+ concentrations in the critical range between 3 and 200 mM are not yet available, in contrast to ion distributions (Morais-Cabral et al., 2001).

The ion-induced structural rearrangements (Capener et al., 2003) related to fast gating of the selectivity filter are different from those described above for slow inactivation processes like C-inactivation. In contrast to C-inactivation, there is no obvious relationship between fast flickering and selectivity as shown in molecular dynamics calculations (Khalili-Araghi et al., 2006) and in physiological studies on mutants of the GYG motif (Lu et al., 2001a). Nevertheless, as C-inactivation also occurs in the selectivity filter not far away from the putative locus of fast gating it seems to be useful to include also the results obtained from the study of C-inactivation in the guidelines for planning future experiments dealing with fast gating.

2.5.2.3. Ion binding in the cavity

In the case of our results obtained in mixed solutions (K^+/Tl^+, chapter 7, Schroeder and Hansen (2008), but also in K^+/Cs^+) we had to consider also ion enrichment in the cavity. In chapter 7 it is shown that fast gating in the presence of Tl^+ seems to be modulated by two different binding sites. The exponential increase with voltage is assumed to be caused by depletion at the luminal side of the selectivity filter, aggravated by the presence of Tl^+. This aggravation, the finding of different characteristic voltages of the increase of the gating factor with voltage and a small decrease in single-channel conductance for different Tl^+ concentrations seems to be mediated by a second binding site. This second site of ion-channel interaction is located at the inner sites of the selectivity filter or in the cavity.

There are several indications that ions can modulate single-channel conductivity and gating at both places. Thus, it is worthwhile to consider what is already known about sites in the cavity and in the filter

According to Zhou and MacKinnon (2003), Tl^+ occupies the same binding sites in the KcsA filter as K^+ does, but with higher average occupancy (0.63 for Tl^+ instead of 0.53 for K^+), in contrast to Rb^+ and Cs^+. The cavity is entered by ions in a fully hydrated form. The ions become partly stabilized near the inner mouth of the narrower selectivity filter by the four dipolar pore helices, which point their negatively charged C-terminal ends towards the hydrated ions (Renart et al., 2006). In some studies, the cavity ion was found to be involved in blocking effects. For instance, Nimigean and Miller (2002) postulated a site in the cavity which is 5 to 7-fold more selective for K^+ than for Na^+, but still mediates a block of K^+ flux at high positive potentials (negative slope) when Na^+ is present. In crystal structure analysis of the Ba^{2+} block in KcsA (Zhou and MacKinnon, 2003), the cavity ion has the role of an internal lock for the Ba^{2+} ion in the inner filter position. Guidoni et al. (2000) employed MD simulations to study the role of the ion in the cavity in stabilizing the two K^+ ions in the filter. Such an effect is involved in the non-selective S177W mutant of the Kir3.2 channel. It becomes K^+ selective when the pore-facing TM2 residues in the central cavity are replaced with negatively charged amino acids, i.e., Asp or Glu (Bichet et al., 2006).

However, all these effects are based on ion-ion interactions and are not of the kind we are looking for, namely an influence of a cavity binding site on filter dynamics. Lu

net al. (2001b) found that the interaction of Tl^+ with at least three C169 in the cavity of Kir2.1 causes a slow decay of single-channel conductance and leads to subconductance states. According to our experience (Schroeder and Hansen, 2007), this decay of single-channel conductance and the occurrence of subconductance levels should be investigated with respect to the involvement of fast gating which becomes feasible because of the high temporal resolution achieved by the work described in chapter 5. The putative role of ion binding in the cavity is discussed in more detail in chapter 7 and by Schroeder and Hansen (2008).

2.5.2.4. Coupling between the gates

As mentioned above, backbone-selectivity filter interaction is a major determinant of the gating properties of the selectivity filter. Interactions from residues of a protein to distant gates are well-known in channel research. The most famous phenomena are Ca^{2+} binding in the Ca^{2+} bowl downstream of RCK2 in the hanging gondola in MaxiK channels (Moss and Magleby, 2001), the effect of the interaction with ions and negative charges also in the hanging gondola of different kinds of channel (Xie et al., 2004; Yeh et al., 2005; Fujiwara and Kubo, 2006) and the action of S4 movement on C-inactivation as mentioned in section 2.5.2.2. Long-range effects on selectivity and gating of the selectivity filter may be become important, as found in the following studies.

In the investigations of C-inactivation which starts after pH-induced opening of the inner gate, evidence for a coupling between the selectivity filter and the inner gate came from the usage of mutants (Blunck et al., 2006; Cordero-Morales et al., 2006b). The mutants E71A and A73E increase open probability of the filter. The bridge E71-D80 (inner part and outer part of the filter) destabilizes the filter and facilitates C-inactivation. A71-G99 (filter-TM2) couples TM2 movement to C-inactivation. When the inner gate is closed, the selectivity filter is kept open by residues M96 and G99 on TM2 adjacent to A73. When the inner gate opens these residues move away, and A73 can relax, and thus induces C-inactivation. In A73E, the more voluminous E prevents the relaxation of the filter. This is consistent with findings for the bacterial NaChBac: Inactivation is not dependent on the position of the voltage-sensor (Blunck et al., 2004; Pavlov et al., 2005). Zhao et al. (2004) could prevent inactivation by the mutation G219P in NaChBac (corresponding to G99 in KcsA).

Coupling between different loci in the protein is also indicated by the observation of Li et al. (2003) i.e., that the mutations V561A on the intracellular end of the S6-helix of Kv1.4 caused speeding of inactivation upon increasing $[K^+]_O$. The locus of the mutation indicates a coupling between inner and outer gates via backbone changes.

These experiments clearly demonstrate that the gating behavior of the selectivity filter is determined by filter-backbone interactions. Thus, such interactions have also to be considered when fast gating in the selectivity filter is to be investigated.

2.5.2.5. Diffusion limitations at the entrances of the channel

In the model of Schroeder and Hansen (2007) described in chapter 6, ion depletion in the selectivity filter and cavity is caused at high positive membrane potentials by diffusion limitation at the cytosolic side. This hypothesis is supported by the influence of different cytosolic concentrations of K^+ (Fig. 6.6).

Brelidze and Magleby (2005) reduced the mobility for K^+ ions by adding different kinds of sugars and found a correlation between single-channel current and diffusion limitation. Our own experiments did not yield the expected effect on fast gating, but further effects, e.g., the direct interaction of the sugars with the protein cannot be ruled out to be the reason for this discrepancy.

Other approaches deal with the modification of the charges on the cytosolic and the luminal entrances. Negative charges at the pore mouth lower the energy barrier for the entrance of ions into the pore (Green and Andersen, 1991) and thus weaken diffusion limitation. Indeed, channels with high conductance carry negative charges at the cytosolic mouth of the pore (Kcv: Tayefeh et al., 2007), and these charges clearly determine the saturation current (MaxiK: Brelidze et al., 2003; MaxiK, MthK: Nimigean et al., 2003). They are absent in low-conductance channels like Kir (Durell and Guy, 2001). In addition, the negative charges in the more distant hanging gondola contribute to the enhancement of current (Xie et al., 2004; Yeh et al., 2005; Fujiwara and Kubo, 2006).

Diffusion limitation at the luminal side seems to be less severe. In chapter 6 (Schroeder and Hansen, 2007), slight indications of gating at negative potentials are ignored. However, in the subsequent investigation (chapter 7) of the Tl^+ effect (Schroeder and Hansen, 2008), fast gating causing an apparent reduction of inward currents became obvious. This is supported by experiments where the luminal negative charges in a mutant of Kir2.1 were neutralized (Alagem et al., 2001; Murata et al., 2002). Similarly, the D992N mutation of MaxiK (Haug et al., 2004) decreased inward current.

An important step ahead in understanding the role of negative charges at the pore mouth was achieved by MD simulation at the cytosolic entrance of Kcv (Rosenberg, 2006). By examining the entropy of the simulated structures, Rosenberg calculated the K^+ distribution at the luminal channel mouth (Fig. 2.7). Partial neutralization of the negative charges (D45N) significantly changed these distributions; the outer pore mouth became less attractive for the ions. The entropy values in the simulations turned out to be directly correlated with the activity (i. e. conductivity) of the channels in patch clamp experiments.
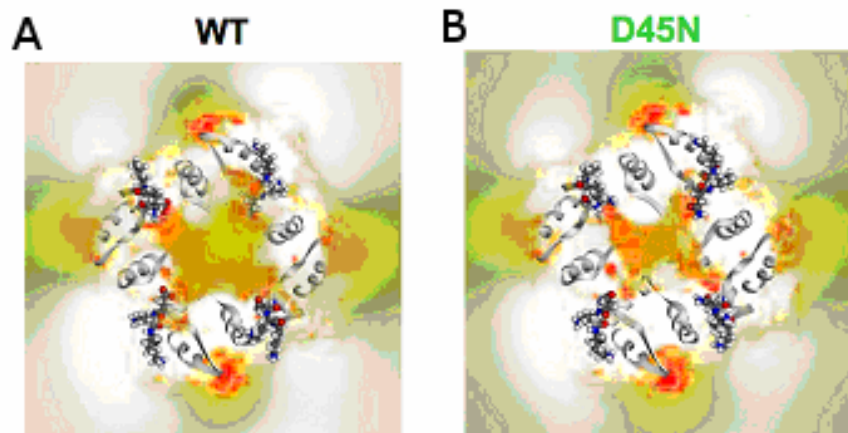
Fig. 2.7. Distribution of K^+ ions at the outer pore mouth of Kcv. Red: high attractivity for K^+, yellow: low. (from Rosenberg, 2006)

More details about diffusion limitation at the entrances of the channel are discussed in chapters 6 and 7 and by Schroeder and Hansen (2007; 2008).

2.5.2.6. Multiple ion binding sites

In the dominant *Chara* channel (Schroeder, 2003) as well as in MaxiK (this thesis), several effects of Tl^+ were found:

1. Gating effect: fast gating with luminal Tl^+ at high negative potentials in MaxiK or gating-induced AMFE in *Chara* (Farokhi et al., 2000).
2. Gating effect: luminal and cytosolic Tl^+ changed the slow gating in MaxiK and *Chara* (chapter 8).
3. Permeation effect with luminal Tl^+: In MaxiK, there was a decrease of true single-channel current; in *Chara* luminal Tl^+ destroyed the AMFE induced by cytosolic Tl^+.
4. Permeation effect with cytosolic Tl^+: In MaxiK, there was a slight AMFE (data not shown), in *Chara* cytosolic Tl^+ increased the channel's conductivity.

These effects are not yet fully understood. Future research has to aim at an identification of the (probably different) bindings sites which mediate these effects. The following results may provide guidelines:

Renart et al. (2006) reported on direct effects of Na^+ and K^+ on KcsA in both detergent-solubilized and membrane-bound forms. Monitoring the changes in the protein intrinsic fluorescence revealed that the two ions bind competitively to KcsA with distinct affinities (K^+ having a 20 – 25-fold higher affinity than Na^+), leading to different conformations of the ion-bound KcsA complexes. Whereas this finding could partly explain ion selectivity by this channel, it could not explain either functional sodium blockade, or the effects of fairly low Na^+ concentrations on the structure and stability of KcsA. The latter was observed by infrared spectroscopy but not by fluorescence, and the authors conclude that this should involve a second class of ion binding sites.

2.6. Blurring the line: Coupling of permeation and gating

Even though several authors correctly draw the attention to the necessity of distinguishing between permeation and gating (Hille, 1992; Hansen et al., 1997; Townsend and Horn, 1999) these two features may become coupled. The following scenario may illustrate the problem: Imagine that the conformational changes leading to gating in the selectivity filter are well identified and fulfill the definition in section 2.3. The rate constants of the underlying processes depend on experimental parameters. Now, a parameter set may occur that the frequency of the conformational changes become higher than the average transition frequency for a single ion. It is still the well identified gating mechanism, but it starts to interfere with the transition of a single ion. Nevertheless, the temporal resolution required for studying this kind of effects has not yet been reached. Thus, the definitions of permeation and gating in section 2.3 can be accepted as useful working definitions. In chapter 6 (Schroeder and Hansen, 2007), open times of the channel were less than 0.5 µs implying that at a current of 16 pA only 50 ions pass the channel during one open period. Faster protein vibrations may reach the

time of the transition of a single ion, especially at a lower current of e.g., 1.6 pA. Furthermore, changing the dynamic properties of a system (spring constant) changes not only the oscillation frequencies but also the amplitudes, which may lead to a different conductance in a non-linear system.

In chapter 7, an effect of Tl^+ on fast gating and on single-channel current is described. Up to now, it is unknown whether these two effects have the same origin. A mechanism as mentioned above may be considered.

3. Methods: Cell culture and patch clamp technique

Summary. The biological objects used in the investigations here were MaxiK channels expressed in HEK cells and the dominant K$^+$ channel in the vacuolar membrane in *Chara*. The main electrophysiological techniques are described, including the principles of current and voltage clamp, the different configurations of the patch clamp technique and the basic circuit design of the Dagan patch clamp amplifier. The excellent signal-to-noise ratio which was crucial for the results in this thesis was obtained by optimizing the grounding of the set-up and by pipette handling as developed in preceding investigations in the lab. A new result is the determination of the temporal resolution of the Dagan amplifier, which is not as good as advertised by the company.

3.1. Subjects of measurements

3.1.1. Chara
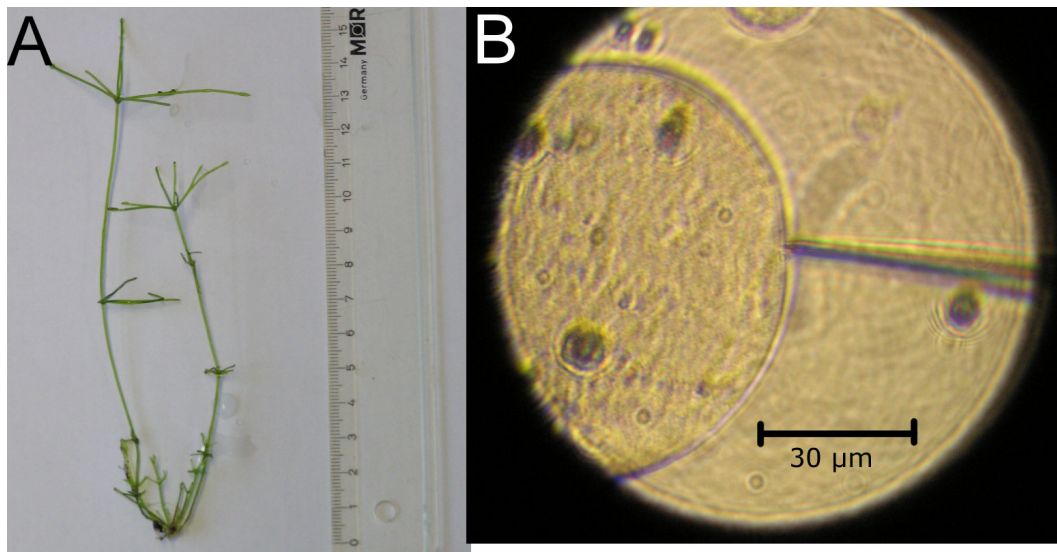
Fig. 3.1. *Chara corallina* (A) whole plant (B) tonoplast vesicle with chloroplasts under the microscope with patch pipette

Culturing of the algae
The freshwater algae *Chara corallina* and its relative *Nitella flexilis* are traditional subjects of electrophysiology: When no squid axons were available, the large internodial cells of characeans were used (e.g., Cole and Curtis, 1938, 1939; Cole and Moore, 1960; Cole, 1968; Hansen, 1969). They are similar in shape, and the quite different mechanism of the action potential could not be recognized at that time (Wacke et al., 2003).

All Characea have large, multinucleated internodial cells (in the case of *Chara corallina* usually 5 - 20 cm long and 0.5 - 1 mm thick) and smaller radial cells. They are also called stoneworts because of their habit of creating a lime crust in water containing calcium carbonate. The algae for the experiments in sections 5.1.3.4 and 5.2.4 were grown at room temperature in tap water in 60-l plastic tubs on a mixture of decomposed

beech leaves and garden turf, covered with sand. An ordinary light bulb was used for illumination 12 hrs per day. The light intensity was approximately 100 µ mole cm^{-2} s^{-1}.

Vesicle preparation
A fully grown internodial cell is taken out of the water and left to wilt on tissue paper. Once the turgor is sufficiently reduced, the cell is cut open directly over the petri dish filled with the measuring solution. The cytosol flows out of the cell, and droplets of 50 – 500 µm in diameter settle on the ground after a few minutes. These droplets are surrounded by a tonoplast membrane (Lühring, 1986; Sakano and Tazawa, 1986).

The dominant potassium channel in the tonoplast
The dominant potassium channel in the vacuolar membrane of *Chara* has been extensively studied in the past (e. g., Tester, 1988; Klieber and Gradmann, 1993; Draber and Hansen, 1994; Farokhi et al., 2000). *Chara* genes have not been cloned yet, but the channel presumably belongs to the same family as the mammalian MaxiK channel (next section). It shows the typical calcium activation, high single-channel conductivity and similar responses to drugs (Tester, 1988).

3.1.2. HEK cells with MaxiK channels

Cell culture
HEK293 (ATCC code [www.atcc.org]: CRL-1573) is a permanent cell line obtained from human embryonic kidney cells that were transformed with adenovirus type 5 by Graham et al. (1977). HEK cells grow in adherent monolayers and tend to „clump" after confluency is reached. They are easy to work with; they grow fast and are relatively robust against slight changes in temperature, pH and to the composition of the culture medium.
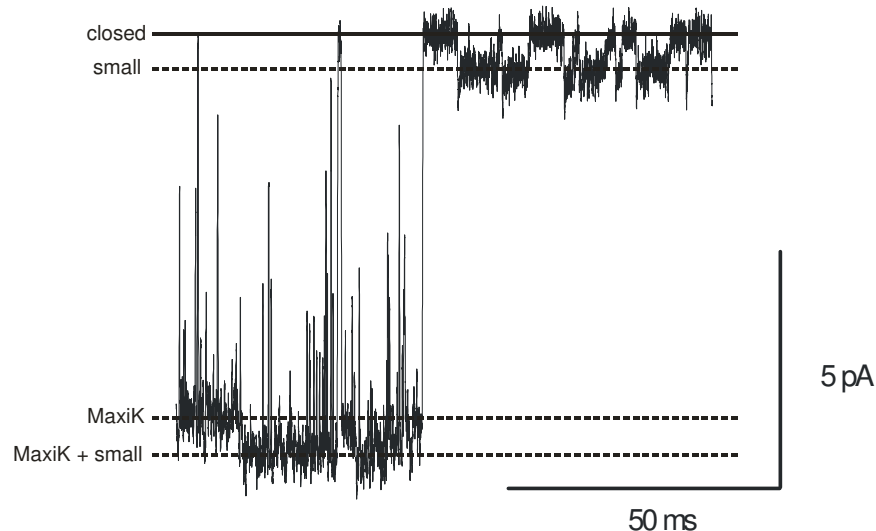
Fig. 3.2. Recording from a HEK cell with a single MaxiK (left) and a small intrinsic (right) channel. Channel openings are presented by downward deflections. Membrane voltage was -60 mV, and 150 mM KCl was on both sides of the membrane.

Stably transfected HEK293 cells were kindly provided by Dr. Andra Schromm, research center Borstel. She transfected the following nucleic acids:

- cDNA of the α-subunit of the human MaxiK potassium channel with a GFP fused to the C-terminus
- cDNA of the β1-subunit of the same channel

Both cDNAs were cloned into the pcDNA3 vector (Invitrogen, Karlsruhe) which codes for a Neomycin resistance and was used to select for transfected cells with G418 (Geneticin). HEK cells have some intrinsic potassium channels, but those can easily be distinguished from MaxiK in the single-channel recordings by their distinctly smaller (~ factor of 10) conductivity (Fig. 3.2).

Several backup vials of the stably transfected strain were kept in liquid nitrogen in the Institute of Biochemistry in the group of Prof. P. Saftig. HEK cells tend to change their properties after several weeks in culture, so a new culture had to be thawed regularly. Freezing with 10% DMSO and thawing was done according to standard protocols (Andra Schromm, personal communication).

The cells were cultivated in an incubator (MCO-17AC, Sanyo/Ewald Innovationstechnik, Bad Nenndorf) at 37°C, 4.5% CO_2 and 100% humidity in 50 ml gas permeable culture flasks (Sarstedt, Nümbrecht). The culture medium (DMEM high glucose, Biochrom, Berlin) was complemented with 10% FCS (Biochrom, Berlin), 1 % Penicillin/Streptomycin (Biochrom, Berlin) and 0.5 mg / ml G418 (Invitrogen, Karlsruhe). It was exchanged every 2-3 days. Cells were split ~ once per week.

Preparation for patch clamp measurements

For patch clamp measurements, cells were transferred in 35 mm petri dishes (Corning, Acton, USA) 16-25 hrs before the experiments to allow them to settle down on the bottom of the dish. The adhesion of HEK cells to the plastic is quite weak; during the preparation for the experiment (section 3.4), they have to be handled with care, because the measurements require cells that are firmly attached to the bottom of the dish.

MaxiK channels

The MaxiK channel is a member of the family of 6 transmembrane – voltage gated potassium channels (Kv), although it has 7 transmembrane helices (see below). The name „MaxiK" (or BK for „big K^+") stems from the characteristically high conductivity of these channels (several hundred sP, depending on the experimental conditions, Latorre et al., 1989). MaxiK is activated by positive membrane voltages. Intracellular Ca^{2+} shifts the activation voltage to more negative potentials, whereas the Ca^{2+} sensitivity spans a wide range from μM-mM concentrations, suggesting the existence of at least two Ca^{2+} binding sites of different affinity (Piskorowski and Aldrich, 2002).

Together with the high single-channel current providing a good signal-to-noise ratio, a second feature makes this channel useful for the investigations here: The S0 helix bring the N-terminus to the luminal side, thus abolishing the inactivation via the ball-and-chain mechanism which follows the voltage activation in all other Kv channels (Bentrop et al., 2001; Li et al., 2003).

MaxiK has not been crystallized yet, but structures are available from channels that are homologue to the different MaxiK domains (Fig. 3.3): The transmembrane domain, i. e., the pore and the voltage sensor are most likely very similar to those of the Shaker channel (Long et al., 2005), another member of the Kv family. A sequence analogue to the intracellular RCK domains can be found in the RCK domains of the

calcium activated channel MthK from *Methanobacterium thermoautotrophicum*, although the homology for the RCK2 domain is quite weak (Jiang et al., 2002a; Giraldez et al., 2005).

MaxiK is regulated by membrane voltage and intracellular Ca^{2+}. Also, it stabilzes membrane voltage close to E_K and thus plays an important role in the coupling of metabolic signals and membrane excitability for body functions like neurotransmission, blood flow, muscle tone, hearing, etc. (Lu et al., 2006). MaxiK often is partnered with different ß-subunits; four of them have been cloned so far. The ß1-subunit present in the experiments here enhances the Ca^{2+} sensitivity of the channel (Orio et al., 2002).
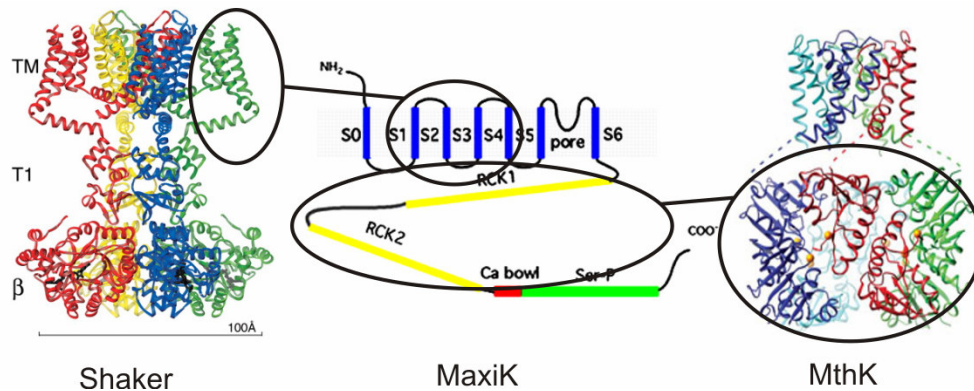
Fig. 3.3. Comparison of MaxiK (center, Giraldez et al., 2005) with homologue channels of known structure. Left: *Shaker* (Long et al., 2005) and MaxiK have the voltage sensing domain S1-S4 in common. Right: The intracellular RCK1 domain of the calcium-gated MthK (Jiang et al., 2002a) is homologue to that of MaxiK.

3.2. Electrophysiological approaches

3.2.1. Current and voltage clamp

For the investigation of the electrical characteristics of biological membranes two standard electrical circuit designs are known: current clamp or voltage clamp.
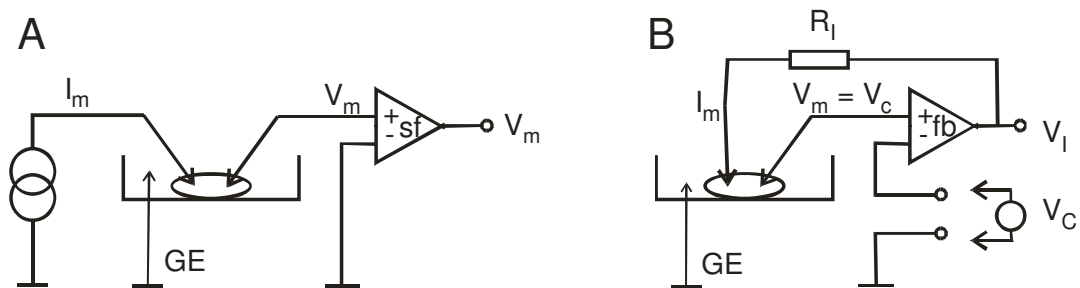
Fig. 3.4. Different modes of electrophysiological measurements with impaled electrodes. (A) current clamp, (B) voltage-clamp. GE = ground electrode, V_m = membrane potential, V_C = command potential, V_I = $R_I I_m$ voltage providing the value of I_m, I_m = membrane current, R_I = feed-back resistor, fb = feed-back amplifier, sf = normal voltage amplifier.

Current clamp is the older approach (Umrath, 1930), although the usage of the name "clamp" is somewhat misleading. There is no sophisticated feed-back loop keeping current constant. Instead, current is injected via the current electrode into the cell from a current source with its output resistance being much higher than the impedance of the biological object. This makes the current constant, i.e., independent of the electrical properties of the biological object. The voltage changes induced by the current are recorded by means of a second electrode, the voltage electrode (Fig. 3.4A). The ground electrode in the bathing medium is common for voltage and current.

Voltage clamp was introduced by Marmont (1949). A feed-back loop was employed which sets the membrane potential of the biological object to the value given by the command potential. This was achieved by adjusting the injected current by means the feed-back loop (Fig. 3.4B).

In Fig. 3.4A,B, current and voltage clamp are shown for recordings from whole cells by means of impaled electrodes, as it was done before Neher and Sakmann (1976) invented the patch clamp technique. The advantages of voltage clamp over current clamp are as follows:

1. When membrane potential is changed, the membrane capacitance C_m of 1 μF cm^{-2} has to be recharged. Under current clamp, the time constant of recharging is $C_m R_m$. With membrane resistances R_m varying between 0.1 to 1000 kΩ cm^2, the time constants can range from 0.1 ms to 1s. Under voltage clamp, R_m is replaced by the resistor of the current injecting pipette and of layers in front of the membrane. These resistances are much smaller than the membrane resistance thus, leading to time constant in the range of μs.
2. Electrophysiologists are interested in the ionic current flowing at a certain membrane potential under certain circumstances. The current obtained under voltage-clamp is a linear sum of the involved ionic currents. In current clamp experiments, the changes in voltage have to be converted mathematically to a change in current by means of often non-linear membrane impedance.

A peculiar version of voltage-clamp (action potential clamp) has been used by Thiel (1995). The time course of the voltage during an action potential in *Chara* was recorded and stored in the computer. Then, one type of ion channel was inactivated by drugs. Now a voltage-clamp experiment was done using the stored time course of the voltage as a command signal. The voltage-clamp amplifier had to generate exactly the current otherwise flowing through the inactivated transporter in order to produce the time course of the command signal at the biological membrane.

3.2.2. Patch clamp technique

Patch clamp (Neher and Sakmann, 1976) is an electrophysiological method that allows the measurement of currents trough the cell membrane or membrane potentials with great accuracy. Neher and Sakmann's accidental (Numberger and Draguhn, 1996) discovery that under certain conditions clean glass electrodes and cell membranes spontaneously form a tight bond (the giga seal) that is both mechanically and electrically stable, revolutionized the field of electrophysiology. It allows low-noise

current recordings with much better resolution than the former employed impalement electrodes.

For the development of this method and "*for their discoveries concerning the function of single ion channels in cells*" (www.nobelprize.org), Neher and Sakmann received the Nobel price in "Physiology or Medicine" in 1991.

Different variations of the technique allow the measurement of both macroscopic currents through the whole membrane of the cell and the tiny currents in the range of 10^{-12} A through a single ion channel. The range of applications is wide. Ion channels (more precisely: mutations of their genes) are the cause of manifold hereditary diseases, such as muscle and heart diseases, mucoviscidosis, several forms of epilepsy and many more (Lehmann-Horn and Jurkat-Rott, 1999; Ashcroft, 2000). Identifying the mutations and their consequences on channel function is the key for better treatment (e. g. the DEND syndrome, Mlynarski et al., 2007). The pharmacological industry widely employs patch clamp as a drug screening method, because many drugs influence the nervous systems whose operation is based on the function of ion channels (pain killers, anesthetics, anti-psychotics, Priest et al., 2007). And from a more academic angle, the properties of the current (e.g., its magnitude, kinetics and responses to external stimuli such as ligands and membrane voltage) provide fundamental insight into the structure and biophysics of the protein.

The formation of a seal requires a clean glass pipette with a very small tip aperture (few µm). It is placed on top or in the immediate vicinity of the cell membrane. The application of a small negative pressure sucks a part of the membrane (the patch) into the pipette and forms the seal. The connection is formed by hydrogen bonds, Ca^{2+} bridges and Van-der-Waals forces (Corey and Stevens, 1983; Opsahl and Webb, 1994). The high leak resistance (up to 1000 GΩ: giga seal) permits low noise current recordings with high temporal resolution. Five patch configurations are distinguished (Fig. 3.5, taken from Hamill et al., 1981):

3.2.2.1. Patch clamp configurations

a) Cell-Attached

The first configuration after the formation of the giga seal is the cell-attached modus. The cell membrane stays intact, and the current through a single or a few channels in their natural environment can be measured. This is advantageous especially in the case of „not-yet-well-investigated" channels which possibly need unknown cofactors like ATP, other membrane proteins or interactions with the cytoskeleton. The disadvantages of this configuration are that only the composition of the luminal solution can be controlled by the experimenter and that the voltage across the seal is the sum of the command potential and the (unknown) resting potential of the cell.

b) Inside-Out

Ripping the patch out of the cell by a quick withdrawal of the pipette from the cell-attached configuration forms an inside-out patch (sometimes called excised patch), exposing the former cytosolic side of the membrane to the bath solution. Usually, the giga seal is stable enough to survive this rough treatment. All measurements in this thesis are done in the inside-out configuration. It allows low-noise single-channel measurements with direct control of membrane voltage and of the solutions on both sides of the membrane.

c) Whole-Cell

To form the whole-cell (wc) configuration, the electrode stays sealed to the cell as in the cell-attached modus. A short voltage pulse or strong suction is applied to break the membrane under the pipette, providing access to the intracellular space. In the wc modus, macroscopic current from all channels of the cell are recorded, making this technique especially useful for screening experiments.

d) Outside-Out

Pulling the pipette back from the whole-cell configuration leads to membrane segments torn away from the cell, but still attached to the pipette. Then, these segments come together and form a new seal which is an outside-out patch with the former cytosolic side of the membrane facing the inside of the pipette. Because there are more steps involved here (and therefore the risk of breaking the seal is increased), most single-channel experiments are rather done in the inside-out modus. Outside-out is the method of choice if the luminal solution (bath) is to be changed during the experiment, e.g., for channels that are controlled by extracellular ligands.

e) Perforated Patch

Whole-cell experiments often suffer from so-called „rundown", i.e., the channel activity decreases over time because needed ligands (mostly ATP) leak from the cell interior into the much larger pipette. This can be circumvented by the perforated patch method (Sala et al., 1991). By adding a small amount (e.g., 100μM) of pore builders, such as gramicidin or nigericin, low-resistance access for ions to the cell is granted, but larger molecules are excluded. Nevertheless, this technique has several drawbacks such as relatively large access resistance (compared to whole cell). Second, the stability of the seal is limited because the induced large pores tend to destabilize the membrane.
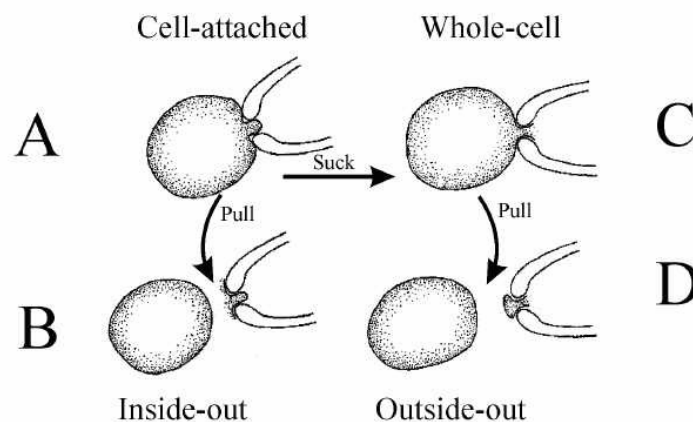
Fig. 3.5. Patch clamp configurations. Descriptions in the text. (Picture taken from: Hille, 1992)

More details about theory and practice of the patch clamp technique, its variations and applications can be found in the literature e.g., Hamill et al. (1981), „Single-Channel Recording" (Sakmann and Neher, 1995) or „Patch-Clamp-Technik" (Numberger and Draguhn, 1996).

3.2.2.2. Electronic circuit for patch clamp

Patch clamp experiments can be performed in the current clamp and in the voltage clamp mode described above with the difference that the electrodes are not impaled, but attached to the membrane. In the case of patch clamp experiments, especially in the single-channel mode, the separation between voltage- and current electrode is no longer necessary, because the resistance of the patch electrode is much smaller than the impedance of the membrane. This makes the handling of electrophysiological experiments much simpler.
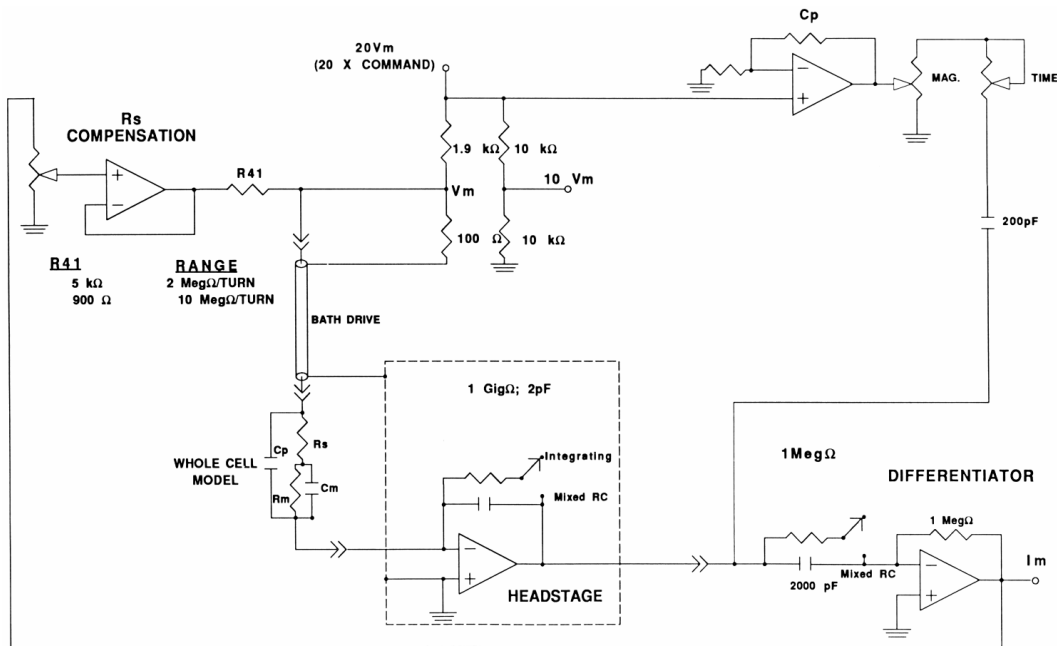
Fig. 3.6. Simplified circuit of the patch clamp amplifier Dagan 3900A in the voltage-clamp modus. The biological membrane is presented by the whole-cell model consisting of two resistors and two capacitors. The headstage is the current/voltage converter. The switch indicates the two options: normal (mixed RC) mode with combined ohmic resistor and capacitor or integrating mode with capacitor only. The subsequent differentiator corrects the over all frequency response. The command voltage is fed into the input "20 Vm" (i.e., the actual command voltage across the membrane is 5 % of the signal fed into "20 Vm". Furthermore the amplifier enables the correction of resistance in series with the biological membrane ("Rs compensation", see whole cell model circuit) by feeding an adequate part of the output signal into the driver voltage for the bath medium, and capacitive compensation for the Cp in the whole cell model by feeding an adequate inverted part of the command signal into the differential amplifier. Source: Manual for the Dagan3900 amplifier.

Fig. 3.6 shows the electronic set-up for the Dagan patch clamp amplifier in voltage clamp mode (as used in this thesis) with the biological object being presented by an equivalent circuit of 2 resistors and 2 capacitors. Patch clamp amplifiers for single-channel recordings are highly sophisticated electronic designs in order to measure pA-currents with a band width of more than 100 kHz and very low amplifier noise.

Reduction of noise of stray capacitances is achieved by bringing the first stage of the amplifier (current/voltage converter) as close as possible to the measuring electrode.

Thus, the head stage is mounted on the manipulator with the patch pipette directly connected to the first transistor (Fig. 3.7 and Fig. 3.8). In order to reduce the weight of the amplifier on the manipulator, head stage and main amplifier are separated.

The Dagan 3900A (Dagan Corp., Minneapolis, USA) employed in the investigations here was for a long time the amplifier with the lowest noise. This was achieved by using a capacitor instead of a resistor in the feed-back loop of the current/voltage converter. This leads to an integrating mode of operation, i.e., to an output signal that increases linearly with time. Because of this, the signal had to be differentiated in the subsequent amplifier stages. The differentiation is not of any concern for the user, it just helps to reach the 100 kHz bandwidth. However, the integrating head stage would suffer from overflow. This is prevented by discharge pulses. These occur in the patch clamp record and have to be eliminated from the time series, mostly by hand in the program *Kiel-Patch*. However, the improvement in noise performance is worth the extra effort.

Furthermore, the Dagan 3900A differs from other amplifiers like the EPC7 (List, Darmstadt, Germany) by the introduction of the command potential in the voltage clamp mode. The negative command potential is fed into the ground electrode of the bathing medium and the input of the current/voltage converter is always kept on ground potential. Further details can be found in the simplified circuit diagram in Fig. 3.6.

3.3. The experimental design

3.3.1. The set-up

A patch clamp set-up has to fulfill several different requirements. First, it has to be protected against mechanical vibration which would detoriate the delicate seals. This is achieved by mounting the set-up on an air-cushioned table (Fig. 3.7). Second, it has to be protected against electrical radiation, especially 50-Hz sine waves. This is achieved by surrounding the set-up by a faraday cage. Here, a huge faraday cage (11 m^2) is used, which allows unhindered access to the set-up. The problem is that instruments powered by 230 V a.c. have to be outside the cage, if possible (see below „Electric shielding and grounding"). A single unearthed wire going through the wall can bring the 50-Hz hum into the cage. The signal from the patch clamp amplifier to the computer outside the cage has to be transferred by a differential amplifier thus excluding the difference between ground inside the cage and ground outside the cage from the signal pathway (Schroeder, 2003). Third, micromanipulators have to be used which enable a smooth docking of the pipette on the cell. Fourth, the patch clamp amplifier has to be able to measure currents in the range of 1 pA.

Here, a set-up was used which was continuously optimized by Draber (1994), Albertsen (1994) and Keunecke (2000). For the investigations reported here, low noise was of crucial importance. This led to a thorough rebuilding of the grounding connections in cooperation with T. Huth (2005). Grounding is voodoo. There are some rules e.g., that star-shaped grounding as recommended by text books may be used for grounding passive elements like manipulators and microscopes, but never for circuitry which is involved in transferring the electric patch clamp signal. The best procedure is as follows: one person touches putative grounding loci, and the other one looks at the oscilloscope and says "better" or "worse". This procedure converges after some days.
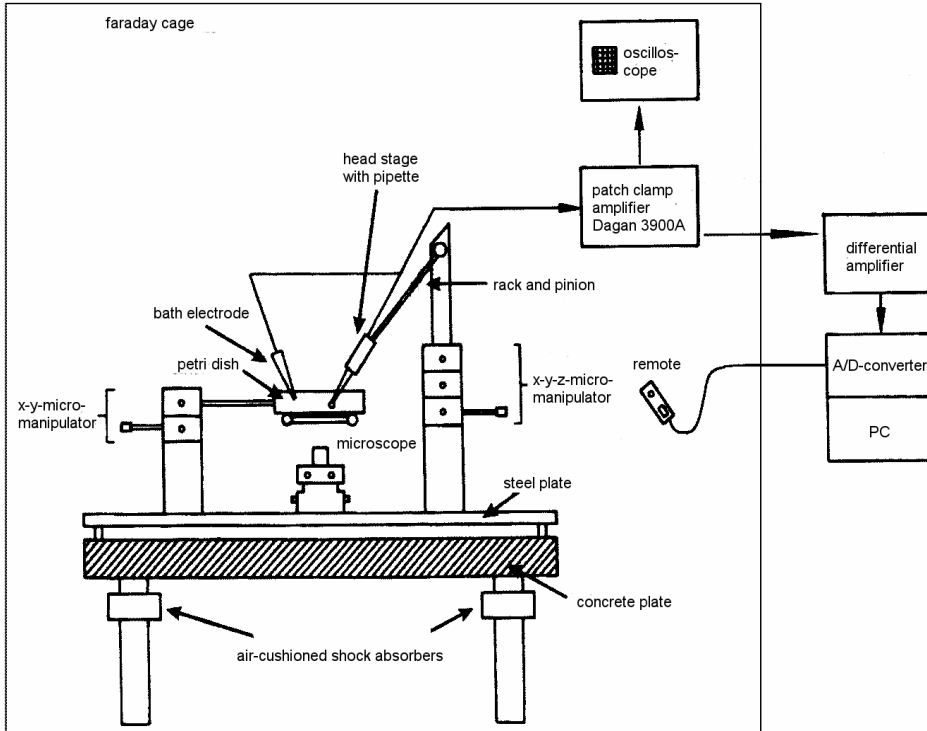
Fig. 3.7. Schematic representation of the patch clamp set-up. The devices are explained in the text.
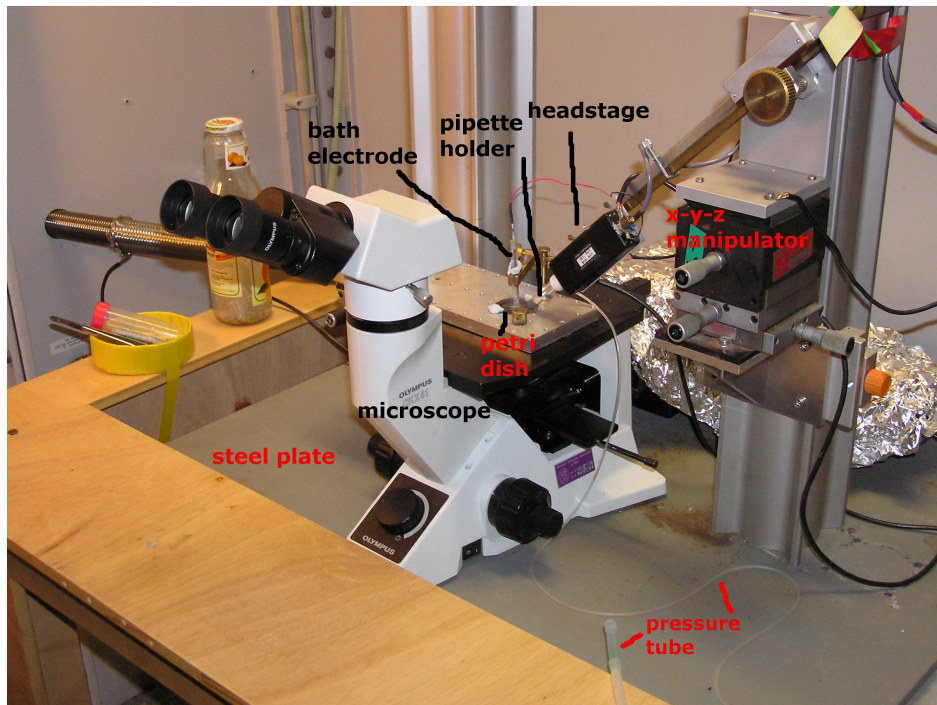
Fig. 3.8. Photograph of the patch clamp setup, cf. Fig. 3.7

Electric shielding and grounding:
The experimental set-up, the amplifier, the oscilloscope and the experimenter were all located in a faraday cage of 11 m^2, in contrast to most other set-ups, where only the set-up on the table (Fig. 3.8) is shielded. Power supplies were outside the cage, and all units were grounded carefully to minimize the electrical noise at the amplifier output. For practical reasons, the amplifier had to be inside the cage. Its 230-V power line was shielded and the grounds for the power supply and the measuring circuits were kept separated. Thereby, 50-Hz hum on the signals could be avoided.

Microscope:
The light source of the inverted microscope (Olympus CKX41, Hamburg, Germany) was removed and neon light from above the cage was used instead, following the motto: less devices and cables = less noise.

Mechanics:
To shield the set-up from mechanical vibrations, it was placed on a concrete plate on an air-cushioned table (Vibraplane9100, Kinetic Systems, MA, USA). A wodden table in front of the setup provides working space without being mechanically coupled to the set-up.

Both the head stage of the amplifier with the pipette (x-y-z) and the holding plate for the petri dish (x-y) were mounted on mechanical micromanipulators. The head stage additionally was mounted on a rack and pinion to allow larger movements. This basic set-up had the advantage that it was very stable with regard to mechanical vibrations which would disturb the measurements.

High and low pressure can be applied to the pipette via a water filled U-tube with a mouth piece and a three-way valve (Fig. 3.8).

Oscilloscope:
The oscilloscope (Philips PM 3215, Hamburg, Germany) was powered by 30 V d.c. from a power supply outside the cage. In order to screen the high-frequency radiation from the high-voltage generator, it was placed in an additional small faraday cage. The shielding was not perfect as can be seen in the noise spectrum in Fig. 3.9, but this had no significant effect in the actual measurements.

3.3.2. Electrodes

3.3.2.1. Manufacturing of the electrodes

Chlorinated silver wires (Ag/AgCl wires, Adam et al., 1988) were used for bath and pipette electrodes, because they are unpolarizable. **Pipette electrodes** were made from 0.3 mm silver wire, bath electrodes from 1 m silver wire. (AG 1000 Degussa Hanau, T. Martens, Dänische Str. 28, 24103 Kiel, Germany). They were chlorinated for 20-30 minutes in 1 M NaCl with 1 mA in a lab-made set-up. Alternatively, electrodes can be chlorinated by immersing them over night in concentrated chlorine bleach liquor („Domestos").

The surface reactions (Cl^- with cations from the solution and Ag^+ with anions from the solution) prevent polarization, i.e., the building of a double layer (Adam et al., 1988) of charges parallel to the electrode surfaces. The electrodes were immerged in

vessels (the pipettes are often also called electrodes), filled with an adequate solution in order to maintain a reproducible environment for the electrode reactions.

Bath electrodes were bigger than the patch pipettes. The chlorinated silver wire was inserted into a shortened Pasteur pipette, filled with 150 mM KCl and 3 % agar. The solution in the electrode was similar to that one used in the bath in order to keep the liquid junction potential small. The agar prevented bulk exchange of the solutions in the electrode and in the bath, especially the contamination of the bath solution with silver ions.

Between the experiments, the bath electrodes were stored at 4°C to prevent molding of the agar. When the electrode potential deviated from 0 mV, or at least after 3 months, electrodes were discarded and replaced by new ones.

Patch pipettes were made from borosilicate glass capillaries ($\emptyset_{in}$ = 0.8 mm, $\emptyset_{out}$ = 1.5 mm, Hilgenberg, Malsfeld, Germany). After cutting them to 6 cm length, the capillaries were coated internally with Sigmacote (chlorinated organopolysiloxane in heptane; Sigma, Taufkirchen, Germany), and left under the exhaust to dry for 3-5 days.

The day before the experiment, pipettes are pulled in a two-step process on an L/M-3P-A puller (List, Darmstadt, Germany). The upper pipette was discarded, because its tip was too long, making it difficult to fill. After filling, the pipette resistance in 150 mM KCl was about 25 – 40 MΩ. Plieth (1996) found in electron microscopy photographs of comparable pipettes that the tip opening was smaller than 1 µm.

3.3.2.2. Reduction of noise by pipette handling

After pulling, the pipettes were dried at 55°C over night (Huth, 2005). The coating with Sigmacote has two effects.

First, the thin polysiloxane layer shields the surface charges of the glass and increases the thickness of the wall. This can reduce the capacitance of about 2 pF mm^{-2} by a factor of 8 (Corey and Stevens, 1983). Pipette capacitance is a major determinant of amplifier noise, and thus its reduction is of crucial importance (Haak, 2000). Keunecke (1995) found that minimizing the immersion depth after docking the membrane to the pipette leads to a tremendous noise reduction. However, in the case of the heated pipettes used here, this did not work. Even worse, often increased capacitive artifacts were observed with the pipette close to the water surface (data not shown). Hence, the technique of Keunecke was not used.

Second, heating the coated pipette over night increased seal probability to virtually 100%, and the seal resistance reached values up to 100 GΩ (Huth, 2005).

3.3.3. Data recording

Data from the patch clamp amplifier were transmitted by a difference amplifier in the wall of the cage. For recording in the computer, they are digitized with a 12-bit analog-digital converter (Dalanco Spry, Rochester, USA). The data acquisition was controlled by the program *sampl250* (Albertsen, 1994). It allowed the recording of time series up to a length of 30 minutes with a sampling frequency of 200 kHz. The start of recording was triggered by a remote switch near the patch clamp set-up. In order to exclude the

difference in noise between the ground of the set-up and the ground of the computers outside the cage from the signal pathway, the signal from the patch clamp amplifier was fed through a differential amplifier in the wall of the faraday cage (Schroeder, 2003).

3.3.4. Testing the set-up

3.3.4.1. Current calibration

The pathway for the signals comprised several units: patch clamp amplifier, differential amplifier, A/D-converter of the computer. In order to make sure that the expected calibration factor was correct, current amplitudes for the analysis in *Kiel-Patch* were manually calibrated with a 10 MΩ resistor. Tests with different square waves and amplification factors proved that the amplifier was linear. The calibration factor was 40 bits/pA at the 50 mV/pA setting of the Dagan 3900A.

3.3.4.2. Noise spectrum

In order to get an estimate of the noise characteristics of the amplifier, the noise spectrum was measured with an ohmic resistor. Fig. 3.9 shows the measured noise spectrum of our patch clamp set-up obtained with a 1 GΩ resistor as "dummy seal". Sampling frequency was 200 kHz, the filter a 4-pole Bessel with a corner frequency of 50 kHz. The frequency response was 1/f until 1000 Hz, then a horizontal range followed until the filter led to a decrease earlier than the nominal 50 kHz (This is examined in more detail in the next section.). The peak at 40 kHz was caused by the oscilloscope. This origin was verified by shutting down the oscilloscope and comparing the spectra. The origin of the peaks above the filter frequency was unknown, probably the measuring computer itself or devices outside of our lab.
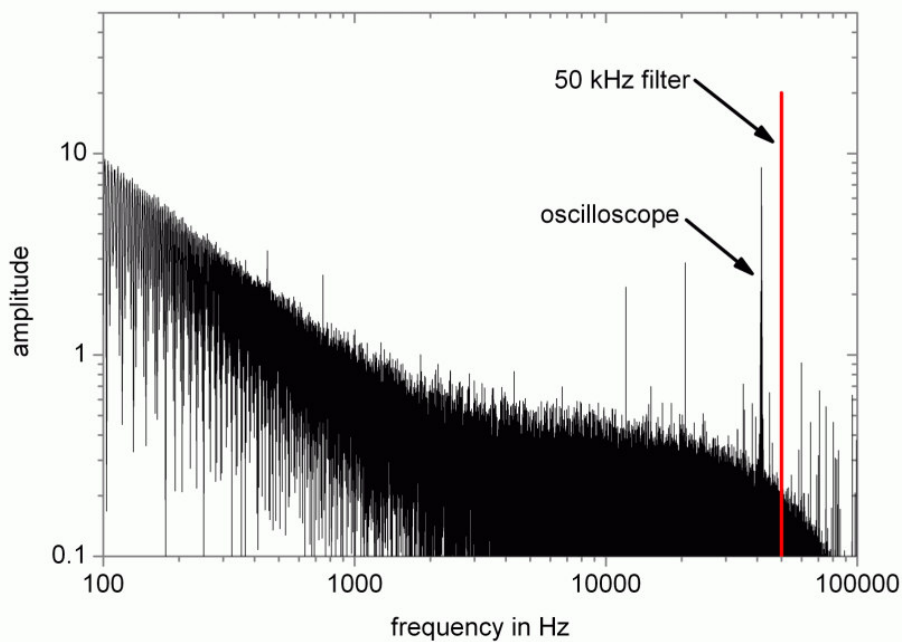
Fig. 3.9. Noise spectrum of the set-up with 50 kHz filter and 200 kHz sampling frequency.

3.3.4.3. Testing the response time of the Dagan amplifier

Crucial for the analysis by means of beta distributions (chapters 5, 6 and 7) is the knowledge of the filter response of the recording apparatus. Sometimes the specifications of the manufacturer do not hold. Because of this, the jump response was measured for the Dagan 3900A with the 50-kHz setting.

Unfortunately, it is very difficult to measure the response, as can easily be demonstrated by the following consideration: At a membrane potential of 100 mV the current through the channel is about 10 pA. If a similar situation is to be used for measuring the filter response, than the current from a 100 mV signal generator has to be injected through a 10 GΩ resistor. However a putative spurious capacitor of 1 pF shunting this resistor has an impedance of 3 MΩ at 50 KHz.

The measurements here were done with a custom-made battery-driven square-wave generator as shown in Fig. 3.10.
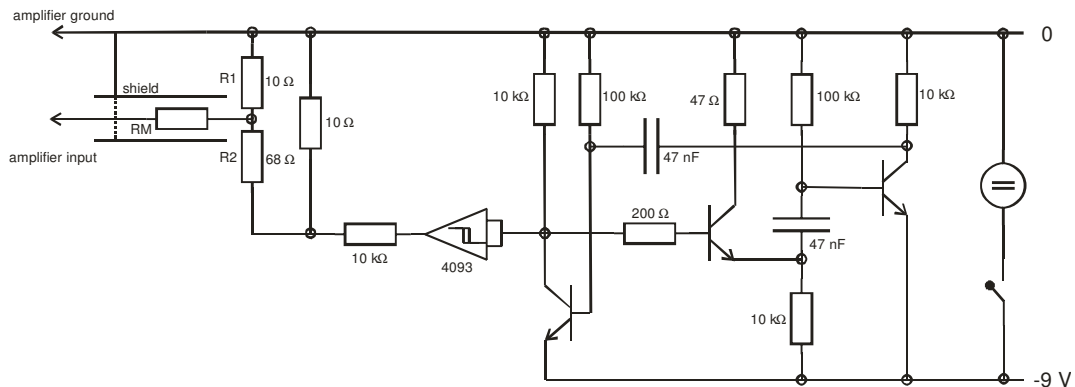
Fig. 3.10. Battery-powered square-wave generator connected to the Dagan amplifier in order to measure the response time of the anti-aliasing filter

The attenuator in the square-wave generator (rise time 0.1 µs) provided square-wave signals of 1 kHz in the range of 0.5 µV to 50 µV. The legend of Fig. 3.11 gives the current of the test signal, the values of the injecting resistor R_M and the slope of the response at the output of the amplifier as recorded by the software *Kiel-Patch*.

Different values of the resistors injecting the current into the headstage were used. Current was adjusted by modifying the voltage attenuator consisting of R_1 and R_2. We found that $R_M = 330$ kΩ to 6 MΩ and different shielding arrangements gave identical results. Injecting via 25 MΩ gave slower responses which were also dependent on the kind of shielding. The finding that for resistors below 6 MΩ the rise times became independent of the resistor indicated that these values were reliable, and that spurious capacitors did not spoil the measurement.
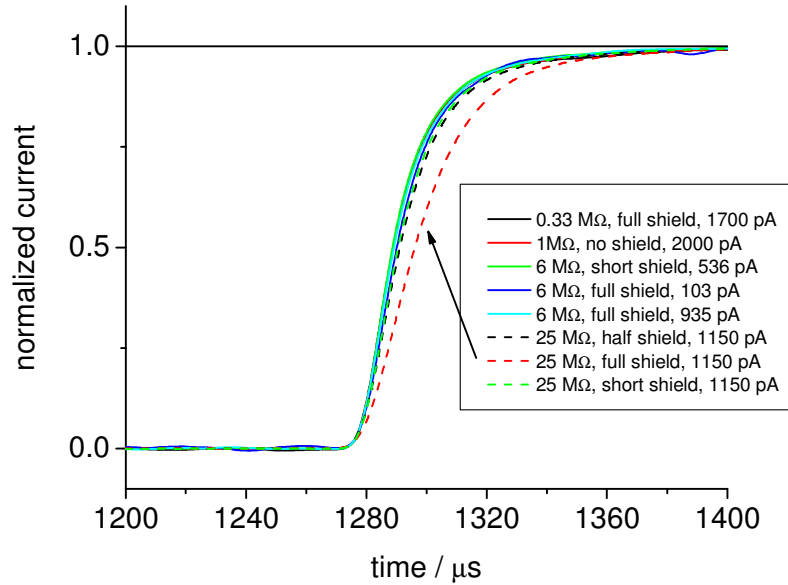
Fig. 3.11. Normalized filter responses of the amplifier to square waves created with different variations of Fig. 3.10. Values of R_M, shield lengths and the magnitude of the test signals are given**.**

In Fig. 3.12, a comparison of the frequency responses calculated by Matlab® for a 4-pole Bessel filter with the measured responses is presented. This reveals that the Dagan amplifier in the 50 kHz setting is slower than promised by the manufacturer.
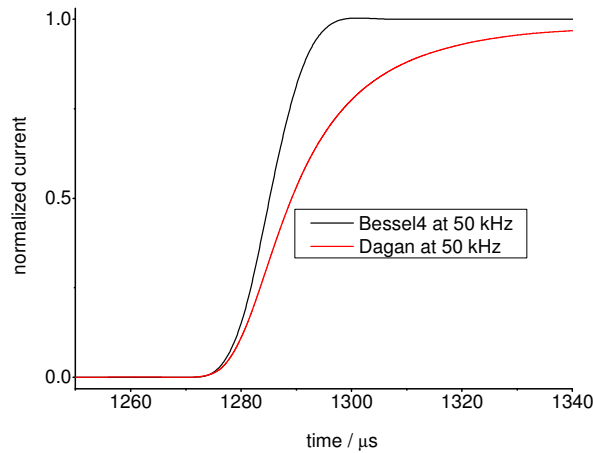
Fig. 3.12. Comparison of a theoretical response of a 4th-order Bessel filter with the average curve of the "good" curves (= excluding 25 MΩ with full shield) in Fig. 3.11.

It was tested of whether the slower rise time found in Fig. 3.12 may result from the differential amplifier. The oscilloscope in Fig. 3.13 shows the fast slope of the square-wave generator (bottom) and the somewhat slower response of the differential amplifier (top). Nevertheless, the value of the rise time, 0.2 to 0.3 µs, is by a factor of 100 faster than that of the Dagan amplifier and thus its influence can be ignored.

45
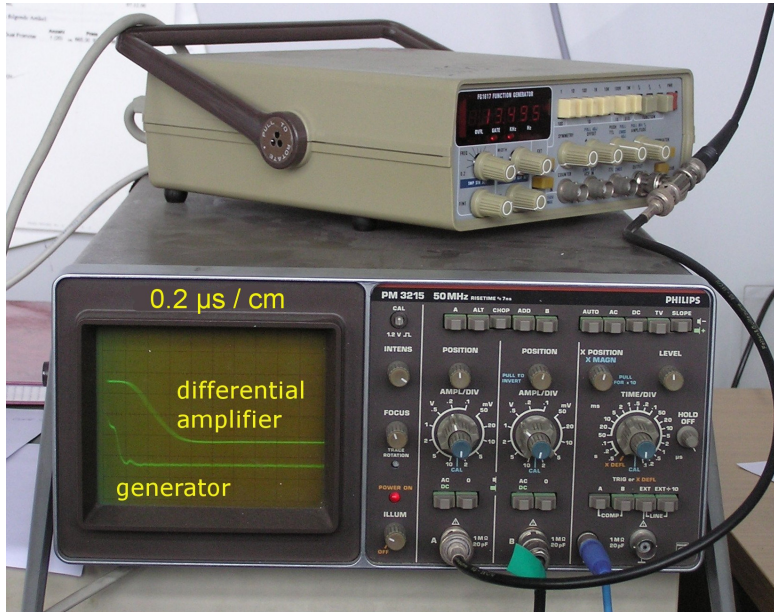
Fig. 3.13. Measuring the rise time of the differential amplifier connecting the Dagan.

3.4. Experimental protocol

Immediately before the experiment, the HEK cells in 35 mm petri dishes were taken from the incubator and washed twice with the bath solution to remove any residuals from the culture medium. Then, the petri dish was filled with ~1.5 ml bath solution. The dish was placed above the objective of the inversed microscope. After an appropriate position was found, the bath electrode was inserted into the solution.

In most experiments, the solutions in the bath and in the pipette contained 150 mM of monovalent cations, e.g., $[K^+] + [Tl^+] = 150$ mM. In all experiments, $[Na^+]$ was never added. As pH buffer, 10 mM HEPES was used and titrated with KOH to a pH of 7.2. Normally, divalent cations were added: 2.5 mM $CaCl_2$ plus 2.5 mm $MgCl_2$. The anion was Cl^- if Tl^+ was not in the solutions. In the presence of Tl^+, Cl^- was replaced by NO_3^-. This did not affect the channel properties, but increased the problems of sealing. In the absence of Na^+, the cells died and detached from the bottom of the dish relatively fast (within 1-2 hours at most). This limited the recording time. Of particular toxicity were solutions with high Tl^+ content, allowing experiments for only 10-30 minutes until a new dish had to be prepared. Besides the bathing solutions mentioned above, different solutions were used as mentioned in the descriptions of the actual experiments.

Immediately before the experiment, patch pipettes were taken from the oven and filled with the pipette solution with a micro filament (Microfil 34 AWG, World Precision instruments, Sarasota, USA). Then, the pipette was mounted on the head stage of the patch amplifier and a small over pressure was applied before entering in into the bath solution. This prevented clogging of the tip by dust, cell debris, etc. The amplifier was switched to voltage-clamp mode, and a 10-mV square wave ("seal test") was applied to allow monitoring of the pipette resistance. Then, the pipette was moved towards the cell from above. A small increase in pipette resistance signaled contact to the cell surface. (The manual offset correction must be done before the pipette touches the cell.). In order to induce the formation of the giga seal, a small negative pressure

46

was applied. With the coated and heated pipettes, the seal typically formed in less than 1 second in over 90 % of all cases (Huth, 2005).

To reach the inside out modus, the pipette was pulled backwards to rip the patch out of the cell. Once it was confirmed that the seal was stable, the seal test signal was turned off. Artefact correction for e.g., series resistance and cell membrane capacity as used in whole-cell experiments was not necessary here.

Currents were recorded for constant commando potentials from –200 - +200 mV in 20 mV intervals. The sensitivity of the current-voltage converter typically was set to 10-50 mV / pA. In all experiments, the 4-pole Bessel filter with a corner frequency of 50 kHz was selected. Usage of the integrating feedback mode (i.e., using a capacitor as feed-back element) reduced the baseline noise by approximately 30 % at 50 kHz bandwidth. The time series recorded by means of the Dalanco250-board (Dalanco Spry, Rochester, USA) were sampled at 200 kHz (Albertsen, 1994). Time series with one constant parameter set (membrane potential) were about 17 seconds long. Measurements were continued until either the seal broke or the channel(s) in the patch went inactive.

4. Methods: Mathematical analysis

Summary. Electrophysiology seeks to find a quantitative description of the phenomena occurring in a measured patch clamp time series. Biophysicists focus on three features:
1. Single-channel current
2. Selectivity
3. Gating behavior.

Here, the traditional methods are summarized which deal with single-channel current and gating behavior. In the next chapter, the methodological improvements developed in this thesis are described in more detail.

In the case of single-channel current, definitions are presented for a state, for apparent single-channel current and for true single-channel current. For the apparent current, the methods of its determination are described here (section 4.1.2), whereas the detailed description of the evaluation of the true single-channel current is given in the next chapter. Gating can be analyzed by four different methods:
1. One-dimensional dwell-time analysis (section 4.5)
2. Two-dimensional dwell-time analysis (section 4.6)
3. HMM fit (direct fit of the time series) (section 4.7)
4. Analysis by means of beta distributions (section 4.8).

Only short descriptions of the methods are given. In the case of dwell-time analysis and HMM fit, detailed descriptions have been given in numerous preceding theses as mentioned below. Furthermore, these approaches are not the main tools of the investigations presented here. The analysis here is mainly based on the evaluation of beta distributions. Since the improvement of the techniques for the analysis of beta distributions is a major topic of this thesis, the new tools are described in chapter 5. Thus, only the traditional part is described in this chapter.

All methods of gating analysis are based on Markov models. Thus, a short introduction is given here (section 4.2), supplemented by techniques like jump detection (section 4.4) and generation of surrogate time series (section 4.9).

4.1. Single-channel current
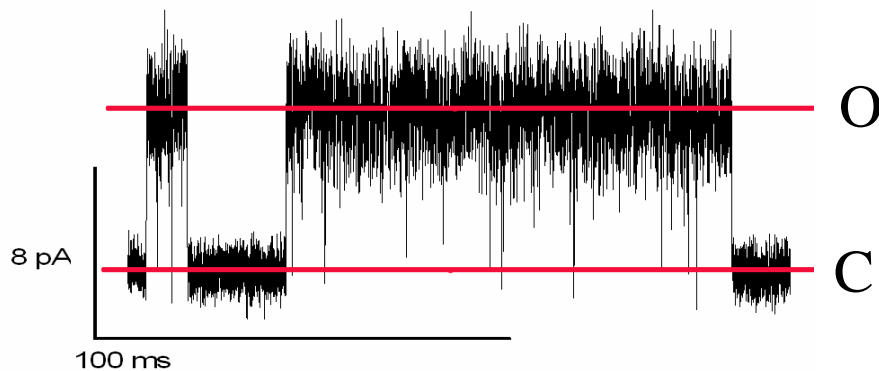
Fig. 4.1. Time series of patch clamp current obtained from a single MaxiK channel expressed in a HEK cell. Membrane potential was +160 mV. The horizontal lines give the current levels of the open and of the closed state. Apparent single-channel current is the difference between the open and the closed level, as determined by one of the methods described in section 4.1.2.

The phenomenological behavior of single ion channels is studied by means of time series as shown in Fig. 4.1. Basically, the determination of single-channel current seems to be quite simple. The apparent current is just the difference between the two horizontal lines in Fig. 4.1.

Unfortunately, the apparent current is not always the true single-channel current. Patch clamp set-ups always contain a low-pass filter of some sorts (see section 3.3.4.3). Due to experimental limitations, it cannot always be ensured that the recording bandwidth is sufficient to resolve all gating events in the channel current. If gating is faster than the temporal resolution of the recording apparatus, an apparent open state can include undetected sojourns into a closed state. Then, the apparent current is smaller than the true current, because it is the weighted average of the current values of the open and the closed state, see Eq. (6.13), below. The problem of a severe underestimation of the real conductivity of the channel (Hansen et al., 1997; Townsend and Horn, 1999) requires a definition of states, true and apparent current which is independent on the actual state of temporal resolution. Such definitions were given by Hansen et al., (2003), see also Schroeder and Hansen (2007):

4.1.1. Definitions of state, true and apparent single-channel current

Definition of a state: The passage of ions through a channel is a stochastic sequence. We call the moment when a transition occurs t_n. Consider the distribution of the time intervals $t_{n+1}-t_n$. A state lasts from t_A to t_E, if the frequency of these time intervals in the range (t_A,t_E) can be described by an asymptotic stochastic function which is independent of the length of (t_A,t_E). Usually, t_E-t_A is too short, and the asymptotic distribution is not reached. Then, assuming ergodicity, ensemble averaging over putative intervals with the same state from the same or additional records has to be employed.

Definition of true current: The true (or real) current I_{true} is the current average in the interval (t_A,t_E).

Definition of apparent current: I_{app} is the current average over a time interval which is assigned to an apparent state in an experimental record.

I_{app} is identical to I_{true} if this interval is included in (t_A,t_E).

4.1.2. Determination of the apparent single-channel current amplitude I_{app}

There are three methods of determining the apparent single-channel current
1. Visual inspection or fit of amplitude histograms
2. Fit-by-eye: placing horizontal lines through the levels of the time series as shown in Fig. 4.1.
3. Automatic level detector as developed by Riessner (1998; 2002) and Woelk (2000).

An amplitude histograms is generated as illustrated in Fig. 4.2. It shows how often in the measured time series a current value between I and ΔI occurs. This number N is plotted vs. current value I. The bin width ΔI can be selected arbitrarily.
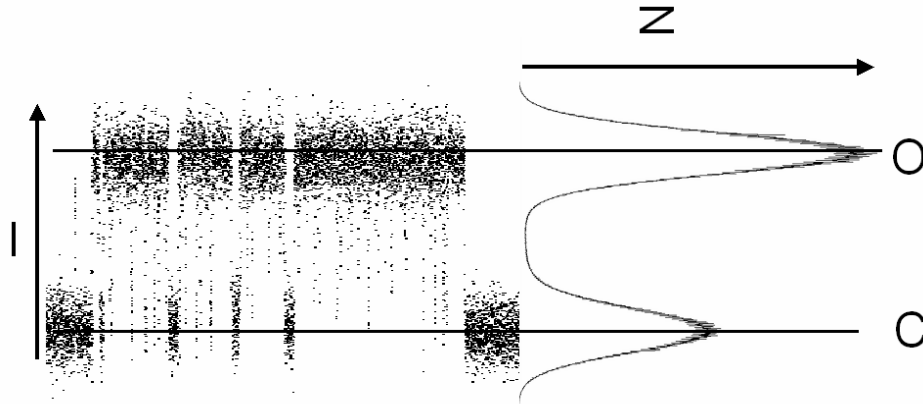
Fig. 4.2. Generation of amplitude histograms from a time series with two channels. *N* is the frequency of the occurrence of current values in the bins of width *ΔI*.

Fig. 4.2 shows that the amplitude histogram displays peaks at the apparent current levels. Using the location of the peak as an estimation of the apparent current is the most common method. The determination of the peaks does not work if the noise of the time series flattens the peaks too much, or if the peaks are skewed. In chapter 7 (Fig. 7.2), the determination of the peaks is replaced by the calculation of the expectance of current from the related distribution-per-level (section 5.1)

$$I_{app} = E[I] = \frac{\sum I \cdot N(I)}{N(I)} \qquad (4.1)$$

with *N*(*I*) being the number of occurrence of the value current value *I*. The sum is over the whole distribution per level (section 5.1).

The fit-by-eye is incorporated in the program *Kiel-Patch*. The lines can be adjusted by means of the cursor keys (Fig. 4.1).

The automatic level detector (Riessner et al., 2002) moves along the time series and looks for jump-free sections. Jump-free is defined via the expectation of whether a measured current value *I* is within the statistical limits given by the previous section obtained after the last detected jump. This algorithm creates ensembles of jump-free sections. From these ensembles, the putative levels are selected by statistical criteria.

Tests (Riessner et al., 2002) have shown that the automatic level detector and the fit-by-eye give about similarly good results. Probably, the human protein computer employs a similar algorithm as the silicon computer running the automatic level detector software. The common approach using amplitude histograms gave much worse results.

In the investigations here, normally the fit-by-eye was used. In critical situations, the reliability of this determination was checked by comparing it with the results obtained from amplitude histograms, using the peaks as in Fig. 4.2 when noise was low or Eq. (4.1) when noise was higher or the distribution was skewed.

4.1.3. Determination of the true single-channel current I_{true}

The development of methods to determine the true single-channel current is a crucial methodological improvement obtained in the present thesis. Thus, details are given in section 5. Here, only a short preview is given.

The trick of determining the true single-channel current of fast gating channels is as follows: When the low-pass filter of the recording apparatus prevents that I_{true} appears at the output of the amplifier, then the filter itself is used as a means of determining I_{true}. This can be done, because filtering distorts the form of the amplitude histogram. There are two effects:

1. The amplitude histogram becomes broader than just given by the noise of the ground level.
2. The amplitude histogram becomes skewed.

Amplitude histograms distorted by the action of a filter are called beta distributions (FitzHugh, 1983), see section 4.8. The determination of the true single-channel current is done as follows:

1. The amplitude histogram of the measured time series is plotted.
2. A distribution-per-level is generated as described in section 5.1.
3. A simple Markov model (section 4.2) is selected to describe the kinetics of the time series in the bursts (ignoring the closed intervals in between).
4. A fit routine varies the values of I_{true} and the rate constants of the Markov model until time series are generated which create the same distribution-per-level as obtained from the measured time series.

The above procedure is that one described in section 5.3. Huth (2005) developed an alternative approach in his PhD thesis. It is also based on the comparison of the amplitude histograms. However, there, the rate constants of the Markov model are obtained from a fit of 2-dimensional dwell-time histograms (sections 4.6 und 5.4).

4.2. Kinetics of gating: Markov models

Ion channels spontaneously switch between conductive and nonconductive states. These gating processes can be described by mathematical models. Most commonly used are Markov models (Colquhoun and Hawkes, 1982). Another approach with fractal models was discussed for a few years (Liebovitch et al., 1987; Calvacanti and Fontanazzi, 1999), but could not establish itself (Korn and Horn, 1988).

Markov models are applied in many different fields like speech recognition (Rose and Juang, 1996), analysis of gene sequences (Siepel and Haussler, 2004) or protein structure (Camproux et al., 2004; Camproux and Tuffery, 2005), description of the course of diseases and the comparison of the effectiveness of different treatments (Konski et al., 2006).

A Markov chain (examples in Fig. 4.3) consists of a discrete set of n Markov states S_1, S_2, S_3, ... S_n. The system jumps randomly between the states, the transition probabilities are given by the rate constants k_{ij}. The description of ion channels usually is restricted to first-order Markov models, i.e., the rate constants are independent of the present state of the system.
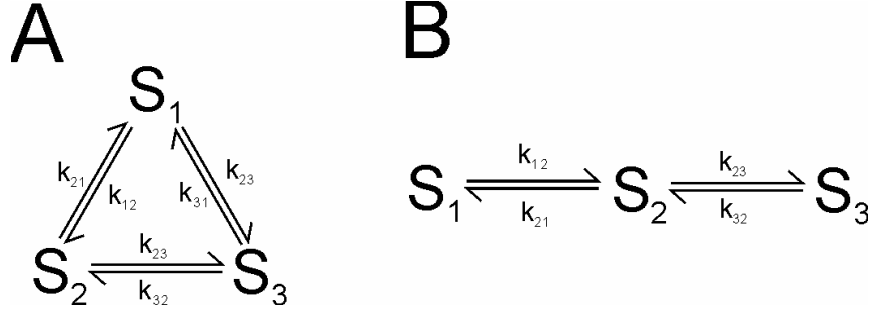
Fig. 4.3. Two three-state Markov models (A) cyclic (B) linear

The transition rate constant k_{ij} defines the average number of jumps from the source state S_i to the sink state S_j per unit time interval (e.g., per microsecond). They are usually displayed as transition matrix K:

$$K = \begin{pmatrix} k_{11} & k_{12} & \cdots & k_{1n} \\ k_{21} & k_{22} & & k_{2n} \\ \cdots & & & \cdots \\ k_{n1} & k_{n2} & \cdots & k_{nn} \end{pmatrix} \quad \text{with} \quad k_{ii} = -\sum_{\substack{j=1 \\ j \neq i}}^{n} k_{ij} \tag{4.2}$$

For the treatment of sampled data, we need the dimensionless transition probabilities p_{ij}

$$p_{ij} = P\left[S_j \text{ at } t \mid S_i \text{ at } t + \Delta t \right] \quad 1 \leq i, j \leq n \tag{4.3}$$

presented by the matrix

$$\underline{\underline{P}} = \begin{pmatrix} p_{11} & p_{12} & \cdots & p_{1n} \\ p_{21} & p_{22} & & p_{2n} \\ \cdots & & & \cdots \\ p_{n1} & p_{n2} & \cdots & p_{nn} \end{pmatrix} \quad \text{with} \quad p_{ii} = 1 - \sum_{\substack{j=1 \\ j \neq i}}^{n} p_{ij} \tag{4.4}$$

Since the p_{ij} are probabilities, they must obviously be non-negative and normalized:

$$p_{ij} \geq 0 \quad \text{and} \quad \sum_{j=1}^{n} p_{ij} = 1 \tag{4.5}$$

The rate constants and transition probabilities are connected by the Kolmogorov equation (Bharucha Reid, 1960):

$$\frac{dP}{d\Delta t} = P \cdot K \tag{4.6}$$

The solution is an exponential equation:

$$P = \exp(K\Delta t) \tag{4.7}$$

53

Here, Δt can be an arbitrary time interval, but usually the sampling interval is used. For small Δt (i. e. $\Delta t \cdot k_{ij} << 1$) it can be approximated as

$$p_{ij} = k_{ij}\,\Delta t \qquad (4.8)$$

The formal definitions are as follows:
The measured time series is presented by

$$Y = \{y_t\}_{t=1,\dots,N} \qquad (4.9)$$

The sequence of states is given by:

$$Q = \{q_t\}_{t=1,\dots,N} \qquad (4.10)$$

The definition of a Markov model consists of two parameters (n, m) and three probability functions (P, A, π_i):

1. n = number of Markov states $S = \{S_i\}_{i=1,\dots,n}$ in the model.
2. m = number of possible output symbols $R = \{R_i\}_{i=1,\dots,m}$. Our data are digitized with a 12 bit AD converter $\Rightarrow m = 2^{12} = 4096$.
3. The transition probabilities are

$$p_{ij} = P\big[q_{t+1} = S_j \,|\, q_t = S_i\big], \quad 1 \le i, j \le n \qquad (4.11)$$

4. The (discrete) probability function $A_{S_j}(R_k) = A_j(k)$ of the output symbols R_k for each Markov state S_j is

$$A_j(k) = P\big[y_t = R_k \,|\, q_t = S_j\big], \quad 1 \le j \le n, 1 \le k \le m \qquad (4.12)$$

In absence of a smoothing filter in the recording apparatus, noise is added equally to each state. $A_j(k)$ in that case represents the gaussian distribution of noise with I_j being the nominal current level of the state S_j.

$$A_j(k) = \frac{1}{\sqrt{2\pi\sigma^2}}\, e^{-\frac{(I_j - I_k)^2}{2\sigma^2}} \qquad (4.13)$$

In the presence of a smoothing filter, the individual gaussian distributions are replaced by beta distributions which may result in different curve shapes of A_j for each level j.

5. The starting probabilities of the occupation of the states S_j for $t = 1$:

$$\pi_j = P\big[q_1 = S_j\big], \quad 1 \le j \le n \qquad (4.14)$$

For the sake of simplicity, *m* and *n* are not explicitly stated, and the model is abbreviated as:

$$\lambda = \left(P, \{ A_j \}, \pi \right) \tag{4.15}$$

Calculation of the occupation probabilities

The occupation probability $[S_j]$ for each Markov state can easily be calculated by solving the 1st order linear differential equation system

$$\frac{d\left[S_j \right]}{dt} = \sum_{\substack{i=1 \\ i \neq j}}^{n} [S_i] p_{ij} - \left[S_j \right] \sum_{\substack{j=1 \\ i \neq j}}^{n} p_{ji} \tag{4.16}$$

In the stationary case with $d[S_j]/dt = 0$, micro reversibility has to be maintained. Fluxes (not rate constants) in opposite directions have to be equal:

$$\left[S_i(\infty) \right] k_{ij} = \left[S_j(\infty) \right] k_{ji} \tag{4.17}$$

Some more definitions

Aggregated Markov models: Several states of a Markov S_j model may lead to the same output function $A_j(k)$. Thus, theses states cannot be distinguished by means of the current levels found in a patch clamp time series. Markov models comprising states which cannot be distinguished by means of the output symbols are called aggregated Markov models.

   Nevertheless, the individual members of aggregated states may be distinguished by means of additional information, e.g., by means of their mean dwell-times obtained from a kinetic analysis of the time series, or by means of other output signals, e.g., fluorescence.

   In the case of aggregated Markov models, the question of the reaction scheme becomes important. For instance, a short C-state ("closed") may be related to a long or a short O-state ("open"). Below it is shown that in some cases such models can be distinguished by 2-dimensional dwell-time analysis (section 4.6), but also by the HMM fit, because the prediction equation (4.46), below, distinguishes between the individual members of an aggregated state.

Hidden Markov models: There is not a unique usage of the term Hidden Markov model. The common view is that the states of the model can be hidden. This may be caused by aggregation of states as described above or by noise. Nevertheless, in most cases this uncertainty of the definition does not matter, because all time series are noisy and most models have aggregated states.

Sublevels: Often channels show several states of conductivity as shown in Fig. 4.4.

The level with the highest current is called the *full level* and the smaller ones *sublevels*. The question is of whether these sublevels are real or whether they present an apparent current reduced in different degrees by fast gating. We found that the latter was the case when sublevels were investigated (Fig. 5.24) with the high temporal resolution established in this thesis (Schroder et al., 2004; Schroeder and Hansen, 2006). However, this finding may not be generalized.
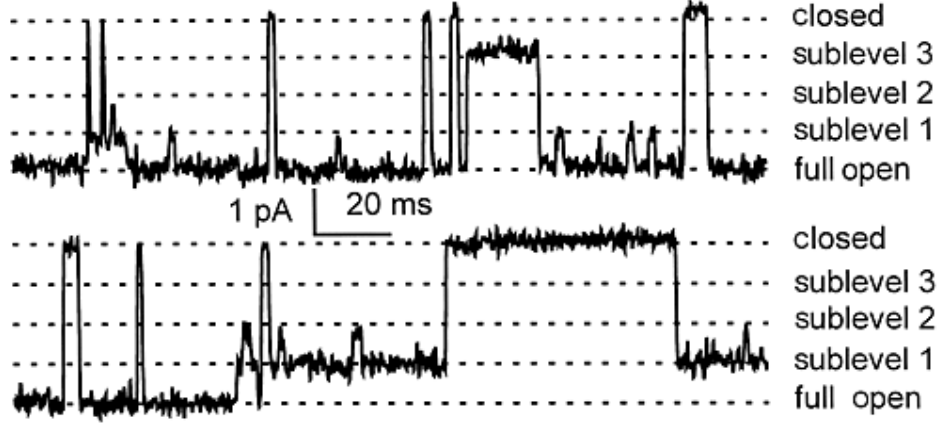
Fig. 4.4. Representative single-channel currents recorded at -100 mV from a mutated Kir channel with 3 subconductance levels. Figure taken from Lu et al. (2001a).

Sometimes the question arises of whether two different values of single-channel current found in a time series arise from one channel with sublevels or from two channels with different conductivities. In our group, two statistical approaches were developed to answer this question (Draber and Schultze, 1994b; Caliebe et al., 2002).

In the present investigation, sublevels were excluded from the analysis, because they were rare, occurred irregularly and showed no apparent correlation with the experimental conditions.

4.3. Equivalence of Markov models

Markov model with different arrangements of states often cannot be distinguished by means of their steady-state kinetic behavior, i.e., by the analysis of the stationary time series. All methods described above designed to reveal the parameters of Markov models cannot distinguish between equivalent models (Kienker, 1989).

Two Markov models Q and K are equivalent if a matrix S exists which has the form

$$\begin{pmatrix} S_{OO} & 0 \\ 0 & S_{CC} \end{pmatrix} \tag{4.18}$$

and which can transform the rate constant matrix (Q) of one Markov model into that one (K) of the other model

$$K = S \cdot Q \cdot S^{-1} \tag{4.19}$$

K and Q have to be presented in a form where the open and closed states are grouped.
Kienker (1989) gives an example for 3 state models
The model

$$C \underset{b}{\overset{a}{\rightleftharpoons}} C \underset{d}{\overset{c}{\rightleftharpoons}} O \tag{4.20}$$

with the matrix of rate constants

$$Q^{(CCO)} = \begin{pmatrix} -d & 0 & d \\ 0 & a & -a \\ c & b & -(b+c) \end{pmatrix} \tag{4.21}$$

can be transformed by

$$S = \begin{pmatrix} 1 & 0 & 0 \\ 0 & \dfrac{-\lambda_2/2}{\lambda_1-\lambda_2} & \dfrac{\lambda_1}{\lambda_1-\lambda_2} \\ 0 & \dfrac{c-\lambda_2}{\lambda_1-\lambda_2} & \dfrac{\lambda_1-c}{\lambda_1-\lambda_2} \end{pmatrix} \tag{4.22}$$

into the model

$$C \underset{f}{\overset{e}{\rightleftharpoons}} O \underset{h}{\overset{g}{\rightleftharpoons}} C \tag{4.23}$$

with the matrix of rate constants

$$Q^{(CCO)} = \begin{pmatrix} -(f+g) & f & g \\ e & -e & 0 \\ h & 0 & -h \end{pmatrix} \tag{4.24}$$

$\lambda_{1,2}$ are the eigenvalues of the matrix $Q_{CC}^{(CCO)}$. The rate constants of the new model are

$$\begin{aligned} e &= \lambda_1 \\ f &= d\,\frac{c\lambda_2}{\lambda_1-\lambda_2} \\ g &= d\,\frac{\lambda_1-c}{\lambda_1-\lambda_2} \\ h &= \lambda_2 \end{aligned} \tag{4.25}$$

In the case of equivalent models, both models can be used to fit the time series.

It is simple to show equivalence in the case of 3-state models. It becomes very difficult for models of higher order. Then, the determination of S is difficult. Equation (4.19) has to be formulated with unknown variables for the S_{ij} and for the rate constants k_{ij} of the elements of the new matrix K. The new reaction scheme of K is represented by the forbidden transitions resulting in zeros in K. The equations for $k_{ij} = 0$ can be used to calculate the unknown S_{ij}. It is obvious that this results in non-linear equations which only can be solved by a fitting routine. If the resulting set of equations is over determined and a solution cannot be found, the two models are not equivalent.

The question is of whether the resulting insight is worth the tremendous effort. Alternatively, the measured time series may be fitted with different models and see whether reasonable results are obtained with which models. However, this suffers from the uncertainties of fitting routines and from the danger that individual time series pretend a general equivalence or non-equivalence. As mentioned below, the usage of channel mutants may be more efficient than persuing the mathematical analysis.

4.4. Jump detection: Hinkley detector

4.4.1. First-order Hinkley detector

A Markov model generates a time series with jumps between different output symbols as caused by the sojourns in the related states. In patch clamp or other time series, the output symbols are superimposed by noise as shown in Fig. 4.5.
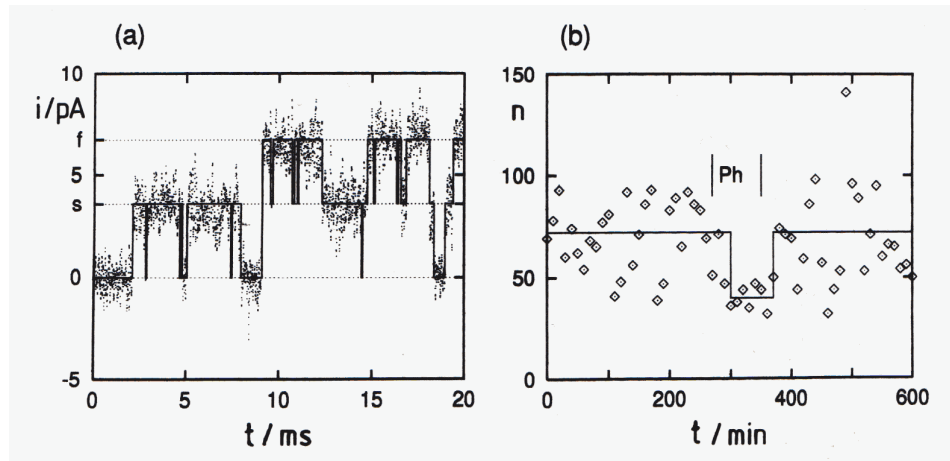
Fig. 4.5. Noisy time series containing jumps of the variable which carries the information. (A) Patch clamp recording from a cytosolic droplet of *Chara* measured at 60 mV. (B) Output signal of a biosensor monitoring the mobility of water fleas. The vertical lines with "Ph" inbetween indicate the addition of 0.1 mM phenol to the tap water. The smooth lines give the reconstructed (noise-free) signal of the original processes as obtained by a Hinkley detector described below (from Hansen et al., 1995).

The superimposed noise renders the determination of the actual symbol at a time t and the detection of the occurrence and the time of jumps difficult. Thus, procedures are required with can reconstruct the "noise-free" time series from a measured time series. In the case of patch clamp analysis this is of crucial importance for dwell-time analysis (section 4.5 and 4.6) or the generation of distributions-per-level (section 5.1).

Reconstructing the original sequence of channel openings and closings from the measured noisy data is mostly done by using a low-pass filter coupled with a half-threshold algorithm (Sakmann and Neher, 1995). In our group, different versions of the Hinkley detector (Hinkley, 1971) are employed for jump detection. Its algorithm replaces low-pass filtering by integration and contains a non-linear element, producing significantly better results with respect to correct reconstruction of the event length, missed brief events as well as to the avoidance of false alarms especially in the presence of colored noise (Schultze and Draber, 1993).

In the case of the first-order Hinkley detector, a cumulative test sum g is calculated for the detection of a jump from the current level μ_0 to μ_1 from the noisy raw data z_t:

$$g_0 = 0 \qquad \text{(initialization)}$$

$$g_t = g_{t-1} + \left(z_t - \frac{\mu_0 + \mu_1}{2} \right) \tag{4.26}$$

This equation is still linear; it just replaces the traditionally used low-pass filter by an integrator. Thus, g rises a little faster after a jump. The non-linear element provides the option of a conditioned reset before each iteration:

$$g_t = \max\left(g_t, 0 \right) = \begin{cases} g_t & \text{if } g_t \geq 0 \\ 0 & \text{if } g_t < 0 \end{cases} \tag{4.27}$$

This prevents negative values of g (i.e. $< \mu_0$) which would slow down the detection process. In other words, Eq. (4.27) keeps the detector awake.
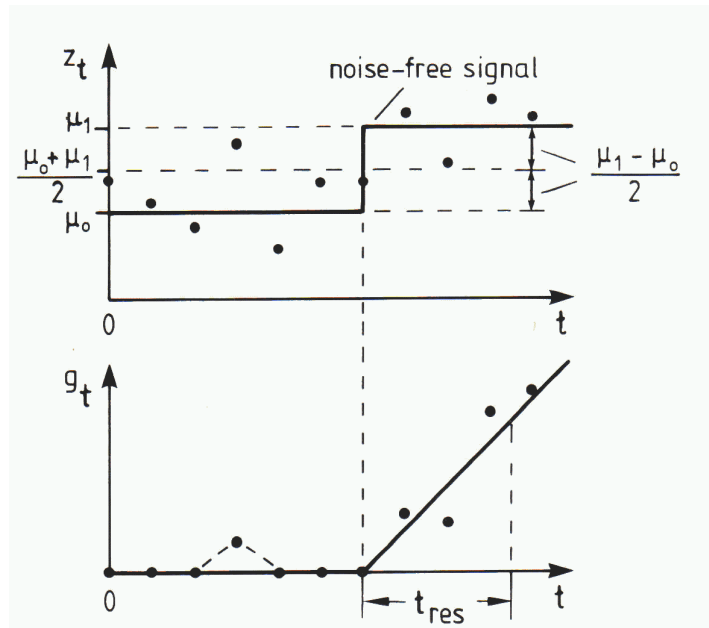
Fig. 4.6. Performance of the Hinkley detector. Top: Noise-free jump from level μ_0 to level μ_1 (solid line) and a noisy jump (circles, z_t). Bottom: Time course of the test value g_t (Eq.(4.26)) for the noise-free jump (solid line) and the noisy jump (circles). The transient increase of g_t by a noise-borne transition of z_t over the half amplitude in the top panel is reset to zero according to Eq. (4.27) (from Hansen et al., 1995).

Fig. 4.6 illustrates the performance of the Hinkley detector as described in the legend. A jump is detected when g_t reaches λ. The time of jump is calculated from the time course of g_t by subtracting t_{res} (Eq. (4.28)) from the time when the detector signals a jump. A guideline how to select λ appropriately for different SNRs is given by Schultze and Draber (1993).

The detection threshold and the temporal resolution are connected as follows:

$$\lambda = \frac{\mu_1 - \mu_0}{2} t_{res} \tag{4.28}$$

The optimum bargain between high threshold (which prevents false alarms) and temporal resolution was considered by Schultze and Draber (1993).

4.4.2. Higher-order Hinkley detector (HOHD)

As known from Bessel filters, the performance of a filter gets better if the order is increased, normally to eight. This also applies to the Hinkley detector. The eighth-order Hinkley detector uses the eighth-order integral (or cumulative sum) of the signal. Thus, the high frequency attenuation is much stronger than that of the standard Hinkley detector (roughly with a f^{-8} slope as opposed to f^{-1}). The jump is detected when the 8th-order test value g_t^8 reaches the threshold.

$$g_t^1 = g_{t-1}^t + \left(z_t - \frac{\mu_0 + \mu_1}{2} \right)$$
$$g_t^2 = g_{t-1}^2 + g_t^1$$
$$g_t^3 = g_{t-1}^3 + g_t^2$$
$$g_t^4 = g_{t-1}^4 + g_t^3 \tag{4.29}$$
$$g_t^5 = g_{t-1}^5 + g_t^4$$
$$g_t^6 = g_{t-1}^6 + g_t^5$$
$$g_t^7 = g_{t-1}^7 + g_t^6$$
$$g_t^8 = g_{t-1}^8 + g_t^7$$

And the resetting is done simultaneously:

$$g_t^i = \begin{cases} g_t^i & \text{if } g_t^1 \geq 0 \\ 0 & \text{if } g_t^1 < 0 \end{cases} \tag{4.30}$$

Schultze and Draber (1993) compared the performance of the Hinkley detectors of first and 8th order with that of low-pass filter detectors and obtained the best results with the higher-order Hinkley detector (HOHD). The HOHD is incorporated in the program *Kiel-Patch*.

4.4.3. Sublevel Hinkley detector (SHD)

Hinkley detectors are just software. Thus, a bench of Hinkley detectors can work in parallel with each one programmed to look at a different current level. If there is a time series with full current levels and sublevels, then one detector can be installed looking at the highest level and one for each lower level. The problem is that all detectors would give alarm if a jump to the high level occurs. Draber and Schulze (1994b) developed

Hinkley detectors in such a way that the detector which detects the jump first is the right one. The key for this behavior is the following equation for the test value h_t

$$h_t = h_{t-1} + p_i \cdot (e_t - p_i) \qquad (4.31)$$

with e_t being the deviation of the measured current at time t from the previous level μ_o, and p_i being the half amplitude of the jump from the previous level μ_o to level μ_i.

The SHD consists of a bench of detectors set to different values of p_i. If a jump to level j occurs ($e_t = 2 p_j$), then all detectors respond according to Eq. (4.32)

$$h_t = h_{t-1} + p_i \cdot (2p_j - p_i) = h_{t-1} + s \qquad (4.32)$$

with s being the speed of the increase of the test value from t-1 to t. In Fig. 4.7, the average speed (slope) s (average because in real records noise is superimposed) is plotted. This shows that Eq. (4.32) results in a parabolic dependence of the rising slope s of h_t in such a way that the velocity is maximum for that detector which looks at the correct level $p_i = p_j$.
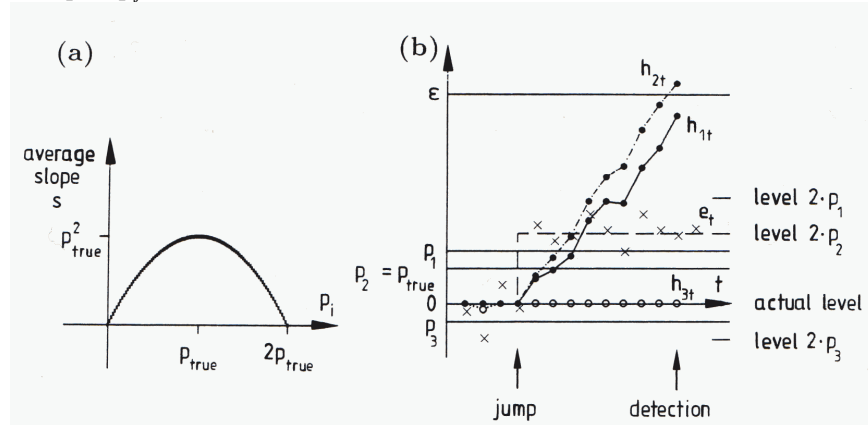
Fig. 4.7. (A) Dependence of the speed s of the increase of the test value h_t as calculated from Eq.(4.32). (B) Behavior of the test value h_t of three different detectors set to different values of the half amplitude p_i of the expected jump (from Hansen et al., 1995).

In Fig. 4.7B, the time courses of the test values of three detectors set to different p_i are shown. The actual jump in the measured current $e_t = 2 p_2$ is presented as a dashed line. Detector 3, looking at p_3 does not react because the jump is in the wrong direction. Detectors 1 and 2 both react with an increasing test value h_t, but detector 2 looking at the correct level p_2 wins the race, i.e., it reaches the threshold ε first. (The selection of the threshold is determined by the signal-to-noise ratio, as given by Schultze and Draber, 1993). If no new jump occurs after the threshold is reached, then there is still an additional observation time, where the race is continued in order to check whether noise may have led to a wrong decision.

The SHD is implemented in the software *Kiel-Patch*. It is used for the generation of distributions-per-level. For distributions-per level, the time series has to be split into sections related to the actual state as identified by the Hinkley detector. All sections belonging to the same state are merged into a new time series per level. The software for sorting of these sections and merging them into the time series per level is installed in the SHD.

4.5. One-dimensional dwell-time histograms

4.5.1. Generation of dwell-time histograms

Markov models jump between different states generating the sequence of states Q (Eq. (4.10)). The time of the sojourn in such a state is called a dwell-time. Dwell-time histograms are generated by means of a book-keeping program counting how often a dwell-time between τ and $\tau + \Delta\tau$ is observed (Colquhoun and Hawkes, 1982). The interval $\Delta\tau$ is called the bin width. Dwell-time histograms are generated for each state. Normally these states are aggregated states, i.e., all states which the same output symbol (current level) are comprised in one dwell-time histogram.

Fig. 4.8. Generation and analysis of one-dimensional dwell-time histograms. (A) A two-state Markov model with rate constants (Eq. (4.2)). (B) Section of a time series simulated (section 4.9) with the model in (A). (C) and (D): Screenshots from *Kiel-Patch* with one dimensional dwell-time histograms from the time series (dots) and their fit with exponentials (continuous line, Eq.(4.39). The time constants are the inverse of the rate constants in (A).

4.5.2. Theoretical background of dwell-time histograms

A dwell-time histogram gives the probability that the Markov process resides in state S_j for exactly the time t. The calculation of this dwell-time distribution is different from that employed to calculate the steady-state probability $[S_j]$ to be in state S_j.

After sorting the states into aggregated states (S_1 to S_L are closed, S_{L+1} to S_Q are open), the steady-state concentrations of S_j are calculated according to the scheme

$$(S_1 \ldots S_L) \quad \rightleftarrows \quad (S_{L+1} \ldots S_Q)$$

closed **open**

The symbol with double arrows indicates the existence of transitions within the aggregated states and between the groups.

The scheme above leads to the following differential equation for the temporal behavior of the occupation probabilities $[S_j]$ due to the familiar reaction kinetic laws of mass conservation.

$$\frac{d}{dt}[S_I](t) = -[S_I](t)(\sum_{\substack{J \in all \\ J \neq I}} k_{I,J}) + \sum_{\substack{J \in all \\ J \neq I}} [S_J](t)k_{J,I} \qquad (4.33)$$

It has to be stressed that this describes concentration changes as obtained e.g., when a state is observed by emitted fluorescence. This is different from the dwell distribution as shown below. From Eq. (4.33), the steady-state concentrations (steady-state occupation probabilities) are calculated for $d[S_j]/dt = 0$.

The dwell-time histograms have to account for the effect that the sojourn in an aggregated state is over when the system jumps out of this state into a state with another output symbol, i.e., from the aggregated state S_1 to S_L to the aggregated state S_{L+1} to S_Q. This is presented by a different scheme:

$$(S_1...S_L) \quad \rightleftarrows \quad (S_{L+1}...S_Q)$$

closed   **open**
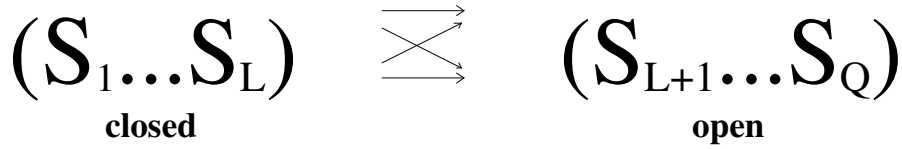
Here, the distribution of dwell-times in the closed states (source states) is considered. The difference to the first scheme is in the single arrows. This implicates that jumps from the sink states (open states) back to the source states are forbidden. With other words, the sink states are absorbing. This leads to differential equations where jumps from the sink states back to the source states are excluded. Jumps within the sink states (S_1 to S_L) are allowed (2nd term in Eq. (4.43)) because they cannot be detected by observing the output symbol.

$$\frac{d}{dt}q_I(t) = -q_I(t)(\sum_{\substack{J \in all \\ J \neq I}} k_{I,J}) + \sum_{\substack{J = closed \\ J \neq I}} q_J(t)k_{J,I} \qquad (4.34)$$

with $q_I(t)$ being the probability that the state variable q in Eq. (4.10) has the value I (i.e., the system is in state S_I) at time t, with I being an index of the closed (sink) states.

Using the reduced rate constant matrix K', Eq. (4.34) can be written in matrix form. It has to be mentioned that k_{ii} is the negative sum of a row of the full matrix K. Thus it presents the first negative term in Eq. (4.34).

$$\frac{d}{dt}(q_1,..........q_L) = (q_1,..........q_L)\begin{pmatrix} k_{1,1} & k_{1,2} & ... & k_{1,L} \\ . & . & & . \\ . & & . & . \\ . & & . & . \\ k_{L,1} & ... & ... & k_{L,L} \end{pmatrix} \qquad (4.35)$$

The solution of this system of linear differential equations is a sum of exponential functions. The experimenter cannot find out which ones of the aggregated closed states is just generating the actually measured output symbol "closed". Thus, the probability of finding a closed state at time t after the last open-closed jump is

$$z(t) = \sum_{1}^{L} q_I(t) \qquad (4.36)$$

$z(t)$ includes also those channels with will continue to stay open after t. Thus, the probability of having a lifetime exactly between t and Δt (not shorter and not longer) has to calculated from the derivative of $z(t)$:

$$f(t) \quad = -\frac{d}{dt} z(t) \qquad (4.37)$$

4.5.2.1. Numerical evaluation of dwell-time histograms: Fitting with time constants

As shown in section 4.5.2, Markov model are linear systems, and dwell-time histograms can be fitted by means of a sum of exponentials. Often, people dislike the explicit solution of the differential equation (4.35). They are satisfied with a phenomenological description of their results and fit the measured dwell-time distributions by a sum of exponentials

$$f_I(t) = \sum_{k=1}^{n_I} A_{I,k} \exp\left(-\frac{t}{\tau_{I,k}}\right) \qquad (4.38)$$

with $\tau_{I,k}$ being the k-th time constant belonging to the dwell-time distribution of state S_i, and $A_{I,k}$ the amplitude factor assigned to $\tau_{I,k}$.

The value of such an analysis is as follows:

1. n_I gives the number of states aggregated in state I.
2. The time constants $\tau_{I,k}$ give a rough estimation of the rate constants of efflux from state I.

However, often, researchers are interested in the rate constants k_{IJ} (Eq.(4.35)). For two-state models (Fig. 4.8), the expression for the dwell-time distributions of the open and closed state are simple exponentials with the inverse rate constants as time constants:

$$f_O(t) = k_{OC} \cdot e^{-k_{oc} \cdot t}$$
$$f_C(t) = k_{CO} \cdot e^{-k_{co} \cdot t} \qquad (4.39)$$

However, in the case of models with more than two states, it becomes extremely difficult to evaluate the k_{IJ} from $\tau_{I,k}$ and $A_{I,k}$ obtained from fitting by means of Eq. (4.38) (Albertsen, 1992; Jackson, 1997). Then a target-fit is recommended.

4.5.3. Numerical evaluation of dwell-time histograms: target fit

The target of a kinetic analysis of ion channel gating is the determination of the rate constants $k_{I,J}$ as they are the physical parameters of the model which are expected to support an interpretation in terms of molecular mechanisms. The target fit uses the explicit solution of Eq. (4.35) as model equation for multi-state Markov models as given by Kijima and Kijima (1987a):

$$f_C(t) = \sum_{k=1}^{L} (2c_k (\sum_{J=1}^{L} [S_I] m_I^{(k)} (\sum_{I=L+1}^{Q} k_{J,I}))^2 \frac{1}{f_{tr}}) \cdot e^{-\lambda_k t} \qquad (4.40)$$

with $[S_I]$ being the steady-state occupation probabilities and $m^{(k)}$ the eigenvectors of the rows of the reduced K-matrix. The relationship between the eigenvector of the columns $n^{(k)}$ and of the rows $m_J^{(k)}$ defines the c_k.

$$n^{(k)} = c_k (m_1^{(k)} [S_1], \ldots \ldots m_L^{(k)} [S_L]) \qquad (4.41)$$

The normalization factor f_{tr} is the average number of jumps per time interval.

$$f_{tr} = 2 \sum_{i=1}^{L} \sum_{j=L+1}^{n} \left[S_j(\infty) \right] k_{ji} \qquad (4.42)$$

The derivation of these equations can be found in Kijima and Kijima (1987a). Blunck et al. (1998) extended the algorithm to multi-channel analysis.

The software for the dwell-time target fit is incorporated in *Kiel-Patch*. A simplex fit routine (Caceci and Cacheris, 1984) varies the rate constants of the Markov model. In each iteration step, theoretical dwell-time histograms are calculated from the k_{ij} via Eq. (4.40). The divergence between the theoretical and the experimental curve guides the search algorithm until a minimum is found. However, a bug which entered the program during conversion from Pascal to C++ leads to errors in the case of 5-state models. The bug survived several attempts to fix it, and then it was given up, because the 1-dimensional dwell-time analysis was not used any more. HMM fit and analysis of beta distribution (described below) provided a much better resolution of fast gating.

4.6. Two-dimensional dwell-time analysis

As mentioned in section 4.3, there is the problem of equivalent Markov models. However, the situation is even worse in the case of 1-dimensional dwell-time analysis. There may be models which are not kinetically equivalent but may lead to equal 1-dimensional dwell-time histograms. They can be distinguished by means of 2-dimensional dwell-time histograms (Magleby and Weiss, 1990b; Magleby and Song, 1992). There reason for this different strength of the two approaches results from the following difference: In 1-D dwell-time analysis only the length of the sojourns in open or closed states is considered. Doing so, important information is neglected, namely the sequence of the sojourns in long or short open or closed states.

In the two models

$$O_L \rightleftharpoons C_L \rightleftharpoons C_S \rightleftharpoons O_S \qquad (4.43)$$

and

$$O_L \rightleftharpoons C_S \rightleftharpoons O_S \rightleftharpoons C_L \qquad (4.44)$$
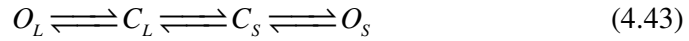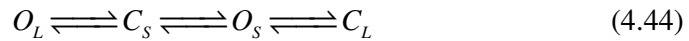
with the indices S = short, L = long, the rate constants can be adjusted to yield the same open and closed 1-D dwell-time histograms. However, the sequence of sojourns is different as illustrated in Fig. 4.9.

In the scheme of Eq. (4.43), a short C cannot follow a long O. This leads to an empty field in the scheme of Fig. 4.9A. In contrast, the scheme of Eq. (4.44) cannot create a long C state after a long open state (and vice versa, because of micro reversibility).
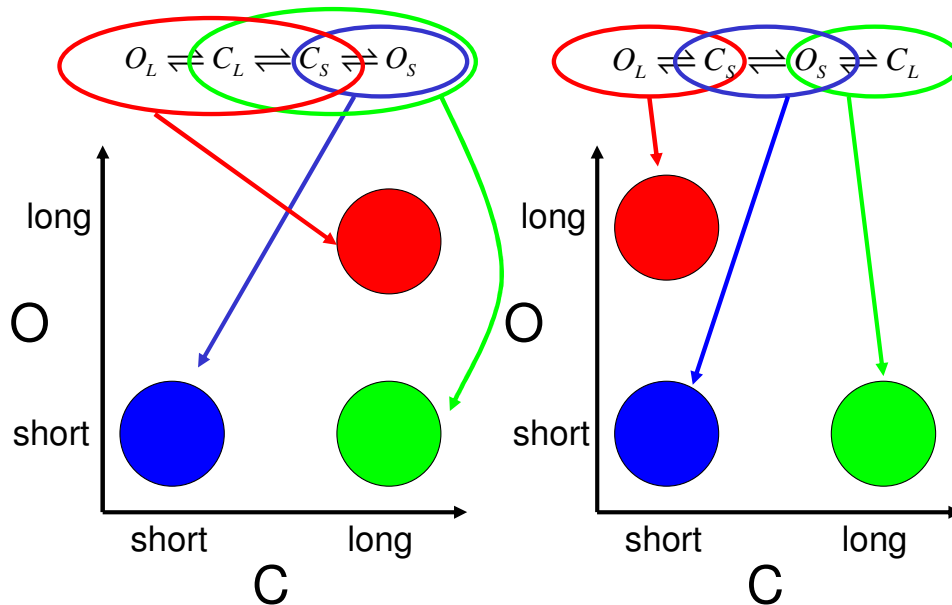
Fig. 4.9. Schematic 2-D dwell-time histograms. Pairs of two subsequently occurring sojourns in an open and in a closed state are considered. The dwell-time of the closed state is given on the x-axis, that of the open state on the y-axis. (A) Generated from Eq. (4.43) (B) generated from (4.44).

The schemes in Fig. 4.9 are 2-D dwell-time histograms which are generated as illustrated in Fig. 4.10. Pairs of sojourns in open and closed states are selected. The dwell-time in the closed states determines the value on the x-axis, the dwell-time in the open state that value on the y-axis. The numbers of occurrence of such pairs in the plane of 2-dimensional bins ($\tau_c + \Delta\tau$, $\tau_O + \Delta\tau$) are presented as topographic lines (Fig. 4.11) or as color code.

The „normal", one-dimensional dwell-time distributions just account for the length of open- and closed events, ignoring their sequence. But as illustrated in Fig. 4.9, the sequences can bear important information about the structure of the underlying Markov model. Different Markov models can generate identical 1-D dwell-time histograms (Blatz and Magleby, 1986; Weiss and Magleby, 1989). Because 2-D dwell-time histograms account for the correlation of events, they can improve model differentiation significantly (Magleby and Weiss, 1990b). Even more, it can be shown that (at least theoretically) 2-D dwell-time histograms already contain all necessary

statistical information to identify the underlying Markov model. The information in higher-order dwell-time histograms (e.g., 3-, or 4-D histograms) is redundant (Löptien, 1999).
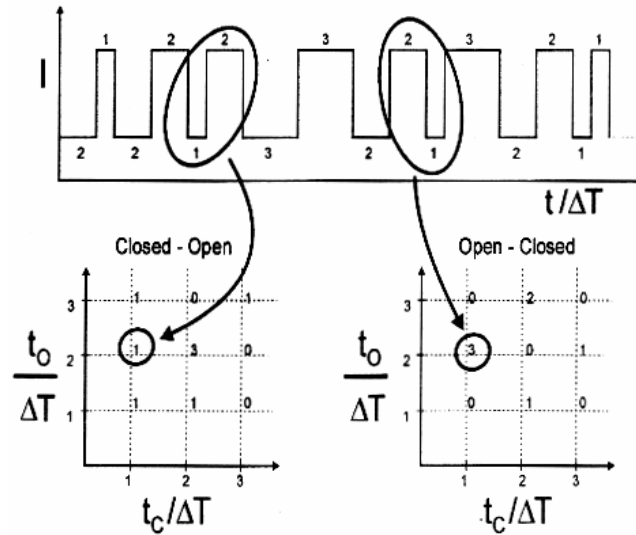
Fig. 4.10. Construction of 2-dimensional dwell-time histograms. Pairs of neighbouring open- and closed-states with dwell-times between t_O and $t_O+\Delta t$, and t_C and $t_C+\Delta t$, respectively, are taken from the noise-free time series (e.g., obtained by a Hinkley detector, section 4.4). The frequency of occurrence of such pairs is plotted against t_O, t_C. (from Huth, 2005)
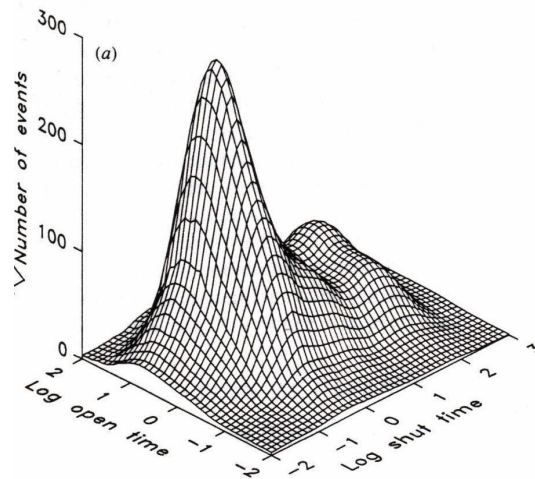
Fig. 4.11. Three-dimensional visualization of a 2-D dwell-time histogram. (Graph taken from Magleby and Song, 1992).

4.7. Hidden Markov model fit

The name Hidden Markov model fit (HMM fit) does not account for the real nature of this approach, because also the dwell-time analysis or the beta fit (section 4.8, chapter 5) are designed to fit Hidden Markov models. More adequate would be the name "direct fit of the time series". Whatsoever, the HMM fit starts from a (Hidden) Markov model

67

with a guessed set of rate constants. From these rate constants a time series is predicted and compared with the measured one by calculating the likelihood that the predicted state at time T is identical to the measured one at time T. If this were done directly for a five-state model for $T = N\Delta t$, then the number of possible pathways to this point is 5^N which results in an impressive high number of calculations if $N = 1\ 000\ 000$.

A way out of this computational problem was provided by Baum et al. (1970) using a 1-step prediction algorithm. Fredkin and Rice (1992) applied this algorithm to the analysis of time series. Their approach was restricted to single-channel records. Albertsen and Hansen (1994) extended the equations for the application to multi-channel records by comprising several channels in a macro channel.

The HMM fit comprises the following steps:
It starts from an putative occupation $\alpha_1(j)$ of the states S_j at time $t = 1$ (**initialization**):

$$\alpha_1(j) = A_i(y_1)\pi_j,\dots 1 \le j \le n \tag{4.45}$$

with π_j being the steady-state concentrations of S_j (Eq. (4.17)) and $A_j(y_1)$ giving the probability that the measured current value y_i belongs to state S_j (Eq. (4.12)).

Then, the 1-step prediction is done recursively by calculating the so-called forward probability (Huang et al., 1990) (**iteration**):

$$\alpha_{t+1}(j) = \left[\sum_{i=1}^{n}\alpha_t(i)p_{ij}\right]A_j(y_{t+1}),\quad 1 \le t \le N-1, 1 \le j \le n \tag{4.46}$$

until the end of the time series is reached at $t = T$. From these final probabilities $\alpha_T(j)$ of the occupation of the state S_j, the likelihood L is calculated

$$L(Y \mid \lambda) = \sum_{i=1}^{n}\alpha_T(i) \tag{4.47}$$

The fit is done under the guidance of a simplex algorithm (Caceci and Cacheris, 1984; Press et al., 1987) which delivers sets of rate constants k_{ij}. From these k_{ij}, the probabilities p_{ij} (Eq. (4.6)) are calculated according to the solution of the Kolmogorov-Feller equations (Eq. (4.7)) in the case of a finite state, stationary Markov model (Bharucha Reid, 1960). The matrix exponential is defined via a Taylor series expansion (Golub and Van Loan, 1983). The simplex algorithm changes the k_{ij} until a maximum likelihood L (Eq. (4.47)) is reached.

The multi-channel HMM fit is described in detail by Albertsen and Hansen (1994). It is implemented in the software *downhill* available under http://www.zbm.uni-kiel.de.

A more sophisticated HMM fit has been developed by Venkataramanan et al. (1998a; 1998b; 2000). This algorithm also includes the frequency response of the anti-aliasing filter and an estimation of the noise. It is not used here, as we feel that the analysis by means of beta distributions (section 4.8 and chapter 5) yields the same temporal resolution and is more robust in the application. However, a short survey over extensions of this algorithm in the literature can be found in section 5.2.1.

4.8. Beta distributions

4.8.1. Generation of beta distributions

Among the different tools for the evaluation of gating employed in our group, the analysis of beta distributions (Schroeder and Hansen, 2006) and of 2-dimensional dwell-time distributions (Huth et al., 2006) turned out to be more efficient than 1-dimensional dwell-time analysis (Blunck et al., 1998) or the direct fit of the time series (Albertsen and Hansen, 1994). In chapters 6 and 7, the approach of Schroeder and Hansen (2006) for the reconstruction of the true current by means of beta distributions (see chapter 5.3) is of crucial importance.

Beta distributions describe the effect of low-pass filtering on gated signals. The theory developed by Pawula (1970) for random telegraph signals was shown to be valid also for two-state Markov processes in patch clamp signals by FitzHugh (1983). The theory enables the evaluation of the original rate constants of the fast (unresolved) gating process by means of fitting the measured amplitude histograms.

Fig. 4.12 illustrates the effect of a filter on gating. If the mean dwell-time in a state is shorter than the rise time of the anti-aliasing filter, the nominal value of the symbol of this state (current) is never reached. Instead, an artificially reduced (apparent) current and some additional noise are measured.
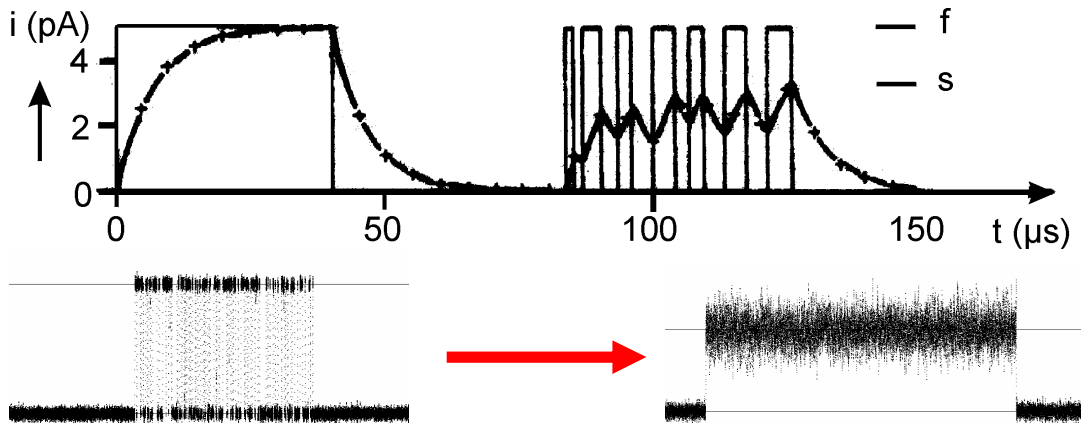
Fig. 4.12. Effects of a low pass filter on slow (left-hand side) and fast (right-hand side) gating. Top: noise-free time series. Bottom: noisy (simulated, section 4.9) time series.

In his diploma thesis, Riessner (1994) extended the underlying system of differential equations to multi-state hidden Markov models, coining the term „extended beta distributions". The distributions-per-level A_i for the Markov states S_i are the solutions of Eq. (4.48).

$$\left[S_i(\infty) \right] A_i'(I) = \frac{(k_{ii}\tau - 1) \cdot \left[S_i(\infty) \right] A_i(I) - \sum_{j \neq i} k_{ji}\tau \cdot \left[S_j(\infty) \right] A_j(I)}{I - I_i} \tag{4.48}$$

with $\tau = 1/2\pi f_{3dB}$ being the time constant of the low-pass filter, $S_i(\infty)$ the steady-state occupation probabilities of the Markov states, I_i their nominal currents and k_{ij} the rate constants, as defined in section 4.2. One problem becomes obvious immediately from

the denominator in Eq. (4.48): the beta distributions have poles at the nominal current values I_i. Riessner (1998) overcame this problem by solving the system of equations (4.48) numerically.

However, all these equations are restricted to 1st-order filters; there is no straight-forward procedure to calculate beta distributions obtained from higher-order filters (Riessner, 1998). Yellen (1984) introduced correction factors for higher order filters (e.g., a 4-pole Bessel filter), but simulations showed that this did not always yield the desired effect (Harlfinger, 2000).

In order to account for higher order filters, Harlfinger (2003) extended the beta fit program of Riessner (1998) by using simulations (as described in section 4.9) instead of deterministic algorithms to provide the theoretical curves. This is quite time-consuming during a fitting routine, but it turned out to be the most efficient way to resolve fast flickering. The theoretical beta distributions are obtained as follows:

1. From a guessed set of rate constants, a time series is simulated, employing the same noise amplitude and filter response as in the measured data (section 4.9).
2. The amplitude histogram $A_I(I)$ of the simulated time series is created by means of the program *Kiel-Patch*. In recording with N channels, multi-channel amplitude distributions (A_N) are calculated iteratively by means of convolution

$$A_N(I) = \int A_I(u) \cdot A_{(N-1)}(I-u)\,du \qquad (4.49)$$

with A_1 being a single-channel amplitude distribution and $A_{(N-1)}$ the distribution for (N-1) channels.

3. The amplitude distribution of noise $W(I)$ is included by convolution

$$A(I) = \int A_N(u) \cdot W(I-u)\,du \qquad (4.50)$$

In the case of gaussian noise, $W(I)$ can be calculated from the knowledge of the variance σ obtained from jump-free sections of the time series.

$$W(I) = \frac{1}{\sqrt{2\pi}\sigma} e^{-\frac{I^2}{2\sigma^2}} \qquad (4.51)$$

In this approach, the spectral distribution of the noise is not important as long as the gaussian amplitude distribution is not distorted. Nevertheless, Eq. (4.50) offers also the possibility to include non-gaussian noise by replacing Eq.(4.51) by the adequate function.

$W(u)$ should not include the noise caused by fast gating. Since the noise of the base line is gaussian, a theoretical distribution can be used with the variance of $W(u)$ obtained from a jump-free section of the time series. Such a section could always be obtained in all our investigations on human MaxiK channels or the dominant K^+ channel in *Chara*, because the related 5-state Markov model had long-living closed states (Farokhi et al., 2000; Hansen et al., 2003).

In all simulations, the corner frequency of the anti-aliasing 4-pole Bessel filter is set to 50 kHz, and the sampling rate is 200 kHz.

4.8.2. Curve fitting

Fitting theoretical beta distributions to measured amplitude histograms on the basis of an assumed Markov model minimizes

$$\text{error sum} = \sum_{i=1}^{N_I} \frac{(A_{\text{exp,i}} - A_{\text{theo,i}})^2}{A_{\text{exp,i}} + 0.1} \tag{4.52}$$

$A_{\text{exp,i}}$ is a data point in the amplitude histogram obtained from the measured time series. $A_{\text{theo,i}} = A_N(I)$ (Eq. (4.50)) is a "theoretical" data point in the amplitude histogram obtained from the time series simulated from an assumed Markov model as described in the previous section. N_I is the number of data points in the amplitude histograms (number of intervals on the current axis, in our case 4096). The denominator prevents that the maximum values of the amplitude histogram get the highest weight. The highest values are close to the gaussian distribution whereas the deviations carrying the information about fast gating are found at the slope of the distribution. 0.1 is added in order to prevent overflow resulting from division by zero.

The procedure is time consuming as each step of the simplex algorithm (Caceci and Cacheris, 1984) requires one simulation of the time series. However, there is the advantage of Eqs. (4.49) and (4.50) which implies that multi-channel beta distributions can be obtained from convolution of single-channel distributions. Thus, they do not require the time-consuming simulation of a macro-channel including the m^N states of a m-state N-channel scenario as in the direct fit of the time series (Albertsen and Hansen, 1994).

4.9. Simulation of surrogate time series

Surrogate time series or simulated time series are generated by computer software on the basis of a model. They are supposed to mimic the kinetic behavior of a measured time series. They are used for two purposes. Firstly, when new analytic tools are to be tested time series are required whose kinetic parameters are known. This is not provided by measured time series, thus surrogate time series have to be used. The test will show whether the analytical tools can reveal these parameters. Secondly, they are employed in fitting routines is order to generate the theoretical time series which is compared with the measured one. This is a crucial element of the beta fit used here for the analysis of fast gating (chapters 5, 6 and 7).

The basic approach of generating time series from a selected Markov model with an assumed set of states and rate constants has been described in previous papers (Blunck et al., 1998; Caliebe et al., 2002; Riessner et al., 2002; Schroder et al., 2004). The software for the generation of surrogate time series has been improved in several PhD theses (Albertsen, 1994; Draber, 1994; Riessner, 1998). The program *simulat* is available at http://www.zbm.uni-kiel.de/software.

The simulations were done by the following routine, described by Riessner et al. (2002). It generates a continuous Markov process, therefore accounting correctly for any dwell-time generated from the Markov model, including those shorter than the sampling frequency. It also accounts for multiple jumps during one sampling period.

The program also includes generation of noise of selectable magnitude and a customizable anti-aliasing filter.

The first Markov state is randomly selected according to the initial starting probabilities π_i. Then, pairs of random numbers are used for each jump during the generation of the time series:

The first number (uniformly distributed, $n_1 \in [0,1]$) is used to calculate the time of the next jump (Δt) from the source state S_i to the sink state S_j. The distribution of dwell-times of the source state S_i is

$$f_{S_i}(\Delta t) = f_i(\Delta t) = \exp(-k_{ii} \cdot \Delta t) \quad \text{with} \quad -k_{ii} = \sum_{j \neq i} k_{ij} \quad (4.53)$$

The jump time Δt is selected from the inversion of Eq. (4.53)

$$\Delta t = -\frac{1}{k_{ii}} \ln(n_1) \quad (4.54)$$

The second random number n_2 (uniformly distributed, $n_2 \in [0,1]$) gives the target of the jump (sink state S_j). For the selection of the target, the section between 0 and 1 is divided into sections of length $k_{im}/(-k_{ii})$ assigned to the states S_m. The state S_j in whose section n_2 happens to fall is called the sink (destination) state. The system still remains in state S_i for the time Δt. Then, the jump to S_j occurs, and after this jump, the algorithm starts again from this new state by generating two new random numbers.

The sequence of states $q(t)$ generates a noise- and filter-free sequence of output symbols (current) $I(t)$ by assigning the nominal current values I_i to the respective Markov states S_i:

$$I(t) = \begin{cases} I_1 & \text{if } q(t) = S_1 \\ \dots \\ I_m & \text{if } q(t) = S_m \end{cases} \quad (4.55)$$

It has been found that a length of 10^7 data points is sufficient to keep the statistical variance of the "theoretical time series" small enough.

The filter is introduced as follows. A measured or calculated filter response to a current jump $s(t)$ of a 4-pole Bessel anti-aliasing filter is stored in the computer. This filter corresponds to that one built into the Dagan amplifier used in the experiments.

For the generation of the surrogate time series, a series of delayed filter responses is created. The responses $s(t\text{-}t_k)$ are added at the times when the Markov process $I(t)$ (4.55) makes a jumps as given by the following equation

$$I_{filt}(t) = \sum_{k=k_{low}}^{k_{up}} \left[I_{ij}(t_k) \cdot s(t - t_k) \right] \quad (4.56)$$

with

$$t_k = \sum_{i=1}^{k} \Delta t_i \quad \text{and} \quad h(t) = 0 \quad \text{for} \quad t < 0 \quad (4.57)$$

with $I_{ij}(t_k)$ being the step in current related to the jump from output symbol S_i to S_j at time t_k. t_k is given in continuous time, and mostly does not coincide with the sampling points. Then, $s(t-t_k)$ is obtained from interpolation of the stored values of the stored responses of the anti-aliasing filter $s(t)$. The lower limit k_{low} of the sum in Eq. (4.56) was determined by the fact that those responses could be omitted if the related $s(t)$ had decreased below one bit of the DA converter.

The last step of the simulations is the superimposition of noise to the time series created by Eq. (4.56). To keep simulation time short, the noise time series was not generated for each simulation, but stored in the computer. White gaussian noise generated by a Box-Muller algorithm (Press et al., 1987) was filtered with the same filter $s(t)$ as the Markov process. The noise time series was scaled accordingly to the chosen signal-to-noise-ratio (SNR) and added to the Markov process.

$$SNR = \left(\frac{\Delta I^2}{\sigma^2} \right) \qquad (4.58)$$

with $\Delta I = I_i - I_j$ being the difference in the nominal currents of the related levels and σ the standard deviation of the background noise.

In all simulations used in this thesis, the assumed sampling rate was 200 kHz, and the anti-aliasing filter was a 4-pole Bessel filter with a corner frequency of 50 kHz.

5. Further development of the methods to resolve fast gating

Summary. For the analysis of fast gating in MaxiK channels, new tools of data analysis had to be furnished which are described in the following sections. The methodological improvements resulted in 4 publications (Schroder et al., 2004; Schroder et al., 2005; Huth et al., 2006; Schroeder and Hansen, 2006). The three first-author papers are given in detail in sections 5.1 to 5.3. The coauthor paper (Huth et al., 2006) has been described in the PhD thesis of Huth (2005). Thus, only the basic messages are summarized in section 5.4.

Section 5.1 (Schroder et al., 2004) deals with distributions-per-level. The initial issue of these investigations was not the analysis of fast gating. The main topics were the creation of a test for the reliability of Hinkley detectors for jump detection and the option to distinguish between different Markov models by means of the errors of the Hinkley detector. At the end of that paper, however, there was a glimpse on what should become of great importance for the research of this thesis: the detection of fast gating (Fig. 5.7 and Fig. 5.8).

In section 5.2, the last point of Schroder et al. (2004), detection of fast gating, came in the focus of interest. Prior to the work reported there, Philip Harlfinger (2003) tried to utilize beta distributions for the detection of fast gating. He worked on an approach to combine two methods: HMM fit for the slow gating up to 30 ms^{-1} and beta fit for faster gating. After he had left, his results were to be published. However, during the manufacturing of the figures for the paper, it became apparent that the approach of Harlfinger was not as powerful as anticipated. This led to a new concept of combining HMM fit and beta fit. The SQ fit (subsequent HMM and beta fit) was created. Testing the algorithm made obvious that gating in the range below one µs could be analyzed by means of beta distributions. This was one of the breakthroughs enabling the access to fast gating in MaxiK channels.

In section 5.3 (Schroeder and Hansen, 2006), a new virtue of the beta fit was detected, i.e., its ability to determine the true single-channel current I_{true}. If gating frequencies become higher than the frequency of the low-pass filter of the recording set-up, then the filter averages over open and closed times, and an apparent current I_{app} occurs at the output of the amplifier which is lower than I_{true} (definitions see section 4.1.1). The finding that the beta fit is a means of reconstructing I_{true} became the key for the analysis of the structure/function relationships presented in sections 6 and 7).

Section 5.4 (Huth et al., 2006) mentions an alternative approach which is based on 2-dimensional dwell-time analysis. High temporal resolution is provided by the generation of the theoretical 2-dimensional dwell-times histograms by means of surrogate time series which automatically account for the effect of the low-pass filter of the set-up. Surprisingly, also this approach turned out to be able to determine I_{true}. However, the enormous requirement of computer time (1 month per time series in contrast to 1 day in the case of beta distributions) led to the exclusive usage of beta distributions for the investigations here.

5.1. Distributions-per-level

(The content of this section was published as Schroder et al., 2004)

5.1.1. Introduction

The kinetic behavior of ion channels is described by Markov models (section 4.2, Korn and Horn, 1988; Yeo et al., 1988; Ball and Rice, 1992; Blunck et al., 1998). There are three main methods for revealing an adequate Markov model and for evaluating the rate constants of the transitions between the states of these Markov models:

1. Applying level and jump detectors in order to create dwell-time histograms (sections 4.4 to 4.6, Schultze and Draber, 1993; Colquhoun et al., 1996; Blunck et al., 1998).
2. Applying a direct fit to the time series using a Maximum Likelihood estimator (section 4.7, Fredkin and Rice, 1992; Albertsen and Hansen, 1994; Klein et al., 1997; Farokhi et al., 2000; Hansen et al., 2003)
3. Creating amplitude histograms and fitting the deviations from gaussians by beta distributions (sections 4.8 and 5.3, FitzHugh, 1983; Yellen, 1984; Klieber and Gradmann, 1993; Riessner, 1998).

Dwell-time analysis requires reliable detectors for estimating the current levels of the time series and for detecting the jumps (times of the transitions from one conducting state to another). The direct fit of the time series needs only a level detector, whereas beta distributions can be generated without any detector. Farokhi et al. (2000) have shown that the direct fit of the time series is more powerful than dwell-time analysis at the edge of temporal resolution. Nevertheless, dwell-time analysis is much less time consuming; analysis and results are more obvious to the researcher, whereas the HMM fit works in the dark tunnel of mathematics, as it does not provide a graphical control of the procedure. The output is just some numbers (rate constants) which the researcher has to believe. Thus, there is still a role for dwell-time analysis (Colquhoun et al., 2003; Huth et al., 2006), and consequently a need for reliable jump detectors. The investigations reported here will show that the analysis of beta distributions, too, can profit from level and jump detection.

Noise and fast gating often lead to malfunctions of the employed detectors. Every jump detector has an integration time to smooth out noise. Increasing this integration time reduces false alarms (fake transitions induced by noise), but increases the number of missed events. Schultze and Draber (1993) employed simulated time series to find an optimum compromise between false alarms and missed events with Hinkley detectors.

Here, it is shown that the generation of distributions-per-level can reveal malfunctions of the detectors. Distributions-per-level can be obtained by adding a simple routine to the software of the Hinkley detector: The detector assigns noisy sections of the time series to estimated levels of the original Markov process. An extra book keeping routine collects the data points belonging to the same level into an array assigned to this level, thus creating time series-per-level. Form this time series-per-level distributions-per-level are created.

Besides their ability to indicate malfunctions of the detectors the distributions-per-level provided some more benefits, namely a means of discriminating different

(sublevel) Markov models suggested for the measured time series. More important, they can enhance the power of beta distribution analysis in order to get a quantitative description of fast gating. This is illustrated here only very shortly and will be applied and discussed more extensively in section 5.3 and chapters 6 and 7.

5.1.2. Generating distributions-per-level

Our program for analysis of patch clamp data (*kielpatch.exe* on http://www.zbm.uni-kiel.de/software) includes three built-in Hinkley detectors: First-Order Hinkley Detector, Higher-Order (8th) Hinkley Detector (HOHD, Schultze and Draber, 1993) and the Sublevel Hinkley Detector (DHD, Draber and Schultze, 1994b) which can also detect sublevels. The Hinkley detectors need *a-priori* information, i.e., the putative current levels and the related variance in order to get optimum settings of the threshold for jump detection (Schultze and Draber, 1993). The levels can be supplied by three different methods (section 4.1.2): a. fit of the amplitude distributions by a sum of gaussians, b. fit-by-eye and c. automatic level detector. Riessner et al. (2002) have shown that fit-by-eye and the automatic detector perform equally well, whereas the analysis of the amplitude histogram by gaussian distributions fails in noisy time series with fast gating.

Distributions-per-level were obtained from a simple book keeping routine added to the software of the Sublevel Hinkley detector (SHD). This routine creates different data arrays, one for each current level. The routine sorts the data points of the measured time series into that array whose level is just indicated by the Hinkley detector. The data points in such an array all belong to the same putative level. They are use to generated the distribution-per-level.

5.1.3. Results

5.1.3.1. Test of level detectors

If a detector works well, the distributions-per-levels of a time series without fast gating should be gaussian distributions around the nominal current values. However, missed events and false alarms (Schultze and Draber, 1993) spoil this nice picture. The suggested test of the performance of the detector is illustrated by means of surrogate data, i.e., by times series simulated from an assumed Markov model as described in section 4.9.

The models used for illustrating the performance of the distributions-per-level are quite simple models with one state for each conductance level. Hidden Markov models (HMM, section 4.2) are not employed because level detectors do not realize jumps between states of equal conductivity (kinetic states that are not distinguished by the applied experimental procedure can be merged into apparent states, Hansen et al., 1983).

Fig. 5.1A shows the amplitude histogram obtained from a O-C model (one open state O and one closed state C) with the parameters given in the legend. Because of high noise, the individual peaks cannot be distinguished. This amplitude histogram should be fitted by the sum of two gaussians (not shown), but a good fit is also obtained with a sum of three gaussian (shown by the gaussians in Fig. 5.1A). The fit with this wrong scenario is quite perfect and supports the statement made by Riessner et al. (2002) that

the fit of amplitude histograms is the least reliable means of determining current levels. Thus, the experimenter erroneously believes that the time series can be fitted with three levels with the currents and variance taken from the gaussians in Fig. 5.1A. The SHD detector with the settings from the three gaussians finds sojourns at the assumed levels. These levels (Z, F, 2F) are given as solid vertical lines in Fig. 5.1C, whereas the true levels O and C are denoted by dotted lines. The distributions-per-level in Fig. 5.1C delivered by the Hinkley detector show two important features (with O, C being the true levels, Z, F, 2F those found by the detector).

1. The distributions related to Z and 2F peak at the true levels C and O (Fig. 5.1C). This indicates that Z and 2F were the wrong choice.
2. The distribution related to F has its peak at level F. This may be unexpected as we know that there is no level F. Here an effect may come into play that is investigated in more detail below, namely the generation of make-believe sublevels by the anti-aliasing filter of the recording apparatus. The filter smoothes the transitions between currents levels, generating data points between the levels. Further, noise may locate some adjacent data points in the range of the detector looking at level F.
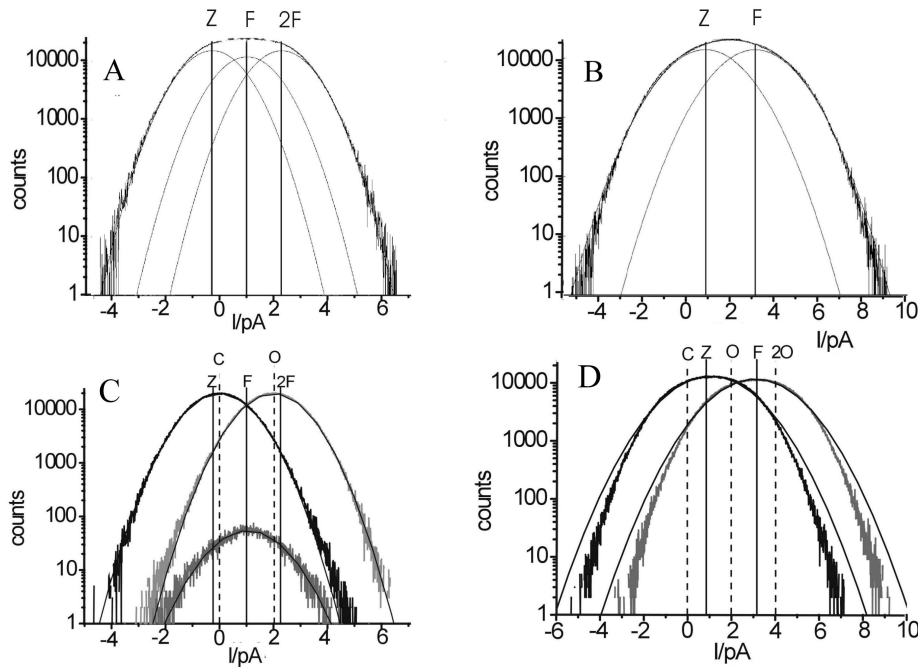
Fig. 5.1. Distributions-per level as a means of detecting malfunctions of the level detectors. (A) Time series simulated from a symmetrical C-O model with the rate constants $k_{CO} = k_{OC} = k = 1000$ s^{-1}. Current of the open state is 2 pA and the noise variance is $\sigma = 1$ pA. The amplitude histogram is fitted by a two-channel model with the states Z (closed), F (one channel open) and 2F (two channels open). The fit yields the following currents: I(Z) = -0.24 pA, I(F) = 1 pA and I(2F) = 2.37 pA. The variance was smaller than that of the simulation $\sigma = 0.92$ pA. The parameters obtained from this fit are used as settings for the Hinkley detector resulting in distributions-per-level shown in (C). The resulting two major distribution functions can be fitted with their peaks located at 0 and 2 pA and $\sigma = 1$ pA, i.e., exactly the values used for the simulation of (A). (B) Here a 2-channel model (2x C-O) with nominal currents at 0 pA, 2 pA and 4 pA and $\sigma = 1.2$ pA is fitted by a simple Z-F model resulting in I(Z) = 0.85 pA, I(F) = 3.16 pA and $\sigma = 1.43$ pA. (D) Distributions-per-level obtained from the 2-state fit of (B) with levels at 0.85 pA and at 3.1 pA with $\sigma = 1.64$ pA.

The deviations of the peaks of the two major distributions clearly indicate that the detector was set to the wrong levels, thus revealing the incorrect hypothesis. In addition, the peaks of these distributions indicate the location of the true levels.

The other way round does not work so well, i.e., generating the time series with a three-state model (C-O-2O) and analyzing it erroneously with a two-state model. Fig. 5.1B shows that a perfect fit of the amplitude histogram can be obtained with two gaussians at level Z and F. Using these parameters as settings for the SHD yields the distributions-per-level in Fig. 5.1D. The two distributions look quite good. The only indication of malfunction is obtained from the comparison with gaussian distributions. Fig. 5.1D shows that at the basis the fitted gaussian distribution (smooth lines in Fig. 5.1D) is wider than the experimentally determined one. This is unusual as in all cases investigated below the base tends to be wider than the top (relative to the gaussian distribution). Nevertheless, this is quite a weak argument for rejecting the incorrect fit of Fig. 5.1B. There are two better approaches. The first one is to look for a jump-free section of the time series. Then it becomes obvious that the noise of the fitted distributions is higher than that of the jump-free section. The second approach would be an attempt to make a fit with a higher number of levels. If the number of estimated levels is higher than that of the measured time series this would be indicated by a phenomenon such as that in Fig. 5.1C.

In the following sections, additional indications of malfunctions are obtained and discussed. However, a probably more important feature of the distributions-per-level will be demonstrated: discrimination between different Markov models and investigation of the origin of sublevels.

5.1.3.2. Model discrimination

Forbidden transitions

The kinetic behavior of channel gating is described by Markov models. Often it is difficult to make a decision as to whether a putative model is the correct one (see also chapter 8). Here some examples are given which show that the distributions-per-level can be helpful. However, it is not possible to distinguish between states of equal conductivity in Hidden Markov models.

The first case deals with the problem addressed previously by Caliebe et al. (2002) and Draber and Schultze (1994b). Two scenarios are compared:

- Scenario 2Ch ("two channels"): two identical channels with three levels: C (closed), S (sublevel) and O (open).
- Scenario 4Ch ("four channels"): A set of four channels, two with the levels C and S and two with the levels C and O.

A time series is generated on the basis of scenario 2Ch, i.e., 2 channels C-S-O. However, the researcher does not know the correct scenario. Imagine that the SHD (Draber and Schultze, 1994b) is set erroneously to analyze the time series on the basis of the wrong scenario 4Ch. The SHD (sublevel Hinkley detectors) search and find events on all levels of the scenario 4Ch, i.e., C, S, 2S, O, O+S, O+2S, 2O, 2O+S, 2O+2S. Thus, seeing only the record of the Hinkley detector (Fig. 5.2A) and the related dwell-time distributions (not shown) the experimenter is tempted to believe that scenario 4Ch (2 small and 2 big channels) holds. (Even though 2O+S and 2O+2S have

not been observed, but the experimenter may believe that these levels occur too rarely). Now, the generation of the distributions-per-level helps to detect a wrong choice of model. Fig. 5.2B shows that the "false" levels do not peak at their nominal current values but at a current level that occurs only in (the correct) scenario 2Ch. This shows that the Hinkley detector has done incorrect assignments. An example of such an incorrect assignment is shown by the arrow in Fig. 5.2A. The channel has jumped to level 2O, but that one of the simultaneously working Hinkley detectors aiming at O+2S has won the race (section 4.4, Draber and Schultze, 1994b). The Hinkley detector thus claims to have seen level O+2S. The distributions-per-level, however, show that O+2S is not an allowed level as it does not peak at its nominal value in Fig. 2B. The peak at 2O indicates that the detector erroneously has taken jumps to 2O as jumps to O+2S as shown in Fig. 5.2A.
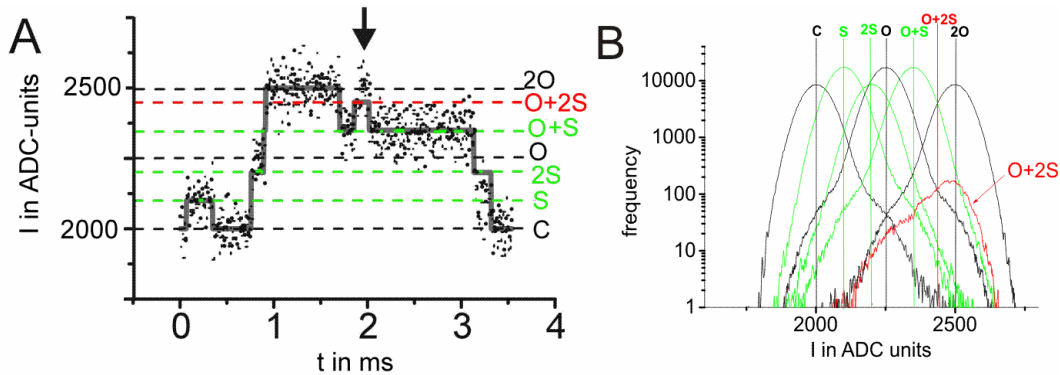
Fig. 5.2. Time series generated by scenario 2Ch (2 cyclic C-S-O-models as in the inset of Fig. 5.4B,C) with all rate constants = 1000 s^{-1} and current in S = 2000 analogue-digital-converter (ADC) units and in O = 2500 ADC-units, variance of the noise σ = 1000 ADC-units. (A) Section of the time series showing the incorrect operation of the Hinkley detector adapted to the wrong model (scenario 4Ch). (B) Distributions-per-level created from the time series in (A).

Sequence of levels

The second case deals with the sequence of levels. Time series are generated for two different scenarios, and it is tested whether the distributions per level can tell which one of the two models was used to generate the investigated time series. Scenario CSO consists of one channel with the Markov model C–S–O. The Markov model of scenario SCO is S-C-O. Thus, the only difference between the two scenarios is the order of states. Time series were generated for both scenarios with the rate constants given in the legend of Fig. 5.3. The Hinkley detector uses the same settings for both scenarios: it looks for the levels C, S, and O, without any restraints regarding the allowed jumps.

Fig. 5.3 shows that the distributions-per level can find out which time series belongs to which scenario. The crucial feature which becomes obvious in Fig. 5.3 is obtained from the comparison of the right-hand slopes of the S-level-distributions (green curves) in Fig. 5.3A and Fig. 5.3B. This slope shows a perfect gaussian shape in Fig. 5.3B, but not in Fig. 5.3A. The reason is obvious: the transition O-S must not occur in scenario SCO in Fig. 5.3B, and levels O and S are never adjacent. Thus, the detector cannot erroneously remain in S when the channel has already jumped into state O, because such a transition does not occur. This criterion corresponds to that of the transition matrices suggested by Draber and Schultze (1994b). On the other hand, the bulge on the right-hand side of C-level distribution extending to level O indicates that the channel

has already jumped from C to O, but the detector has failed to realize this. The same holds for the left-hand side of the O-level distribution. The origin of the bulges on the slopes of the distributions in Fig. 5.3B lies in the fact that the detector has failed to realize in time the jump from C to O, or missed events have occurred, i.e., jumps into state O that have not been realized by the detector.
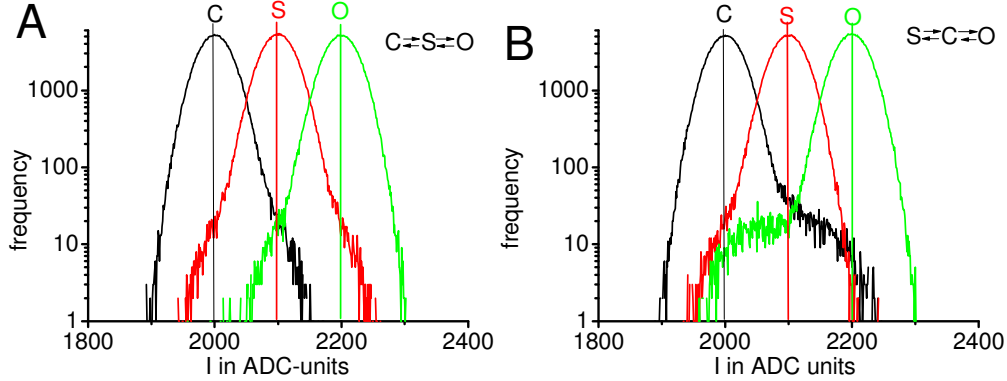
Fig. 5.3. Revealing the sequence of states. (A) Distributions-per-level obtained from a time series simulated for a C-S-O model with the following settings: all rate constants 1000 s^{-1}, current levels are C = 2000 AD-converter units, S = 2100, O = 2200, variance of the noise σ = 50 ADC-units (B). Distributions-per-level obtained from a time series simulated for an S-C-O model with the same currents and rate constants.

Cyclic vs. linear Markov models

The third case shows that cyclic models can be distinguished from linear models. Scenario CYC is the cyclic model and scenario LIN the linear model, both are shown in Fig. 5.4B-E.

Time series were generated for both models with the rate constants as given in the legend of Fig. 5.4. Fig. 5.4B and E reveal a feature that is already known from Fig. 5.3: In the model O-C-S (Fig. 5.4E) the transition between S and O must not occur. This is indicated by the gaussian slope on the right-hand side of the distribution of level S. The bulge on the left-hand side of O may be considered as an example against this argument. However the long extension of the bulge indicates that it results from undetected O $\rightarrow$ C jumps, similar to the right-hand bulge of the C-level distribution resulting from C $\rightarrow$ O jumps.

Thus, it is already possible to distinguish between scenario CYC and scenario LIN on the basis of the criterion applied in Fig. 5.3: Deviations from the gaussian slope indicate that a transition may occur. (This means that the sleepiness of the detector helps to reveal existent transitions).

However, there is another test. The software of the Hinkley detector provides the option to forbid certain transitions. The distributions-per-level in Fig. 5.4C and Fig. 5.4E are obtained under the constraint that the transitions between S and O are forbidden. This constraint should not affect scenario LIN, because this transition must not occur. Basically, the distributions in Fig. 5.4D and 4E look very similar. The only difference is that in Fig. 5.4D a bulge also occurs on the right-hand side of the S-distribution. This is difficult to understand. A solution may be as follows. If there are jumps S $\rightarrow$ C $\rightarrow$ O, and the sojourn in C is not realized by the detector (or if a double jump has occurred), then a jump S $\rightarrow$ O seems to have occurred in the experimental data. If the detector is

fast enough this rare events would not spoil the slope in Fig. 5.4D. However, if the transition S → O is forbidden, then the detector remains in the nominal level S, but the data points belong to O.
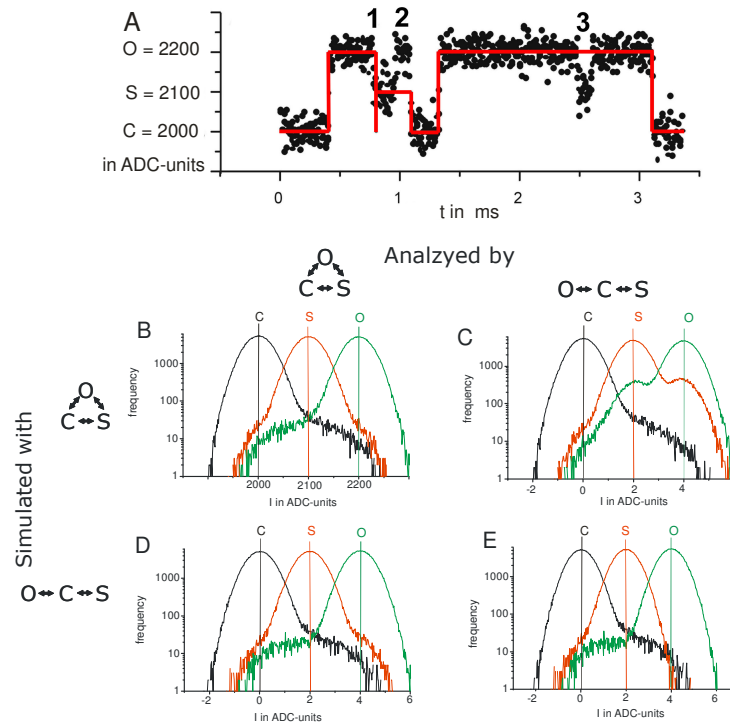
Fig. 5.4. Distributions-per-level obtained with and without restriction for the Hinkley detector from time series generated from two different models as indicated by the insets. (A) Simulated time series obtained from the cyclic model of (B) and (C). The smooth red line gives the reconstructed time series provided by the Hinkley detector. Numbers indicate malfunctions. (B, C) Cyclic model with all the rate constants being 1000 s^{-1}. (D,E) Linear Markov model with all the rate constants being 1000 s^{-1}. (C) and (E): Distributions-per-level from level detectors working under the constraint that the transitions S-O are forbidden.

Thus, the introduction of the restriction inactivates the criterion of Fig. 5.3, but a better criterion is obtained instead: now, the distributions of level S and O in Fig. 5.4C display enormous satellite peaks at the wrong levels. In the cyclic model, transitions between O and S do occur, but the detector is not allowed to follow them.

Examples are shown in Fig. 5.4A. At label "1", the time series jumps from O to S. The detector, however, can jump to S only via the allowed transitions O-C-S. This may occur also with restriction, and consequently the extensions of the C-distributions into the range of the S and O distributions is of the same magnitude in Fig. 5.4B and Fig. 5.4C. The interesting events occur at labels "2" and "3". At "2", the time series jumps from S to O, but the detector is not allowed to follow. Thus, data points of O are assigned to level S, leading to the satellite peak of the S-distribution at level O in Fig. 5.4C. The situation at label "3" in Fig. 5.4A gives an example of the generation of the satellite peak of the O-distribution at level S in Fig. 5.4C.

The situations indicated by arrows 2 and 3 do not occur in the S-C-O model. The restriction has an effect only if double jumps occur. However, these are rare. Nevertheless they may lead to the small difference between Fig. 5.4D and Fig. 5.4E discussed above.
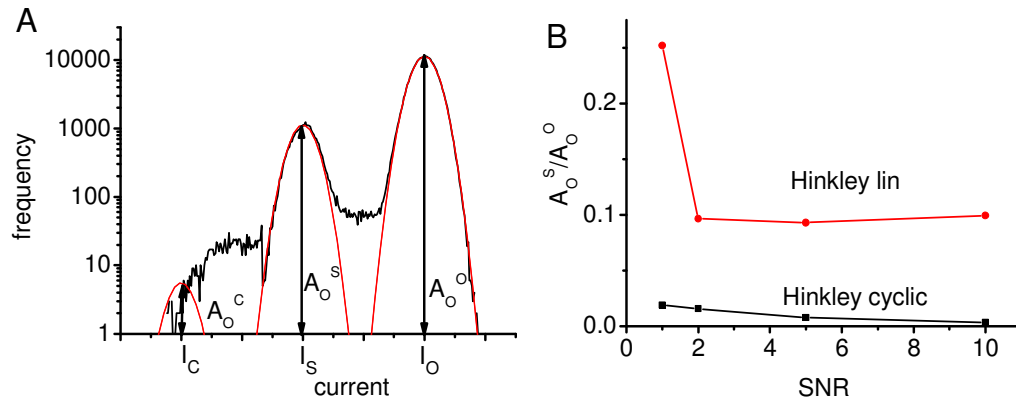
Fig. 5.5. Quantification of the model discrimination in Fig. 5.4 (A) O-distribution of a time series simulated with the cyclic model and (wrongly) analyzed with the linear model (corresponds to the green curve in in Fig. 5.4C). A sum of three Gaussian distributions of equal σ, centered at the nominal current levels of the three states C, S and O is fitted to the histogram. (B) Amplitude factors from the gaussian distribution at I_{S0} in (A) for different signal-to-noise ratios (SNR). Black: Distributions-per-level were constructed from the right model (cyclic), Red: from the wrong model (linear, as in (A)).

The "leakage" from one current level into the other when the wrong Markov model is used to construct the distributions-per-level can easily be quantified. This is demonstrated in Fig. 5.5. A time series was simulated with the cyclic model and distributions per level were constructed with 1. the cyclic model and 2. the (wrong) linear model. The resulting open distribution was fitted with a sum of three gaussian distributions with equal standard deviation and centered at the current levels of the three states C, S and O. An example for the fit of open distribution obtained with the linear model is shown in Fig. 5.5A (same situation as in Fig. 5.4C). The resulting amplitude factors were normalized and are shown in Fig. 5.5B for different signal-to-noise ratios. The wrong settings for the Hinkley detector (linear model, red in Fig. 5.5B) lead to an obvious increase of A_O^S (= fraction of the O-histogram that leaked over from S).

However, this direction was not followed further, because the focus of the research shifted from model discrimination to the analysis of the fast flickering. This promised (and yielded) insights into channel function in a more straightforward way.

5.1.3.3. Revealing fast gating: mode switching in MaxiK

The detection of fast gating in a measured time series is still a difficult problem. Farokhi et al. (2000) have shown that dwell-time analysis fails near the corner frequency of the anti-aliasing filter. The direct fit of the time series with a Hidden Markov model can extend the range to higher rate constants (and thus was successful in detecting the fast gating causing the reduction of the apparent single-channel current in the AMFE, (Farokhi et al., 2000; Hansen et al., 2003). However, an even more powerful means is the analysis of beta distributions describing the gating-induced deviation of the amplitude histogram from the gaussian distribution caused by the noise of the jump-free time series (section 4.8 and 5.3, FitzHugh, 1983; Yellen, 1984; Klieber and Gradmann, 1993; Riessner, 1998; Schroeder and Hansen, 2006, 2007; Schroeder and Hansen, 2008). The generation of beta distributions by fast gating is illustrated in Fig. 5.7, below. In experimental data, the beta distributions of individual levels may be hidden in the sum of the distributions of all levels.

Here we show that the distributions-per-level may be helpful. Fig. 5.6A shows a time series obtained from a MaxiK channel measured as described in section 3.4. The solution in the pipette (luminal) was 5 mM KNO_3, 140 mM $NaNO_3$, 1.2 mM $Mg(NO_3)_2$, 4.17 mM $NaHCO_3$, 0.44 mM KH_2PO_4, 0.34 mM Na_2HPO_4, and in the bathing medium (cytosolic) it was 10 mM TlCl, 140 mM KCl, 5 mM $MgCl_2$, 10 mM HEPES. pH 7.2 was on either side.

After a long record with moderate switching, all on a sudden the channel enters a mode of fast gating. At the right-hand side of Fig. 5.6A, it returns to the original mode. This time series clearly demonstrates how fast gating leads to a reduction of apparent single-channel current. In Fig. 5.6A, the effect is immediately obvious. This is similar to the situation of the Cs^+ block of the K^+ channel in *Chara* (Draber and Hansen, 1994), whereas in the case of the K^+/Tl^+ AMFE in *Chara* the reduction of apparent single-channel current by fast gating had to be revealed by means of a long mathematical analysis (Farokhi et al., 2000). In MaxiK, (non-spontaneous) fast flickering was induced by ion depletion at high positive voltages (chapter 6) and K^+/Tl^+-mixtures (chapter 7).

The interval of fast flickering in Fig. 5.6A is used for the generation of the distributions in Fig. 5.6B and C. Fig. 5.6B gives the overall-amplitude distribution. It is obvious that details cannot be recognized. However, the distributions-per-level in Fig. 5.6C clearly show the occurrence of beta distributions. The distribution of the closed state is asymmetrical and the O-distribution has become broader than the distribution of apparent jump-free sections of the time series (smooth lines in Fig. 5.6C).

Here, the data from the MaxiK channel serve to demonstrate the new approach opened by the distributions-per level. The detailed analysis of the beta distributions in Fig. 5.7 is a foretaste of the investigation of the in chapter 6 and 7.
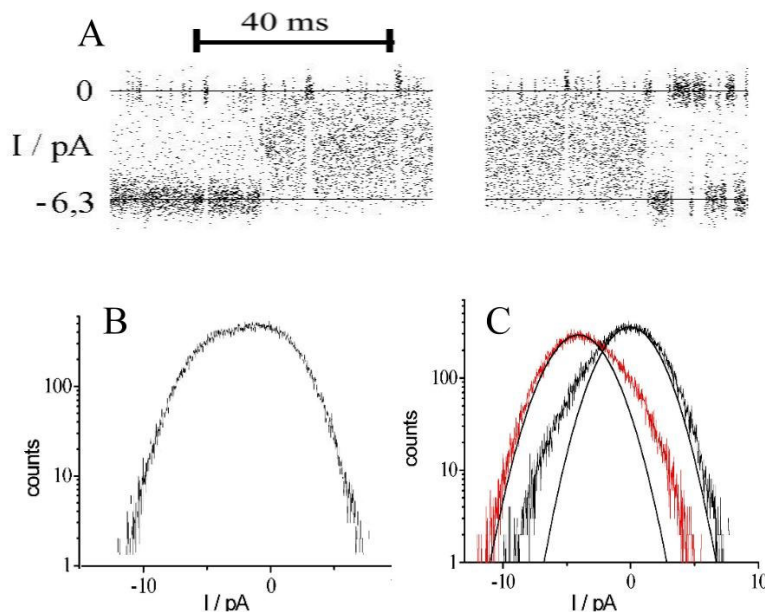
Fig. 5.6. Revealing beta distributions as caused by fast gating by means of the distributions-per-level. (A) Time series obtained from a MaxiK channel showing mode switching i.e., a spontaneous change in the kinetic properties of the channel (The middle part of about 150 ms has been omitted in order to show the transitions with higher temporal resolution). (B) Overall amplitude histogram of the middle section of (A) showing fast flickering. (C) Distributions-per-level. The smooth lines give the gaussian distribution of the noise as obtained from the section of the time series with slow gating (right- and left-hand side of (A)).

5.1.3.4. Sublevels and fast gating in Chara
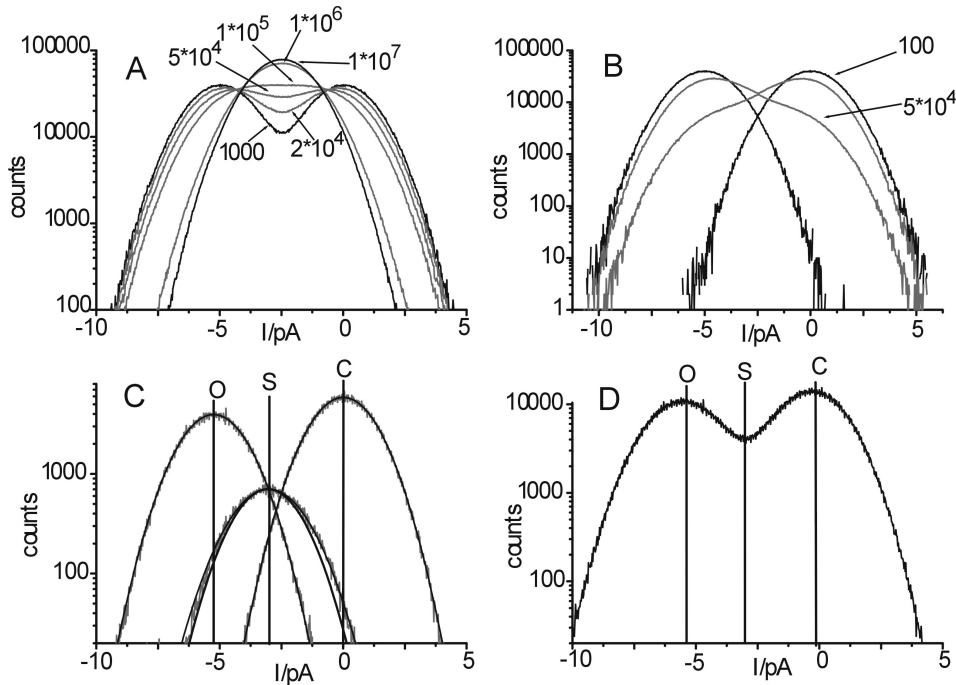
Fig. 5.7. Comparison of sublevels generated by fast flickering in surrogate data and those measured in inside-out recordings from the dominant K^+ channel in the tonoplast of *Chara*. Simulated and real data with $I(O) = -5$ pA, noise $\sigma = 1$ pA, bandwidth of 4-pole Bessel filter = 50 kHz. (A) Simulated data in a symmetrical C-O model with the rate constants $k_{CO} = k_{OC} = k$ as given on the curves in s^{-1}. (B) Distributions-per-level at $k = 50\ 000\ s^{-1}$ and at $k = 100\ s^{-1}$. (C) Distributions-per-level obtained from *Chara*. (D) The overall amplitude histogram from *Chara*.

Patch-clamp measurements for Fig. 5.7C and D were performed on cytosolic droplets of *Chara* as described in section 3.4. The pipette (luminal) was filled with 250 mM KNO_3 + 5 mM $Ca(NO_3)_2$ and the bathing medium (cytosolic) contained 230 mM KNO_3 + 20 mM $TlNO_3$ + 5 mM $Ca(NO_3)_2$.

In our experiments on the K^+ channel in *Chara*, there were times when sublevels occurred very frequently, and at other times they did not occur for months. There were two questions which could not be settled. 1. What conditions caused their appearance? 2. Were they true conductance levels, or were they just apparent levels as caused by averaging over fast gating? We do not see how to tackle the first question, but the distributions-per-level may provide a means of solving the second question. If the sublevels arise from fast gating, distributions-per-level may reveal beta distributions as in the example of Fig. 5.6.

In order to study what kinds of effect can occur, fast flickering producing an apparent sublevel was generated by an O-C model. A two-state model is sufficient, because longer sojourns in the C- and O-state do not contribute to the putative flickering causing the sublevel (section 5.3, Schroeder and Hansen, 2006).

Fig. 5.7A shows distributions resulting from a fast flickering O-C model. The rate constants k_{OC} and k_{CO} are equal. This is to be expected because the sublevel has been found to occur in the middle between C and O. Fig. 5.7B gives an estimate in what

range of rate constants the generation of a sublevel by fast flickering can occur and what effects on the shape of the distributions-per-level are to be expected.

The curves in Fig. 5.7A show that there is a limited range of rate constants where the distribution functions would reveal gating as the origin of the sublevels. If the rate constants are too slow (up to k = filter bandwidth) analysis would identify the two original levels O and C. If they are too fast (10^7 s^{-1}), the filter smoothes out the effects of gating, and the beta distribution does not get wider than the gaussian distribution of the superimposed noise.

The curves in Fig. 5.7A are compared with that one obtained from the sublevel (S) of the measured data in Fig. 5.7C. Since these sublevels are in the middle between O and C, the putative rate constants of the flickering have to be symmetrical. This implies that there is no skewness of the beta distributions as in the C-level distribution in Fig. 5.6. The only candidate for indicating fast gating is the width of the beta distribution. The distribution of the sublevel in *Chara* is only 10 % broader than that of the gaussian distribution of the noise of a jump-free time series (inner smooth line in the middle distribution of Fig. 5.7C). In Fig. 5.7A, 10% broadening is obtained for k = 10^6 s^{-1}. No sign of this broadening can be observed in the overall amplitude histogram of Fig. 5.7D. The detailed analysis by means of beta distributions (Schroeder and Hansen, 2006) will be addressed in section 5.3 and applied in chapters 6 and 7.

5.1.4. Discussion

Usually, level detectors work hidden in an encapsulated sphere of mathematics. There are few and not very efficient statistical means of controlling their operation by means of simulations (Schultze and Draber, 1993; Riessner et al., 2002). The determination of the distributions-per-level turns out to provide a look into this dark sphere and watch the performance of the level detectors. The size of the bulges in Fig. 5.3 provide an estimate of how many data points were assigned to the wrong levels.

However, distributions-per-level may not only act as supervisors of level detectors (Fig. 5.1 and Fig. 5.2); the ability to distinguish between different Markov models as shown in Fig. 5.2 to Fig. 5.4 may become a useful means of modeling. A general theory is not yet available; but simulations can help. It has to be recommended that every statement obtained from this kind of analysis has to be tested on surrogate data. Simulations have to be employed in order to check whether the model obtained from the analysis generates exactly the time series and distributions functions which have been obtained directly from the data. In a second step, alternative models have to be used for the generation of the simulated time series and to check whether the related distributions differ significantly from those of the measured data. This would be an indication of how unique the evaluated model is.

Subsequently, beta distributions, as in Fig. 5.6 and Fig. 5.7, could be developed into a very important means of increasing temporal resolution (section 5.3). Crucial for this is the reliability of the distributions-per-level obtained by the extended software of the Hinkley detector. As shown in Fig. 5.1 to Fig. 5.4 deviations from the gaussian form may be caused by malfunction of the Hinkley detector. However, the comparison of Fig. 5.1 to Fig. 5.4 with Fig. 5.6 and Fig. 5.7 shows that the beta distribution have a more harmonic curve shape than those resulting from the failures of the detector. And indeed, in the following investigations, no hints were found that the 'shoulders' of the distribution causes by wrongly assigned jumps might disturb the beta distributions noticeably.

5.2. SQ fit: A combination of HMM- and beta fit

(The content of this section was published as Schroder et al., 2005)

5.2.1. Introduction

Ion channels are not rigid cylinders which facilitate a steady stream of ions across biological membranes. Instead, they are vibrating proteins leading to spontaneous or agent-induced interruptions of the stream. The resulting closures and openings are modeled by means of Markov models (section 4.2, Korn and Horn, 1988; Ball and Rice, 1992; Blunck et al., 1998). The rate constants of the transitions between the states of the Markov model even in a single channel span a wide range from about 1 s^{-1} to at least 1 μs^{-1} (chapter 6, Schroeder and Hansen, 2007). However, the temporal resolution of classical evaluation algorithms leads to a limit which is about 100 000 s^{-1} (Parzefall et al., 1998; Farokhi et al., 2000; Zheng et al., 2001; Hansen et al., 2003).

The different approaches commonly employed for the evaluation of patch clamp time series offer different potencies for the analysis of fast gating. Widely applied is dwell-time analysis (Blunck et al., 1998). In order to account for fast gating, missed-events corrections have been suggested (Ball et al., 1993; Draber and Schultze, 1994a). However, Farokhi et al. (2000) have found a horizontal dependence of the evaluated rate constants on the "true" rate constants which is not the optimum condition for correction algorithms. Dwell-time analysis can become powerful if 2-dimensional histograms are evaluated (Magleby and Weiss, 1990a; Huth et al., 2006).

The beta fit is based on the generation of amplitude histograms and fitting their deviations from gaussians by beta distributions (FitzHugh, 1983; Klieber & Gradmann, 1993; Riessner, 1998; Yellen, 1984). The restriction to two-state Markov models was overcome by Riessner (1998), but only for 1st-order filters.

So far, the best results have been obtained with the prediction fit which is a direct fit to the time series using a Maximum Likelihood estimator (Fredkin and Rice, 1992; Albertsen and Hansen, 1994; Klein et al., 1997). Even the classical prediction fit can work quite well with rate constants higher than the filter frequency (Farokhi et al., 2000; Hansen et al., 2003).

The most comprehensive approach is that of Venkataramanan et al. (1998a; 1998b; 2000). The memory introduced by the filter response is included into the prediction equations by using so-called meta states. The ensemble of Markov states observed at time *t* is expanded to a Markov field comprising the states at *t*, *t-1* to *t-n* with *n* being determined by the order of the filter. Filter order and thus the size of the Markov field was reduced by deconvolution of the time series with the inverse filter. Colored noise, open-channel noise and the effect of the filter on the noise are included into calculated amplitude distribution functions per meta state using an autoregressive (AR) filter. Furthermore, the drift of the base line can be incorporated according to Venkataramanan and Sigworth (2002). This general concept has been modified by other authors, mainly in order to shorten computing time. Qin et al. (2000) used a direct optimization approach which yields the rate constants and not the transition probabilities (Fredkin and Rice, 1992; Albertsen and Hansen, 1994). This was achieved by replacing the Baum-Welch algorithm by a fit routine. Decreasing computing time was obtained by reducing the number of meta states by clustering states of equal conductance for single- and multi-channel records. Fredkin and Rice (2001) achieved a tremendous acceleration of the computations by excluding unlikely meta states. Michalek et al. (2000) also excluded unlikely meta states. However, the replacement of

the AR filter by an ARMA filter for the filter response increased computer time. This was compensated by using an approximated likelihood.

Nevertheless, the computing times are still very long. Single-channel records in our lab usually have 2 to 16 x 10^6 data points sampled at 200 kHz. Often, there are at least two channels in a record, and each channel has to be modeled by 5 states (Farokhi et al., 2000; Hansen et al., 2003), probably even more (chapter 8). This takes 4 to 32 h on a 2.5-GHz Athlon computer, still using the basic algorithms of Albertsen and Hansen (1994). In order to account for the filter without increasing computing time too much, we considered two approaches: First, we tried an approach (EP fit) which can be visualized as an extreme reduction of the method of Venkataramanan et al. (1998a; 1998b; 2000). The introduction of the filter into the prediction algorithm of the direct fit of the time series was further simplified, and we did not consider the effect of the filter on the noise. Second, it is tested whether a combined evaluation based on the direct fit of the time series with simple prediction (SP fit) and on the analysis of amplitude histograms (beta fit) can move the time resolution to faster rate constants. (The beta fit makes use of the observation that fast gating causes deviations from the gaussian shape of the measured amplitude histograms, see sections 4.8 and 5.3).

5.2.2. Mathematical Tools

5.2.2.1. Illustration of the problem

The problem (and chance) of high temporal resolution is illustrated in Fig. 5.8. In the theory of Markov processes applied to ion channel analysis, it is assumed that the noise-free signal immediately jumps from one state of conductivity to another. In a real experiment, the transition is soft as caused by the inevitable anti-aliasing filter. Fig. 5.8 shows the response of a 4th-order Bessel filter with the sampling frequency being four times the corner frequency of the filter. The black vertical line shows the true jump of the Markov process at $t/T = 0$. The filter output, presented in green, gives a delayed response.
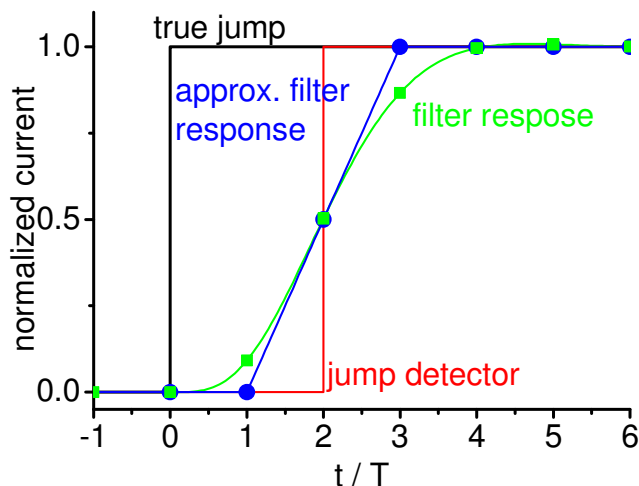
Fig. 5.8. Response of a 4-pole Bessel filter (green) with a cut-off frequency of 4/T (T being the sampling interval) to a jump in noise-free channel current (black) at t = 0. The green squares show the current values sampled at the output of the filter. The red curve indicates the jump as determined by a threshold jump detector. The blue circles present the approximated response of the filter used in the fit with extended prediction (EP fit) below.

The red line shows where a level detector would see the jump. This is also the location which is delivered by the classical prediction fit of the time series as the average expected time of the jump, because in 50% of the investigated events this intermediate level would be assigned to the lower level and in 50% to the higher level.

In Fig. 5.8, the data points before the jump of the red curve have a higher probability of being assigned to the lower level, and those behind it are presumably assigned to the upper level. The location of the detected level is delayed by two sampling periods. However, this is not of concern because the jump out of the level is delayed by the same interval, thus leaving the dwell-time in the level unaffected.

The major problem that is caused by the filter results from the fact that the channel may switch back before the filter has reached the threshold in Fig. 5.8. Thus, short jumps may remain undetected. Jumping is a stochastic process: the rate constants related to a transition of the Markov model result in an exponential distribution of dwell-times, with the average of these dwell-times being the inverse of the rate constant (section 4.5). If the short transitions are not detected then the average dwell-time is moved to longer time constants and the apparent rate constant is slower than the original one.

5.2.2.2. Fitting Strategies

Note: In contradiction to section 4.7, the Hidden Markov fit (HMM) is called here single-step prediction fit (SP) to distinguish it from the extended prediction fit (EP).

Two approaches provide the fundaments for the investigations here; the prediction fit (section 4.7) and the beta fit (section 4.8). The prediction fit uses a prediction equation (see Eq. (5.5), below) in order to give an estimate of the Markov state at the next sampling point of the time series (Fredkin and Rice, 1992; Albertsen and Hansen, 1994; Klein et al., 1997). It is also called a direct fit of the time series. The beta fit utilizes the deviations of the measured amplitude histogram from that of a gaussian one (FitzHugh, 1983; Yellen, 1984; Klieber and Gradmann, 1993; Riessner, 1998).

All approaches discussed here are target fits. This implies that the fit seeks to provide results which are the target of our interest. In the case of Markov models, the rate constants are the natural parameters of modeling. If Molecular Dynamics simulations will be applied to channel gating, the rate constants, not the transition probabilities (see Eq. (4.6)), are the experimental parameters suitable for testing the predictions of the model. This is different from some approaches such as dwell-time analysis which normally yields amplitude factors and time constants of exponentials (Colquhoun et al., 1996). However, also dwell-time analysis can be done as a target fit (section 4.5.3, Kijima and Kijima, 1987b; Blunck et al., 1998; Csanady, 2000). Targets fits avoid the cumbersome conversion of amplitude factors and time constants to rate constants (Jackson, 1997), but the evaluations depends on *a-priori* knowledge (assumption) of the generating Markov model.

5.2.2.3. Markov models

The gating of ion channels can be described by Markov models (Korn and Horn, 1988 and section 4.2), which consist of several states. These states may have different conductivities or different kinetic behavior. Different Markov models are used for

testing the algorithms developed here. For investigations which are to illustrate basic insights or which are presented in order to show the failure of a suggested approach, a simple two-state model

$$C \underset{2q}{\overset{q}{\rightleftharpoons}} O \qquad (5.1)$$

is used. The factor q is changed in the range tests below. In order to show that a suggested approach works even under more complicated conditions, a 5-state model with two open (A, O) and three closed states (G, C, Z) is used. It has been used by Farokhi et al. (2000) for the description of the gating of the dominant K^+ channel in *Chara*.

$$A \underset{0.5}{\overset{1.5}{\rightleftharpoons}} O \underset{7q}{\overset{10q}{\rightleftharpoons}} G \underset{4}{\overset{3.5}{\rightleftharpoons}} C \underset{0.2}{\overset{0.5}{\rightleftharpoons}} Z \qquad (5.2)$$
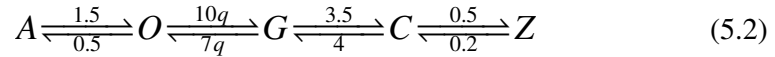
(rate constants in ms^{-1}). Its suitability as a model for testing algorithms arises from the feature that it comprises a wide spectrum of rate constants from very fast ones to very slow ones.

5.2.2.4. Curve fitting

Below, different convergence criteria are employed: Maximum Likelihood for the direct fit of the time series (section 4.7) and Least Square for the amplitude histogram (section 4.8). In either case, fitting is done under the guidance of a simplex algorithm (Caceci and Cacheris, 1984). According to former experiments in this lab in many fields of numerical evaluations of biological data, gradient-based methods mostly fail when the number of free parameters exceeds 2 or 3.

Failures of the fitting process can result from two causes: First, the convergence criterion may not have the correct dependence on the parameters sets. It can be too flat (as in the case of beta distributions for slow rate constants) or it can even have its optimum value at the wrong parameter set (as in the case of the SP fit at high rate constants) and lead to the wrong solution. Second, the fitting algorithm (here the simplex) might not be able to find its way from the start simplex to the correct parameter set.

Here, simulated data (their generation is described in section 4.9) are used to test the suggested evaluation algorithms. Thus, the true parameter values are a-priori known (in contrast to a real experiment).

5.2.2.5. Generation of the start simplex

A simplex is a geometrical figure with $N+1$ corners (vertices) in an N-dimensional parameter space. The simplex fitting routine starts from a start simplex which has to be suggested by the investigator. Then it moves like an amoeba (Press et al., 1987) through the N-dimensional parameter space and searches for the optimum value of the convergence criterion.

The start simplex is generated as follows: A set of parameters ($s_{1,n}$) is guessed by the experimenter. This set equals a point (vertex) in the N-dimensional space of the fit

parameters with $n = 1...N$ being the index of the fit parameters, e.g., obtained from k_{ij} after arranging them in a sequential order. The simplex with $N+1$ vertices is generated as follows. The first vertex is $(s_{1,n})$. Additional vertices ($s_{m,n}$ with $m = 2$ to $N+1$) are calculated from the following equation:

$$s_{m,n} = s_{1,n} \cdot w^r \qquad (5.3)$$

with w being the selected width of the start simplex and r a random number between -1 and 1. In section 5.2.4, the first vertex ($s_{1,n}$) is obtained from the rate constants k_{ij} of the simulations

$$\left\{ s_{1,n} \right\} = \left\{ a \cdot k_{i,j} \right\} \qquad (5.4)$$

with the factor a being chosen as explained below. A width of $w = 2$ was found to be useful for the simple prediction fit, and $w = 10$ for the amplitude fit (beta fit). The random number r has to be taken N^2 times from a random generator in order to generate the elements of the $N \times (N+1)$ matrix which represents the $N+1$ vertices. This set of $N+1$ non-degenerate vertices is called the start simplex.

Start simplex 1 including the correct parameter set $(s_{1,n}) = (k_{i,j})$ or $a = 1$ in Eq. (5.4) is employed if it is to be shown that a fit algorithm fails according to the statement "even if the correct value is known, the algorithm cannot reveal it from fitting the data".
Start simplex 2 excluding the correct parameter set. Using a start simplex which excludes the true values with $a \neq 1$ resembles the situation of a real experiment, where the true parameter set is not known. Then both features are tested: the existence of a correct convergence criterion and a smooth error landscape that opens a path to the correct parameter set.

5.2.3. Development of new approaches

5.2.3.1. First improvement of the SP fit: Extended prediction algorithm accounting for the slope of the filter in the prediction algorithm

The classical SP fit has been discussed in detail e.g., by Fredkin and Rice (1992), Albertsen and Hansen (1994) and Klein et al. (1997). More sophisticated approaches accounting for the filter response are mentioned in section 5.2.1. Here, we test whether computer time can be reduced by a strong simplification of these approaches. The incorporation of meta states (Venkataramanan et al., 1998a; Venkataramanan et al., 1998b; Venkataramanan et al., 2000) are replaced by a case differentiation in the prediction equation, and the effect of the filter on the noise is ignored. The filter response is approximated by the blue slope in Fig. 5.8. This approximation simplifies the prediction algorithm described below. It coincides with the true response at $t/T = 2$, but has minor deviations at $t/T = 1$ and $t/T = 3$. The improvement over the classical approach is the smaller deviation from the filter response (green), as compared to the red line in Fig. 5.8 which is used in the simple prediction algorithm.

Again, the jump is realized too late (here it is only one sampling period). However as mentioned above, the parallel shift of the times of the jumps into and out of a level does not change dwell-times.

In the classical approach which does not take the filter into account, the prediction (forward calculation) for the open state of a two-state O-C model is (section 4.7)

$$a_k(O) = a_{k-1}(O)p_{OO}A_O(I_k) + a_{k-1}(C)p_{CO}A_O(I_k) \qquad (5.5)$$

with $a_j(B)$ being the probability of being in state B at time $t = jT$ ($j = k$, k-1), p_{AB} being the probability of a transition from state A to state B, $A_B(I_k)$ being the probability that the measured current I_k measured at time $t = kT$ can be assigned to the current of state B (Eq (4.12). The probability $A_B(I)$ is obtained by fitting the overall amplitude histogram by a sum of gaussians:

$$A(I) = \sum_B A_B(I) = \sum_B F_B \exp\left(\frac{(I - I_B)^2}{2\sigma_B^2}\right) \qquad (5.6)$$

Here, we assume that all σ_B are equal to σ, the noise of the jump-free time series. The scaling factors F_B are omitted, because the distributions per level are normalized to 1.
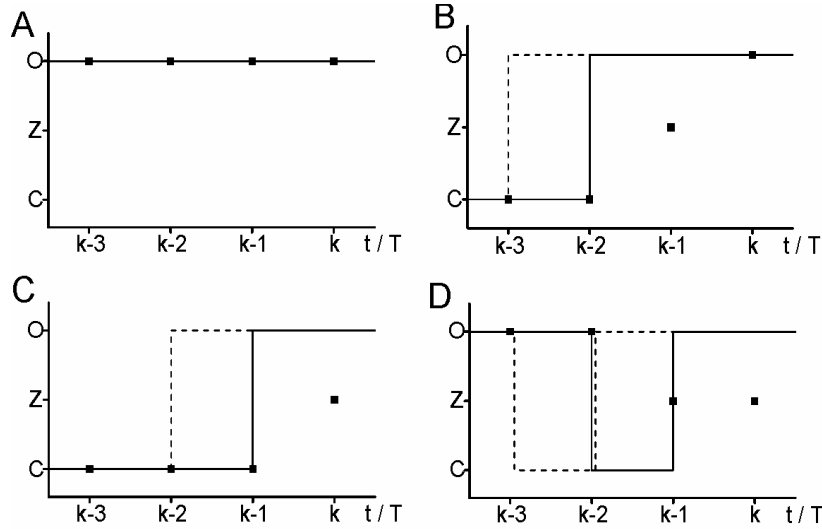
Fig. 5.9. Different scenarios which lead to an open state at time kT. The dotted lines show the true jumps of the Markov model. The continuous line presents the jump which is delayed by one sampling period. This delayed jump is the input signal of a filter approximated by the blue symbols in Fig. 5.8. The squares give the approximated sampled output currents of the anti-aliasing filter (green squares in Fig. 5.8). The four graphs show the filter response for different gating scenarios that would be detected if the prediction algorithm would work properly. This detected jump is delayed by one period as illustrated in Fig. 5.8. (A) No jump has occurred. All values remain at the same level. (B) A jump occurs at $t/T = k-3$. Then the channel is still at the initial level at $t/T = k-2$ and at the intermediate level Z at $t/T = k-1$. This scenario corresponds to Fig. 5.8. (C) The jump occurs at $t/T = k-2$. Then $t/T = k-2$ and $t/T = k-1$ are still at the initial value. The intermediate value is reached at $t/T = k$. (D) A double jump has occurred. Then, the initial value is measured still at $t/T = k-2$, and the values at $t/T = k-1$ and $t/T = k$ are at the intermediate level.

If a filter is involved intermediate values of output current can occur. Fig. 5.9 shows the four different scenarios which describe the different ways from a closed into an open state at time k. The dotted lines in Fig. 5.9B,C and D present the true jump occurring in the channel current. As mentioned above, the approximation of the filter response by the blue slope in Fig. 5.8 results in the delay of the detected jump by one sampling period.

For the sake of simplicity, this effect is ignored. Ignoring this delay has the effect that the thick vertical line in Fig. 5.9 presents the jump which is delivered by the evaluation algorithm.

The squares in Fig. 5.9 present the intermediate level Z (not related to the Markov state Z in Eq. (5.2)) resulting from the filter response in Fig. 5.8. The partial amplitude histogram related to the intermediate level Z is calculated from the noise of the jump-free time series with

$$A_Z(I_k) = \frac{1}{\sqrt{2\pi}\sigma} \exp\left(\frac{\left(I - \frac{1}{2}(I_p + I_a)\right)^2}{2\sigma^2}\right) \qquad (5.7)$$

with I_p and I_a being the levels before and after the jump, respectively.

From Fig. 5.9A,B,C,D, the extended prediction equation can be derived. The scenarios in Fig. 5.9A,B,C,D correspond to the four terms in Eq. (5.8), respectively, as can easily be seen from a comparison of Eq. (5.8) with Fig. 5.9.

$$\begin{aligned} a_k(O) = &\, a_{k-1}(O)\, p_{OO}\left[A_O(y_{k-1})A_O(y_k) + A_Z(y_{k-1})A_O(y_k)\right] \\ &+ a_{k-1}(C)\, p_{CO}\left[A_C(y_{k-1})A_Z(y_k) + A_Z(y_{k-1})A_Z(y_k)\right] \end{aligned} \qquad (5.8)$$

It is important to realize that only the probabilities a_k and a_{k-1} occur explicitly in Eq. (5.8), but not a_{k-2} at $t/T = k$-2. The probability a_{k-2}, however, is implicitly included in Eq. (5.8) by the differentiation of the four cases in Fig. 5.9.

Equations like Eq. (5.8) have to be set up for each one of the involved states of the Markov model. Further, the number of products in each equation increases with the number of states.

In the above equations, there is the inherent assumption that the jumps occur at the sampling points. This, of course, is not quite true, Nevertheless, the following analysis shows that Eq. (5.8) is already an improvement over the classical SP fit with the simple prediction in Eq. (5.5) (section 4.7 and Albertsen and Hansen, 1994), but below it is shown that this holds only for very good SNR.

In order to determine the rate constants from a fitting routine the likelihood L is calculated

$$L = \prod_{k=1}^{N_s} \sum_B^M a_k(B) \qquad (5.9)$$

with N_S being the number of all samples. B stands for all M states with $M = m^N$ of the macro-channel (Colquhoun and Hawkes, 1977, 1990; Blunck et al., 1998) representing N channels with m states. a_k is calculated iteratively from Eq. (5.5) or (5.8). The rate constants k_{AB} are related to the transition probabilities p_{AB} as follows (Albertsen and Hansen, 1994)

$$P = \exp(K \cdot T) \qquad (5.10)$$

with P and K being the matrices related to p_{AB} or k_{AB}, respectively. If the time interval is short with respect to k_{AB}, the relationship is simpler

$$p_{AB} = k_{AB}T \tag{5.11}$$

The Simplex algorithm (see section 5.2.2) employed in the fitting routine uses k_{AB} and calculates p_{AB}. Thus, Eq. (5.10) (or Eq. (5.11)) has not to be inverted.

5.2.3.2. Beta fit

Theoretical beta distributions created from the assumed Markov model were created as described in section 4.8. The fit (also described there) minimizes

$$X^2 = \sum_{i=1}^{N_I} \frac{(A_{\text{exp},i} - A_{theo,i})^2}{A_{\text{exp},i} + 0.1} \tag{5.12}$$

with $A_{exp,i}$ being the measured and $A_{theo,i}$ the theoretical amplitude histogram, respectively, and N_I the number of intervals on the current axis.

5.2.3.3. The simultaneous fit of beta distributions and time series

Below it is shown that the fit of amplitude histograms (beta fit) yields good results for high rate constants whereas the direct fit of the time series (SP fit) gives better approximation for slow rate constants and is less sensitive to noise.

In order to merge both fits into one routine the convergence criterion of the joint fit has to be a function of the convergence criteria of two individual fits. The SP fit maximizes the likelihood L (Eq. (5.9)) whereas the beta fit minimizes X^2 (Eq. (5.12)). Thus, the sum of X^2 and the inverse of L is minimized

$$g \ln X^2 + \ln \frac{1}{L} \rightarrow Min \tag{5.13}$$

The logarithm of L is used because L becomes very small and this would lead to numerical problems in a computer if the product $1/L$ instead of the sum of $-\ln a_k$ (Eq. (5.9)) would be calculated. This implies also the usage of $\ln X^2$, otherwise the error functions related to X^2 would be much steeper, and the effect of X^2 would override that of $\ln L$ in a fitting routine. Furthermore, there is a big difference in magnitude between $\ln X^2$ and $\ln L$. Thus, a weighting factor g is introduced. $g = 0$ implies that the fit is completely based on the SP fit, whereas very high values of g (e.g., higher than 10^6) lead to the dominance of the beta fit.

5.2.3.4. The subsequent simple prediction/beta fit (SQ fit)

Here, the direct fit of the time series with simple prediction (SP) and the beta fit with 4th order Bessel filter are not combined in parallel but subsequently: The robustness of the SP fit is used to give a first estimate of the rate constants. These results are used to generate a start simplex 1 for the beta fit. Since the beta fit has problems to determine slow rate constants they are fixed during this second fitting step. This means that the simplex

algorithm leaves the slow rate constants fixed at the values obtained from the SP fit and varies only the fast rate constants in order to fit the amplitude histogram. The threshold between "fast" and "slow" was set to ¼ of the filter frequency (12.5 ms^{-1}, in the investigations here).

As final result, the slow rate constants from the SP fit and the fast ones from the beta fit are taken.

5.2.4. Results

Testing the algorithms is mainly based on two kinds of test. The range test is to investigate the temporal resolution. A set of about 250 (Fig. 5.10 and Fig. 5.11) or 50 (Fig. 5.12 and Fig. 5.15) time series is generated (see section 4.9) with the pair of fast rate constants k_{ij} set to $q \cdot k_{ij,0}$, (Eqs. (5.1) or (5.2)) with q being the number of the time series and $k_{ij,0}$ being the rate constants of the "slowest" time series. These time series are subject to the inspected algorithm, and it is determined up to which q the algorithm still yields the rate constants used in the simulation. The noise test deals with the sensitivity to noise. Time series having all the same rate constants k_{ij} are superimposed by noise of different strength. This yields the SNR (signal-to-noise ratio) down to which the true rate constants can be revealed by the algorithms.

5.2.4.1. Extended prediction fit accounting for the filter response
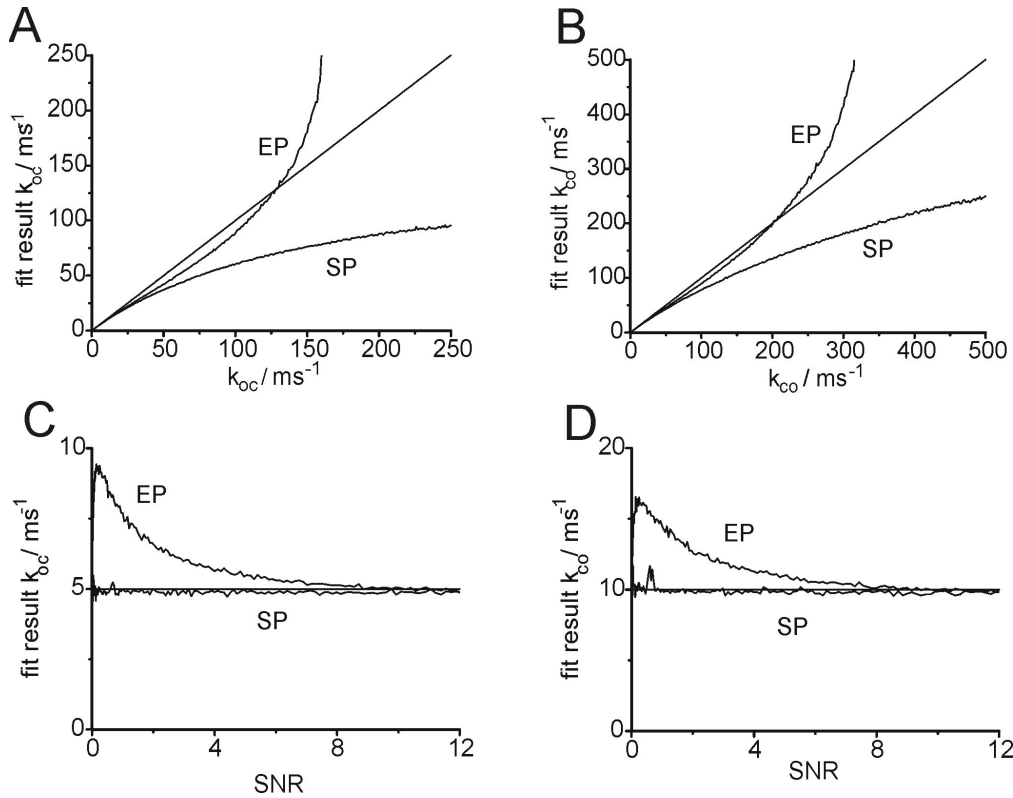
Fig. 5.10. Comparison of the performance of the direct fit of the time series with simple (SP, Eq. (5.5)) and extended prediction (EP, Eq. (5.8)) for a 1-channel 2-state model. The start simplex comprised the true rate constants (a = 1 in Eq. (5.4)). The straight lines mark the correct results. (A,B) Range test with $k_{CO} = 2\,k_{OC}$ as given on the x-axis and SNR = 10. (C,D) Noise test with $k_{OC} = 5$ ms^{-1} and $k_{CO} = 10$ ms^{-1}.

For the investigations of what the direct fit of the time series with simple and extended prediction can do, a simple C – O model is used, and the start simplex includes the true parameter set. In Fig. 5.10, the rate constants are about equal, namely $k_{OC} = q$ 1 ms^{-1} and $k_{CO} = 2\ k_{OC}$ (with q = 1 to 250). The performance of the new approach is compared with that of the classical SP fit (simple prediction fit). With simple prediction, the evaluated rate constants are slower than the real ones as known from Farokhi et al. (2000). The results of the new approach (extended prediction fit) are much closer to the real values. However, at rate constants higher than 150 ms^{-1} the fitted rate constants start to exceed the real ones.

The "noise of the fit" gets obvious from the scatter in Fig. 5.10 as the curves are obtained from 250 independent fits with different rate constants. It is quite low for both algorithms in Fig. 5.10A, B. The start simplex includes the true rate constants, however, this is not of any relevance in the case of the prediction fit, because it is fairly independent of the starting values (see, for example left hand side of Fig. 5.13).

However, the situation is not as good as may be suggested by Fig. 5.10A and B because these simulations are done with low noise, SNR = 10. Fig. 5.10C, D show the dependence on noise for a slow C – O model with $k_{CO} = 10$ ms^{-1} and $k_{OC} = 5$ ms^{-1}. It is obvious that under the conditions of Fig. 5.10A,B, (SNR > 8) the fit works quite well. However, the deviations become serious with SNR close to one. In contrast, the classical direct fit of the time series with simple prediction (SP) is quite insensitive to noise (The low rate constants are chosen because they are in the range, where both fits do equally well at very good SNR).

The reason for the failure of the new approach at high noise levels seems to be quite obvious: often the noise pretends values close to I_Z, the value of the current on the slope of the filter (Fig. 5.8). The assignment of these values to I_Z gets a high weight via Eq. (5.6), and the assignments to the true full level gets low weights. In the classical SP fit the noise has to shift the current by half a level to cause a false alarm, whereas in the new approach a quarter is enough.

Because of this high sensitivity to noise, it has to be stated that the extended prediction algorithm does not yield a tremendous improvement over the classical SP fit. If high temporal resolution is desired, patch clamp recordings get very noisy. With a 50 kHz filter, the SNR is rarely better than 4, more often it is close to 2. Thus, it has to be concluded that this approach can be applied only to patch clamp data with very good SNRs. With bad SNRs, the importance of the inclusion of filtered noise (Venkataramanan et al., 1998a; Venkataramanan et al., 1998b; Venkataramanan et al., 2000) becomes obvious.

5.2.4.2. Beta distributions

Application of the beta fit to a 2-state model

In Fig. 5.11, again a simple C-O model is used for the comparison of the performance of the first-order beta fit and the higher-order beta fit with that of the SP fit. Fig. 5.11A shows that the higher-order fit based on simulations reaches the same good results as the first-order fit of the data filtered by a first-order filter. The results are much better than those of the direct fit of the time series with simple prediction, but also better than those of the extended prediction algorithm (Fig. 5.10).

The noise test in Fig. 5.11B shows that the 4th-order beta fit of a two-state model (Eq. (5.1)) is reliable for signal-to-noise ratios down to about 2.
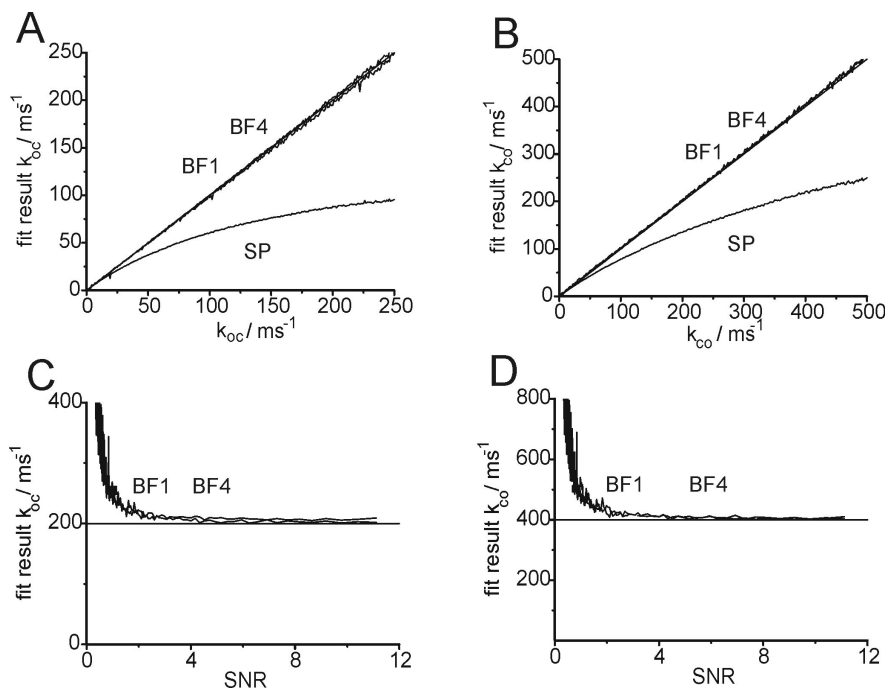
Fig. 5.11. Comparison of the performance of the beta fits with first- and fourth-order filters (BF1 and BF4, respectively, graphs not distinguishable) and the direct fit of the time series with simple prediction algorithm (SP) for a 1-channel 2-state model. The start simplex comprised the true rate constants ($a = 1$ in Eq. (5.4)). The straight lines mark the correct results. (A,B) Range test with $k_{CO} = 2\,k_{OC}$ as given on x-axis and SNR=10. (C,D) Noise test for the beta fits with $k_{OC} = 200$ ms^{-1} and $k_{CO} = 400$ ms^{-1}.

Application of the beta fit to a 5-state model

In order to compare the direct fit of the time series with simple prediction (SP) and the beta fit with 4-th order filter (BF4), the 5-state model of Eq. (5.2) is used. The SP fit starts from start simplex 2 with $a = 0.5$ (Eq. (5.4)), the beta fit from start simplex 1. Fig. 5.12 shows the results. It is impressing that the SP fit does quite well at low and medium rate constants. Only at the fast rate constants k_{OG} and $k_{GO,}$ the SP fit does not reach the original values. The SP fit has the advantage of being robust. Even though it underestimates the fast rate constants (Fig. 5.12C,D) it does so with high reproducibility. Many runs with different start simplexes showed that it is quite independent on the starting conditions (data not shown).

The beta fit is very successful when fitting the fast rate constants of the C-O model (Fig. 5.11). However, it fails completely when applied to the 5-state model (Fig. 5.12) even if the start simplex includes the correct values ($a = 1$ in Eq. (5.4)).

It is obvious that the slow rate constants cannot be determined by means of the beta fit, because they do not cause a deviation from the gaussian shape of the amplitude histogram. However, a better performance could be expected for the fast rate constants k_{OG} and k_{GO}. But even though the slow rate constants do not influence the shape they contribute to the steady-state occupancies of the states and consequently to the height of the amplitude distributions. Thus, an error in the slow rate constants may spoil the estimation of the fast rate constants.
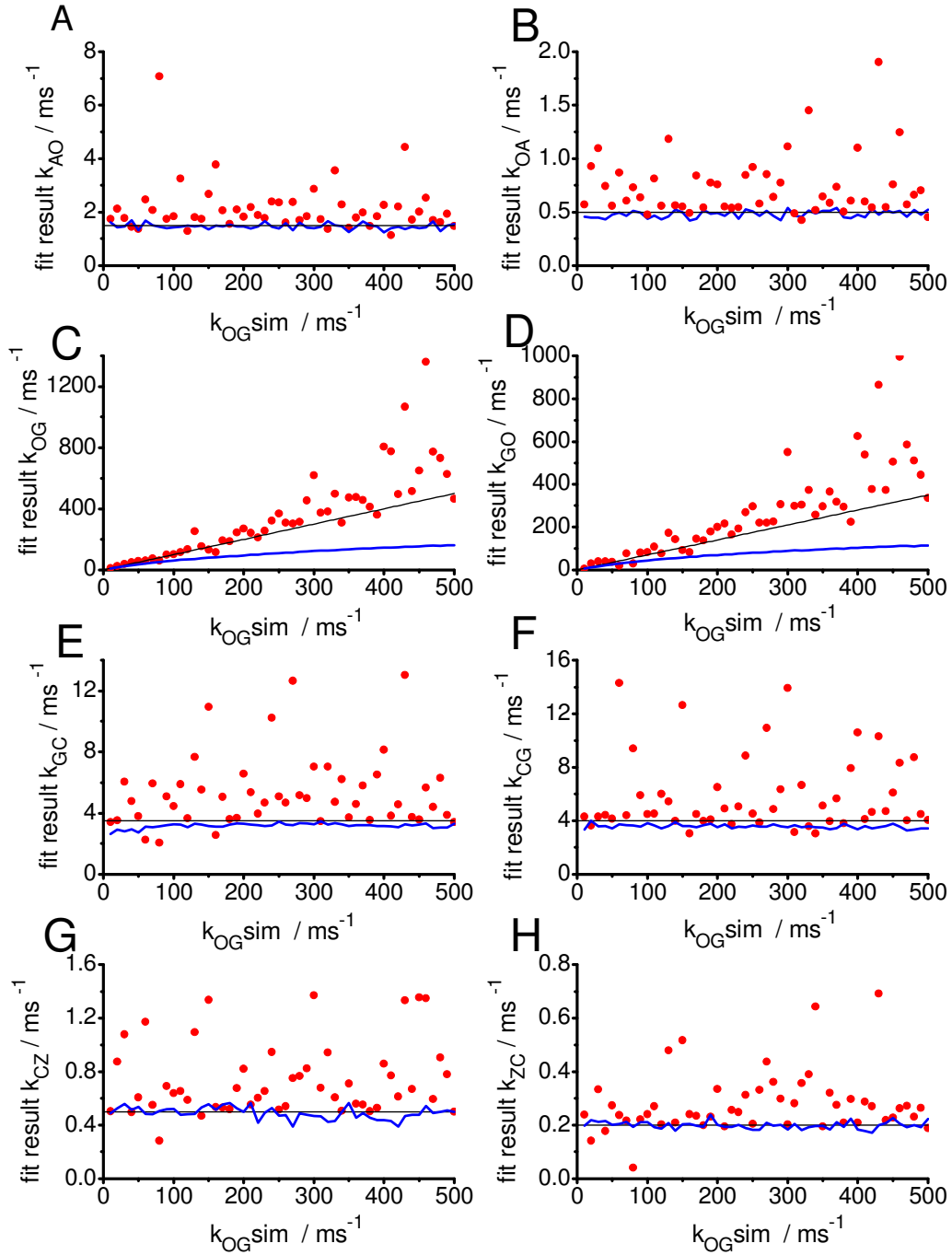
Fig. 5.12. Comparison of SP fit (SP, blue) and beta fit with 4-th order filter (red) using the 5-state model of Eq. (5.2) by studying the influence of the fast rate constants $0.7\ k_{OG} = k_{GO}$ of the "measured" time series (given on the x-axis in all graphs) on the rate constants delivered by the fits. The black lines give the true values (used for the simulation of the "measured" time series). In the case of the simple prediction fit, the start simplex (Eq. (5.3)) is obtained with $w = 2$ and $a = 0.5$ (Eq. (5.4)), and for the beta fit it included the correct set ($a = 1$ in Eq. (5.4)), and w in Eq. (5.3) is 10.

5.2.4.3. Combining SP fit and beta fit in a simultaneous fit

In order to combine the benefits of the SP fit (high reliability at slow rate constants, high independence of fit performance on start simplex) with those of the beta fit (correct fit of fast rate constants), a joint fit is done as described in the section 5.2.3.
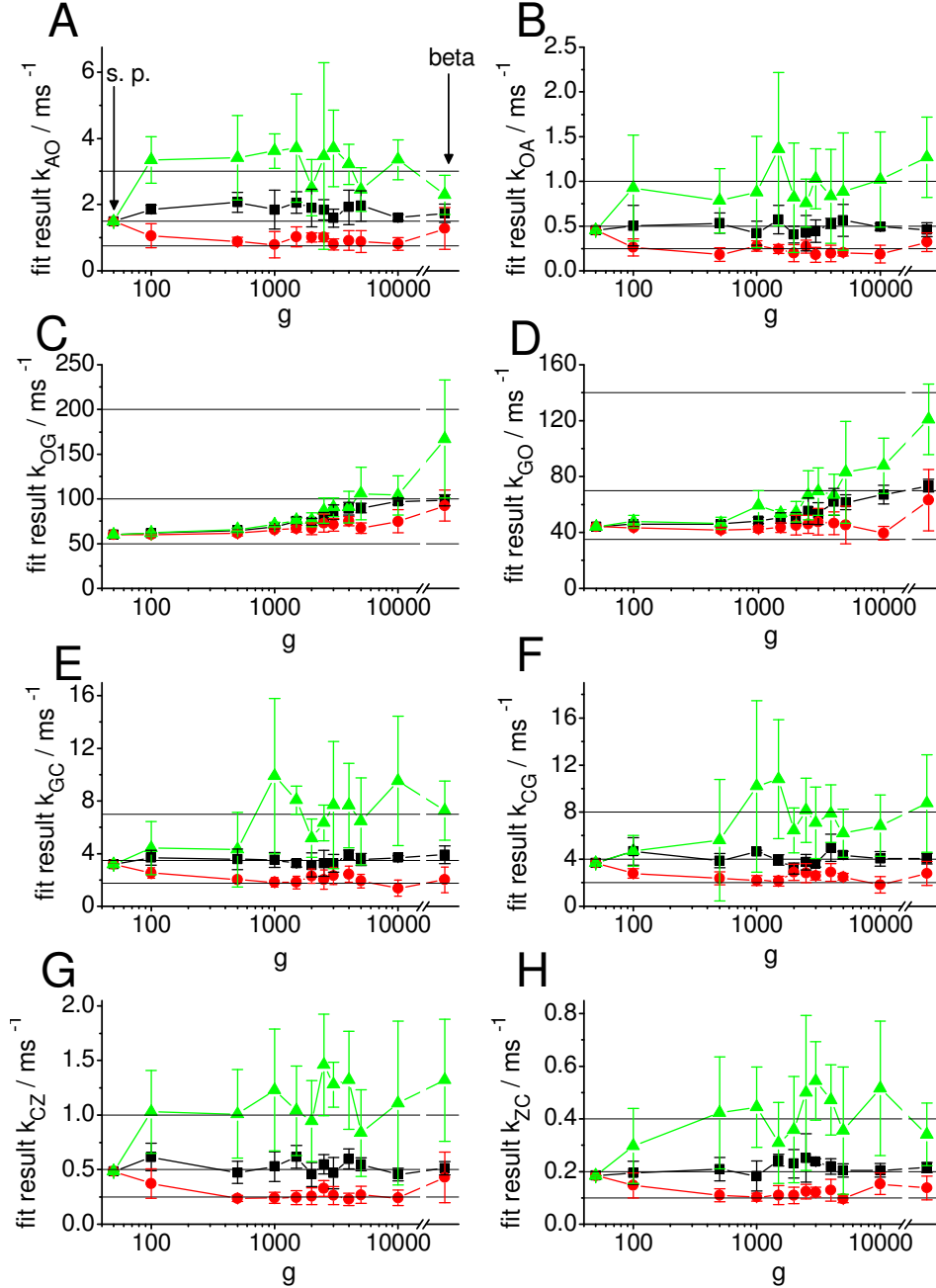
Fig. 5.13. Simultaneous fit of simple prediction fit and beta fit. The dependence on the weighting factor g (Eq. (5.13)) is tested for the 5-state model of Eq. (5.2) (averages and SEM of 5 runs) using three different start simplexes (Eq. (5.4)) with $a = 0.5$ (green triangles, upper horizontal line), 1 (black squares, middle horizontal line) and 2 (red circles, lower horizontal line). The width w of the start simplex in Eq. (5.3) is 2 for the prediction fit and 10 for the beta fit. The k_{ij} of the $s_{1,n}$ vertex (Eq. (5.4)) of the start simplex are given as horizontal lines. The outermost left- and right-hand points result from the pure SP fit ($g = 0$) and from the beta fit ($1/g = 0$), respectively, as indicated by the arrows in (A).

Fig. 5.13 shows the dependence of the results of the simultaneous fit on the weighting factor g (Eq. (5.13)). The results of the simultaneous fit are not encouraging. In the case of the slow transitions the joint fit inherits the high scatter from the beta fit. For the fast transitions, the rate constants increased monotonously with g from the too low values of the pure SP fit ($g = 0$) to the higher and correct values of the amplitude fit (g very high). There is no reduction of the scatter of the fit by the incorporation of the SP fit.

It is to be mentioned that the pure SP fit (left-hand side of all graphs in Fig. 5.13) always finds the same parameters independently of the start simplex. The pure beta fit is not successful (right-hand side of all graphs in Fig. 5.13) as already seen in Fig. 5.12.

The beta fit seemingly is not capable of leaving the start simplex. The reason may be as follows: In one vertex ($s_{1,n}$) of the start simplex the ratios of backward and forward reactions are already identical to the real values. This vertex already leads to occupations of the Markov states (and thus of relative heights in the amplitude histograms) which are already very good. All other vertices have random occupation probabilities and therefore produce worse amplitude histograms than ($s_{1,n}$). This can prevent that the simplex of the beta fit begins to crawl away from the start simplex. In Fig. 5.13, it can be seen that the fit results presented in red and green coincide with the horizontal lines representing $a = 0.5$ and $a = 2$ in Eq. (5.4), respectively. The SP fit, in contrast, puts more weight on the absolute values of the rate constants, and thus is not constructed by violations against the occupation probabilities. The important message of Fig. 5.13 is that the fitting performance cannot be improved by an adequate choice of the weighting factor g in Eq. (5.13).

5.2.4.4. Two-step approach of SP fit and beta fit (SQ fit)

The simultaneous fit above fails because SP fit and beta fit have contradicting aims. In the case of the SP fit, the (too) low values of the fast rate constants yield the best criterion of fitness (maximum likelihood), and in the case of the beta fit the higher (correct) rate constants give the better criterion (minimum error). This conflict can be avoided by the subsequent approach: First, the SP fit is used to give a first estimate of the rate constants. Then, the beta fit is employed starting from these results.
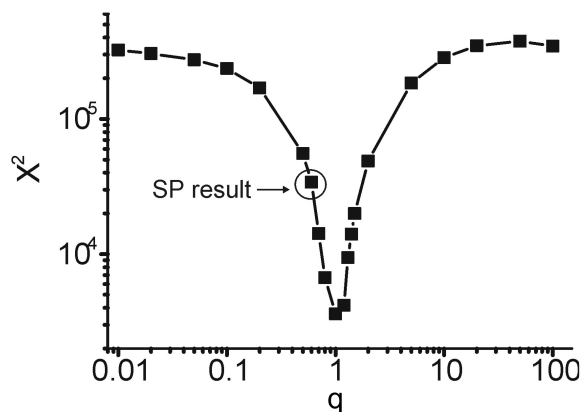
Fig. 5.14. One-dimensional error landscape for the beta fit: The model of the "measured" time series is that of Eq. (5.2) with $k_{OG,0} = 300$ ms^{-1} and $k_{OG,0} = 210$ ms^{-1}. X^2 is calculated by means of Eq. (5.12) as a function of the deviation of the value of $k_{OG} = q\ k_{OG,0}$ and $k_{GO} = q\ k_{OG,0}$ from the true values ($q = 1$). The circle gives the X^2 for the value obtained from the SP fit.

100

In Fig. 5.14 the 5-state model of Eq. (5.2) with the fast rate constants being $k_{OG,0} = 300$ ms^{-1} and $k_{GO,0} = 210$ ms^{-1} is used to simulate the "measured" time series. Then, the "fitted" time series are obtained with $k_{OG,0} = q$ 300 ms^{-1} and $k_{GO,0} = q$ 210 ms^{-1} (q given at the x-axis in Fig. 5.14) and the error sum X^2 is calculated by means of Eq. (5.12). The result is very encouraging: Plotting X^2 over q shows that the solution of the SP fit is on the slope of the valley in Fig. 5.14, and that the best solution ($q = 1$) is at the bottom of the error valley. This shows that the error landscape of beta fit provides optimum conditions for finding the "true" values.

Fig. 5.15 shows a range test for the subsequent SP/beta fit (SQ). The slow rate constants are not shown as their behavior is that of the pure SP fit (Fig. 5.12). In Fig. 5.15, the SP fit shows the underestimation of the fast rate constants as already known from previous simulations (Fig. 5.10-Fig. 5.13). The results of the beta fit are mainly found with the +/- 10% error range up to values of 500 ms^{-1}.
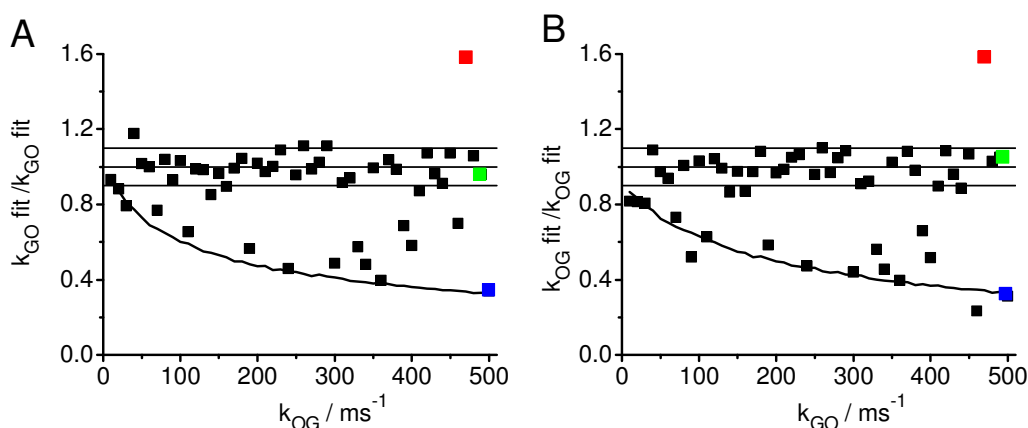
Fig. 5.15. Range test of the subsequent SP/beta fit. The middle horizontal line gives the true values and the parallel horizontal lines present 10% deviation. The smooth descending curve presents the results of the SP fit. The squares show the results of the subsequent SP/beta fit. Start simplex was generated with $a = 0.5$ (Eq. (5.4)) for the SP fit. The subsequent beta fit started from the fast rate constants of the SP fit with $a = 1$. In Fig. 5.16, the resulting amplitude histograms are shown for the three colored SQ results.

Not all beta fits in Fig. 5.15 resulted in reliable k_{ij} as becomes obvious from the points between the line presenting the SP fit and the horizontal lines giving the 10% error range around the true values. However, this is not a major problem, because the investigator has a simple means of detecting the failure of the fitting routine.

First, if the beta fit does not move away from the result of the SP fit, the fit should be repeated. There is an important feature in Fig. 5.15, i.e., there are nearly no results of the beta fit that are too high. If a fit is repeated those values of the rate constants which are higher are expected to be closer to the true ones.

Second, the amplitude histograms of the results of the beta fits should be inspected. Fig. 5.16 shows amplitude histograms calculated from the highlighted values in Fig. 5.15.

Fig. 5.16B shows a perfect fit for the correct solution marked in green in Fig. 5.15. The amplitude histograms in Fig. 5.16A show a weak deviation for the rate constant that are too fast (red in Fig. 5.15) and a more significant deviation in Fig. 5.16C for the rate constants that are too slow (blue in Fig. 5.15). Even if the deviations are small in Fig. 5.16, they are an indication that the fit should be repeated. Fig. 5.16 also shows that the sum of squares (X^2 given inside the histograms) can be used to

distinguish the better solution from the less successful ones. Thus, the experimenter has a means at hand to check the reliability of the fit results.
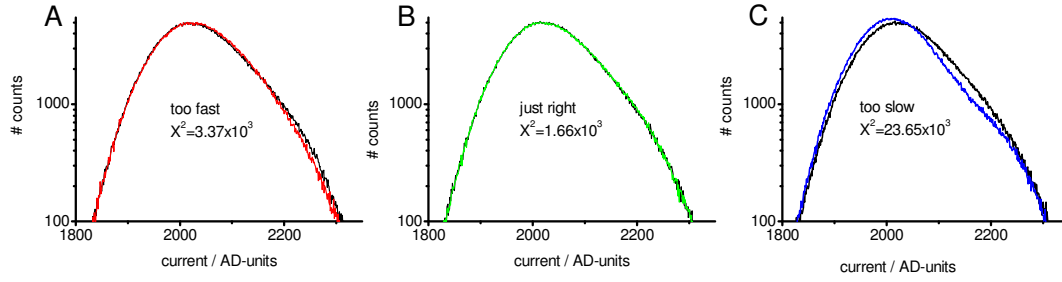
Fig. 5.16. Amplitude histograms as a means of detecting misfits in Fig. 5.15. The histograms belong to time series generated from a 5-state model (Eq. (5.2)) with the slow k_{ij} of the SP fit and k_{OG} and k_{GO} improved by the beta fit which are (A) too large (red in Fig. 5.15), (B) correct (green), and (C) too small (blue). The simulated time series is filtered by a fourth-order Bessel filter at 50 kHz.
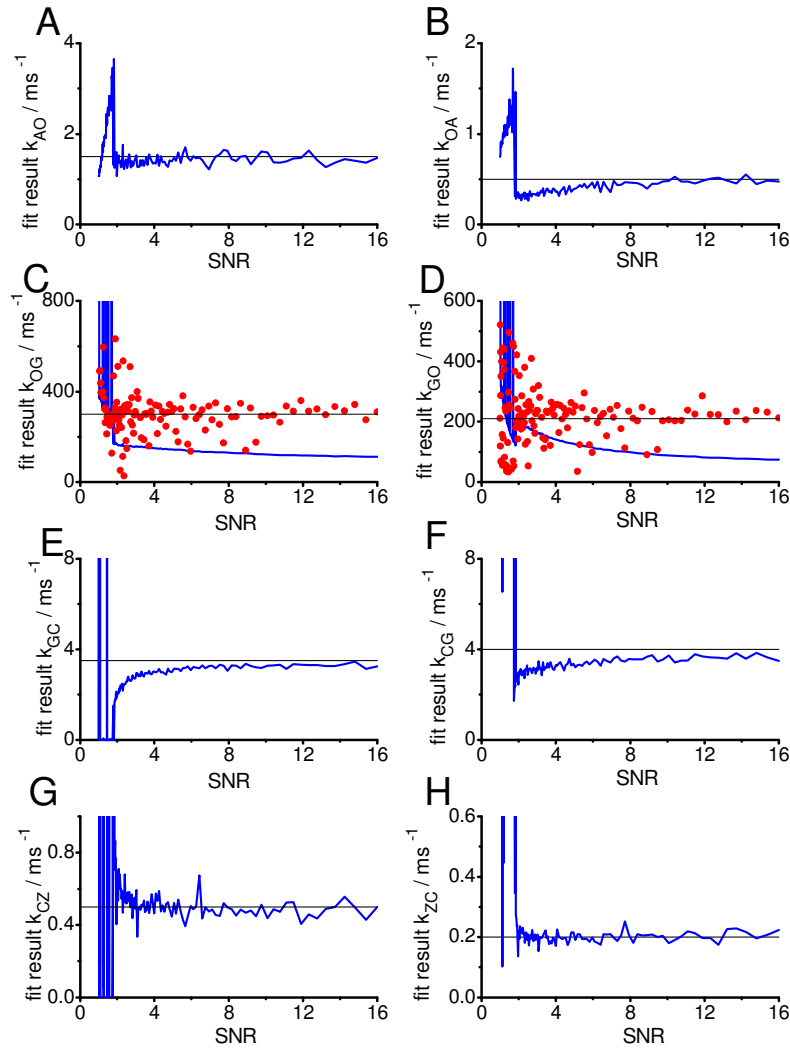
Fig. 5.17. Noise test of the subsequent SP/beta fit for the model in Eq. (5.2) with q = 30. The start simplex of the fit is obtained with $w = 2$ and $a = 0.5$ in Eqs. (5.3) and (5.4). The pure SP fit is given by the blue line in most cases close to the true values (horizontal black line). The subsequent beta fit (red dots) is restricted to the fast rate constants k_{OG} and k_{GO} (C and D).

Fig. 5.17 shows the results of a noise test. It is evident that the SQ fit does well down to SNR of about 2. The low time constants determined by the pure SP fit are determined with sufficient accuracy as already found in Fig. 5.12. The subsequent beta fit also achieves that the fast rate constants k_{OG} and k_{GO} are determined with high accuracy. However, as already shown in Fig. 5.15, the scatter of the fit is serious. The absence of any monotonous correlation with the SNR shows that this scatter is of statistical origin related to the bad fitting performance of the beta fit. As mentioned already when discussing Fig. 5.15 and Fig. 5.16, it is recommended to repeat the fit and use the comparison of amplitude histograms (Fig. 5.16) as a means of discarding misfits. The variability of repeated fits is introduced by the stochastic generation of the start simplex (Eq. (5.3)) and the stochastic simulation of the time series.

Table 5.1 gives an estimate of the computing time for simulated data. Fitting a measured time series can take much longer depending on the data quality. Especially, often fits have to be repeated several times. The random choice of the start simplex and the generation of the simulated time series of the amplitude histograms provide the chance to escape local extrema. The likelihood and the error of the amplitude histograms are used to select the best solution. For instance, a single SQ fit from *Chara* (5 states, 2 channels, $2*10^6$ data points) took about 4 h, and the solution shown in Fig. 5.18 was the best one out of ten.

Table 5.1. Computation time of some of the algorithms. Fits were performed on a Pentium 4 (2.5 GHz) under the following conditions: The length of the simulated time series was 10^6 sampling points, and the start simplex was constructed as described above. The Markov model is given by Eq. (5.2) for $q = 30$.

	SP	BF4	SQ
1 channel	10 – 20 mins	10 – 20 mins	15 – 25 mins
2 channels	60 – 90 mins	10 – 20 mins	60 – 100 mins

5.2.4.5. Application to real data
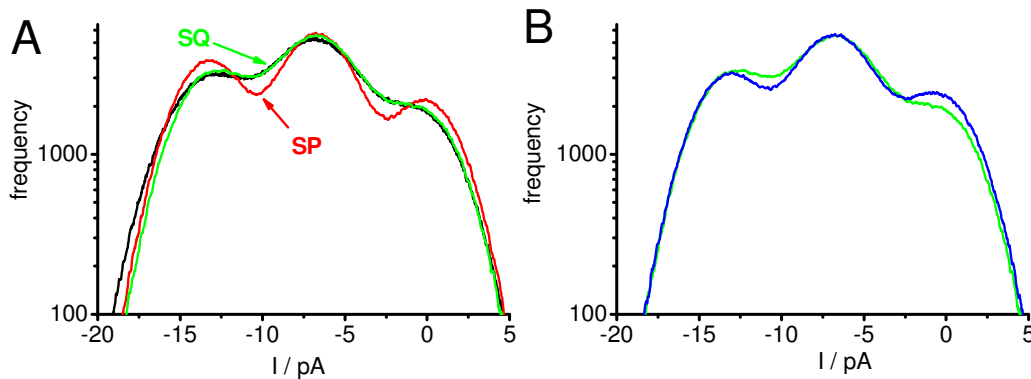
Fig. 5.18. (A) Comparison of the amplitude histograms obtained from time series generated from the results of the SP fit (red) and of the subsequent beta fit (SQ, green) of a 2-channel time series from *Chara*. The amplitude histogram of the experimental data is given by the black line. (B) Demonstration of the necessity of using three rate constants for the fit of the amplitude histogram of the model in Eq. (5.15). Green curve: Best fit result of SQ, same curve as in (A) (Eq. (5.15) with the rate constants as given at the arrows). Blue curve: Eq. (5.15) with k_{OA} and k_{OG} being doubled.

103

The SQ fit is applied to patch clamp data from *Chara*. Unfortunately, we have not been able to achieve 1- or 2-channel recordings. Thus, sections with only two channels open are cut out of the whole record and analyzed by the direct fit of the time series with simple prediction. It was already stated by Colquhoun and Hawkes (1982) that this procedure affects only the slow rate constants between shut states (in this case k_{CZ} and k_{ZC}). The SP fit resulted in the following rate constants

$$A \underset{28}{\overset{3.8}{\rightleftharpoons}} O \underset{41}{\overset{43}{\rightleftharpoons}} G \underset{2.8}{\overset{5.4}{\rightleftharpoons}} C \underset{0.2}{\overset{0.4}{\rightleftharpoons}} Z \qquad (5.14)$$
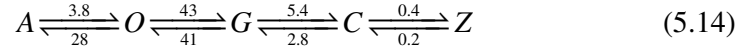
(rate constants in ms^{-1}). From these rate constants a time series is simulated ($\sim 2.3 \cdot 10^6$ data points, same length as the measured time series), and the amplitude histogram for two channels is drawn. It is obvious that the amplitude histogram of the simulated time series (SP, red curve in Fig. 5.18) significantly deviates from the measured one (black curve). Now the subsequent beta fit is performed. It used the slow rate constants as obtained by the SP fit. The fast rate constants k_{OA}, k_{OG} and k_{OG} are free. k_{OA} is not significantly modified by the subsequent beta fit but k$_{OG}$ and k$_{OG}$ are strongly increased, leading to the improved Markov model.

$$A \underset{28}{\overset{3.8}{\rightleftharpoons}} O \underset{939}{\overset{1000}{\rightleftharpoons}} G \underset{2.8}{\overset{5.4}{\rightleftharpoons}} C \underset{0.2}{\overset{0.4}{\rightleftharpoons}} Z \qquad (5.15)$$
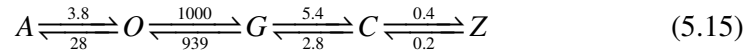
This set of rate constants results in a much better fit of the measured amplitude histogram (green curve in Fig. 5.18). The resulting rate constants are quite high (k_{OG} = 1000 ms^{-1} and k_{GO} = 939 ms^{-1}). Thus, a time series with rate constants being half as fast as those resulting from the beta fit is simulated. This doubles the deviation at the peak of the amplitude histogram, thus indicating that the transition rates between O and G are really in the range of 1µs^{-1} (data not shown). These values are similar to those given by in Fig. 5.7 in section 5.1 which have been evaluated from distributions-per-level obtained from *Chara* (Schroder et al., 2004). Rate constants in the same range were later on determined by Schroeder and Hansen (2007; 2008, chapters 6 and 7).

It may be questioned whether it makes sense to use three free parameters in the amplitude fit. Simulations have shown that the SP fit may cause the following problem: a misfit of k_{OA} can be compensated by a misfit of k_{OG} in such a way that the relative occupation probabilities are preserved. Fig. 5.18B shows the results of two simulations: the green is identical to the green in Fig. 5.18A. This is the best fit with the rate constants of Eq. (5.15). The blue curve in Fig. 5.18B is obtained also from the model in Eq. (5.15) but with k_{OA} and k_{OG} being doubled (this preserves the occupation probability of the open states). The difference in Fig. 5.18B is quite obvious and can be used by the fitting routine to distinguish the two parameter sets. Thus, all three rate constants have to be included in the amplitude fit in order to repair the failure of the SP fit. However, it has to be mentioned that for values of k_{OA} below 30 000 s^{-1} the SP fit alone has found the correct value. It has not been investigated whether it is a general rule that this limit is always close to half of the sampling frequency.

In contrast to the investigations with simulated data as used in Fig. 5.10 - Fig. 5.17, the fit of the measured amplitude histogram in Fig. 5.18 is not quite perfect. However, a better fit cannot be achieved on the basis of the employed 5-state model. The data shown are the best out of 30 fits, each taking about 3 to 5 hours because they were 2-channel fits. It has to be stated that real data is more complicated than simulated data.

In order to test the solution of the SQ fit a new time series is simulated with the rate constants of Eq. (5.15) using artificial white noise with the same σ as the measured time series. The SP fit of this time series results in

$$A \underset{28}{\overset{3.3}{\rightleftharpoons}} O \underset{138}{\overset{130}{\rightleftharpoons}} G \underset{3.6}{\overset{8.2}{\rightleftharpoons}} C \underset{0.5}{\overset{0.9}{\rightleftharpoons}} Z \qquad (5.16)$$
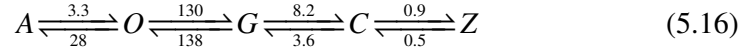
(rate constants in ms^{-1}). If the simulated time series is an accurate representation of the measured one, then both should look identical to the SP fit, i.e., the rate constants in Eq. (5.16) should be the same as those in Eq. (5.14). However, the values of k_{OG} and k_{GO} are twice as high. In a next attempt, a time series is generated from Eq. (5.15) as above, but the colored noise is taken from an obviously jump-free time series at 0 mV from the same patch. Using "real" noise changes the result of the SP fit of this time series to

$$A \underset{20}{\overset{3.8}{\rightleftharpoons}} O \underset{59}{\overset{43}{\rightleftharpoons}} G \underset{3.3}{\overset{6.6}{\rightleftharpoons}} C \underset{0.3}{\overset{0.7}{\rightleftharpoons}} Z \qquad (5.17)$$
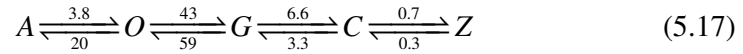
(rate constants in ms^{-1}). The rate constants of Eq. (5.17) are very close to those of Eq. (5.14). This leads to two conclusions. First, the rate constants of Eq. (5.15) are the best estimates of those of the measured time series. Second, the choice of the correct noise is important. This stresses the importance of using filtered noise in the approach of Venkataramanan et al. (1998a; 1998b; 2000).

5.2.5. Conclusion

Two basically different approaches have been tested to increase temporal resolution of the direct fit of the time series, one trying to improve the prediction algorithm of the SP fit (EP fit) with moderate increase of computing time, the other one combining the SP fit with the beta fit (subsequent SP/beta fit). The simulations above show that inclusion of the filter response into the prediction algorithms of the direct fit of the time series can yield a higher temporal resolution. However, this holds only if the signal-to-noise ratio is excellent. This is a severe restriction for the application of this method, because in broadband recordings of patch clamp current the SNR is usually worse than 4. Thus, it has to be concluded that the usage of filtered noise is a salient feature of the method of Venkataramanan et al. (1998a; 1998b; 2000). The SQ fit provides an alternative approach to account for filtering without increasing computing time too much.

In contrast to our expectations, the simultaneous fit of the time series and of beta distributions is not efficient. Obviously, it inherits only the faults of its parents, but not the benefits. This is probably caused by the fact that in the case of fast rate constants SP fit and beta fit are led by contradicting criteria of convergence to different optimum parameters sets.

Much more successful is the subsequent SP/beta fit. Even though the "theoretical" amplitude histograms have to be obtained from simulations of the time series for each iteration step in the curve fitting routine, the extra cost of computing time is still small as compared to that required for the calculation of the Likelihood of the time series (Eq. (5.9)). Fig. 5.15 , Fig. 5.17 and Fig. 5.18 show that a high temporal resolution far beyond the corner frequency of the anti-aliasing filter can be achieved even for 5-state models. Thus, this approach has the power to improve the temporal resolution of most of the patch clamp recordings occurring in a real experiment. It will be applied to data in section 8.3.

5.3. Beta fit: determination of the true current level

(The content of this section was published as Schroeder and Hansen, 2006)

5.3.1. Introduction

The transport properties of ion channels are of crucial importance for living cells. Their physiological function is determined by channel number, single-channel current and gating behavior, i.e., by spontaneous or agent-induced transitions between conducting and non-conducting states. Short-term effects of the adaptation to metabolic requirements are mostly achieved by modulation of gating (Tamargo et al., 2004). Also, many chanellopathies are due to a change in gating (Lehmann-Horn and Jurkat-Rott, 1999; Shieh et al., 2000).

Prior to the investigation of the effects on single-channel current, a distinction between permeation and gating effects has to be achieved. A modification of apparent current by a permeation effect would imply that the (average) time between the transitions of two ions is changed. In the case of a gating effect, the statistical characteristics of ion transition remain unchanged for a certain time interval, called open event, but the individual open events are separated by sojourns of the channel in a closed (non-conducting) state (Hansen et al., 1997; Townsend and Horn, 1999).

In many experiments, the distinction between gating and permeation effects is not trivial. There are several reports that gating may be very fast with mean dwell-times in the open or closed state of 1-10 µs (Heinemann and Sigworth, 1991; Parzefall et al., 1998; White and Ridout, 1998; Zheng et al., 2001; Schroder et al., 2004; Schroder et al., 2005) or even less (Weise and Gradmann, 2000). Averaging over very short closed and open intervals occurs in the inevitable anti-aliasing filter thus leading to an apparent reduction of single-channel current.

The correct knowledge of the true current level is not only important for revealing the mechanism of the action of drugs and messengers. It is also an important parameter in the investigation of the biophysical behavior of the channel. Firstly, it is a measure of the efficiency of a channel to translocate ions. This value may be a keystone for predictions of Molecular Dynamics calculations. Secondly, the correct value of single-channel current is required for the analysis of gating. Below, an example is given which shows that the assumption of a false current level also leads to false rate constants of the assumed Markov model. Apparent (i.e., measured) current levels that deviate from the true single-channel current can originate from fast gating (Hille, 1992; Hansen et al., 1997; Townsend and Horn, 1999).

There are several approaches to determine single-channel current from measured patch clamp data (section 4.1). Riessner et al. (2002) investigated the efficiency of three different approaches: 1. Fitting the amplitude histogram with gaussians, 2. Evaluation of the time series on the computer screen (fit-by-eye), 3. An automatic procedure searching for jump-free sections in the time series and sorting them according to length and frequency of occurrence. Using simulated data, Riessner et al. (2002) found that the fit-by-eye and the automatic detector gave better results than the fit of the amplitude histogram by gaussians.

However, the three approaches tested by Riessner et al. (2002) can only be employed if the sojourns in the open and closed states are long enough, i.e., longer than the averaging time of the inevitable anti-aliasing filter. If fast gating and averaging of open and closed

106

times in the anti-aliasing filter would diminish the measured single-channel current, the true value remains hidden.

Venkataramanan and Sigworth (2002) included the value of single-channel current in their fitting routines using a highly elaborated version of the direct fit of the time series (HMM fit). Huth (2005) suggested to use 2-D dwell-time histogram fits (sections 4.6 and 5.4). He showed that the shape of the reconstructed amplitude histogram was sensitive to the correct choice of the true single-channel current. (In the SQ fit (section 5.2), the beta distributions were only used to determine the rate constants while the current was assumed to be known.)

Here, a simpler approach requiring less computing time is proposed which can find the true current value even if fast gating has led to a reduced apparent current level. This is achieved by fitting the amplitude histograms by beta distributions (FitzHugh, 1983; Yellen, 1984; Klieber and Gradmann, 1993; Riessner, 1998). The approach utilizes the effect that averaging over fast gating causes deviations of the amplitude histogram from such one which is merely shaped by gaussian caused by noise. These deviations carry information about the rate constants of the involved Markov process.

The first analytical methods to calculate theoretical beta distributions were restricted to two-state models with first-order filters (FitzHugh, 1983; Klieber and Gradmann, 1993). Yellen (1984) proposed a correction factor for higher-order filters. Heinemann and Sigworth (1991) examined the higher order cumulants of open-channel noise, but this method required some rather strict assumptions about the gating (very short and infrequent gaps). Riessner (1998) developed an analytical algorithm to evaluate Hidden Markov models with more than two states and more than one channel. However, this analysis was also restricted to first-order filters which have little relevance in patch clamp analysis. Correction factors did not solve the problem in the case of multi-state models (probably also not in the case of two-state models, Riessner, 1998).

White and Ridout (1998) designed a method for fitting amplitude histograms which already comprised multi-state Markov models and higher-order filters. They calculated the theoretical beta distribution by considering all possible state sequences within the filter rise time.

Here, an alternative method is proposed. The increased computer power since 1998 rendered possible the use of simulations to generate artificial time series for the construction of the theoretical amplitude histograms originating from higher-order filters and multi-state multi-channel models (Harlfinger, 2003). This approach is very powerful because all features of noise and filtering can easily be implemented. In contrast to the above mentioned papers, the investigations here do not aim on rate constants. Instead, the beta fit is used to reconstruct the (a priori unknown) single-channel current.

5.3.2. Materials and Methods

5.3.2.1. Electrophysiological measurements

Patch clamp measurements were performed as described in section 3.4. The pipette solution contained 150 mM KNO_3, 2.5 mM $Mg(NO_3)_2$, 2.5 mM $Ca(NO_3)_2$, 10 mM HEPES/KOH, pH = 7.2. The solutions in pipette and bath were identical, if not otherwise stated.

Distributions-per-level

Distributions-per-level were generated as described previously in section 5.1 (Schroder et al., 2004): A Hinkley-detector (section 4.4, Schultze and Draber, 1993) was used to reconstruct the jump-free time series. All data points were grouped according to their assignment to the different current levels by the detector. From each level, a separate amplitude histogram was built, including filter response and missed events. Thus, missed events corrections (Milne et al., 1989; Crouzy and Sigworth, 1990; Draber and Schultze, 1994a) are not required.

5.3.2.2. Curve fitting

The theoretical amplitude distributions needed for the fitting algorithm were generated as described in section 4.8. Briefly, a filtered, noise-free single-channel time series was simulated as described in section 4.9, and the amplitude histogram was constructed by convoluting it with the base line noise. In all simulations, the corner frequency of the anti-aliasing 4-pole Bessel filter is set to 50 kHz, and the sampling rate is 200 kHz.

The simplex algorithm of the fitting program *downhill* minimizes the (weighted) quadratic error sum (see also Eq. (5.12)).

5.3.3. Development of the level fit

5.3.3.1. Illustrating the necessity of knowing the true current

The time series shown in Fig. 5.19A is used to demonstrate the necessity of knowing the true current level when the rate constants of the underlying Markov model are to be determined. In most patch clamp records with fast gating, only the apparent current level is observed. Fortunately, on some rare occasions during fast gating with reduced apparent current, MaxiK stays in the open state long enough for the true level to be reached. The time series in Fig. 5.19A belongs to this kind of record. Especially, it is a suitable example because these sojourns in the true level were so seldom, that they may have been overlooked, thus mimicking the situation as found in most experiments.

Here, we consider two scenarios:
1. The experimenter is aware of the short sojourns in the long open state and therefore able to use the true current level for the kinetic analysis.
2. Only the apparent current level is observed and falsely assumed to be the true one.

For the kinetic analysis in both scenarios, the linear 5-state Markov model

$$O1 \rightleftharpoons O2 \rightleftharpoons C3 \rightleftharpoons C4 \rightleftharpoons C5 \qquad (5.18)$$
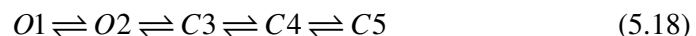
was used which is a good approximation for the MaxiK analogon in *Chara* (Farokhi et al., 2000; Hansen et al., 2003). For MaxiK, however, this model is only a very rough first approximation as discussed in chapter 8.
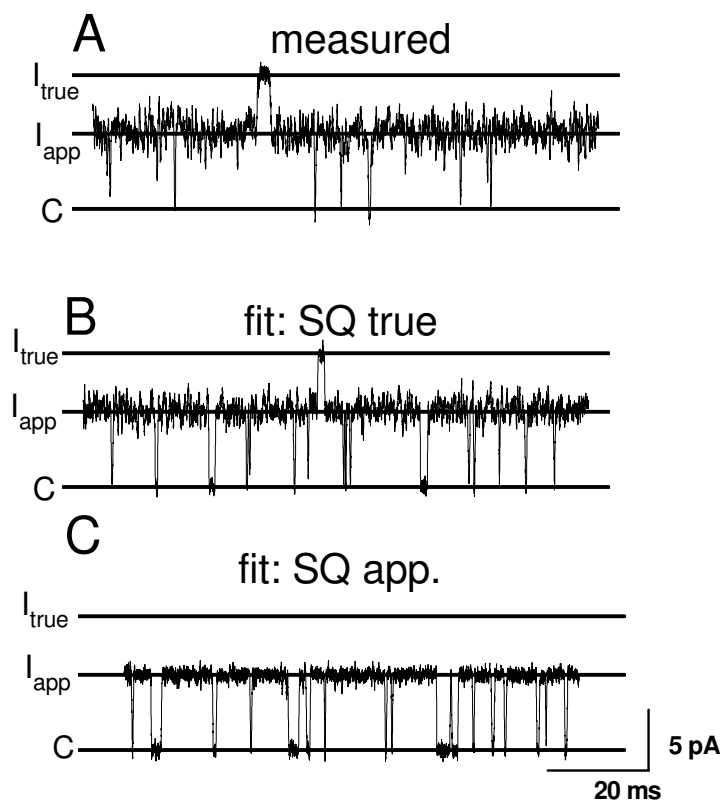
Fig. 5.19. (A) Measured time series from MaxiK at +200 mV in 150 mM KNO$_3$, 2.5 mM Mg(NO$_3$)$_2$, 2.5 mM Ca(NO$_3$)$_2$, 10 mM HEPES/KOH, pH = 7.2, sampled at 200 kHz presented with a 20-point moving average filter. Gating is very fast, resulting in the apparent open level I_{app}. At ~ 40 ms, the true open level I_{true} becomes visible. (B,C) Time series simulated from the rate constants of the best SQ fit (B) with the true current level I_{true}, (first row in Table 5.2, average of the best 10 out of 20 fits), (C) with the apparent current level I_{app} (17 out of 25. Rate constants not shown but similar to those in row 3 of Table 5.2).

The measured time series was fitted by means of the SQ fit (section 5.2) with the current level taken from the rare sojourns in the slow open state (scenario 1: I_{true} in Fig. 5.19A) or from the apparent current level (scenario 2: I_{app}). The rate constants obtained from this analysis were used to construct the related simulated time series in Fig. 5.19B and C. The comparison of Fig. 5.19A and B shows that the measured time series and that one simulated under scenario 1 look very similar, as expected. Especially, the rare sojourns in the true current level are well reproduced. This verifies that both levels in Fig. 5.19A originate in fact from the same original current level. In contrast, scenario 2, using the apparent (wrong) current level inevitably yields rate constants which produce a quite different time series (Fig. 5.19C).

Even though visual inspection of time series may give a first hint that an analysis has failed (Fig. 5.19C), a more quantitative illustration of the effect of an incorrect current estimation is presented in Table 5.2 and Fig. 5.20. Simulated data are used to show that fits under scenario 2 yield incorrect rate constants of the Markov model.

The simulated time series was generated from the rate constants obtained from the SQ fit of the measured time series (first row in Table 5.2). It is, of course, identical to the time series in Fig. 5.19B. This time series (which now replaces the measured one in Fig. 5.19A) was fitted by

1. the SQ fit assuming the true correct level (scenario 1)
2. the SQ fit with the apparent current level (scenario 2).

The results are shown in Table 5.2, second and third row.

Table 5.2 Rate constants in s^{-1} obtained from the simulated time series of Fig. 5.19B with the two different fitting strategies (best error sum out of ten fits, respectively) described in the text.

Fit strategy	k_{O1O2}	k_{O2O1}	k_{O2C3}	k_{C3O2}	k_{C3C4}	k_{C4C3}	k_{C4C5}	k_{C5C4}
Simulated	**4237**	**24**	**575472**	**787231**	**1053**	**4987**	**73**	**396**
SQ true (scenario 1)	2169	12	760439	1103290	1243	4349	55	325
SQ app. (scenario 2)	1834	1151	2982	126734	44200	5448	78	368

The SQ fit assuming the correct current level should reproduce the rate constants used for simulation. However, there are some deviations due to the superimposed noise and insufficient lengths of time series. The rate constants of the O-C transition are a bit overestimated, but it has to be kept in mind, that they are more than ten-fold faster than the anti-aliasing filter (50 kHz). The rate constants between the two open states are wrong by a factor of two. This is due to the extreme low occupation probability of O1 (below 0.3 %), providing not enough events to reach the statistic equilibrium. In contrast, the results obtained by fitting with the apparent current level (scenario 2) are completely wrong, in some cases by several orders of magnitude.

In the case of measured time series, the experimenter does not know the true rate constants, thus the detection of wrong rate constants cannot serve as an indicator of wrong current levels. Fig. 5.19C shows that the comparison of the measured time series and that one simulated from the fit results may give a first hint that something is wrong. However, a more powerful analysis should be based on beta distributions, which serve a double purpose: helping to find the true current level and detecting a failure of the analysis. The utilization of beta distributions to determine the true current before the analysis by the SQ fit or other methods of determining the rate constants is described in the next sections.

The second feature is illustrated in Fig. 5.20 which shows the full amplitude histograms of the time series simulated from the rate constants in Table 5.2. Because of the bad SNR, only one peak is visible. The SNR was 4 when calculated for the apparent current level and 12.4 for the true level. Fig. 5.20 shows that the amplitude histogram constructed from the rate constants obtained from fitting with the true level (row 2 in Table 5.2) coincides very well with that one of the measured original time series (row 1 in Table 5.2), whereas a clear deviation becomes obvious in the case of the amplitude histogram obtained from the fit results using the apparent current level (row 3 in Table 5.2).
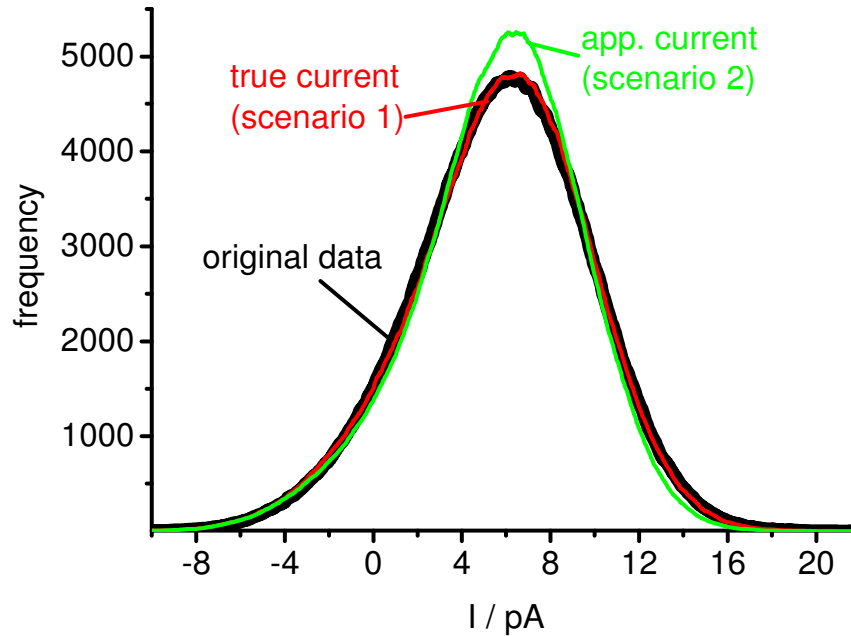
Fig. 5.20. Amplitude histograms generated from time series simulated from the three sets of rate constants presented in Table 5.2. Black curve: Rate constants used for the "original" time series (First row in Table 5.2 The thickness of the curve is not caused by noise, but chosen for better demonstration of the coincidence of the curves). Red curve: Rate constants obtained from the SQ fit of the "original" (simulated) data with the correct single-channel current. Green curve: Rate constants obtained from the SQ fit using the apparent single-channel current. In both scenarios, the fit with the best error sum (Eq. (5.12)) out of ten runs is shown.

5.3.3.2. Relationship between beta distributions and current reduction

The reduction of single-channel current by fast gating is illustrated in Fig. 5.21. Simulated time series were used to demonstrate that the same apparent single-channel current can be produced by quite different true single-channel currents. The degree of current reduction depends on the parameters of the gating process. For the illustration of this effect, time series were generated using the following Markov model:

$$O \underset{x \cdot 5 \cdot 10^5 \, s^{-1}}{\overset{5 \cdot 10^5 \, s^{-1}}{\rightleftharpoons}} C \qquad (5.19)$$

All these simulations resulted in the same apparent open-channel current, even though quite different true current levels were used for simulating the time series. (The values of I_{true} were chosen to create equal value of I_{app}.) The choice of the kinetic parameters in Eq. (5.19) was the origin of the current reduction. This is indicated by the very different curve shapes of the amplitude distributions. In other words, measuring an apparent single-channel current does not always yield the true single-channel current. Below, details of the technique of reconstructing the true current level from the amplitude histogram of a measured time series are presented. Simulated and measured data are used to test the performance of the algorithms.
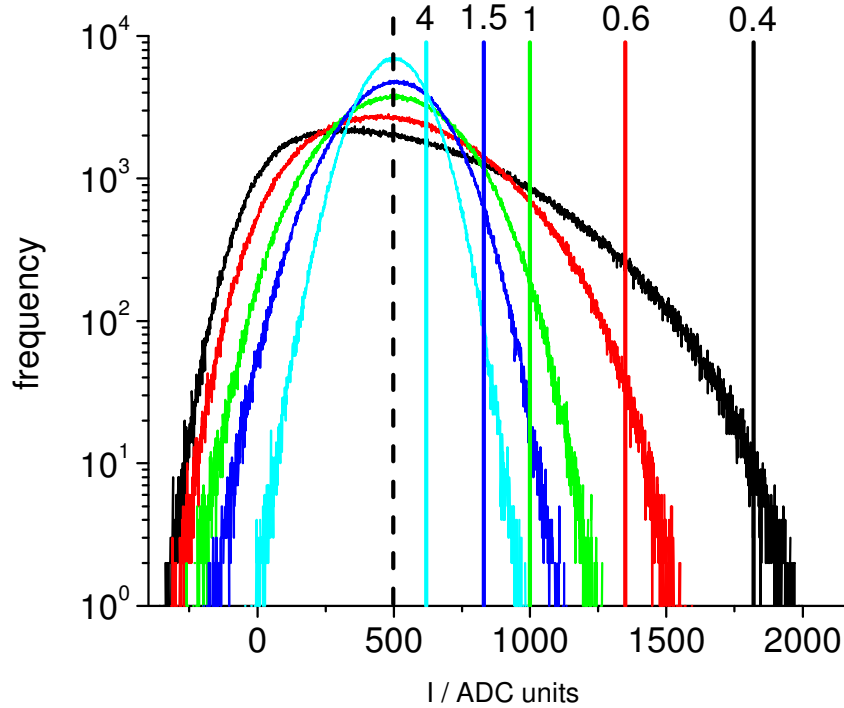
Fig. 5.21. Different curve shapes lead to different true single-channel currents. Time series were simulated which resulted in the same apparent single-channel current (dashed black line), but which had different rate constants of fast gating (labels give x in Eq. (5.19)) and different true currents (solid vertical lines). Sampling frequency: 200 kHz, filter frequency: 50 kHz.

5.3.3.3. Successful reconstruction of the current level using distributions-per-level

As implicated by Fig. 5.21, the true current level can be obtained by fitting the amplitude histogram with beta distributions. The following example shows that the efficiency of the approach can strongly be increased by using distributions-per-level (see 5.3.2 or 5.1) instead of the overall amplitude histograms.

Distributions-per-level have been used by different authors for different purposes. They occur in the prediction equation of the direct fit of the time series (HMM fit, Fredkin and Rice, 1992; Albertsen and Hansen, 1994). Other examples are visualization and comparison of baseline and open-channel noise, e.g., Weise and Gradmann (2000) and Rosenmund et al. (1998). Their usefulness for model identification has been discussed by Schroeder et al. (2004) and in section 5.1.

Fig. 5.22A shows a simulated record, including fast gating. The two levels that can be seen are the closed level and the apparent open level. The true open level (indicated by the horizontal line "I_{true}") is hidden. The apparent open state includes sojourns in the fast open and in the fast closed state. Thus, the apparent level and the excess noise result from averaging over these states. The visible sojourns in the closed state are caused by long events related to a second slower closed state. By means of distributions-per-level, the fast O-C transition can be separated from the sojourns in the slow closed state. This enables the usage of a simpler model for the fit of the beta distributions.
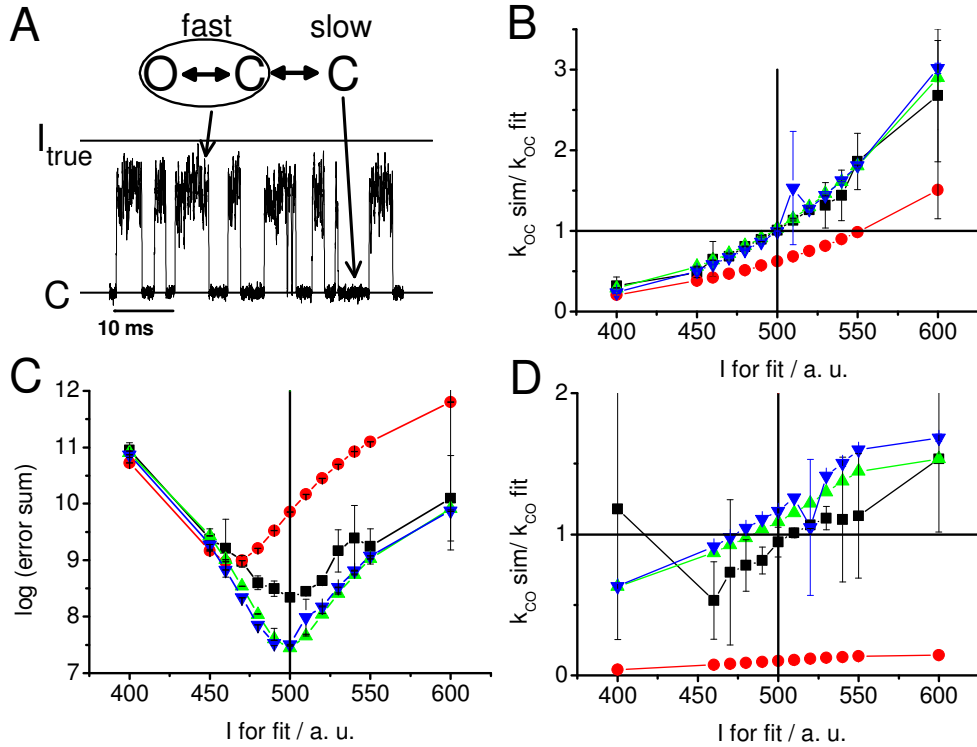
Fig. 5.22. Finding the correct current level. A time series was simulated with true current level (500 a.u.) from the OCC-model in Eq. (5.20), and the influence of the assumed current on the error sum of the beta fits are investigated. Each data point presents the average of three runs. Four different fit strategies were employed to adjust the rate constants, but not the fixed current given at the abscissa: The over-all amplitude histogram was fitted with the correct OCC-model (■) or a reduced OC-model (●). Both triangles were obtained from fitting the noisy apparent O-level (distributions-per-level in (A)) with the reduced OC-model. The two curves differ by the current setting of the Hinkley detector. One uses the apparent current level (400 units, ▲) and the other one the true level (500 units, ▼). The parameters used for the simulation are represented by horizontal (rate constants) and vertical (current) lines. (A) The apparent flickery open level is formed by the fast O-C-transition. (C) Error sums. (B) and (D): rate constants.

The benefit of this approach is illustrated by means of the time series in Fig. 5.22A. It was generated from the following model (rate constants in s^{-1}):

$$O \underset{2\cdot 10^5}{\overset{1\cdot 10^5}{\rightleftharpoons}} C \underset{200}{\overset{1000}{\rightleftharpoons}} C \qquad (5.20)$$

The true current value in the simulation was 500 a.u., the resulting apparent current was 400 a.u.

The final goal is the reconstruction of the true current. The fitting routine employs two sets of variables, one set for the rate constants and one for the current. In order to show the strong dependence of the error sum on the assumed current value, we use a parametric approach for Fig. 5.22 instead of fitting all parameters simultaneously. In the following series of fits, the current is kept constant at different values, and we use the fit only for the determination of the rate constants.

Four different fitting strategies were tested. For each strategy, fits were done at different current levels.

1. The fit tries to approximate the over-all amplitude histogram on the basis of the correct OCC-model (black squares in Fig. 5.22B, C and D). This works fine, both rate constants and the current are determined correctly. However, the problem arises that the beta fit often becomes unstable with more than two states (as implicated by the error bars e.g., in Fig. 5.22D).
2. The fit tries to approximate the over-all amplitude histogram on the basis of a reduced OC-Model. The error sum becomes minimal at a wrong current value and the rate constants are misestimated (red circles in Fig. 5.22B, C and D).
3. The fit assumes the reduced OC-Model. In contrast to the above two approaches, not the whole amplitude histogram, but only the apparent O-distribution is fitted. The Hinkley detector was set to the apparent current level (400 units, green upright triangles)
4. Same as strategy 3, but the Hinkley detector was set to the true level (500 units, blue inverted triangles). Strategies 3 and 4 both estimate the current and the rate constants with good accuracy.

The fit of the over-all amplitude histogram is sensitive to the choice of the correct model, as becomes obvious from curve 2 (red circles in Fig. 5.22B, C, D). This problem can be overcome by using distributions-per-level. The results show that fitting distributions-per-levels is tolerant to the usage of reduced models. This is of great advantage because complex models lead to instabilities when fitting beta distributions. From the comparison of the results of strategies 3 and 4, we can also conclude that this approach is quite robust with respect to the settings of the Hinkley detector, which is important for the application to measured data, when fast flickering impairs the assignment of current levels.

5.3.4. Testing the level fit

5.3.4.1. Testing single-channel scenarios

Above, it has been shown that the error sum of the beta fit yields a sharp minimum when the correct true current level is assumed. The full version of the fitting program (*beta_leveldetektor* at www.zbm.uni-kiel.de/software) optimizes both parameter sets: rate constants and current level, in contrast to the investigations in Fig. 5.22. The performance of this fit algorithm is tested on three simulated time series which showed apparent current reduction. The test comprises the following steps:
1. Simulation of the time series
2. Generation of the apparent open-distribution from the time series (distribution-per-level)
3. Fitting beta distributions to the open-distribution, with the current and the rate constants as free parameters

The models used for simulation are (rate constants in s^{-1}):

$$O \underset{200,000}{\overset{100,000}{\rightleftharpoons}} C \underset{200}{\overset{1,000}{\rightleftharpoons}} C \qquad (5.21)$$

$$O \underset{10,000}{\overset{50,000}{\rightleftharpoons}} O \underset{300,000}{\overset{100,000}{\rightleftharpoons}} C \underset{1,000}{\overset{500}{\rightleftharpoons}} C \qquad (5.22)$$

(with superscripts above states: (0.25/10μs) O, (0.125/5μs) C, (0.625/5000μs) C for (5.21); and (0.12/20μs) O, (0.59/9μs) O, (0.20/3.3μs) C, (0.10/1000μs) C for (5.22))

$$O \underset{500,000}{\overset{1,000,000}{\rightleftharpoons}} \overset{(0.24/1.8\mu s)}{C} \underset{10,000}{\overset{5,000}{\rightleftharpoons}} \overset{(0.12/93\mu s)}{C} \underset{200}{\overset{700}{\rightleftharpoons}} \overset{(0.41/5000\mu s)}{C}$$

with the leftmost state labelled $\overset{(0.12/1\mu s)}{O}$ and a vertical branch $100,000 \uparrow\downarrow 50,000$ to $O_{(0.12/10\mu s)}$

$$(5.23)$$
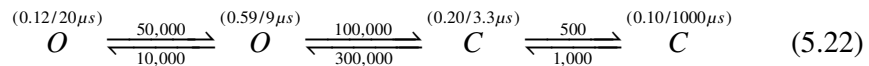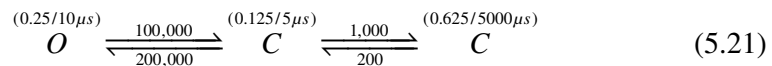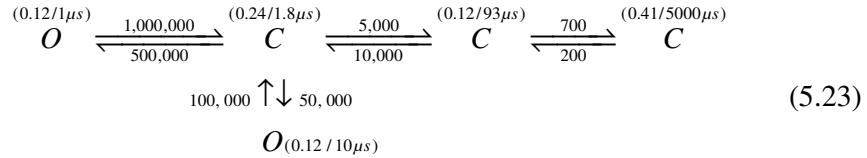
The steady-state occupation probabilities of the states and their individual lifetimes are given in brackets above the state symbols in Eqs. (5.21) to (5.23). The first model (Eq. (5.21)) corresponds to that one used in Fig. 5.22A (Eq. (5.20)). Here, it is tested whether the minimum in Fig. 5.22C can automatically be found by the full version of the program.

All simulations used a true current of 500 AD converter units. The resulting apparent currents are given in Table 5.3. Also given in the table are the true and the fitted values of the current, the C-O and O-C rate constants.

The omission of the slow C-state in the model of Eq. (5.21) (first row in Table 5.3) does not impair the accuracy of the fit. The current level and the rate constants come close to the values used for the simulations.

Good results are also obtained for the case of the linear model of Eq. (5.22). Replacing the two open states by one results in the correct current level, and also the rate constants are acceptable. Using both open states (OOC, row 3 in Table 5.3) only minimally improves the quality of the fit, showing that fitting by a reduced model is legitimate.

Table 5.3. Influence of the usage of a reduced model (second column) for fitting distributions-per-level from different simulated time series. The parameters obtained from the fits with the smallest error sums are given with SEM (on the average, 18 out of 30 fits were successful for each model).

Simulated model	Fitted model	Apparent current	True current	Fitted current	k_{OC} sim / ms^{-1}	k_{CO} sim / ms^{-1}	k_{OC} fit / ms^{-1}	k_{CO} fit / ms^{-1}
OCC (Eq. (5.21))	OC	400	500	501 ± 2	100	200	103±3	230±4
OOCC (Eq. (5.22))	OC	440	500	504 ± 1	100	300	86±1	310±2
OOCC (Eq. (5.22))	OOC	440	500	500 ± 1	100	300	102±5	322±4
OOCCC (Eq. (5.23))	OC	350	500	553 ± 5	1000; 100	500; 50	271±11	408±8
OOCCC (Eq. (5.23))	OCO	350	500	536 ± 15	1000; 100	500; 50	301±27; 149±53	355±49; 66±49

The situation is different for the branched model (Eq. (5.23), OOCCC, rows 4 and 5 in Table 5.3). It serves as an example where the estimation of the true current is reasonably correct, but the rate constants have to be refitted by another fitting program.

Fitting an O-C-model to the open-distribution results in a true single-channel current that is about 10% higher than the nominal value (row 4 in Table 5.3). Including the second open state into the fit again does not improve the accuracy (last row in Table 5.3). The bias of 10% may be tolerable. The rate constants k_{OC} and k_{CO} obtained from fitting with the reduced model (column 3 in Table 5.3) are different from those used for the simulations of the time series. Using the more correct OCO-model yields a slightly better current estimation. Also the slower O-C-transition can be identified (simulated: 100 and 50 kHz, fitted: 149 and 66 kHz, respectively), but the rate constants of the fast

O-C-transition have little relation to the simulated model (simulated: 1000 and 500 kHz and fitted: 301 and 355 kHz, respectively).

The resulting message is that the true current level is correctly reconstructed by the fit, even though the estimation of the rate constants may be poor. In a real experiment, the experimenter cannot check the influence of the usage of the reduced model on the fitted rate constants. Thus, it is recommended to use the true single-channel current obtained from the analysis described above for a new SQ fit (section 5.2) in order to determine the rate constants.

5.3.4.2. Time series with two channels

In order to demonstrate the performance of true-level reconstruction for more than one channel, a time series was simulated from the OCC-model of Eq. (5.21) with two identical channels. Fast gating causes current reduction in both open levels. For the reconstruction of the true current level, distributions-per-level were constructed as shown in Fig. 5.23A. The distributions of the C and the O level show bulges at the right-hand slope which result from missed transitions to the higher current level (section 5.1). The distribution-per-level for two channels open (2O, green in Fig. 5.23A) shows a clear asymmetric beta distribution which seems to be most suitable for the reconstruction of the true current.
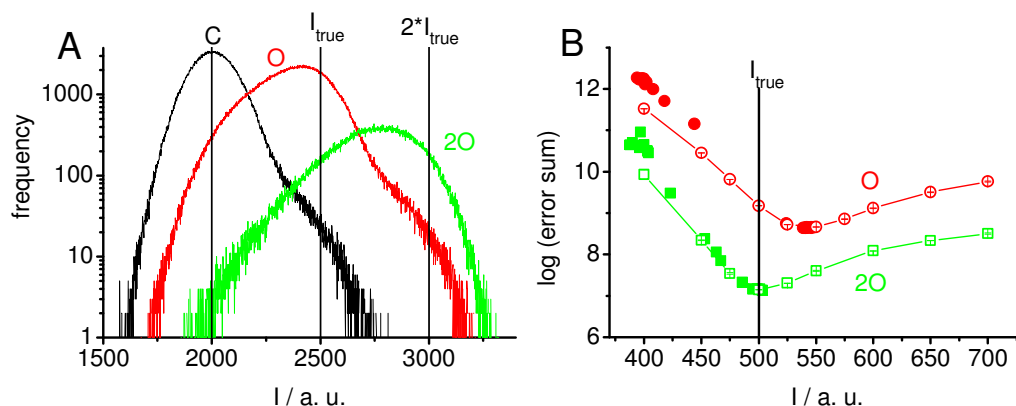
Fig. 5.23. Test of the level fit for time series simulated with two channels of the OCC-model of Eq.(5.21). The time series showed current reduction by fast gating in both open levels. (A) Distributions-per-level related to the three apparent levels. The true current levels of the closed state (C, black), of one (O, red) and two open channels (2O, green) are given by vertical lines. (B) Dependence of the error sum on the estimated current. Red symbols: The O-distribution was fitted with one OC-channel. Green symbols: The 2O-distribution was fitted with two OC-channels. Closed symbols: fits with the current as a free parameter. Open symbols: fit with the current as fixed parameter. The true current I_{true} is indicated by the vertical line.

Fitting of distributions-per-level with beta distributions has an inherent problem: It has a tendency to end up in local minima. Variability of the fitting results, which is useful to overcome this problem, can be introduced by the choice of the starting values for the rate constants k_{CO} and k_{CO} and for the current I. Further variability is introduced by the randomness of the generation of the time series which serves to create the "theoretical" beta distribution (Eqs. (4.50)).

Fortunately, as shown in Fig. 5.22C, the error sum is a helpful guide to find the global minimum. Plotting the error sum of the fits versus the estimated current shows that the error sum obtains a clear minimum at the true single-channel current (which is

known in simulated data and is indicated by a vertical line in Fig. 5.23B). The suitability of the error sum as a guide line in the totally free fit (rate constants and current are free parameters, presented by filled symbols in Fig. 5.23B,) was tested by the comparison with fits with fixed current (open symbols in Fig. 5.23B). The results of both approaches (not surprisingly) coincided.

The fit of the 2O-level gave a clear minimum at the true current level (green squares in Fig. 5.23B, 8 out of 30 fits reached the optimum), whereas the fit of the O-level results in a minimum a at current value which was 10 % too high (red circles in Fig. 5.23B, 12 out of 30 runs reached the minimum). The reason for the different performance of these two fits gets obvious from Fig. 5.23A. The distribution-per-level for the 2O-level looks like a smooth beta distribution, whereas the curve shape of the distribution of the 1O-level is distorted by events missed by the Hinkley detector. Values which probably should have been assigned to the higher level occur in the distributions of the C- and 1O-levels. This increases the deviation from the gaussian shape, especially at the right-hand slope and pretends a higher true current.

The results of Fig. 5.23 lead to the following conclusions. 1. Multi-channel fits are possible, but only the highest level seems to be not distorted by undetected transitions to a higher level, and therefore is most suitable for current reconstruction. 2. The results should be verified by repeating the fits with different starting conditions until a clear minimum is obtained in a graph similar to that in Fig. 5.23B.

5.3.4.3. Testing the algorithm on measured data

Testing the algorithms with real measured data is difficult because, in contrast to simulated data, the true single-channel current is usually unknown. Fortunately, we could observe some time series in which both levels occurred, the true one and the apparent one. One of these time series is shown in Fig. 5.19A. Another type of such time series showed mode switching as also shown in Fig. 5.6. In the time series displayed in Fig. 5.24A, there were sections in which the ratio of open to closed time within a burst was so high, that the true current level appeared at the output of the anti-aliasing filter. However, the channel could spontaneously (and reversibly) switch to another mode where the open probability within the burst decreased (indicated by the 4.5-fold increase of k_{OC} in Table 5.4), so that current was reduced (the section is indicated by the red dashed box in Fig. 5.24A).

The time series in Fig. 5.24A was used to test whether the true level could be reconstructed from those sections which delivered only the apparent current. As described in the previous section, the distribution of the apparent open state was generated from the section in the dashed box, showing only the reduced current level (Fig. 5.24C). As discussed above, it is sufficient to use a simple OC-model for the fit of the open-histogram (distribution-per-level). Fitting by beta distributions with the current as a free parameter is not straight forward. The fitting routine may end up in local minima. Thus, 20 different fits were done. They differed by the set-file giving the starting value and by the simulated time series because of the randomness of the simulation procedure. Consequently, different estimated current levels were delivered by individual fits. Fortunately, this problem could be overcome by the inspection of the error sum. It helped to find the correct solutions. In Fig. 5.24E, the error sum is plotted versus the current delivered from the fitting routine. The curve of the error sums takes a minimum very close to the true current of 7.54 pA, which here is fortunately known from the sections of the time series in the "normal" gating mode (Fig. 5.24A, left- and right-hand sections).
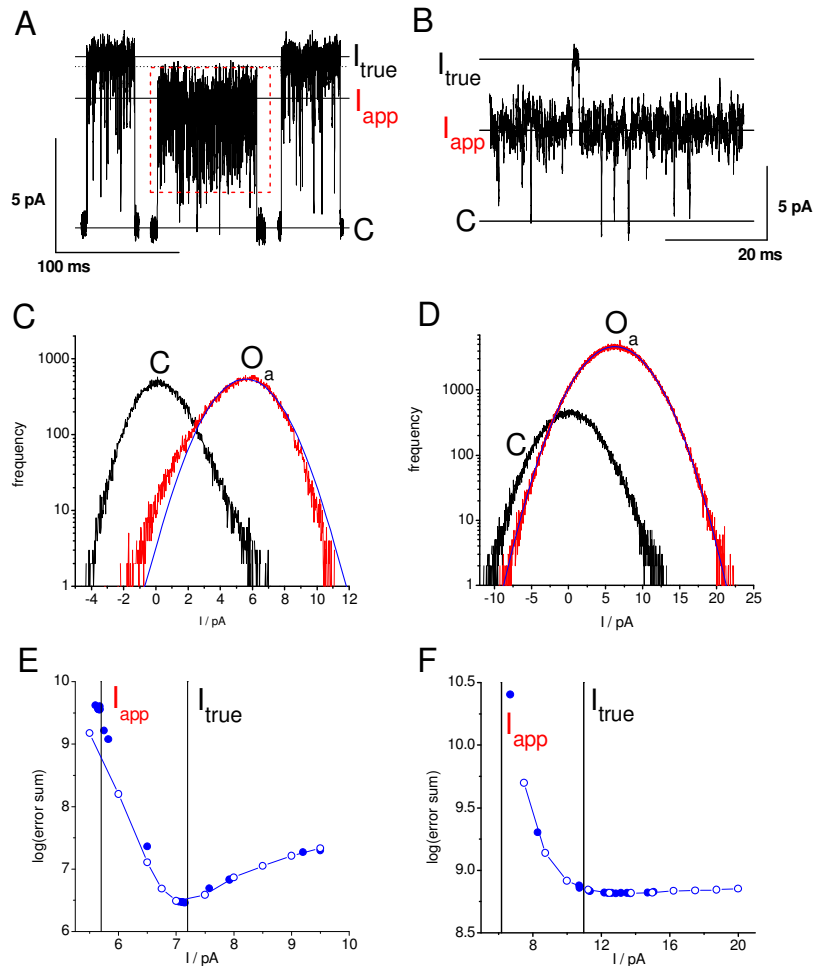
Fig. 5.24. Time series from MaxiK which displayed both the true and the apparent single-channel current which was reduced by fast gating. (A) Time series measured at + 60 mV with spontaneous mode switching. There were sections with gating that was so slow that no current reduction occurred (left- and right-hand section) and section where fast gating reduced the single-channel current (dashed box in the middle). The bath solution contained 100 mM Tl$^+$ and 50 mM K$^+$ instead of 150 mM K$^+$ (see section 5.3.2). (B) Time series obtained at +200 mV with current reduction by fast gating (I_{app} = apparent current level) and some rare long sojourns in the true open level (I_{true}). (C) and (D) distributions-per-level for the apparent open (O$_a$, red) and the closed state (C, black) from the time series in (A) and (B), respectively. The smooth blue curves give the best approximation by a gaussian distribution. (E) and (F) Dependence of the log error sum (Eq.(5.12)) on the estimated current obtained from different fits of the O$_a$-distributions in (C) and (D), respectively. •: fits with current as a free parameter, ○: fits with fixed current. True (I_{true}) and apparent (I_{app}) current level are indicated by vertical lines.

In order to test the fitting routine, the beta distribution in Fig. 5.24C (red curve, O$_a$) was fitted again under the constraint that the single-channel current was set to a fixed value, and only the rate constants were determined. The resulting errors sums coincided with the curve of the completely free fit in Fig. 5.24E, indicating a close relationship between error sum and the quality of estimation of the true single-channel current.

Table 5.4. Fit results of the two gating modes of the time series in Fig. 5.24A. The mode-switching is caused by a change in a single rate constant (As far as can be seen by the reduced model). The average is shown for the best 5 fits out of 20 (fast part) and 14 out of 30 (slow part), respectively.

	Apparent current	Fitted current	k_{OC} / ms^{-1}	k_{CO} / ms^{-1}
Fast part	5.73 pA	7.14 pA	164 $\pm$ 6	510 $\pm$ 8
Slow part	7.54 pA	-/-	36 $\pm$ 9	504 $\pm$ 67

5.3.4.4. A caveat related to gaussian distributions

In the time series in Fig. 5.19A (measured at +200 mV), there was no mode switching. Instead it showed the peculiarity that it contained some sufficiently long open events among the otherwise unresolved fast flickering. They allowed the determination of the full single-channel current. The value of 11.1 pA (label "I_{true}" in Fig. 5.24B) was determined manually by visual positioning of the current level in the raw data, as described in section 4.1.2. The average apparent single-channel current in this record was 6.2 pA (label "I_{app}" in Fig. 5.24B). Distributions-per-level were constructed for the apparent single-channel current (Fig. 5.24D). This distribution still contained some data points from the long open state. However, their number was so small that they did not influence the curve shape.

The distribution-per-level for the apparent O-level is broader than that of the long lasting C-levels (Fig. 5.24D). Because of this, it could be expected that this distribution is an effective means of determining the true current level as in the case of the time series in Fig. 5.24A. However, in Fig. 5.24D, the O_a histogram (red) can be fitted perfectly well with a gaussian amplitude histogram. This leads to a caveat which has to be kept in mind when the distribution-per-level becomes gaussian.

Fig. 5.24F shows the error sums obtained from 15 free fits and from fits with fixed current level. It does not show a clear minimum. On the left-hand side (at low current values) the error decreases with the estimated current level approaching the true level of 11 pA (which is known from the few sojourns in the true level I_{true} in Fig. 5.24B). However, for values higher than the true level, the error sum does not increase again as it does in the case of Fig. 5.24E. This bears the following message: In the case of symmetrical gaussian distributions, the fitting routine can only reveal a lower bound for the true current level but cannot exclude values which are too high.

This problem is inherent to the gaussian shape of the distribution in Fig. 5.24F. If gating is much faster than the filter frequency then the distribution always approaches a Gaussian distribution (Central Limit Theorem, Feller, 1968). In that case, a higher value of the true apparent current can be reduced to the same apparent current by selecting the adequate duty cycle (ratio of open times to closed times). The width of the distribution can be adjusted by the selection of the adequate rate constants. Because of this, the gaussian distribution does not provide enough information to exclude currents which are too high. The situation is more favourable in the case of asymmetrical beta distributions (Fig. 5.24).

5.3.4.5. Application: The negative slope of MaxiK is a gating effect
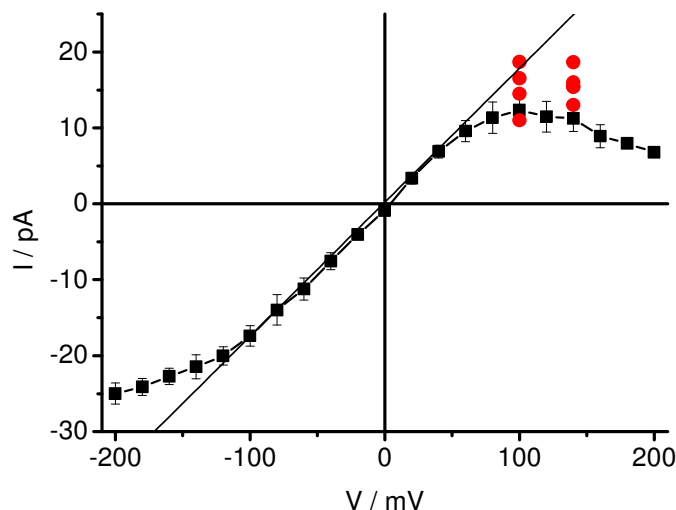
Fig. 5.25. Reconstruction of true single-channel currents in the range of the negative slope of the MaxiK IV-curve in symmetric 150 mM K$^+$. Measured (I_{app}, ■) and reconstructed (I_{true}, ●) single-channel currents from some individual patches (note the large scatter).

The motivation for the development of the current reconstruction with the beta fit was the negative slope in the IV curve of MaxiK. It is accompanied by an increase in open channel current, indicating unresolved fast gating. Fig. 5.25 shows the first preliminary results regarding the negative slope. Some of the reconstructed data points reached the extrapolated linear IV curve. Some, however, showed increased current, but it did not reach the linear IV curve. At the time when the levelfit was published (2006), we did not yet understand these results. But experiments with different potassium concentrations in chapter 6 led to a model of fast gating linking ion depletion and selectivity filter stability.

5.3.5. Discussion

5.3.5.1. Using beta distributions for current reconstruction

Fast gating and the related averaging over closed and open intervals in the inevitable low-pass filter of the experimental set-up can cause severe differences between measured apparent single-channel current and true single-channel current as illustrated in Fig. 5.21. Fortunately, this reduction in current is coupled to a distortion of the curve shape of the related amplitude histograms. In Fig. 5.22, it is shown by means of simulated data that the error sum (Eq. (5.12)) resulting from the comparison of the amplitude histograms of measured and reconstructed time series strongly depends on the assumption of the correct true single-channel current. This is a solid basis for the reconstruction of the hidden true single-channel current.

One finding presented in Fig. 5.22 and Table 5.3 is very important, namely that the distributions-per-level can be fitted with a smaller model than used for the analysis of the kinetics, i.e., for the determination of the rate constants of the assumed Markov model. Using a smaller model increases the stability of the fit. From the shape of beta

distributions, only a very small number of parameters can be determined. In the successful approaches above (Fig. 5.22 and Table 5.3) this is restricted to 3 or 5, i.e., one or two pairs of rate constants and one current value.

Reconstruction of the true single-channel current adds a new competency to the repertoire of beta distributions. So far, they were employed for the determination of the rate constants of very fast gating processes (FitzHugh, 1983; Yellen, 1984; Heinemann and Sigworth, 1991; Klieber and Gradmann, 1993; Tsushima et al., 1996; White and Ridout, 1998; Weise and Gradmann, 2000; Schroder et al., 2004; Schroder et al., 2005). They enable to look far beyond the corner frequency of the anti-aliasing filter i.e., dwell-times in the range of 1 μs where obtained from time series filtered by 50 kHz.

5.3.5.2. Distributions-per-level

Better results were obtained by using distributions-per-level instead of the overall-amplitude histograms (Fig. 5.22). This is not a surprise as the exclusion of sections with long sojourns in a full state decreases the number of relevant states in the Markov model and thus allows fitting with a smaller one. The frequent failure of larger models is described by White and Ridout (1998) with the words "In a three-state model, the precision of estimates depended in a complex way on all rate parameters in the model". Here, a welcome side effect of the normally undesired limited time resolution of the jump detector (section 4.4) is utilized. When gating becomes fast, the detector is no longer able to realize the short sojourns in the closed state occurring during a burst. Thus, the fast events originating from a small part of the complex Markov model (mainly an OC-model) are merged into one apparent open level. The related section of the time series can be modeled with an OC-model with a very short-lived closed state (see Fig. 5.22).

It should be mentioned that fitting distributions-per-level with a reduced number of states may lead to severe errors in the determination of the rate constants (Table 5.3, last two rows). In distributions-per-level, not only the sojourns in the slow (closed) states are omitted, but also those of the faster states which occur in the tail of the dwell-time distribution. Because of this, the kinetic analysis delivering the rate constants should be repeated utilizing the knowledge of the reconstructed true current obtained from the beta fit. For this purpose, the HHM fit as suggested by the Sigworth group (Venkataramanan and Sigworth, 2002), the SQ fit (section 5.2, Schroder et al., 2005) or the 2-D dwell-time fit (section 5.4, Magleby and Weiss, 1990a; Huth et al., 2006) is recommended.

Even though the usage of distributions-per-level may lead to errors in the determination of the rate constants, all simulations done so far yielded a correct estimation of the true current level as shown in Fig. 5.22 and Fig. 5.23, and Table 5.3.

5.3.5.3. The benefit of current reconstruction

The importance of estimating the correct true current level is illustrated by means of two examples. For a kinetic analysis, Fig. 5.19 and Table 5.2 illustrate that fitting a time series under different assumptions for the original single-channel current can lead to completely different rate constants. There have been several successful approaches to determine simultaneously both rate constants and current (Michalek et al., 2000; Qin et al., 2000; Venkataramanan and Sigworth, 2002). Here, an alternative approach has been

developed, i.e., determining the current first, and fitting the rate constants in a second step. This method has two advantages: First, simple algorithms are much faster than more sophisticated programs. The current reconstruction takes 1 min to 1 hour (depending on the length of the time series and the rate constants; the simulation is the time-consuming step) on a personal computer (1.4 GHz, 512 MB RAM). The simple HMM fit (section 4.7, Fredkin and Rice, 1992; Albertsen and Hansen, 1994)(section 4.7) using the reconstructed current takes approximately the same time. Consequently, this procedure is adequate for the analysis of a large number of time series. Second, most fitting programs, especially the beta fit, tend to get unstable with large parameter sets. Thus, splitting the fitting procedure in two parts improves the stability.

5.3.5.4. Limitations in real data

In the last three sections (Fig. 5.24 and Fig. 5.25), it has been shown that the success of this method of current reconstruction is not restricted to idealized simulated data. The application on measured data, too, yields reliable results. This will lead to the scientific results represented in chapters 6 and 7. However, these data have to be of excellent quality. The baseline noise should be as low as possible. Otherwise, the excess noise (resulting from gating) can no longer be distinguished from the basic noise. Additionally, the time series must be absolutely drift-free, because even a tiny drift would distort the amplitude histogram. Alternatively, the use of a very good drift elimination algorithm may overcome this problem.

5.4. Two-dimensional dwell-time histograms

(The content of this section (and more) was published as: Huth, Schroeder and Hansen, 2006)

2-D dwell-time analysis (Magleby and Weiss, 1990a, b) is a means of distinguishing between different Markov models as described in section 4.6. Huth (Huth, 2005; Huth et al., 2006) improved the fit algorithm by the following features: normalizing it to time and not to the number of events, employing a Hinkley detector for jump detection, introducing a genetic fit algorithm and replacing maximum likelihood by a least square criterion

$$E^2 \;=\; \sum_{i,j}(M_{ij} - H_{ij}\frac{T_{mes}}{T_{sim}})^2 \tag{5.24}$$

with E being the error, M, H being the measured and theoretical frequencies per bin in the 2-D dwell-time histograms, respectively, T_{mes} and T_{sim} the durations of the measured and the simulated time series, respectively and averaging over 9 or 25 bins

$$E^2 = \sum_{i,j}\left(\sum_{k=i-m}^{i+m}\sum_{k=j-m}^{j+m} M_{ij} - \sum_{k=i-m}^{i+m}\sum_{k=j-m}^{j+m}\frac{T_{mes}}{T_{sim}}H_{ij}\right)^2 \tag{5.25}$$

with $m = 1$ for 9 bins and $m = 2$ for 25 bins. Furthermore, using simulated time series for the generation of the "theoretical" 2-D dwell-time histograms from assumed Markov models enabled the incorporation of the measured filter response and noise.

Together with T. Huth (Huth et al., 2006) the improved 2-D dwell-time fit was compared with the SQ fit (section 5.2) with respect to the temporal resolution (Fig. 5.26). The temporal resolution of the two most efficient algorithms, the 2-D dwell-time fit and the subsequent HMM/beta fit (SQ fit, section 5.2), enabled the determination of rate constants which were ten times faster than the corner frequency of the low-pass filter. The requirement of computing time is a problem of the 2-D dwell-time fit (ca. 100 times that of the HMM fit), but can now be handled by personal computers.

Furthermore, it has to be mentioned that the 2-D dwell-time fits can also be used for the determination of the true single-channel current (Fig. 5.27). Thus, it provides an alternative method to the usage of beta distributions as described in section 5.3. In this thesis, we used the fit of the beta distributions rather than the 2D dwell-time fit, because the computing time was shorter by a factor 30 to 100.
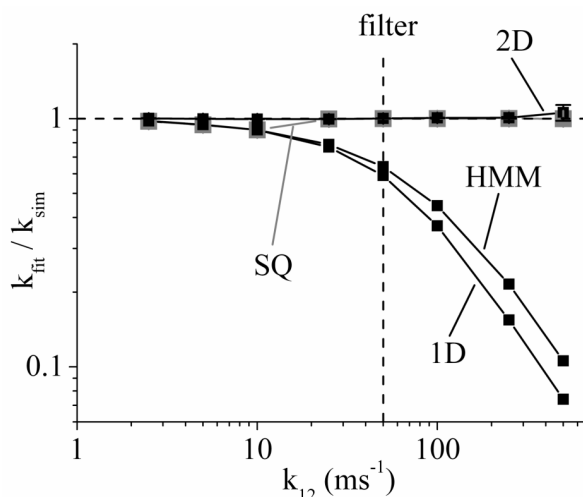
Fig. 5.26. Performance of different fit strategies in dependence on rate constants of patch clamp data. For this range test, a simple C-O Markov-Model $C \underset{k_{21}}{\overset{k_{12}}{\rightleftharpoons}} O$ was used to simulate the "measured" time series. It was analyzed by the 2-D dwell-time fit algorithm (2D), a 1-D dwell-time fit (1D), a HMM fit (HMM) and an SQ fit (SQ). There are no error bars at the results of the HMM and 1D fit, because these are analytical approaches, where repetitive fits yield identical results. The dashed horizontal line indicates correct solutions (k_{fit} / k_{sim} = 1). The settings were: filter frequency = 50 kHz, sampling = 200 kHz, k_{12} = k_{21}, length of the time series t_s = 50 s, SNR = 8 and error calculation for the 2D fit was done with the least square method (9 bins). Because of the simple model, a faster simplex algorithm was employed instead of the genetic algorithm. (From Huth et al., 2006).
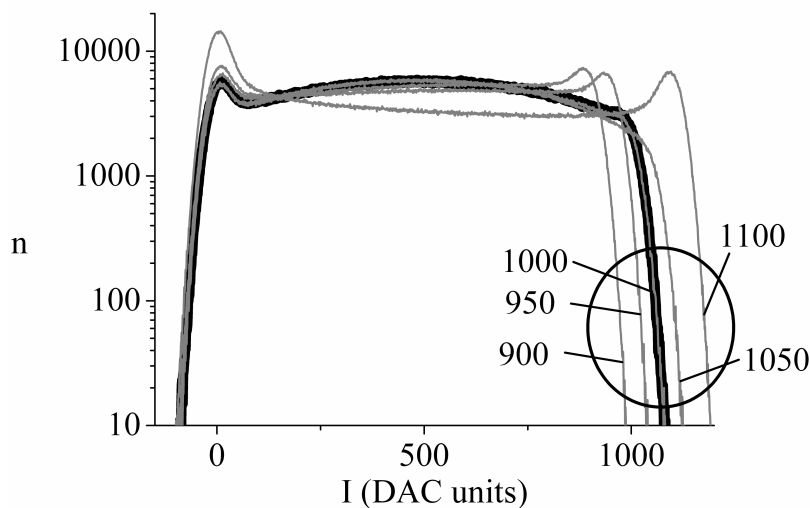
Fig. 5.27. Detection of the true single-channel current in time series where apparent single-channel current is reduced by fast gating. A "measured" time series was generated from a 3-state COC Markov-model $C \underset{5ms^{-1}}{\overset{50ms^{-1}}{\rightleftharpoons}} O \underset{200ms^{-1}}{\overset{200ms^{-1}}{\rightleftharpoons}} C$ by simulation, and amplitude histograms of current were constructed (black traces). Filter frequency was 50 kHz, sampling rate 200 kHz, length of the time series = 50 s, SNR = 8 and simulation current level was set to 1000 DAC (Digital to Analog Converter) units. The "measured" time series was analyzed with the 2D fit (LS, 9 bins, genetic algorithm) for different assumed current levels. Using the resulting rate constants, "theoretical" time series were simulated and amplitude histograms were constructed for each one of these levels (numbers at the grey traces). (From Huth et al., 2006).

124

6. Ion-channel interactions: Fast flickering at positive potentials as induced by K^+ depletion

(The content of this section was published as Schroeder and Hansen, 2007)

Summary. The MaxiK channels used in our lab have rather peculiar single-channel current/voltage curves (IV curves): Even in the absence of potential blockers, the IV curve at membrane voltages > +100 mV (i.e., at high outward currents) has a negative slope resistance caused by an unresolved flickery block (see Fig. 4.12). The analysis of the amplitude histograms by beta distributions in this chapter suggests that current in this voltage range is reduced by two effects: rate limitation at the cytosolic side of the selectivity filter and gating with rate constants 10 to 20-fold higher than the cut-off frequency of the filter (i.e., dwell-times in the μs range). The model created from the investigations of this chapter (Fig. 6.8) postulates a coupling between both effects: If the voltage over the selectivity filter withdraws ions from the cavity at a rate higher than that of refilling from the cytosol, the selectivity filter becomes instable because of ion depletion, and current is interrupted by the resulting flickering. The fit of the IV curves revealed a characteristic voltage of 35 mV (Fig. 6.4, Table 6.2). In contrast, the voltage-dependence of the gating factor R, i.e., the ratio between true and apparent single-channel current, could be fitted by exponentials with a characteristic voltage of 60 mV (Fig. 6.6, Table 6.2), suggesting that only part of the transmembrane potential is felt by the flux through the selectivity filter.

6.1. Introduction

The current through ion channels is determined by three characteristics: single-channel conductance, selectivity and gating. These features are of great importance in medical research, (Lehmann-Horn and Jurkat-Rott, 1999; Ashcroft, 2000) and a challenge for biophysicists. Biophysicists seek to understand the relationship of these parameters to the properties of the transport protein. Recent results have achieved tremendous progress with respect to this goal and there is also some hope that the findings in the present and in the subsequent chapter may contribute to the understanding of the involved mechanisms.

As described in section 2.5.1, ion channels posses three (known) different kinds of gates, each of them a potential candidate for the observed gating. The N-terminal chain and ball mechanism (Armstrong et al., 1973) which actually is a finger in K^+ channels (Bentrop et al., 2001) and a hinged lid in Na^+ channels (Catterall, 2000) plays an important role in inactivation processes especially during action potentials of nerves (Catterall, 2000). Structural analysis has provided clear evidence for channel closing by the inner gate (Perozo et al., 1999; Liu et al., 2001) as mediated by bending of the S6 (TM2) helix (del Camino et al., 2000; del Camino and Yellen, 2001; Jiang et al., 2002b; Zhao et al., 2004). An alternative mechanism of closing the inner gate is implemented by the N-terminus in the virus encoded Kcv channel (Tayefeh et al., 2007).

For the investigations presented in this and the next chapter, the selectivity filter is in the focus of interest. Traditionally, the selectivity filter was assumed to be responsible for selectivity and for the magnitude of the single-channel current. Especially after the MacKinnon group had resolved the crystal structure of KcsA (Doyle et al., 1998), it seemed that modern research would focus one the mechanism of permeation (determining

the single-channel current) and selectivity. As mentioned in section 2.4, the concept of *snug fit*, already anticipated by Mullins (1959), led to the postulate of a rigid structure of the selectivity filter, reinforcing the suggestion of Armstrong and Bezanilla (1972) that the "oxygens of the cage" can substitute for the water shell of the permeant ion. The rigidity was considered to be requisite for adjusting the distance of the carbonyl groups required for the correct substitution of the water shell for K^+ ions, but not for smaller Na^+ ions. Several experiments supported the snug fit hypothesis, e.g., the finding of Kiss et al. (1999) that during C-inactivation the *Shaker* K^+ channel is converted to a Na^+ channel due to the shrinkage of the tryptophane ring (Larsson and Elinder, 2000; Loots and Isacoff, 2000).

However, flexibility has come back on the scene. Molecular dynamics simulations (MD) have shown that a completely rigid selectivity filter cannot conduct ions (Berneche and Roux, 2005; Noskov and Roux, 2006; Varma and Rempe, 2007; Kast et al., 2008). Thus, a softer picture of the channel has emerged coming closer to the field strength model of Eisenman (Eisenman, 1962; Eisenman and Horn, 1983). Here, selectivity is determined by the energy required to replace the binding of an ion to its water shell by the binding to the carbonyl groups. Hille (1973) highlighted the basic difference between both models: For the snug fit hypothesis it is important that the carbonyl groups are held rigidly at the diameter of a K^+ ion (2.66 Å), whereas for the concept of field strength it "*would be useful if the dipoles of the channel … can be pulled in by small ions and pushed back by large ones*".

Renart et al. (2006) have employed intrinsic tryptophane fluorescence in order to demonstrate that K^+ and Na^+ lead to different structural changes in the selectivity filter. These results are a contradiction to the almost absolute maintenance of the protein structure in the presence of permeating and non-permeating ions as found by Zhou and MacKinnon (2003) in KcsA crystals. The results indicate that the flexibility of the protein is higher than suggested by crystal structure analysis.

Recently, the analysis of crystal structure and MD simulations heads for a convergence of both models. Varma and Rempe (2007) found a narrow window of flexibility within which the selectivity filter achieves selective K^+ ion partitioning. The same message resulted from MD simulations by Noskov and Roux (2006) and Noskov et al. (2004). If the filter were too rigid K^+ ions could never physically partition from one binding site to another. If the filter were too flexible like a liquid, K^+/Na^+ selectivity could not occur. The simulations have shown that only K^+ occupies the well-ordered S0 to S4 positions in the filter. In contrast, Na^+ (Kast et al., 2008) and also Rb^+ (Morais-Cabral et al., 2001) coordinate at intermediate sites leading to different activation energies of permeation.

So far, most of the evidence for the flexibility comes from MD simulations, but not from experimental results. Thus, it should be considered of whether the flexibility of the filter is reflected in the slow and fast gating properties of the channel. Several experiments indicate gating originating from the selectivity filter.

A very slow process is C-inactivation (Choi et al., 1991; Lopez-Barneo et al., 1993; Starkus et al., 1997; Yellen, 1998; Kurata and Fedida, 2006) which closes the channel after prolonged depolarization. It is promoted by low K^+, and thus is also called a foot-in-the-door effect (Gibor et al., 2007). Its relationship to the selectivity filter becomes obvious when low pH fully opens the inner gate of KcsA. Then, slow gating can be observed which is related to voltage-dependent E71 – D80 interactions (Cordero-Morales et al., 2006a; Cordero-Morales et al., 2006b). Blunck et al. (2006) employed fluorescence measurements to prove that KcsA was really open when E71-related gating occurred. In GIRK, gating of the selectivity filter became obvious when the inner gate was locked in the open state by

mutations (V188G, Yi et al., 2001). Involvement of the selectivity filter also in faster (or medium with respect to the rate constants found here) gating was found in Kir channels (Proks et al., 2001; Claydon et al., 2003; Xie et al., 2004). Furthermore, the occurrence of subconductance levels during channel opening and deactivation in the T442S mutant of *Shaker* (Zheng and Sigworth, 1998) was considered to be related to fast structural changes in the selectivity filter.

In the LQT mutant L273F of KCNQ1, two types of selectivity filter-mediated inactivation mechanism were found (Gibor et al., 2007). The fast one also occurring in WT was voltage-independent and had little effect on current. It became obvious only in the tail currents. The slow one was voltage-dependent. In contrast to C-inactivation, this kind of gating was promoted by elevated concentrations of external K^+. While Gibor et al. (2007) stated that K^+ simply trapped the blocker ion Ba^{2+} in the pore, Immke et al. (1999) explained the acceleration of inactivation by external K^+ Kv2.1 with direct K^+ protein interaction near or in the selectivity filter, leading to a conformational change of the channel.

Involvement of the selectivity filter in very fast gating was found in Kir channels (Proks et al., 2001; Claydon et al., 2003; Xie et al., 2004). Furthermore, the occurrence of subconductance levels during channel opening and deactivation in the T442S mutant of *Shaker* (Zheng and Sigworth, 1998; Zheng et al., 2001) was considered to be related to fast structural changes in the selectivity filter.

In the investigations presented here it is shown that very fast gating of the selectivity filter may be involved in the generation of the negative slope of the apparent single-channel current/voltage relationship in MaxiK channels. The analysis of the effects leads to a model which may build a bridge between physiological observations and MD simulations of the protein dynamics. A linear increase of the current with driving force (electrical potential and concentration gradient) is found only in the vicinity of the reversal potential. At higher negative and/or positive potentials, the measured (apparent) current may become independent of driving force (saturation) or may even start to decline with increasing driving force (negative slope or negative resistance).

Negative slopes are often observed in whole-cell data and occur at outward and inward currents in different kinds of channels in plants (Beilby, 1985; Tester, 1988), animals (e.g. in Kir channels: Alagem et al., 2001; Murata et al., 2002; Yeh et al., 2005) (in MaxiK: Cox et al., 1997; Ransom and Sontheimer, 2001) and viruses (Kang et al., 2004). Often its occurrence has been attributed to the interaction with divalent (e.g., Ba^{2+} in Kir 2.1: Alagem et al., 2001; Murata et al., 2002; Ca^{2+} in MaxiK: Ransom and Sontheimer, 2001; Mg^{2+} in ROMK1: Lu and MacKinnon, 1994) or monovalent cations (e.g., Cs^+ in MaxiK: DeCoursey et al., 1996 or Tl^+ in Kir2.1: Yeh et al., 2005). This started with the early observation of Bezanilla and Armstrong (1972) that the entry of Na^+ or Cs^+ into the K^+ channel of the squid axon caused a negative slope.

Negative slopes were also found in single-channel records (DeCoursey et al., 1996; Cox et al., 1997; LeMasurier et al., 2001; Sorensen et al., 2001; Nimigean and Miller, 2002; Zhang et al., 2006; Pagliuca et al., 2007). Also here, an important role of blocking ions was documented in many studies. For instance, the presence of Na^+ caused a negative slope in KcsA (Nimigean and Miller, 2002). In *Chara*, single-channel currents of the large Ca^{2+}-activated K^+ channel showed negative slopes in a K^+/Cs^+ solution (Draber and Hansen, 1994) or in Na^+ (Weise and Gradmann, 2000). In the single-channel current of mammalian MaxiK, millimolar concentrations of cytosolic Na^+ (Marty, 1983; Kawahara et al., 1990; DeCoursey et al., 1996) and Ca^{2+} (Cox et al., 1997) were shown to induce negative slopes. On the other hand, negative slopes in

single-channel current without blockers like in the data presented in this chapter, were observed only rarely (Cox et al., 1997; Shim et al., 2007).

The physiological role of the negative slope is still unknown, maybe there is none. Especially at positive potentials, the negative slope is found in a voltage range which would not occur in a living organism (> +100 mV). Nevertheless, for the investigation of the biophysical principles of permeation and gating mechanisms in transport proteins, a clear description and understanding of the deviations from linear effects can provide important keystones.

In whole-cell experiments, the occurrence of negative slopes can easily be related to gating phenomena (Sakmann and Trube, 1984). In the case of single-channel recordings only a few investigations in *Chara* reached the temporal resolution to reveal fast gating as a cause of apparent current reduction, (e. g., Klieber and Gradmann, 1993; Draber and Hansen, 1994). Revealing fast gating as the cause of the negative slope in human MaxiK was until recently impeded by insufficient temporal resolution. This limitation could be overcome by the approach of Schroeder and Hansen (2006) employing filtering with a corner frequency of 50 kHz and an analysis based on beta distributions (FitzHugh, 1983; Yellen, 1984; Moss and Moczydlowski, 1996; Riessner, 1998; Schroder et al., 2005) for the determination of the true single-channel current. The benefit of such an approach is the assignment of saturation and gating effects to different functional units of the channel protein and the detection of interactions. The analysis leads to the hypothesis that fast gating at high positive potentials is caused by ion depletion in the cavity and/or the selectivity filter. Early hints to such a mechanism came from the effect of the permeant ion on gating (Almers and Armstrong, 1980).

6.2. Materials and Methods

Growth of the HEK cells, patch clamp technique and recording apparatus are described in chapter 3. Chapters 4 and 5 provide the analytical tools. Thus, only the experimental solutions are mentioned here:

Four different solutions were used symmetrically in the pipette and in the bath. Their compositions are shown in Table 5.1. pH was titrated with KOH to 7.2. In some experiments, NO_3^- was used instead of Cl^-. This did not affect the channel properties (data not shown), so the data with equal cation compositions were pooled. In the solution without added Ca^{2+} and Mg^{2+}, 10 mM EDTA was given to chelate spurious divalent cations.

Table 6.1. Solutions used in this chapter. In all experiments, the same solution was used in bath and pipette. pH was titrated to 7.2 with KOH.

KCl / mM	CaCl$_2$ / mM	MgCl$_2$ / mM	HEPES / mM	EDTA / mM
50	2.5	2.5	10	0
150	2.5	2.5	10	0
400	2.5	2.5	10	0
150	0	0	10	10

6.3. Results

6.3.1. Apparent single-channel and steady-state macroscopic currents

Steady-state single-channel traces on inside-out patches in symmetrical 150 mM K^+ with $CaCl_2$ and $MgCl_2$ were recorded with a sampling frequency of 200 kHz and a 4-pole Bessel filter with a corner frequency of 50 kHz. Fig. 6.1A and B show typical records obtained at +80 and +160 mV, respectively. Note the increased open-channel noise at +160 mV.

In Fig. 6.1C, the apparent single-channel current (black squares) and the open-probability (red circles) are given. The channel is activated by positive membrane potential as known for MaxiK. The most striking feature of the single-channel IV curve is the negative slope at high positive voltages.
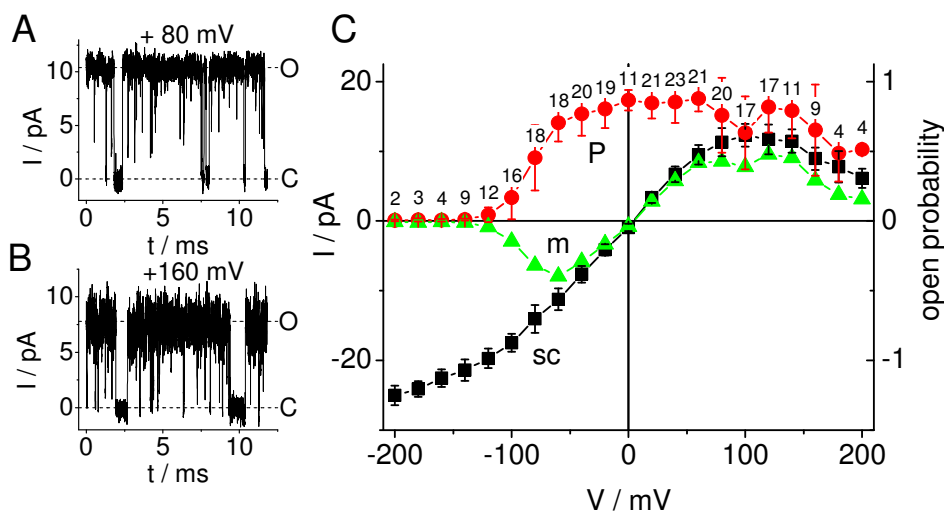
Fig. 6.1. Correlation of single-channel current, open probability and macroscopic current. (A, B): Representative sections of time series measured in 150 mM K^+ and 2.5 mM Ca^{2+} and Mg^{2+} at (A) +80 mV and (B) +160 mV. Off-line averaging over 10 data points was used only for clearer display, not for analysis. The apparent single-channel currents are 10.4 pA and 7.8 pA, respectively. (C) Dependence of apparent single-channel current (*sc*, black squares) and open-probability (*P*, red circles) on membrane potential as obtained from inside-out patches with 1 to 3 channels in symmetric 150 K^+ solution. The "steady-state macroscopic IV curve" (*m*, green triangles) was reconstructed from the single-channel data by means of Eq. (6.1). The numbers of independent experiments are indicated for each voltage. Error bars represent SEM.

The occurrence of negative slopes has been reported more frequently from macroscopic MaxiK IV curves at negative and at positive potentials (e. g. Cox et al., 1997). Gating of channel conductivity in different time-domains influences single-channel and macroscopic currents in different ways. This is illustrated in Fig. 6.1C. Steady-state macroscopic currents I_m were calculated from the product of single-channel current I_{SC}, the number n of channels in the membrane and the open probability p:

$$I_m = I_{SC} \cdot n \cdot p \qquad (6.1)$$

The resulting "macroscopic" IV curve (presented by the green triangles in Fig. 6.1C) is normalized to $n = 1$ for the sake of comparison. This IV curve shows the typical features of macroscopic IV curves observed in the presence of high Ca^{2+} concentrations (Cox et al., 1997), namely the occurrence of negative slopes in both voltage ranges. Even though the two negative slopes look quite similar, their origin is different. The negative slope of the macroscopic current at negative potentials is due to a decreasing open-probability caused by slow (observable) gating. It does not originate from an effect on the single-channel current which shows saturation, but no negative slope (curve *sc* in Fig. 6.1C). In contrast, at high positive potentials (above +100 mV) the negative slope is mainly inherited from the apparent single-channel current.

In addition to the measurements in 150 mM K^+, single-channel experiments were also done at 50 mM and at 400 mM. In Fig. 6.2A, the resulting IV curves are compared with that one in Fig. 6.1C. The negative slope at positive membrane potentials occurs under all three conditions. However, the bending is shifted to higher positive membrane potentials with increasing K^+ concentration. A significant influence of K^+ concentration on the voltage-dependence of the open probability cannot be verified (Fig. 6.2B).
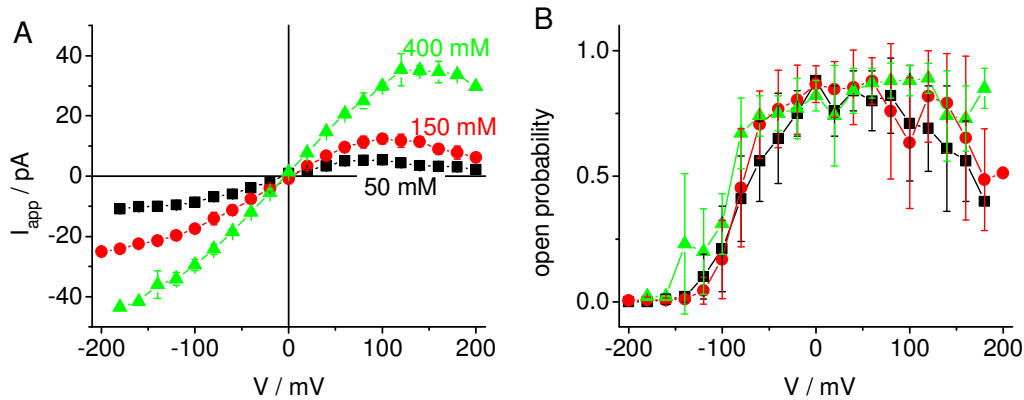
Fig. 6.2. Influence of K^+ concentration on channel properties. (A) Apparent single-channel IV curves for low (50 mM, black squares), standard (150 mM, red circles) and high (400 mM, green triangles) K^+ concentrations. (B) Voltage-dependence of the open-probabilities measured at 50, 150 and 400 mM K^+. Measurements were done in symmetrical K^+ concentrations with 2.5 mM Ca^{2+} and 2.5 mM Mg^{2+} on either side. Data points and error bars present mean values and SEM from 1 to 23 experiments.

6.3.2. True single-channel IV curves

The comparison of the time series in Fig. 6.1A and B with the IV curves in Fig. 6.1C reveals that the negative slope of the apparent single-channel current at higher positive membrane voltages is accompanied by an increase in open-channel noise. The noise indicates that unresolved fast gating may hide the true current level (Hille, 1992; Hansen et al., 1997; Townsend and Horn, 1999). Thus, the effect of fast gating has to be eliminated in order to detect the true single-channel current. This is done by means of the extended application of the beta fit with a two-state model as developed in section 5.3.

A typical example for this kind of analysis is illustrated in Fig. 6.3. From traces like those in Fig. 6.1A and 1B, amplitude histograms were generated (Fig. 6.3A). The full amplitude histogram was split into distributions-per-level (Schroder et al., 2004;

Schroeder and Hansen, 2006), see section 5.1, as presented in Fig. 6.3A by the colored curves labeled O and C. The O-level distribution was fitted by the following 2-state model

$$O \underset{k_{CO}}{\overset{k_{OC}}{\rightleftharpoons}} C \qquad (6.2)$$

with the assumed single-channel current I_{fit} as a constant parameter. In Fig. 6.3B, the dependence of the error sum (Eq. (4.52)) on the assumed single-channel current I_{fit} (as given on the abscissa) is plotted. The minimum is quite shallow (due to the logarithmic scale), but the best fit (minimum error sum) can clearly be obtained around 13 pA (arrow) resulting in a ratio $R = I_{true}/I_{app} = 1.7$. The related approximation of the O-level distribution is very good as shown in Fig. 6.3C.
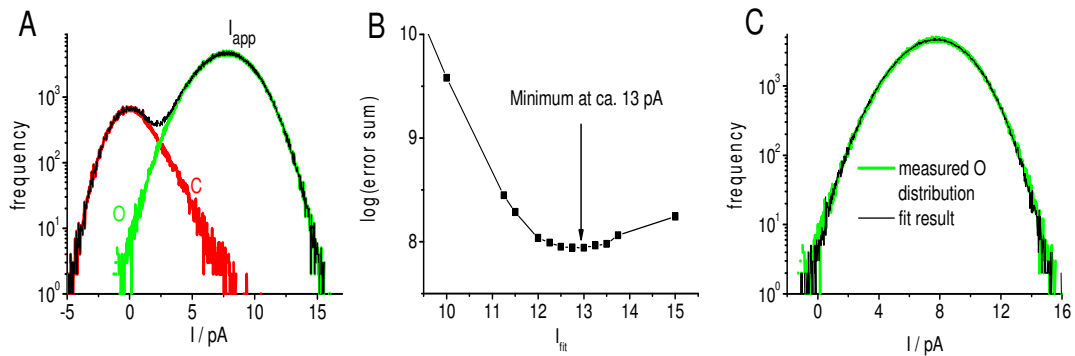
Fig. 6.3. Example for the analysis of a single-channel time series, recorded at +160 mV in 150 K$^+$ with Ca^{2+} and Mg^{2+} (see Table 6.1) on both sides of the membrane. (A) Full amplitude histogram (black) and distributions-per-level (O: green, C: red). The apparent current I_{app} was 7.6 pA. (B) Dependence of the error sum (Eq. (4.52)) on the putative single-channel current (I_{fit}). Beta fits determined the optimum pair of rate constants for the O-C model (Eq. (6.2)) with different assumed single-channel currents I_{fit} which are given at the abscissa. The best fit could be obtained with $I_{fit} = 13$ pA. (C) Comparison of the measured O-distribution (green, the same as in (A)) and the simulated one obtained from the best fit in (B) (black). The coincidence is so good that the two curves are nearly indistinguishable.
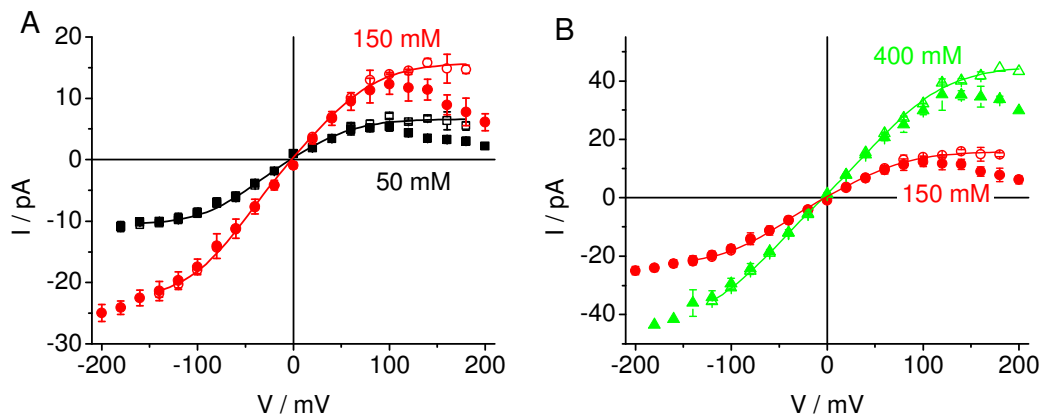
Fig. 6.4. Apparent (I_{app}, closed symbols) and true (I_{true}, open symbols) single-channel IV curves for three different K$^+$ concentrations: 50 mM (black squares), 150 mM (red circles) and 400 mM (green triangles). Solid lines: Fit of I_{true} with Eq. (6.3), parameters are listed in Table 6.2. Numbers of experiments are given in Fig. 6.1 and Fig. 6.6. (A): 50 and 150 mM, (B): 150 and 400 mM.

The analysis was applied to the data in Fig. 6.2A for the whole voltage range. It resulted in corrected IV curves presenting the true single-channel current ($I_{true} = I_{fit}$ at the minimum in Fig. 6.3). In Fig. 6.4, three pairs of IV curves are shown. Each pair consists of the apparent single-channel current (closed symbols) as already presented in Fig. 6.2A, and the true single-channel current (open symbols). It has to be mentioned that the IV relationship of the true single-channel current I_{true} is asymmetrical: Saturation at positive voltages leads to smaller currents than at negative voltages (see also Table 6.2).

6.3.3. Saturation currents

In order to get a more reliable determination of the saturation currents of the true single-channel current in Fig. 6.4, the IV curves were fitted by means of Eq. (6.3)

$$I_{true} = F \frac{\kappa_{oi} \cdot k_{io,0} \cdot \exp\left(\dfrac{V}{V_s}\right) - \kappa_{io} \cdot k_{oi,0} \cdot \exp\left(-\dfrac{V}{V_s}\right)}{k_{io,0} \cdot \exp\left(\dfrac{V}{V_s}\right) + k_{oi,0} \cdot \exp\left(-\dfrac{V}{V_s}\right) + \kappa_{oi} + \kappa_{io}} \tag{6.3}$$

Equation (6.3) is identical to the equation derived for the enzyme kinetic model of ion transport (Hansen et al., 1981; Hansen, 1986) with $k_{io,0}$, $k_{oi,0}$ being the scaling factors of the outward and inward voltage-dependent translocation steps, respectively, and κ_{oi} and κ_{io} including the binding of the ion on the cytosolic and on the luminal side, respectively. Because of the absence of an accepted transport model, V_s, the characteristic voltage of ion translocation, is just a phenomenological parameter. In simple models, it is related to the temperature potential $u_T = kT/e = 26$ mV and the relative location of the energy barriers in the translocation path (Hansen et al., 1981). F, V, T, k and e have their usual meanings. This cyclic model is evident for cotransporters (Abramson et al., 2003; Huang et al., 2003), but has also been found suitable for ion channels (Fisahn et al., 1986; Gradmann et al., 1987; Hansen and Fisahn, 1987), probably because of the cyclic scheme of site occupation as suggested by Morais-Cabral et al. (2001) or Bernèche and Roux (2005). Inspecting the mathematics behind different approaches shows that the crucial features of Eq. (6.3) also apply to other models including the law of mass conservation (probability normalization criterion) for the states in the filter (like that one of Nelson, 2002), based on a concerted single-file motion (Khalili-Araghi et al., 2006), or just voltage-independent loading reactions as in the simple four-compartment model in Fig. 6.8, below. The real biophysical background cannot be resolved without further experiments; the Tl^+ effects in chapter 7 will provide further clues.

The saturation currents are obtained for V approaching $-\infty$ or $+\infty$:

$$I_{sat-} = -F\kappa_{io} \quad \text{and} \quad I_{sat+} = F\kappa_{oi} \tag{6.4}$$

The curves resulting from the fits of the averaged data are shown in Fig. 6.4 as solid lines, and the parameters are given in Table 6.2, below.

Fig. 6.4 and Table 6.2 show that saturation currents are asymmetrical for the two lower potassium concentrations. The loading reactions on either side of the selectivity filter have at least two major components: diffusion limitation and exchange of the water shell for the carbonyl groups of the filter. The asymmetry is stronger for low potassium concentrations indicating that the entry from the cytosolic side has a stronger diffusion component. This is in line with the results of Brelidze and Magleby (2005) that diffusion limitation induced by sugars can be overcome by high K^+ concentrations in the cytosol.

6.3.4. Rate constants of flickering

The rate constants of flickering as delivered by the beta fit and their ratio are shown in Fig. 6.5A and B, respectively. Despite the large scatter and the possible errors imposed by model truncation, the following statements would also be obtained from a more refined (5-or more-state model) analysis:

1. The dominant voltage dependence can be attributed to k_{OC}. The increase of k_{OC} at positive voltages leads to shorter open-dwell-times and thus to a decrease of the apparent (averaged) single-channel current. (On a side note: Also in the spontaneous mode switching, Fig. 5.24A and Table 5.4, k_{OC} was the changes parameter.)
2. The high scatter impedes the detection of small effects of the ion concentration on the rate constants.
3. The determination of the ratio of the rate constants (Fig. 6.5B) is much more reliable than that of the absolute values, thus making the influence of concentration obvious which is scarcely detectable in Fig. 6.5A.
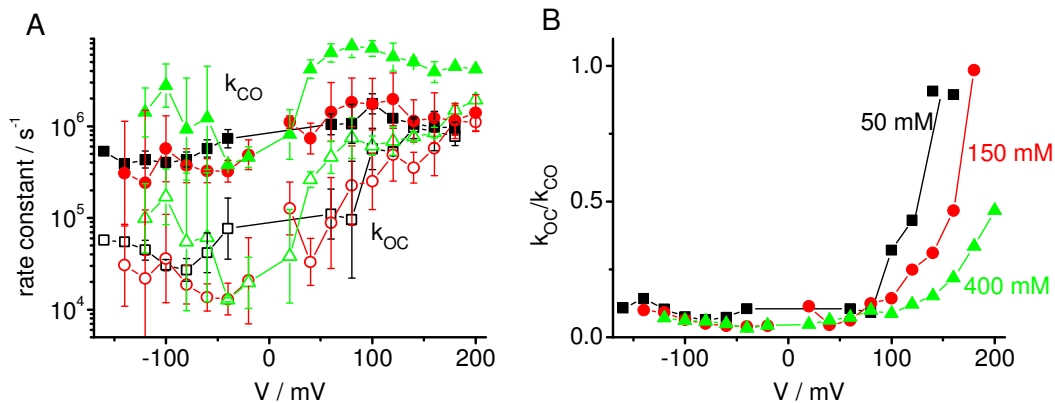
Fig. 6.5. Rate constants for the reduced two-state Markov model (Eq. (6.2)). Black squares: 50 mM K^+; red circles: 150 mM K^+; green triangles: 400 mM K^+. (A) Absolute values of the open-close- (k_{OC}, open symbols) and the closed-open-transitions (k_{CO}, closed symbols). (B) Ratio of k_{OC} and k_{CO} as calculated from the data in (A). Numbers of experiments are given in Fig. 6.6.

6.3.5. Model-based analysis: Mechanisms of current reduction

The current reduction by fast gating, i.e., the ratio of I_{true} and I_{app} in Fig. 6.5, was analyzed with the model described in section 6.5: It is based on the assumption that ion depletion in the cavity/selectivity filter caused the filter to flicker. The background of this assumption is discussed below in Sections 6.4.2 - 6.4.4. This model predicts that the voltage dependence of the gating factor $R = I_{true} / I_{app}$ is a simple exponential function of the membrane voltage V:

$$R = \frac{I_{rue}}{I_{app}} = 1 + R_k \exp\left(\frac{V_0}{V_G}\right) \tag{6.5}$$

Indeed, Fig. 6.6A-C shows that the data can neatly be fitted by Eq. (6.5). Fig. 6.6D presents a comparison of the three fitted curves in (A), (B), and (C). The parameters resulting from the fits are given in Table 6.2.

Fitting the R-curves in Fig. 6.6 resulted in V_G = 51, 57 and 62 mV for 50, 150 and 400 mM K^+, respectively (in brackets in Table 6.2). The low signal-to-noise ratio found in 50 mM K^+ decreased the reliability of the data (Fig. 6.6A). In order to get comparable estimates of the factor $1/R_K$, all R-curves were fitted additionally with a fixed V_G of 60 mV (average of the values at 150 and 400 mM K^+).
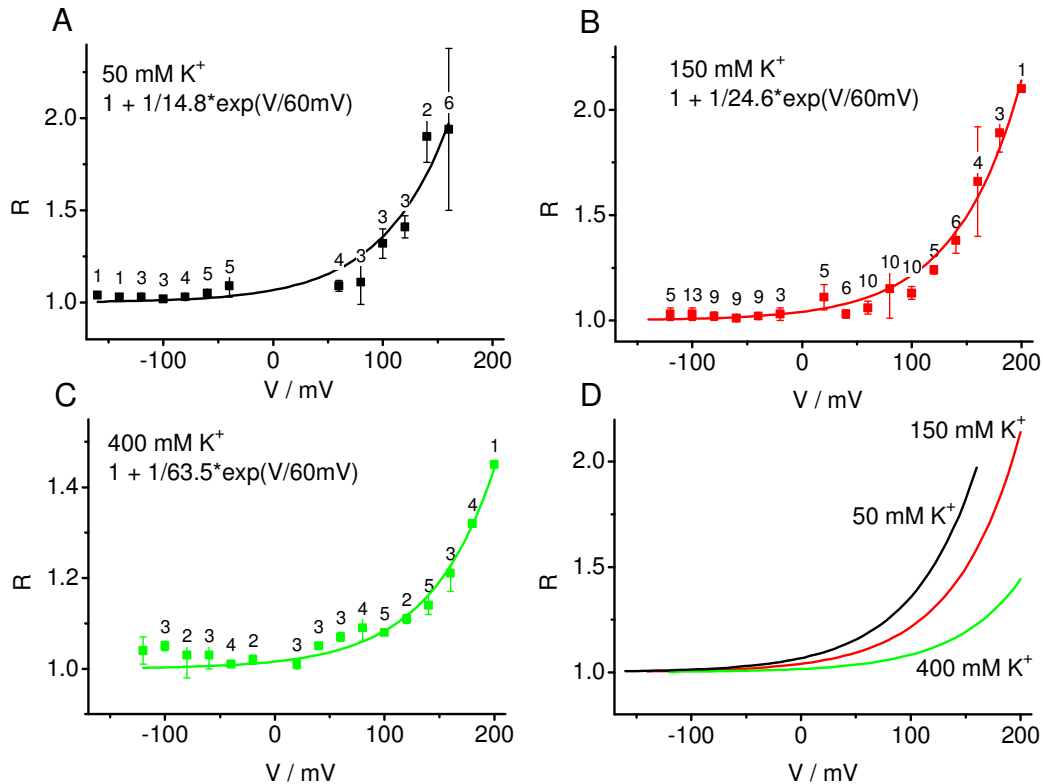
Fig. 6.6. Fit (smooth lines, with fixed V_G = 60 mV) of the current reduction R (I_{true}/I_{app} in Fig. 6.4) for three K^+ concentrations by means of Eq. (6.5): (A) 50 mM, (B) 150 mM, (C) 400 mM. The parameters of the fits are given in the graphs and in Table 6.2. (D) Comparison of the fitted curves in (A), (B), and (C). Numbers of individual experiments are given at the curves.

Table 6.2. Summary of the parameters obtained from the analysis of the true IV curves and of the gating factors. *a: g_{slope}*: slope conductance was determined by a linear fit of the IV curves in the voltage range ± 60 mV. b: $I_{sat+/-}$, $k_{oi,0}$, $k_{io,0}/k_{oi,0}$, V_s: parameters of the true IV curves (I_{true}, Fig. 6.4, Eq.(6.3)), c: V_G, R_K: parameters of the gating factor (Fig. 6.6, Eq. (6.5)). R_K was determined with V_G fixed at 60 mV. Fit results for V_G as a free parameter are given in brackets. For fitting, averaged data were used, and the errors were estimated from the variance-covariance matrix as provided by the fitting routine in Origin®.

	g_{slope}^a / pS	I_{sat+}^b / pA (=Fκ_{oi})	I_{sat-}^b / pA (= -Fκ_{io})	F $k_{oi,0}^b$	$k_{io,0}/k_{oi,0}^b$	V_s^b /mV	V_G^c / mV	$1/R_K^c$ ($V_G = 60$ mV)
50 mM	91 ± 5	6.6 ±0.3	-10.6 ±0.6	3.2 ± 2	2.0 ±0.4	29 ±9	60 (51 ± 7)	15 ± 0.9
150 mM	176 ± 3	15.8 ± 0.5	-23.0 ± 1.2	7.1 ± 2.5	1.7 ± 0.2	33 ± 6	60 (57 ± 3)	25 ±0.7
400 mM	330 ± 2	45.3 ± 2.1	-44.2 ± 0.9	16.5 ± 2.3	1.2 ± 0.1	39 ± 4	60 (62 ± 5)	63 ±2.3

6.3.6. Independence on Ca^{2+}/Mg^{2+}

It has often been reported that Ca^{2+} and Mg^{2+} do not only activate MaxiK channels, but also block at millimolar concentrations (e. g. Ferguson, 1991; Bertl et al., 1993; Cox et al., 1997).

   To exclude such an effect, measurements were carried out under zero Ca^{2+}/Mg^{2+} conditions (with 10 mM EDTA, Table 6.1) and compared with those done under saturating concentrations of the two divalent ions (2.5 mM each). The well-known influence on open probability was observed (Fig. 6.7B), but there was no significant effect on the single-channel IV curves (Fig. 6.7A). The analysis with beta fits shows that also the current reduction caused by fast flickering stays the same with and without divalent cations (Fig. 6.7C). Thus, it can be ruled out that the negative slope at positive potentials results from a Ca^{2+} or Mg^{2+} block. This corresponds to the findings of Cox et al. (1997) who reported a slight, $[Ca]_i$-independent negative slope in MaxiK channels at internal Ca^{2+}-concentrations below 124 µM. This is similar to the findings of Bertl et al. (1993) that rate constants related to the closed state of the Ca^{2+}-activated K^+ channel in *Saccharomyces cerevisiae* (probably a MaxiK) which cause flickering in the sub-millisecond range are not sensitive to Ca^{2+}, in contrast to the rate constants of the other two closed states with slower gating. This was also observed for fast gating in MthK (Li et al., 2007). The independence on a blocking ion is a crucial feature for the model created from the analysis of the data.
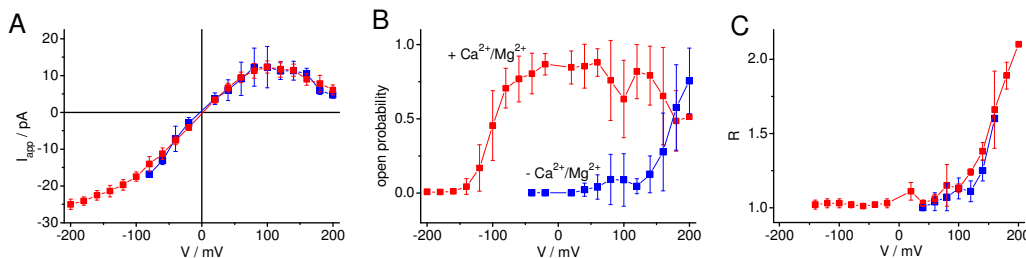
Fig. 6.7. Effect of divalent cations. Red squares present data obtained from solutions with divalent cations, blue squares those without divalent cations. In both cases, $[K^+]$ was 150 mM. (A) The negative slope of the single-channel current is independent of Ca^{2+} and Mg^{2+}. (B) The open probability of the channel is strongly reduced without divalent cations. (C) Also the ratio of true and apparent current (*R*, Eq. (6.5)) is not influenced. Data with divalent cations are taken from Figs. 1 and 6. There are 3 to 9 experiments without divalent cations per data point in (A) and (B) and 1 to 5 in (C).

6.4. Discussion

6.4.1. Reliability of the separation of gating and permeation effects

The results in Fig. 6.4 and Fig. 6.6 stress the importance of high temporal resolution for the distinction of the effects resulting from gating and permeation (Moss and Moczydlowski, 1996; Hansen et al., 1997; Townsend and Horn, 1999; Farokhi et al., 2000; Abramson et al., 2003; Hansen et al., 2003). After elimination of the gating effect in the apparent open-channel current, the IV curve of single-channel current shows saturation at high positive membrane potentials. The negative slope is eliminated.

The definition of I_{true} (see section 4.1.1) is based on effects still outside the reach of present experimental tools. Thus, it has to be asked whether also the saturation effect of what is called true single-channel current at high positive and negative potentials (Fig. 6.4) might originate from even faster gating processes which cannot be resolved in the experiments reported here. At very high gating frequencies, beta distributions become gaussian and narrow again (Central Limit Theorem, Feller, 1968) as shown in Fig. 5.21 (= Fig. 4 in Schroeder and Hansen, 2006). The temporal resolution obtained by the experiments above reached about 0.5 µs. This has to be compared with the average time required for a passage of a single ion which is 10 ns for a current of 16 pA. Thus, there is an average number of 50 ions passing the channel in 500 ns. There is not much numerical freedom for the introduction of additional undetected fast gating effects if the concept of classical Markov modeling is employed. If assumed gating frequencies come into the range of the average time between the transitions of two ions, gating and permeation mechanisms can no longer be separated. Since this kind of effect cannot be verified experimentally, and since there are reasonable biophysical mechanisms (discussed below in section 6.4.4) leading to saturation, it is assumed here that permeation effects and gating effects are clearly separated in the data of Fig. 6.4.

6.4.2. A mechanism correlating saturation and gating

A key for revealing the mechanism causing fast gating may be found in the observation that reduction of the true current by saturation (permeation effect) and by flickering (gating effect) occur (more or less) concomitantly (Fig. 6.4). In Fig. 6.8, the sensing compartment S plays the crucial role. S may be assigned to the cavity and/or the selectivity filter. If assigned to the cavity, a binding site may be assumed. For instance, Lu et al.(2001b) suggested that C169 binds Tl^+ in Kir2.1. Alternatively, the protein backbone may feel the coordination forces for the ion in the cavity. Here, we prefer a crucial role of the selectivity filter, keeping in mind that a role of the cavity cannot be excluded.

With increasing positive membrane potential, the rate constant k_{SL} (comprising k_{SE} and k_{EL}) of emptying the compartment S (Eq. (6.9), Fig. 6.8) exceeds the rate constant k_{PS} of refilling. This results in a depletion of ions in the cavity and/or the selectivity filter. The depletion leads to an instability of the selectivity filter and causes fast flickering as described by the gating factor R in Fig. 6.6.:
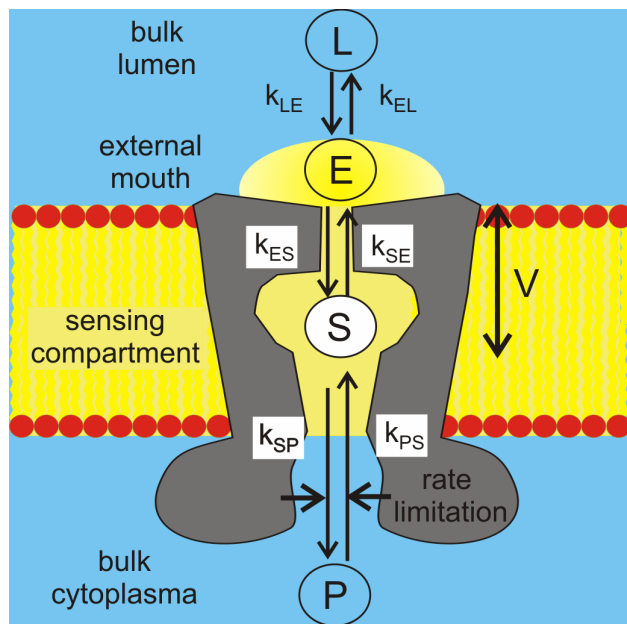
Fig. 6.8. Model for ion movement between bulk cytoplasma (*P*), the "sensing compartment" (*S*, cavity and/or selectivity filter), the external vestibule (*E*) and the bulk lumen (*L*). The rate constants on the arrows are those employed in the calculations in appendix 6.5.

Three features of the model of Fig. 6.8 described in quantitative terms in appendix 6.5 below have to be mentioned

1. "Ion concentration" in the cavity/filter has to be replaced by the average dwell-time of probably about four ions in the cavity and filter.
2. The ion concentration does not exert a direct effect, but a parametric effect. A direct effect would imply that the efflux to the lumen decreases the ion concentration in *S* until the filter shuts. It would reopen when refilling from the cytosol has restored the ion concentration. Such a direct effect does not lead to dwell-times in the microsecond range, because the reservoir *S* containing only a few ions would be filled up in the 10-ns range. The essential feature of the parametric effect is that the rearrangement of the protein backbone has a time constant which leads to integration over several periods of ion depletion during the open states of the flickering selectivity filter. The resulting conformational changes modulate the open/close ratio of the fast gating (in the model in appendix 6.5 this is done via Eq. (6.12)).
3. This parametric effect keeps the ion concentration at an average value which prevents the complete and possibly irreversible collapse of the filter.

Fitting the *R*-factor in Fig. 6.6 with Eq. (6.15) leads to plausible results, i.e., the exponential increase of *R* with membrane potential making obvious that the exponentially increasing (Eq. (6.11)) rate constant k_{SL} of ion transfer in the selectivity filter results from a typical voltage-driven ion transfer mechanism (Läuger and Stark, 1970; Hansen et al., 1981; Hansen, 1986). However, the comparison with the fits of the IV curves in Fig. 6.4 by means of Eq. (6.3) reveals a discrepancy: the characteristic voltage $V_G = 60$ mV (gating, Eq. (6.15)) is higher than the characteristic voltage $V_S = 35$ mV (IV curve, Eq. (6.3)). Both of them should be higher than $u_T = 26$ mV (Hansen et al., 1981), but equal in the simplest form of the model in Fig. 6.8.

This discrepancy makes obvious that the mathematical description of this model (spelled out in detail in appendix 6.5) needs further refinements. The most likely extension would start from the assumption that k_{SE} of the selectivity filter feels only the part bV of the full membrane potential V (leading to $V_G = 26$ mV/b), and that another part of the membrane potential influences the loading reaction k_{PS}. Then, k_{PS} would consist of a voltage-independent term (which determines the saturation current $F\,k_{PS}$, e.g., exchanging the water shell for the channel environment) and a voltage-dependent component. The voltage-dependent part of k_{PS} (and its equivalent κ_{oi}) exerts its influence in the numerator for the IV curves (Eq. (6.3)), but in the R-factor both numerator and denominator would be voltage-dependent (Eq. (6.14)). This may explain why V_G is higher than V_S.

There are still other mechanisms feasible leading to different V_S and V_G. Thus, it does not make sense to implement a more sophisticated version of k_{PS} (κ_{oi}) in Eq. (6.3) and in appendix 6.5, because the present experimental findings do not provide any means to distinguish models. The basic message is that a voltage drop over the loading reaction k_{PS} is a likely explanation for the difference between V_S and V_G.

A similar problem is found in the comparison of the concentration dependence of the saturation currents (Table 6.2 and Fig. 6.9B) and $1/R_K$ resulting from the gating analysis (Table 6.2 and Fig. 6.9A). In either case, a linear relationship to $[K^+]_P$ would be expected for a simple model (Eqs. (6.7)), whereas a Michaelis-Menton-like dependence is predicted by the models including a probability normalization criterion (Hansen et al., 1981; Fisahn et al., 1986; Hansen, 1986). Linearity roughly holds for the saturation currents, but it is weaker for $1/R_K$. Also here, a more elaborated kinetic model would be premature as long as the real kinetic scheme and putative superimposed direct effects of K^+ concentration and of voltage on channel structure are not supported by experimental findings.
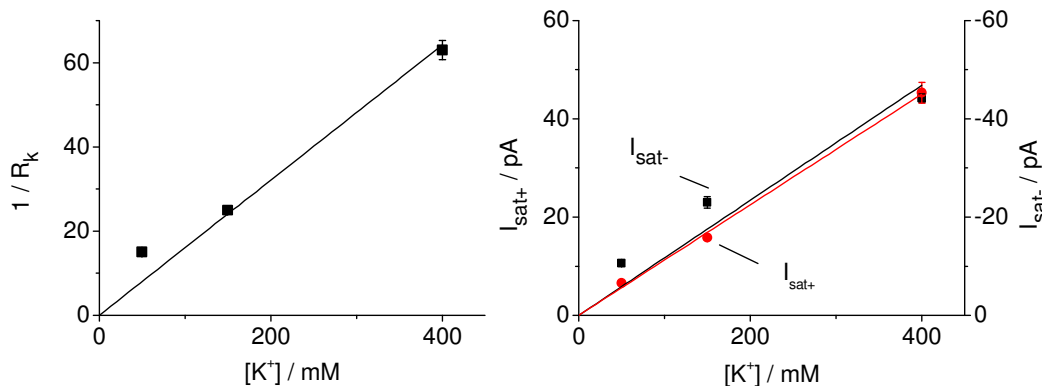
Fig. 6.9. Concentration dependence of (A) R_k and (B) saturation currents. Data are taken from Table 6.2. Lines are linear fits through the origin, according to the model predictions in Eq. (6.15) for R_k, and Eqns. (6.7) and (6.8) for $I_{sat-/+}$.

The model is based on two assumptions: 1. The gating takes place in the selectivity filter and is induced by ion depletion. 2. There is a voltage independent rate limitation for ion movement at the cytosolic entrance of the pore. Both are discussed and backed up by the literature discussed in the next two sections.

6.4.3. Assumption 1: gating by the selectivity filter

The crucial role of the selectivity filter in the model of Fig. 6.8 may be uncommon in the light of the majority of investigations where the inner gate (Perozo et al., 1999; Loussouarn et al., 2000) or the ball-and-chain mechanism (Catterall, 2000; Bentrop et al., 2001) are the preferred candidates. In the MaxiK channel, the S0 helix brings the N-terminus to the luminal side. This eliminates inactivation by the ball-and-chain mechanism (Koval et al., 2007) and makes the MaxiK a favorite object of patch clamp analysis. Thus, the decision has to be made between inner gate and selectivity filter in MaxiK.

Fluorescence studies revealed that gating probably arising from the selectivity filter became apparent when the inner gate was open (Blunck et al., 2006). The involvement of the selectivity filter in gating gets strong support from concomitant changes in ion selectivity (Zheng and Sigworth, 1997; Kiss et al., 1999). The question of whether fast gating originates from the selectivity filter or the inner gate finds ambiguous answers in the literature. It seems that both gates are capable of fast and slow gating. Some papers assign the fast gating to the inner gate and slower processes to the selectivity filter (Kir2.1: Lu et al., 2001a; 2001b; Xie et al., 2004; Yeh et al., 2005; Fujiwara and Kubo, 2006; GIRK: Yi et al., 2001; KcsA: Cordero-Morales et al., 2006a; 2006b). In other papers, it is just the other way round (Kir 6.2: Trapp et al., 1998; Proks et al., 2001; Proks et al., 2005; MthK: Li et al. ; 2007 ; *Shaker*: Zheng et al., 2001). This discrepancy may be resolved by findings of Xie et al. (2004) indicating that in Kir2.1 fast gating can be mediated by either gate, depending on whether mutations are located near the GYG motif or in the cytosolic ring. In MaxiK channels, the relationship between slow gating and the inner gate was revealed in mutants with modified length of the linker between the inner gate and the cytosolic gating ring (Niu et al., 2004).

Whereas the studies mentioned above have demonstrated that altering the channel's backbone changes the gating behaviour, e.g., by disruption of salt bridges in the P-loop of IRK1 mutants, (Yang et al., 1997), here an interaction between the ionic milieu and the protein is postulated. This is in line with many observations in earlier papers. Almers and Armstrong (1980) have observed in squid axons "that a K^+ channel is normally occupied by one or more small cations, and becomes non-functional when these cations are removed". This so-called "foot-in-the-door-effect" (Yeh and Armstrong, 1978) or "modulation of gating by a site inside the pore" (Matteson and Swenson, 1986) has been verified by a plethora of papers up to now in different kinds of channel, e.g., K^+ channel in squid: Swenson and Armstrong (1981); delayed rectifier: Spruce et al. (1989); MaxiK: Demo and Yellen (1992); *Shaker*: Melishchuk et al. (1998); KcsA: LeMasurier et al. (2001); *Shaker* and *Shab*: Ambriz-Rivas et al. (2005); Kv2.1: Immke et al. (1999); Wood and Korn (2000); Kv1.5: Wang et al. (2000). Constriction of the filter is indicated by the conduction of Na^+ in the absence of K^+ (Immke et al., 1999).

Searching for a mechanism mediating the influence of the ionic milieu on filter stability, it is tempting to assume a mechanism related to the collapse of the selectivity filter found in KcsA channels crystallized at very low K^+ concentrations (3 mM, Zhou et al., 2001b). This structure with flipped backbone carbonyl groups is similar to that predicted in molecular dynamics simulations of V127T mutations of Kir6.2 (Capener et al., 2003). Bernèche and Roux (2005) found in free energy molecular dynamics simulations of the filter of KcsA that the occupation of the S2 position by a K^+ ion is important for preventing the 180°-turn of a single V76-G77 amide plane followed by reorientation of T75 - V76. Relaxation from this stable non-conducting state of broken symmetry is expected to be in the range of 0.1 ms, far too slow for the events observed

here. It may be tempting to assign the fast flickering at positive membrane potentials to the reversible reorientation of the V76-G77 amide plane. However, further experimental work is required to prove whether this or other mechanisms are the origin of the fast flickering. A snapshot of the postulated induction of flickering in dependence on ion concentration seems to have been found in KcsA crystals grown in Tl^+ solutions around a midpoint concentration of 80 mM. The selectivity filter is poorly defined in these structures, but ion occupancy measurements show that about half the channels in the crystal are in the conductive and half in the collapsed state (Zhou and MacKinnon, 2003). However, up to now, structural data from the filter in K^+ concentrations in the critical range between 3 and 200 mM are not yet available, in contrast to ion distributions (Morais-Cabral et al., 2001).

The ion-induced structural rearrangements (Capener et al., 2003) related to fast gating of the selectivity filter seem to be different from those of slow C-inactivation. In contrast to C-inactivation, there is no obvious relationship between flickering and selectivity as shown in molecular dynamics calculations (Khalili-Araghi et al., 2006) and in physiological studies on mutants of the GYG motif.

For the data presented here, the above considerations would imply that k_{OC} and k_{CO} in Fig. 6.5A are the inverse dwell-times in the conducting and in the collapsed state, respectively. Fast flickering as a consequence of a disturbed ionic milieu in the filter of MaxiK channels was also suggested by Piskorowski and Aldrich (2006) in the presence of Tl^+. Similar results are described in chapter 7. In the presence of luminal Tl^+, a negative slope occurred also at negative potentials. In chapter 7 (Schroeder and Hansen, 2008), these results are interpreted in terms of a gating mechanism induced by K^+ depletion on the luminal side which is enhanced by the interaction of Tl^+ with the filter. Nevertheless, Ambriz-Rivas et al. (2005) pointed out that different K^+ channels may behave differently with respect to K^+ depletion and presence of Na^+.

There are still open questions like that of irreversibility. Almers and Armstrong (1980) found that the depletion of ions caused irreversible loss of conductivity. It may be imagined that, once K^+ is excluded from the filter, the collapsed structure prevents re-entering and opening. Two aspects of the model in Fig. 6.8 may prevent this. Firstly, the hypothesis neglected above may gain importance, namely, that the sensor for K^+ depletion is not in the filter, but in the cavity. It may control the exit of ions from the filter and thus prevent the collapse, but also the transport. Such an imprisoning of the ion under depletion may provide an explanation for the findings of Baukrowitz and Yellen (1996) that the exit rate of the last ion from the K^+ channel was 100 times lower than the normal transfer rate. Alternatively, the final collapse of the filter may be related to structural rearrangements with time constants longer that those of flickering. Then flickering would prevent that the average ion concentrations in the cavity and in the filter would fall below a critical value. Furthermore, the above model may lead to the question of whether this flickering does also occur when bundle crossing prevents the delivery of ions from the cytosol. Answering these questions is still beyond the scope of present experimental approaches.

6.4.4. Assumption 2: voltage-independent rate limitation

As mentioned above, rate limitation by k_{PS} in Fig. 6.8 may have two components: 1. Exchange of the water shell for the channel environment and 2. Diffusion limitation. Even though the channel mimics the water shell quite well, the transition is probably not absolutely smooth, and thus may create a rate-limiting energy barrier.

One component of diffusion limitation arises from the capture radius at the entrance of the channel. In gramicidin channels, this was found to be more important for rate limitation than dehydration (Andersen and Feldberg, 1996). Surface charges as occurring in K^+ channels can enrich the ions near the channel entrance (Green and Andersen, 1991) and thus weaken diffusion limitation. Indeed, channels with high conductance carry negative charges at the cytosolic end of the inner helix (Kcv: Tayefeh et al., 2007), and these charges clearly determine the saturation current (MaxiK: Brelidze et al., 2003; MaxiK, MthK : Nimigean et al., 2003). They are absent in low-conductance channels like Kir2.1 (Durell and Guy, 2001). Nevertheless, also here the negative charges in the more distant hanging gondola contribute to the enhancement of current (Xie et al., 2004; Yeh et al., 2005; Fujiwara and Kubo, 2006). Diffusion limitation at the luminal side seems to be less severe (but see chapter 7). Nevertheless, neutralizing the luminal negative charges in a mutant of Kir2.1 (Alagem et al., 2001; Murata et al., 2002) decreases inward current.

A more direct approach to the effect of diffusion limitation seems to be provided by experiments with sugars on the cytosolic side (Brelidze and Magleby, 2005). Sugars putatively hinder diffusion and result in a decrease of outward saturation current of MaxiK channels as would be predicted by the model in Fig. 6.8. However, in the data of Brelidze and Magleby (2005) there are no signs of stronger flickering. Preliminary experiments in a student's course (data not shown) have revealed that the voltage-dependence of the factor R in Fig. 6.6 was not influenced when 400 mM sucrose decreased the saturation current.

These experiments seem to be in contradiction to the predictions of the model in Fig. 6.8. Even though the model explains the effect of different cytosolic K^+ concentrations (Fig. 6.6) quite well, the necessity to incorporate additional effects, e.g., direct interaction of sugar and channel structure cannot be denied. Roux (2006) commenting on the results of Ahern et al. (2006) stated that the discrepancy between physiological findings and molecular dynamics simulations on one side and structural data on the other side in the case of TEA binding from the external side may be "the tip of a large iceberg of surprises and misconceptions" about the structure of the pore. Thus, apparently inconsistent results should be interpreted with care as long as more precise results are not available.

In the chapter 7 (Schroeder and Hansen, 2008), the hypothesis gains more weight, that rate-limiting step is given by the hopping of the ion into the sites of the selectivity filter. This mechanism may by less sensitive to diffusion limitation by sugar.

6.5. Appendix: A quantitative model describing the putative influence of ion concentration in S (cavity/filter) on fast gating

With the basic assumptions supported by the arguments above, the four-compartment model of Fig. 6.8 is employed for a quantitative model of fast gating at higher positive voltages. The compartments are the cytoplasm (index P) and the lumen (index L), both representing the bulk phases on each side of the channel, and two intermediate compartments (indices S and E). E is the external vestibule of the channel, and S is called the sensing compartment, because the stability of the protein (and thus the rate constants of flickering) depends on the ion concentration in this compartment as described in the Discussion (section 6.4.3). In our calculations, this sensing compartment (S in Fig. 6.8) can be the cavity and/or the selectivity filter.

In a simple model, with voltage-independent loading (k_{PS}, k_{LE}) (section 6.4.4) and discharge reactions (k_{SP}, k_{EL}) on either side and voltage-sensitive translocation through the selectivity filter (k_{SE}, k_{ES}), the current is

$$I_{true} = F \frac{k_{PS} k_{SE} k_{EL} [K^+]_P - k_{LE} k_{ES} k_{SP} [K^+]_L}{k_{SE} k_{EL} + k_{SP} k_{EL} + k_{SP} k_{ES}} \qquad (6.6)$$

with F being the Faraday constant. At extreme voltages, the currents saturate and take the constant values

$$I_{sat+} = I_{true} (V \rightarrow +\infty) = F \kappa_{oi} = F k_{PS} [K^+]_P \qquad (6.7)$$

$$I_{sat-} = I_{true} (V \rightarrow -\infty) = -F \kappa_{io} = -F k_{LE} [K^+]_L \qquad (6.8)$$

with κ_{io} and κ_{oi} being the voltage-independent loading reactions of Eq. (6.3) (Hansen et al., 1981; Hansen, 1986) and k_{PS} and k_{LE} the loading rate constants for $[K^+]_{P,L} = 1$ mM.

The ion concentration in the sensing compartment during the open state of the filter can be calculated from the balance of influx from the cytosol (k_{PS}) and efflux to the lumen (k_{SL}). Because of the low capacity of S (maximum 3 ions in the filter, 1 in the cavity, Zhou and MacKinnon, 2003; Compoint et al., 2004) and the resulting very fast equilibration, steady-state conditions can be assumed leading to

$$[K^+]_S = \frac{k_{PS} [K^+]_P + k_{LS} [K^+]_L}{k_{SP} + k_{SL}} \qquad (6.9)$$

with k_{SE}, k_{EL} being represented by the gross reaction k_{SL}. At high positive voltages, backflow from the lumen can be ignored, and $k_{SE} \gg$ *all others*. This results in the approximation (see also Eq. (7.9))

$$[K^+]_S = \frac{k_{PS} [K^+]_P}{k_{SL}} = \frac{k_{PS} [K^+]_P}{k_{SE}} \qquad (6.10)$$

It has to be mentioned that ion concentration means average dwell-time of ions in S. During the closed time of the filter, equilibrating with the cytosol leads to a recovery of the concentration in S. At high positive potentials, outward current is determined by the entry reaction from the cytosol into the Eq. (6.7). However, in contrast to the constant current, the concentration $[K^+]_S$ decreases with increasing k_{SE} in the numerator of Eq. (6.10). This leads to flickering according to the findings of crystal structure analysis (Zhou et al., 2001b; Zhou and MacKinnon, 2003) and molecular dynamics simulations (Compoint et al., 2004). The presence of ions in S is required for structural stability probably in order to compensate electrostatic forces (Zhou and MacKinnon, 2003). The role of K^+ for stabilizing the tetrameric filter structure became also obvious from the demand of permeant ions for protecting the oligomer of Kcv from dissociation upon heating (Pagliuca et al., 2007).

In order to set up a quantitative description of the effect on gating behavior we have to make two assumptions:
1. For the voltage-dependence of k_{SL} we assume that the ions have to jump over at least one energy barrier (in the selectivity filter) resulting in

$$k_{SL} = k_{SL,0} \exp\left(\frac{V}{V_G}\right) \qquad (6.11)$$

2. For the relationship between gating and $[K^+]_S$, a very simple approach is chosen:

$$k_{OC} = k_{OC,1}[K^+]_S^{-1} \qquad (6.12)$$

implying that the open-close transitions become faster with decreasing $[K^+]_S$. This probably is an oversimplification. However, considering alternative approaches including averaging over closed and open times of the filter showed that already this simple version can create an understanding of the basic processes. A higher sophistication would become detached from the available experimental background.

Fig. 6.5A indicates that k_{CO} is not significantly dependent on membrane potential (or concentration in S of Fig. 6.8). This implies that the relaxation from the closed state is quite independent of the distorting parameter (compare Fig. 6.5). When the rate constants of gating k_{CO} and k_{OC} are faster than the filter frequency, the apparent current is proportional to the open probability:

$$I_{app} = \frac{k_{CO}}{k_{CO} + k_{OC}} I_{true} \qquad (6.13)$$

Inserting Eqs. (6.12), (6.10), and (6.11) into Eq. (6.13) leads to

$$\frac{I_{app}}{I_{true}} = \frac{k_{PS}[K^+]_P k_{CO}}{k_{SL,0} \exp\left(\dfrac{V}{V_G}\right) k_{OC,1} + k_{PS}[K^+]_P k_{CO}} \qquad (6.14)$$

with $k_{SL,0}$ being k_{SL} at 0 mV. Equation (6.14) is a Boltzmann-type equation. The inverse relationship can be fitted by an exponential

$$R := \frac{I_{true}}{I_{app}} = 1 + R_k \exp\left(\frac{V}{V_G}\right) \quad \text{with} \quad R_K = \frac{k_{OC,1}k_{SL,0}}{k_{CO}k_{PS}[K^+]_P} \qquad (6.15)$$

6.6. Conclusion

The crucial assumption of the model in Fig. 6.8 that ion depletion in the selectivity filter causes flickering explains the data of the present investigation quite convincingly and in addition is supported by many observations dealing with the effect of the permeant ion on gating and filter stability. However, in experiments which artificially establish rate limitation on the cytosolic side by high sugar concentrations, flickering is not modified. This indicates that the model in the section 6.5 is still an oversimplification (for the sake of analytical tractability) and additional effects have to be incorporated like direct action of potential and solutes on the filter structure. Nevertheless, it yields a stimulus to

reconsider many experimental findings, e.g., those dealing with binding sites near or inside the filter. Eliminating an effect by a mutation does not necessarily mean that a binding site has been eliminated. Instead, it has to be taken into account that a protein is a quivering mechanical device. Mutations at one place may change the geometrical conditions for ion-filter interaction along the whole filter length and modify ion/filter interaction at a quite distant location.

7. Fast gating related to luminal Tl$^+$

(The content of this section was submitted as Schroeder and Hansen, 2007)

Summary. Ion depletion (chapter 6) is one way to probe ion-pore interactions. Changing the permeant ion or using ion mixtures is another approach that is used here: Currents from single MaxiK channels were recorded in asymmetrical solutions containing 150 mM K$^+$ on one side of the membrane and a K$^+$/Tl$^+$ mixture with [K$^+$] + [Tl$^+$] = 150 mM on the other side. Outward current in the presence of cytosolic Tl$^+$ did not show a gating behavior which was significantly different from that in the absence of Tl$^+$. With luminal Tl$^+$ at negative membrane potentials below -40 mV, the single-channel IV curve showed a negative slope resistance concomitantly with a flickery block, resulting in an artificially reduced apparent single-channel current. Again, analysis by beta distributions enabled the estimation of the true single-channel current and the rate constants of the simple 2-state O-C Markov model for the gating in the bursts. The voltage dependence of the gating ratio $R = I_{true}/I_{app} = (k_{CO}+k_{OC})/k_{CO}$ again could be described by exponential functions. But here the characteristic voltage V_G was found to depend on the Tl$^+$ concentration. The true single-channel current decreased with Tl$^+$ concentrations up to 50 mM and stayed constant thereafter. This concentration dependence (Fig. 7.7A) was very similar to that of V_G. Different models are considered. The most likely one employs two sites of action: The exponential increase of the gating ratio is caused by ion depletion at the luminal side of the selectivity filter. The characteristic voltage of these exponential functions and of the value of I_{true} were dependent on Tl$^+$ concentration. This was assumed to be mediated by Tl$^+$/protein interaction at the inner side of the selectivity filter or in the cavity.

7.1. Introduction

The findings in the previous chapter (Schroeder and Hansen, 2007) show that the fast gating of the selectivity filter can yield information about the rigidity of the selectivity filter and its interaction with the permeant ion. It is shown that potassium depletion caused by cytosolic diffusion limitation leads to fast flickering. A possible candidate for the underlying structural changes in the selectivity filter is the metastable reorientation of the G-V plane when the S2 site is empty (Berneche and Roux, 2005)

Another approach to the relationship between ionic milieu and stability of the selectivity filter may be provided by the flickering currents (often indicated by negative slopes in the IV curves) observed in the presence of a second monovalent cation besides K$^+$, like e.g., Na$^+$ (Kawahara et al., 1990; Weise and Gradmann, 2000; Nimigean and Miller, 2002), Cs$^+$ (Klieber and Gradmann, 1993; Draber and Hansen, 1994) or Tl$^+$ (Blatz and Magleby, 1984; Farokhi et al., 2000; Ilan and Goldstein, 2001). In the case of Tl$^+$, Piskorowski and Aldrich (2006) revealed features which are similar to those described by Schroeder and Hansen (2007): 1. The locus of interaction is in the pore since flickering in single-channel records of MaxiK channels is induced when voltage drags Tl$^+$ into the channel. 2. Flickering results from a destabilization of the open-state. The authors argue that Tl$^+$ is less effective than K$^+$ in stabilizing the open state as indicated by the observations of Zhou and MacKinnon (2003) that only 20 mM K$^+$ are required to keep crystal structure of the channel in the open state, but 80 mM in the case

of Tl^+. Results similar to those from MaxiK were also obtained from Kir2.1 channels (Lu et al., 2001b).

Here, it is shown, that the picture becomes further refined when the analysis of Tl^+-induced fast flickering is done with the high temporal resolution provided by the analysis of amplitude histograms by means of beta distributions.

7.2. Materials and Methods

Measurements and data analysis were done along the protocols as described in chapters 3 and 6. Four different mixtures of $TlNO_3$ and KNO_3 were used in this chapter with $[TlNO_3] + [KNO_3] = 150$ mM. Because TlCl is virtually insoluble in water, nitrate salts had to be used. In all experiments, there was 150 mM KNO_3 on at least one side (pipette or bath), as given in the figure legends.

Table 7.1. K^+/Tl^+- mixtures used in this chapter. All solutions further contained 2.5 mM $Ca(NO_3)_2$ plus 2.5 mM $Mg(NO_3)_2$ and 10 mM HEPES; pH was 7.2.

$TlNO_3$ in mM	KNO_3 in mM
0	150
25	125
50	100
150	0

7.3. Results

7.3.1. Finding a definition of I_{app} being appropriate for model testing

The definitions of states, apparent and true single-channel current have been given in section 4.1.1. Briefly, the true single-channel current is the average current in a time interval during which the stochastic function of ion transition does not change. The apparent current I_{app} is the current average over a time interval in a filtered experimental record which can include several unresolved gating events and therefore changes in I_{true}.

This basic definition of I_{app} worked well for the potassium data in the previous chapter. But in the case of luminal Tl^+, the gating characteristics made things more difficult. This is illustrated in Fig. 7.1. The apparent single-channel current I_{app} as obtained by fit-by-eye (horizontal lines in Fig. 7.1A,B, Riessner et al., 2002) or from the evaluation of the amplitude histograms (vertical lines in Fig. 7.1C,D) depends strongly on the integration time of the anti-aliasing filter of the recording set-up. In Fig. 7.1, different integration times are mimicked by the length of an offline moving average filter.

Four different definitions for the single-channel current have to be distinguished. Two of them are shown in Fig. 7.1: $I_{app,1}$ and $I_{app,n}$ which are obtained by a fit-by-eye (Riessner et al., 2002) as described in section 4.1.2 from the patch clamp time series filtered by the inherent anti-aliasing filter without offline averaging ($n = 1$, Fig. 7.1A) and with moving averaging over n data points (Fig. 7.1B), respectively. In addition, there are the asymptotic value $I_{app,\infty}$ which is obtained with a moving average filter of sufficient length (if the burst length is long enough) and I_{true} as defined in section 4.1.1

(Hansen et al., 2003; Schroeder and Hansen, 2007) which can be measured directly only when gating is much slower than the corner frequency of the anti-aliasing filter.
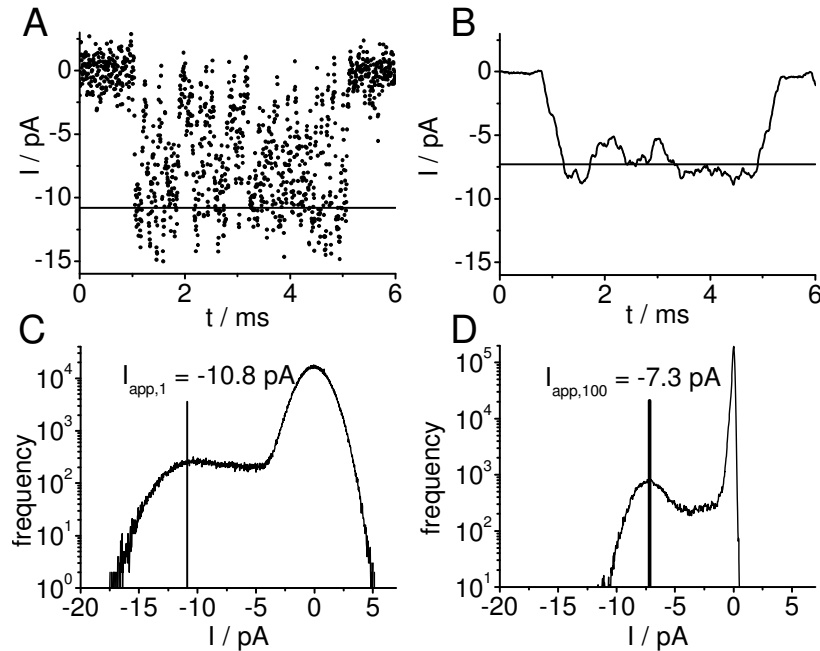
Fig. 7.1. The effect of filtering on the apparent single-channel current. (A,C) No moving average filter (= raw data). (B,D) The same data with moving average filter over 100 data points separated by 5 µs. (A,B) The horizontal lines present I_{app} as obtained by fit-by-eye (Riessner et al., 2002). (C,D) The vertical lines present I_{app} as obtained from the maxima of the amplitude histograms of the time series above them. Time series were recorded at -120 mV with 50 mM Tl$^+$ + 100 mM K$^+$ in the pipette (luminal) and 150 mM K$^+$ in the bathing medium (cytosolic).
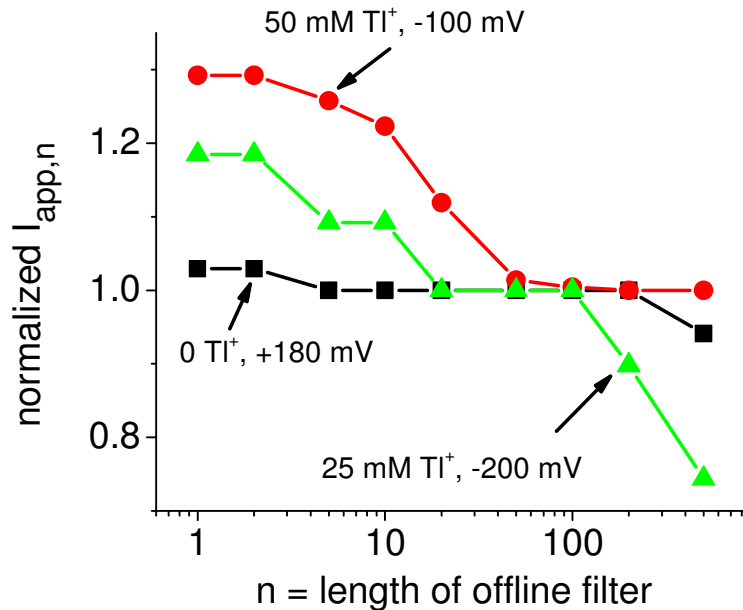
Fig. 7.2. Dependence of $I_{app,n}$ on the number n of data points included in offline averaging. Results from three representative time series are shown.

In Fig. 7.2, the dependence of $I_{app,n}$ on n, the number of data points used in the moving average filter, is shown for three time series with different gating properties. The graphs start at $I_{app,1}$. It has to be mentioned that $I_{app\ 1}$ is not I_{true}. I_{true} has to be evaluated by beta fits as described in section 5.3 (Schroeder and Hansen, 2006) and as done below. The left-hand plateau does not assign a peculiar role to $I_{app,1}$, because it is nothing more than an artifact resulting from the fact that the distance between the sampling points is 5 µs and the time constant of the inherent anti-aliasing filter of 50 kHz is 20 µs.

With increasing length n of the averaging interval, $I_{app,n}$ decreases until it reaches a plateau around $n = 50 - 200$. If the plateau is well pronounced, the current at the plateau equals $I_{app,\infty}$, because here the averaging time is already long enough to reach the asymptotic value. The plateau ends when gaps between the bursts (sojourns in long-living C-states) become included in the averaging process (green curve in Fig. 7.2). If a plateau is not found it is recommended to cut out all sojourns in closed states from the original time series and apply the averaging process to the remaining time series. This can be done manually by a cut routine in *Kiel-Patch*. In some time series (e.g., in those ones measured in 50 mM Tl$^+$), flickering is interrupted by so many sojourns into a very short closed state that cutting out of these states is nearly impossible. Then, the distributions-per-level can be generated by *Kiel-Patch* (Section 5.1 and Schröder et al., 2004), and $I_{app,\infty}$ is obtained from the expectance of the current.

In the case of the data from solutions with K$^+$ as the sole monovalent cation (black curve in Fig. 7.2), the difference between $I_{app,1}$ and $I_{app,\infty}$ is only 3%. This results from the high rate constants at high positive voltages making this kind of gating so fast (closed times less than 1 µs, Fig. 6.5 and Schroeder and Hansen, 2007) that the integration time of 20 µs of the inherent anti-aliasing filter is already long enough to reach $I_{app,\infty}$ without additional offline filtering.

However, Tl$^+$-induced gating at negative voltages is slower. The curves in Fig. 7.2 make obvious that now the problem arises of which value of the curves is to be used to represent the apparent current. This becomes of crucial importance when measured data are to be compared which the predictions of a putative model of the underlying molecular mechanism.

Here, it is recommended to use the value of the current of the plateau in Fig. 7.2. Of course, by means of a convolution of I_{true}, the anti-aliasing filter and the averaging process, the model could provide $I_{app,n}$ for each value of n. However, extracting the gating behavior from a putative molecular model of the channel already is complicated enough. Thus, it would not be wise to introduce further complications by involving convolution integrals. This caveat holds for $I_{app,n}$ (including $n = 1$) unless n reaches the plateau in Fig. 7.2. The value of $I_{app,\infty}$ as obtained from the plateau should be equal to $I_{app,k}$ which can easily be calculated from the model parameters by means of Eq. (7.2), below.

7.3.2. Negative slopes and Tl$^+$-induced gating

Recordings obtained at -100 mV for four different concentrations of luminal Tl$^+$ are shown in Fig. 7.3. At constant membrane potential, an increase in Tl$^+$ concentration causes an increase in open-channel noise and a decrease in apparent single-channel current. The analysis here deals only with the bursts.
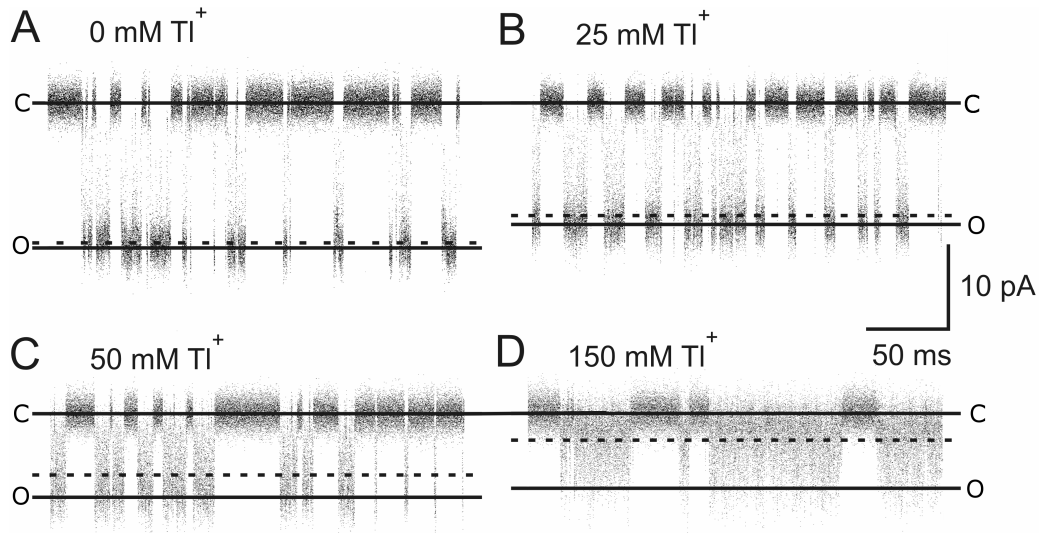
Fig. 7.3. Sections of four current records with different K^+/Tl^+ mixtures on the luminal side (pipette). $[Tl^+]$ is given at the traces with $[K^+] = 150$ mM $- [Tl^+]$. Cytosolic solution contained 150 mM K^+. Membrane potential was -100 mV for all records. Channel openings result in downward deflections. With increasing Tl^+ concentration, the open-channel noise increases, and the apparent current decreases, indicating the increase of unresolved gating events. The upper horizontal lines give the base line (closed channel). The dotted lines show the apparent current $I_{app,\infty}$ taken from a plateau like those in in Fig. 7.2. $I_{app,1}$ obtained from fit-by-eye is presented by solid horizontal lines.

From records like those in Fig. 7.3, IV curves of $I_{app,\infty}$ were evaluated. In most cases, a moving average over 100 data points resulted in the asymptotic value $I_{app,\infty}$ as indicated by the plateaus in Fig. 7.2, but in the case of some data obtained at 50 mM Tl^+ the expectance of the distribution-per-level had to be used instead. In the time series measured at 25 mM Tl^+, the sojourns into the additional closed state interrupting the bursts were long enough to be excluded. At 150 mM Tl^+, they were so short and rare that they did not spoil the determination of the bursts. However, in the 50 mM data, they were so often and so short that the Hinkley detector of *Kiel-Patch* did a more reliable job than the human eye.

The resulting IV curves are shown in Fig. 7.4A. At positive membrane potentials where current is solely carried by K^+, all curves show the same negative slope as the K^+ data do (compare section 6.3 and Schroeder and Hansen, 2007); Tl^+ does not seem to have any significant effect. However, at negative voltages, when Tl^+ is drawn from the lumen into the pore, a second negative slope is induced. The effect obviously increases with increasing Tl^+ concentration in the mixed solution. Similar to the negative slope on the positive side, the involvement of unresolved gating becomes obvious from the appearance of flickery current traces (Fig. 7.3).

The true single-channel current was obtained from the analysis of beta distributions as described in section 5.3. The IV curves of the true single-channel current in Fig. 7.4B show strong saturation at positive and weak saturation at negative membrane potentials. In the previous chapter, the IV curves obtained from pure K^+ solution were fitted with a Class I model (Hansen et al., 1981). However, the related type of equation applies to many mechanisms and thus does not carry a very important message. Nevertheless, there is one interesting feature in Fig. 7.4B: the negative true single-channel current I_{true} in the presence of luminal Tl^+ is smaller than that in pure K^+ solution.

Fig. 7.4. (A) Apparent ($I_{app,100}$) and (B) true single-channel current/voltage relationships (IV curves) of MaxiK with different luminal K^+/Tl^+-mixtures (pipette). The Tl^+ concentrations are attached to the curves in (A) with $[Tl^+] + [K^+] = 150$ mM. (C). Apparent IV curves obtained with cytosolic K^+/Tl^+ mixtures (bath). Besides in the region of the negative slope at positive potentials, I_{app} and I_{true} are identical.

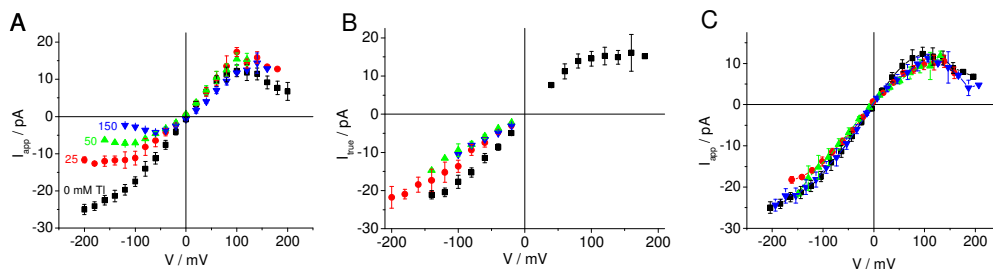Fig. 7.4C shows IV curves obtained with Tl^+ on the cytosolic side and K^+ as the only monovalent cation on the luminal side. At positive potentials, there is no extra fast gating with respect to the curve obtained without Tl^+. The negative slope starts even a little bit later. This may be related to the somewhat smaller conductivity in the presence of Tl^+ which was also observed in Fig. 7.4A. The absence of a dramatic effect of cytosolic Tl^+ is in contrast to the findings of Piskorowski and Aldrich (2006), of LeMasurier et al. (2001) and to our own results obtained from dwell-time analysis (chapter 8). This difference results from the clear separation of fast and slow gating effects by means of the high temporal resolution employed here. Since Fig. 7.4C does not yield new information with respect to the findings already found in chapter 6 (Schroeder and Hansen, 2007) for solutions without Tl^+, the following analysis only deals with the data in Fig. 7.4A and B obtained in the presence of luminal Tl^+.

The beta fit of the time series in Fig. 7.3 also delivers the rate constants of the 2-state O-C model causing the gating in the bursts.

In the presence of luminal Tl^+, a biphasic dependence of the rate constants on Tl^+ concentration is found. k_{OC} (Fig. 7.5A) increases up to 50 mM Tl^+, i.e., the open state becomes less stable. Then, k_{OC} is constant above 50 mM Tl^+. The opposite trend is found in k_{CO} (Fig. 7.5B). It is relatively constant at concentrations below 50 mM Tl^+ and decreases strongly above 50 mM.

In Fig. 7.5A and B, rate constants are also shown for the Tl^+-free solution. In Schroeder and Hansen (2007), fast gating at negative potentials was ignored. However, the open-level distributions were slightly broader than those of the closed state, indicating the existence of a marginal current reduction by fast gating (data not shown).

The analysis by beta distributions is quite reliable in determining the ratio R_k (Eq. (7.3)), but may have problems to estimate the absolute values of the rate constants. Thus, it was checked whether the opposite trends in Fig. 7.5A,B may result from fitting artifacts. In Fig. 7.5C and D, k_{OC} and k_{CO} were multiplied by a common factor. This procedure has no effect on the ratio R_k (Eq.(7.2)). At 150 mM, the common factor had to be 4 in order to get a horizontal line between 50 mM and 150 mM Tl^+ in the k_{CO} plot (Fig. 7.5B) and a monotonously increasing line in the k_{OC} plot (Fig. 7.5A). Fig. 7.5D shows that the resulting beta distribution differs strongly from the measured one already for a factor of 2. This implies that the decay in Fig. 7.5B is not a fitting artifact. Similarly, lowering k_{CO} and k_{OC} at 50 mM Tl^+ by a factor of 3 leads to a beta distribution not representing the experimental results (Fig. 7.5C). Similarly, the absolute values at 25 mM Tl^+ must not be changed (data not shown). Thus, the tests presented by Fig. 7.5C and D verify the biphasic behavior shown in Fig. 7.5A and B.
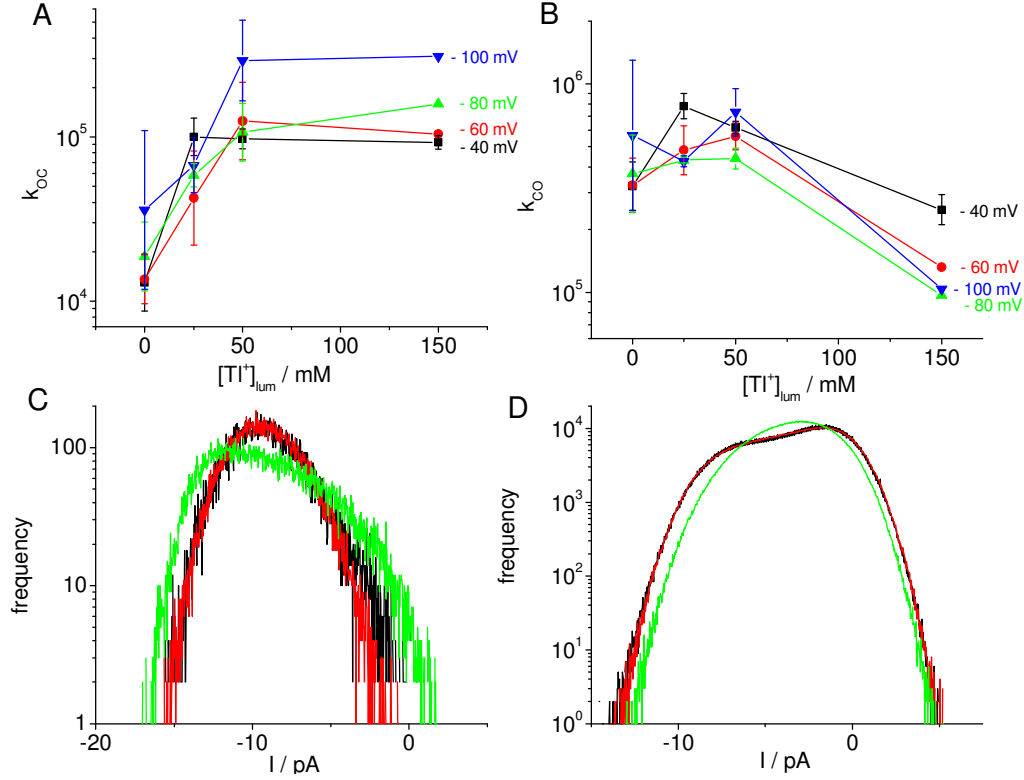
Fig. 7.5. Dependence of the rate constants (A) k_{OC} and (B) k_{CO} of a 2-state model on luminal Tl⁺ concentration at different membrane potentials as obtained from the beta distributions of the current amplitudes in the bursts. (C) and (D) present tests of whether the absolute values in (A) and B are determined correctly. The black histograms are generated from the measured time series. The coinciding red curves result from simulated time series using the rate constants in (A) and (B) with (C) 50 mM Tl⁺ at -100 mV and (D) 150 mM Tl⁺ at -80 mV. The deviating histograms (green) are obtained by multiplying the rate constants k_{CO} and k_{OC} with a common factor of (C) 0.33 and (D) 2.

From the rate constants in Fig. 7.5, $I_{app,k}$ can be calculated.

$$I_{app,k} = \frac{k_{CO}}{k_{OC} + k_{CO}} I_{true} \tag{7.1}$$

with k_{CO} and k_{OC} being the rate constants of the closed-open and open-closed transitions, respectively, of the O-C 2-state model employed for the beta fit.

This can be used for checking whether the relationship $I_{app,\infty} = I_{app,k}$ holds and for the calculation of the gating factors R_k and R_I defined as follows

$$R_k = \frac{k_{CO} + k_{OC}}{k_{CO}} \tag{7.2}$$

$$R_I = \frac{I_{true}}{I_{app,\infty}} \tag{7.3}$$

151

In Fig. 7.6, R_k as calculated by Eq. (7.2) is compared with R_I as obtained from Eq. (7.3). Both gating factors are plotted vs. membrane potential for different Tl^+ concentrations. The coincidence of R_I and R_k indicates that the relationship $I_{app,\infty} = I_{app,k}$ holds.

In the presence of Tl^+, the interesting gating occurs at negative potentials, whereas the behavior at positive potentials is not shown in Fig. 7.6 as it is not different from that in pure potassium. The voltage dependence of R_k at negative potentials in the presence of Tl^+ was fitted with an exponential function

$$R_k = 1 + R_{k,0} \exp\left(\frac{-V}{V_G}\right) \tag{7.4}$$
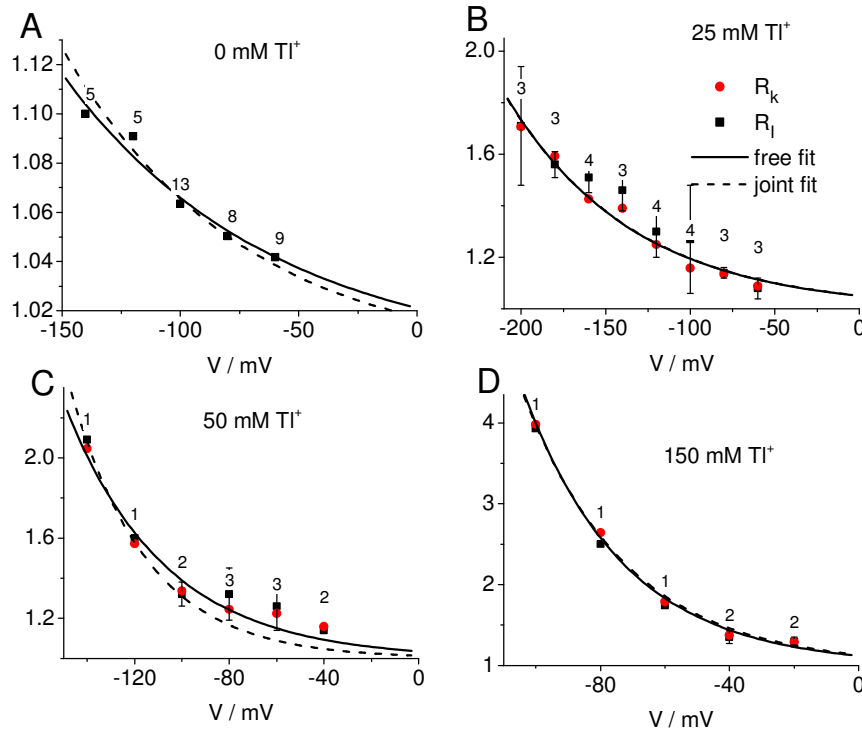
Fig. 7.6. Dependence of the gating factor R_k (black squares, Eq. (7.2)) and R_I (red circles, Eq. (7.3)) on membrane potential as calculated from the data in Fig. 7.5A,B and Fig. 7.4A,B, respectively. The flickering bursts occurring in records at 50 mM Tl^+ were very short due to sojourns in very short closed events. There, $I_{app,\infty}$ was obtained from the expectance of current from the distributions per level (Schröder et al., 2004), see section 5.1. They coincided with $I_{app,k}$ indicating the high reliability of the beta fit. The smooth lines present the free fits of R_k (Eq.(7.4)) with the parameters in Table 7.2. Errors bars represent SEM. Number of data points are given at the curves.

In order to test whether all curves in Fig. 7.6 share the same characteristic voltage (as in the case of the different potassium concentrations in Fig. 6.6), a joint fit with shared V_G and free $R_{k,0}$ was attempted. This approach failed completely (data not shown). However, it turned out, that a reasonable joint fit with common V_G is possible for the pairs 0/25 mM Tl^+ and 50/150 mM Tl^+ (dashed lines in Fig. 7.6A,B and C,D, respectively, and last columns in Table 7.2), even though the bending was somewhat too sharp for the 0- and 50-mM data. The more likely free fit resulted in quite similar V_G for 50 and 150 mM Tl^+, but in a definitely different V_G for 0 and 25 mM Tl^+ (3rd column in Table 7.2), explaining the failure of the joint fit of all concentrations. The amplitude factors $R_{k,0}$ obtained at 50 mM and 150 mM (2nd column of Table 7.2) are proportional

to the concentrations (within the scatter). This does not hold for $R_{k,0}$ obtained at 0 and 25 mM Tl$^+$. These numbers seem to indicate that different mechanisms are involved at 25 mM on one side and at 50 or 150 mM Tl$^+$ on the other side.

In Fig. 7.7, the dependence of g_{true} on Tl$^+$ concentration (Fig. 7.7A) is compared with the dependence of V_G (Fig. 7.7B). The similar saturation behavior may lead to the suggestion that both effects result from the same mechanism. Especially, the role of 50 mM Tl$^+$ becomes obvious from these curves, i.e., the amplitude factor $R_{k,0}$ changes its behavior at 50 mM (Fig. 7.7C).
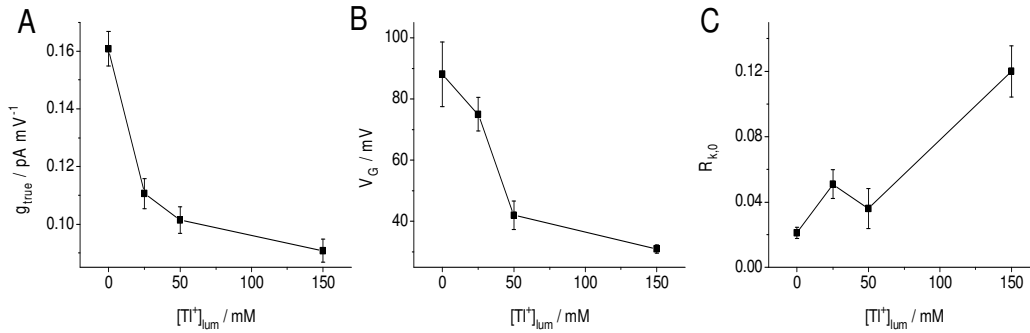
Fig. 7.7. Dependence of (A) true single-channel conductivity obtained at negative potentials in Fig. 7.4B, (B) characteristic voltage V_G (Fig. 7.6, Eq. (7.4)), and (C) amplitude factor $R_{k,0}$ (Fig. 7.6, Eq. (7.4)) on [Tl$^+$] with [Tl$^+$]+[K$^+$] = 150 mM.

Table 7.2. Parameters of Eq. (7.4) as obtained from fitting the voltage dependence of the gating factor R in Fig. 7.6. [Tl$^+$]$_{lum}$ + [K$^+$]$_{lum}$ = 150 mV.

	Free fit		Joint fit 0/25 and 50/150 mM	
	$R_{k,0}$	V_G	$R_{k,0}$	V_G
0 mM Tl$^+$	0.021 ±	88 ± 10 mV	0.017 ± 0.003	76 ± 4 mV
25 mM Tl$^+$	0.051 ±	72 ± 6 mV	0.052 ± 0.007	76 ± 4 mV
50 mM Tl$^+$	0.036 ±	42 ± 5 mV	0.014 ± 0.003	32 ± 2 mV
150 mM Tl$^+$	0.121 ±	31 ± 1 mV	0.13 ± 0.02	32 ± 2 mV

7.4. Discussion

The application of high temporal resolution led to results partly different from those of Piskorowski and Aldrich (2006) which were obtained from dwell-time analysis of time series filtered at 20 kHz. Using dwell-time analysis, we, too, found a symmetrical effect. Tl$^+$ induced a shift in the dwell-times of the open and closed state when it was dragged into the channel from the cytosolic or from the luminal side (section 8.1.1). However, the results from dwell-time analysis were in contrast to the findings for fast gating in Fig. 7.4 where Tl$^+$-induced gating occurred only when Tl$^+$ entered from the luminal side. The discussion here is restricted to the fast gating events which seem to be the most promising candidate for providing an access to the mechanistic background of ion-channel interaction.

Nevertheless, in spite of the different temporal range and the role of cytosolic and luminal Tl^+ concentrations, there is one peculiar similarity to the data of Piskorowski and Aldrich (2006), i.e., the role of the Tl^+ concentration around 50 mM. Piskorowski and Aldrich found that the dependence of the mean open time and the number of openings per bursts saturated around 50 mM Tl^+. Fig. 7.7A and B show that the dependencies on $[Tl^+]$ of single-channel conductance (g_{true}) and of the characteristic voltage of gating (V_G) are similar. Saturation for both curves starts at about 50 mM Tl^+. The peculiar role of mole fractions with concentrations around 50 mM Tl^+ is also found in the absolute values of the rate constants k_{OC} and k_{CO}, i.e., the Tl^+-induced change in mean open times ($1/k_{OC}$ in the range of 1 to 2.5 ms) in the experiments of Piskorowski and Aldrich (2006) ended at these concentrations. At higher concentrations, mean open times stayed constant. This corresponds to the increase of k_{OC} up to 50 mM in Fig. 7.5A and the horizontal line at higher concentrations.

Results are different with respect to the mean closed time. Whereas Piskorowski and Aldrich (2006) have found no effect on the mean closed time (about 100 µs), Fig. 7.5B shows a decrease of k_{CO} at concentrations faster than 50 mM. However, it has to be kept in mind that the rate constants given in Fig. 7.5 are by factor of at least 10 higher than the inverse time constants obtained from the dwell-time analysis of Piskorowski and Aldrich (2006).

The question arises of whether the different behavior found by Piskorowski and Aldrich are artifacts resulting from the temporal limitation of dwell-time analysis or from additional mechanisms besides those generating the fast gating reported here. This cannot be solved without the analysis of our data in terms of the full Markov model which is discussed in chapter 8.

Here, possible mechanisms of Tl^+-induced fast gating are considered which can explain the following features:

1. The exponential increase of the gating factor R_k with negative membrane potential
2. The dependence of the characteristic voltage in Eq. (7.4) on the mole fraction Tl^+/K^+.
3. The absence of these effects for cytosolic Tl^+.

In the case of fast gating found in outward currents with K^+ as the only monovalent cation, the exponential increase of the gating factor R_k was explained by K^+ depletion in the cavity or in the selectivity filter (chapter 6). This K^+ depletion was assumed to result from cytosolic diffusion limitation which becomes evident when a high outward driving force empties the cavity or sites in the selectivity filter faster than they can be refilled from the cytosol. The favored molecular mechanism which might cause this K^+ depletion-induced gating was that found by Bernèche and Roux (2005) in molecular dynamics simulations: K^+ ions in the selectivity filter are necessary to compensate the repulsive forces of the carbonyl groups of the filter. K^+ depletion in the S2 site of the selectivity filter results in reorientation of the amid group between G of GYG and the neighboring V. This metastable closed state would be converted to a more stable closed state when the V-T plane, too, reorientates. However, Schroeder and Hansen (2007) assumed that interrupting the K^+ flux through the filter by the flickering of the metastable state keeps the average K^+ concentration at a moderate value, thus preventing the full transition into the long-lived closed state (about 0.4 ms).

Transferring the hypothesis of cytosolic diffusion limitation to the data in Fig. 7.5 and Fig. 7.6 is tempting but leads to unlikely consequences as follows: It may be suggested that at negative potentials cytosolic diffusion limitation causes an enrichment of Tl^+ in the cavity. This would be in line with the findings of Lu et al. (2001b), i.e., that

interaction of Tl$^+$ with C169 in the cavity of Kir2.1 induces structural changes which lead to a flickery state and subconductance levels (which also may result from fast unresolved gating). However, an exponential increase of [Tl$^+$] in the cavity as necessary to explain the curves in Fig. 7.6 would be unlikely because of the limited capacity of the cavity (being occupied by nearly one ion all the time, Zhou and MacKinnon, 2004). If we ignore this feature, the situation becomes even worse: ion accumulation in the cavity would lead to an exponentially increasing inward current which is in contradiction to the curvature found in Fig. 7.4B which indicates saturation at high negative potentials.

Thus, voltage-driven Tl$^+$ enrichment does not provide a key for the understanding of the gating effects in Fig. 7.5 and Fig. 7.6. However, the inconsistencies of the model above may be avoided if we keep the idea that negative voltage leads to a slight accumulation of Tl$^+$ in the cavity. The exponential increase of R_k, however, has to be mediated by an additional mechanism, for instance by a direct action of voltage on the gating properties. This may be mediated by the S4 helix or by other voltage sensors. The viral channel Kvc (Kang et al., 2004) has no S4 helix but shows voltage-dependent gating and negative slopes in whole-cell currents indicating the existence of a voltage sensor (Gazzarrini et al., 2002; Gazzarrini et al., 2006). The Kcv also produces a negative slope in single-channel measurements (Shim et al., 2007). Thus, the S4 is not the only choice for mediating a direct effect of voltage on the protein. However, I dislike the hypothesis of a direct voltage action on gating because it employs unproven ad hoc assumptions not backed by the data presented here. Furthermore, it ignores the similarities of the dependence of g_{true} and V_G on [Tl$^+$] (Fig. 7.7A, B).

Furnishing a model which accounts for the apparent relationship between single-channel current and fast gating has to account for the insight that the effects in Fig. 7.6 (exponential increase of R) and in Fig. 7.7A,B (effect of Tl$^+$ concentration on V_G and I_{true}) have to be implemented by two different mechanisms (appendix 7.5). For the voltage dependence in Fig. 7.6 equations are provided for two different reaction kinetic models of ion transport through the channel which differ by the mechanism which leads to saturation of I_{true}. For the explanation of the curves in Fig. 7.7B, modulatory sites have to be considered which modify the voltage-induced gating behaviour in Fig. 7.6. Indications that the gating mechanisms considered in appendix 7.5 can be modulated by other sites, e.g., changes in backbone/filter interactions came from spontaneous changes in gating behaviour of MaxiK. A transition from a slow gating mode with $I_{app} = I_{true}$ to a fast gating mode with smaller I_{app} and back could be shown to be related to a spontaneous change in k_{OC}, i.e., in the lifetime of the open state (Table 5.4 and Schroeder and Hansen, 2006) similar to the effect of K$^+$ depletion (Schroeder and Hansen, 2007).

The first one of the two putative mechanism causing the exponential increase in R_k (Fig. 7.6) starts from the assumption of diffusion limitation on the luminal side as corresponding to the cytosolic diffusion limitation assumed by Schroeder and Hansen (2007) for gating at positive potentials. It may be argued that diffusion limitation at the sink side would limit the effect of exponential increase of the voltage-driven rate constants in the selectivity filter. Equations (7.5) and (7.6) show that it does not. Thus, a model relating fast gating to diffusion limitation on both sides is feasible. Diffusion limitation at the luminal side is less obvious and becomes apparent only when the negative charges at the pore mouth are neutralized by mutations e.g., in Kir2.1(Alagem et al., 2001; Murata et al., 2002). Nevertheless, there is a small gating effect at negative potentials in wild type MaxiK at negative potentials as shown in Fig. 7.6A. This small gating effect may be aggravated by the accumulation of Tl$^+$ in the cavity or in the selectivity filter as discussed below.

155

The second mechanism causes current saturation by the introduction of the law of transport site conservation as postulated in the Class I model of Hansen (Hansen et al., 1981; Hansen, 1986) or the single-file model of Nelson (2002). Ion depletion occurs at the outmost inner or outer ion binding site of the selectivity filter for outward or inward currents, respectively. This depletion is presented by the empty oxygen ring shown in the 1,3 or 2,4 position of Morais-Cabral et al. (2001) as shown in Fig. 7.8.
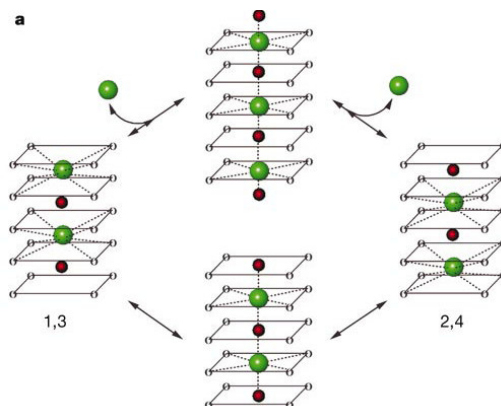
Fig. 7.8. Ion hopping in the selectivity filter of KcsA during transport (from Morais-Cabral et al., 2001).

The occupation of these sites (near the cavity for outward current or near the external vestibule for inward currents) decreases exponentially with the driving force. Similar to the model in Schroeder and Hansen (2007), we assume that the gating factor R increases with the inverse occupation of these sites.

As mentioned above, the two models in appendix 7.5 only describe the exponential increase of V_G. They do not account for the dependence of Tl^+ concentration and the similar behavior of I_{true} and V_G in Fig. 7.7A, B. This requires the assumption of additional sites of interaction. Candidates are Tl^+ binding sites at the luminal surface, the filter or the cavity. Since there is no evidence for luminal Tl^+ binding sites, selectivity filter and cavity have to be considered. It may be assumed that roughly the same mole fraction holds throughout the channel because the maximum change of I_{true} with the mole fraction is 40% (Fig. 7.7B). Thus, the Tl^+/K^+ ratio in the cavity or the filter should reflect the luminal mole fraction.

Lu et al. (2001b) found that interaction of Tl^+ with C169 in the cavity of Kir2.1 induces structural changes which lead to the flickery state and subconductance levels (which can probably be shown to be related the same mechanism if temporal resolution were high enough). Bichet et al. (2006) found an influence of the cavity ion on the chance of another ion to leave the filter, thus influencing conductivity. Thus changes in the ion concentration in the cavity can exert a parallel effect on V_G and on I_{true}.

Destabilizing of the selectivity filter by Tl^+ is even more established. Zhou and MacKinnon (2003) found that 20 mM K^+ are necessary to stabilize the open crystal structure of KcsA, whereas in the case of Tl^+ 80 mM were required. Zhou and MacKinnon found higher electron densities for Tl^+ than for K^+ in the filter sites. Furthermore, interaction of Tl^+ with the carbonyl groups in the filter destabilizes the open state and increases the unblocking rate for Ba^{2+} Lu et al. (2001b).

The last feature which has to be explained is that an effect of Tl^+ on fast gating (inducing a negative slope in I_{app}) is only observed in inward, but not in outward currents (Fig. 7.4C). Outward currents lead to ion depletion in the cavity and/or the

innermost sites of the filter. This may attenuate the difference between the ion/channel interactions of Tl^+ and K^+.

The second model in appendix 7.5 may also shed some new light on the model in section 6.5 (Schroeder and Hansen, 2007). There, one problem is mentioned, i.e., current reduction by cytosolic sugars (as suggested by the experiments of Brelidze and Magleby, 2005) did not influence fast gating in outward currents. However, if the ion depletion is caused by the second model and not solely by cytosolic diffusion limitation, then the sugar experiments need not to be a contradiction to the basic concept of the model in appendix 6.5.

The discussion of the models above shows that it is difficult to extract a unique model from the physiological data. Nevertheless, there is a clear message: The selectivity filter is a wobbly device whose stability depends on the proper ionic milieu. This implies that a great portion of flexibility is required when the *snug fit* hypothesis is employed to explain the transport mechanism of the selectivity filter. The experimental results reported here will be useful to test future molecular dynamics studies.

7.5. Appendix

If fast gating is influenced by changes in ion concentrations or by the occupation of putative sites, then the effects have to be considered which determine the current through the channel. There are two different mechanisms which alone or together can result in saturating IV curves as found in Fig. 7.4B. It has to be mentioned that rate limitation by the loading reaction is already involved when the IV curve increases linearly instead of exponentially with membrane potential. Saturation in its common meaning, i. e. a sublinear curve shape occurs only at very high negative potentials in Fig. 7.4B.

A. A linear scheme.

The same four-compartment model as in Fig. 6.8 is used: cytosol (P), cavity (S =sensing compartment), external vestibule (E), lumen. The transition $S \rightleftharpoons E$ through the selectivity filter, again, mediate the main voltage dependence.

The gross reaction constants k_{PL} and k_{LP} of transfer of one ion from one side of the membrane to the other one are proportional to the entering reactions k_{PS} or k_{LE}, respectively, since they do not occur in the denominator of Eqs. (7.5) and (7.6) (arrows from A to B represent the rate constant k_{AB}. Arrows in a row are multiplied, and the products of the rows are added, Sanders and Hansen, 1981).

$$
k_{PL} = \cfrac{\overset{P \quad S \quad E \quad L}{\longrightarrow \longrightarrow \longrightarrow}}{\begin{array}{c} \longrightarrow \longrightarrow \\ \longleftarrow \qquad \longrightarrow \\ \longleftarrow \longleftarrow \end{array}} = \frac{k_{PS}k_{CE}k_{EL}}{k_{SE}k_{EL} + k_{SP}k_{EL} + k_{ES}k_{SP}} \xrightarrow[\substack{k_{SE} \gg \text{all others}}]{V \ll 0} \approx k_{PS} \qquad (7.5)
$$

157

$$k_{LP} = \frac{\begin{array}{cccc} P & S & E & L \end{array}}{} = \frac{k_{LE}k_{ES}k_{SP}}{k_{SE}k_{EL} + k_{SP}k_{EL} + k_{ES}k_{SP}} \xrightarrow[k_{ES} \gg \text{all others}]{V \gg 0} \approx k_{LE} \qquad (7.6)$$

The voltage-dependent rate constants are marked in red. At high negative or positive voltages potentials (when k_{SE} or k_{ES} become very great), the voltage-independent loading reactions k_{PS} and k_{LE}, respectively, limit the gross reaction constant and therefore the saturation of I_{true}, although the asymptotic value is only reached at the positive side in the experiments here (Fig. 6.4 and Fig. 7.4B).

The depletion of the intermediate compartments S or E with increasing k_{SE} or k_{ES}, respectively, is obtained from the balance of influx and efflux (ignoring back flow through the filter)

$$[S] = \frac{k_{PS}}{k_{SP} + k_{SL}}[P] \qquad\qquad [E] = \frac{k_{LE}}{k_{EL} + k_{EP}}[L] \qquad (7.7)$$

The rate constants k_{SE} and k_{ES} being part of k_{SL} and k_{EP}, respectively, are voltage dependent. (s = fraction of the membrane voltage, that drops over the filter).

$$k_{ES} = k_{ES,0}\exp\left(\frac{-esV}{kT}\right) \quad \text{and} \quad k_{SE} = k_{SE,0}\exp\left(\frac{esV}{kT}\right) \qquad (7.8)$$

For the ion depletion in the intermediate compartments S or E, it is important that the exit rate constants k_{EL} or k_{SP} do not limit the exponential increase of the voltage sensitive rate constants k_{SE} or k_{ES}, respectively.

$$k_{SL} = \frac{\begin{array}{ccc} S & E & L \end{array}}{} \approx k_{SE} \quad \text{and} \quad k_{EP} = \frac{\begin{array}{ccc} P & S & E \end{array}}{} \approx k_{ES} \qquad (7.9)$$

Thus, depletion by diffusion limitation can work for either direction of the current. It may be different for outward and inward currents depending on the rate constants k_{SP} and k_{LE}, respectively.

B. Introduction of the law of site conservation for the selectivity filter

In cyclic reaction schemes like the Class I model of Hansen et al. (1981) or the single-file model of Nelson (2002), another effect causes saturation, namely the law of transport site conservation. In both models, the sum of configurations with empty sites on the luminal and cytosolic site (plus those ones with all sites occupied, Nelson, 2002) is constant, e.g., "1" in single-channel experiments. However, the ratio of open sites (ready to accept an ion) close to the external vestibule (Θ_E) to those close to the cavity (Θ_C) is

$$\frac{\Theta_E}{\Theta_C} = \exp\left(\frac{e_o sV}{kT}\right) \qquad (7.10)$$

with s being the electrical distance, e_0, k,T having their usual meaning, V membrane potential.

Since enrichment on one side cannot exceed Θ_C or $\Theta_E = 1$, the occupation at the other side has to decrease exponentially with V, i.e., Θ_C for outward currents and Θ_E for inward currents.

In terms of the scheme of site occupation (Fig. 7.8) as suggested by Morais-Cabral et al. (2001), the transport cycle for outward currents would be as follows: State 2,4 with empty outer oxygen ring sits there and waits for a K^+ ion to jump into the filter. After the jump, all three K^+ ions move in a concerted single-file action, and one K^+ ion exits at the cavity side leaving the channel in the 1,3 configuration. The 1,3 configuration is converted to the 2,4 configuration via an intermediate state with the ion and the water in the plane of the oxygen rings. At negative potentials, the ratio of the lifetime of 1,3 configuration (Θ_E) to that of the 2,4 configuration (Θ_C) is given by Eq. (7.10) (ignoring the other two states which may be adequately be included in Θ_E or Θ_C). Thus, the occupation of the outer oxygen ring by an ion decreases exponentially with negative membrane potential. This would create the behavior in Fig. 7.6 if we assume that the lifetime of the open state τ_O is proportional to the average lifetime of the occupation of the configurations with a K^+ in (or near) the outer oxygen ring. This holds for concentrations below 50 mM Tl^+

$$\frac{1}{k_{OC}} = \tau_O = c_1(\overline{[conf\,1,3]}) \qquad (7.11)$$

with $\overline{[conf\,1,3]}$ being the average lifetime of the 1,3 configuration.

Above this concentration, the lifetime of the closed state τ_C would be shortened.

$$\frac{1}{\tau_C} = k_{CO} = c_2(\overline{[conf\,1,3]})\,. \qquad (7.12)$$

8. Finding the "Great Markov Model" which includes all gating processes

Summary. The description of the complete kinetic behavior of the MaxiK channel by means of the "Great Markov Model" has not yet been achieved. This chapter reports on Tl^+-induced gating effects which would require the analysis with the full Markov model, but also on the problems of finding such a model. Dwell-time histograms reveal features in addition to those found in chapter 7 by the analysis of fast gating, namely Tl^+-induced gating effects occurring not only when Tl^+ is dragged into the pore from the luminal side but also from the cytosolic side. Direct fits of the time series (HMM fits) based on an O1-O2-C3-C4-C5 model show that mainly the O1-O2 transitions and the C3-C4 transitions are affected by Tl^+ in MaxiK, similar to the findings from *Chara*. However, the fits were done with the apparent current, thus merging the bursts and short living C-states into the apparent O-state. The results regarding the C3-C4 transitions are probably reliable. Employing the SQ fit in order to account for fast gating showed that the O-O-C-C-C model was not suitable for fitting the full amplitude histogram. An inspection of the deviations between measured and theoretical amplitude histograms led to the insight that the C and the O state had to be connected to short-living sink states causing short peaks in order to fill the gaps close to the main peaks. This led to models with separated open states like C-O-C-C-O. This came as a surprise. However, it may carry the message that channels are rattly: the open state is not really open and the closed state is not really closed, because the protein is a quivering dynamic entity. The analysis was not finished. Testing alternative models with all available data sets by SQ fits with the present state of (non)comfort of our software would take more time for data processing and computing than a normal PhD thesis can tolerate (the fit of just a single time series of 10 s keeps a 3-GHz computer busy for 1 to 3 days).

8.1. Questions requiring the knowledge of the "Great Markov Model"

8.1.1. The Tl^+-effect as found in dwell-time analysis

The analysis of fast gating in Schroeder and Hansen (2007; 2008) was based on a simple 2-state C-O model (chapters 6 and 7). The legibility of using this reduced model has been shown in section 5.3 (Schroeder and Hansen, 2006).

Using a simple 2-state model was sufficient for the analysis of the effect of ion depletion on the stability of the selectivity filter. However, a more complete analysis should also include additional gating mechanisms which may occur in the selectivity filter and/or in other locations like the inner gate. The occurrence of much slower processes is indicated in Fig. 8.1 which shows the effect of cytosolic Tl^+ on gating as obtained from dwell-time analysis. These results are very similar to those obtained by Piskorowski and Aldrich (2006).
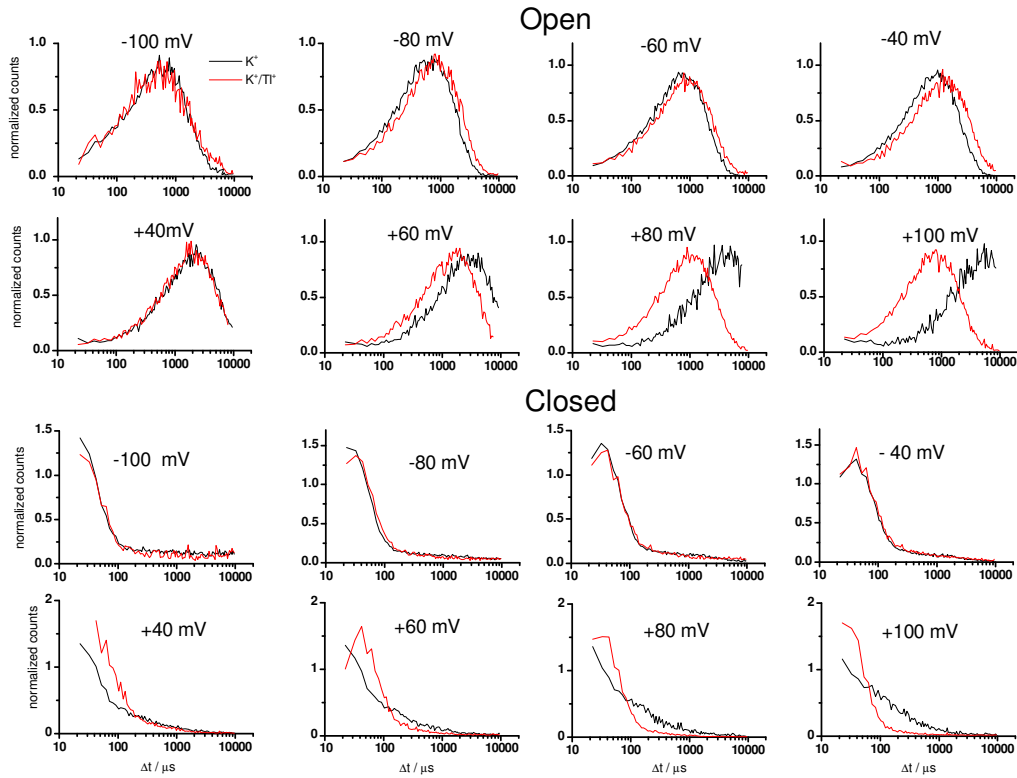
Fig. 8.1. Dwell-time histograms with 50 mM Tl$^+$ + 100 mM K$^+$ on the cytosolic side, showing that Tl$^+$ has a significant effect on gating in MaxiK only when it is dragged into the channel by the current flow (i.e., at positive voltages).

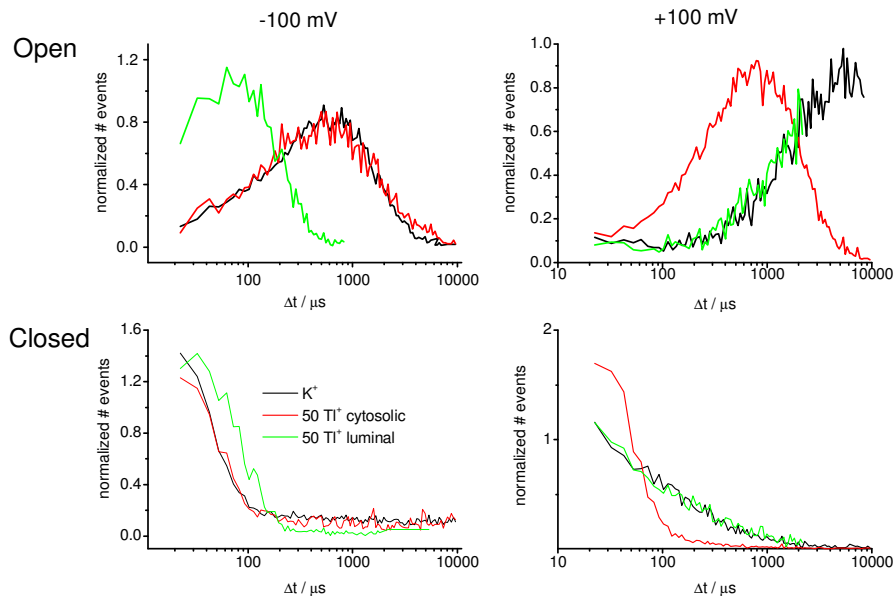**Fig. 8.2.** Dwell-time histograms for +/- 100 mV with no Tl$^+$ (black), with 50 mM Tl$^+$ + 100 mM K$^+$ on the cytosolic (red) or luminal (green) side, showing that Tl$^+$ has a significant effect on gating in MaxiK only when it is dragged into the channel by the current flow.

In Fig. 8.2, the effects of luminal and cytosolic Tl^+ are shown in one graph for dwell-time histograms obtained at -100 mV and +100 mV. This makes obvious that a Tl^+-induced effect is only observed when Tl^+ is dragged with the electric current into the channel. At a first glance, the effect of luminal Tl^+ in Fig. 8.2 is similar to that found in chapter 7, i. e. the average open dwell-time is shortened.

However, the findings of Fig. 8.1 are in contrast to the findings obtained with high temporal resolution in chapter 7 or in Schroeder and Hansen (2008). The analysis of very fast effects revealed that Tl^+ influences gating only when it comes from the luminal side (Fig. 7.4), but not from the cytosolic side. Furthermore, the rate constants of the transitions between open and closed states are much higher then the inverse time constants indicated by the peaks in Fig. 8.1 and Fig. 8.2.

Dwell-time analysis ignores fast gating in the µs range. The question arises of whether these results obtained with dwell-time analysis have to be considered to be "wrong". However, it cannot be denied that there is a message in this data, i.e., that there is slow gating which is induced by cytosolic Tl^+, an effect which is absent from Fig. 7.4 (Schroeder and Hansen, 2008).

Fig. 8.1 and Fig. 8.2 draw the attention to the existence of Tl^+-effects which are in a temporal range not included in the analysis of fast gating. Because of this, a closer inspection of this data is represented here, even though this analysis does not employ the full temporal resolution. The related problems are discussed at the end of the next section.

8.1.2. Demonstration of what kinds of effects may be revealed by the analysis with a higher-state Markov model: HMM fit

The following analysis by means of the HMM fit was started in continuation of the results of Farohki et al. (2000) obtained from the dominant K^+ channel in *Chara* in the presence of Tl^+. For the dominant K^+ channel in *Chara*, the O-O-C-C-C model works well for the analysis by means of the HMM fit (direct fit of the time series, section 4.7, Albertsen and Hansen, 1994) when applied to the AMFE in K^+/Tl^+ solutions (Farokhi et al., 2000; Hansen et al., 2003). Lühring (1999), too, using *Kiel-Patch* for dwell-time analysis in *Chara* obtained the most convincing results with the O-O-C-C-C model. However, also other models would have given similar results which could hardly be distinguished by the Likelihood of the fit (Farokhi et al., 2000).

From the present point of view, the analysis should have been done by means of the SQ fit in order to utilize its high temporal resolution (section 5.2 and Schroeder et al. 2005). However, as shown below, fitting these data by means of the SQ fit raised so many problems that the analysis was not continued. Because of this, the following results obtained with the HMM fit (section 4.7) are presented here because results of these preliminary studies indicate the existence of some interesting effects. The knowledge of what kinds of finding can be expected from a more sophisticated analysis should be preserved.

Fits were done by means of an O-O-C-C-C model. They used the apparent single-channel current (definition see section 4.1.1). The rate constants obtained in MaxiK at +100mV are shown in Fig. 8.3 and compared with those found in *Chara* (Farokhi et al., 2000).

Chara:

$250\,mM\ K^+:$
$$O1 \underset{6800}{\overset{5700}{\rightleftarrows}} \overset{0.83}{O2} \underset{69900}{\overset{14800}{\rightleftarrows}} \overset{0.16}{C3} \underset{4500}{\overset{9900}{\rightleftarrows}} \overset{0.39}{C4} \underset{20}{\overset{170}{\rightleftarrows}} \overset{(3.2)}{C5}$$
with $O1$ labeled 1.

$230\,mM\ K + 20mM\ Tl^+:$
$$O1 \underset{400}{\overset{1600}{\rightleftarrows}} \overset{4}{O2} \underset{87000}{\overset{68000}{\rightleftarrows}} \overset{3}{C3} \underset{1400}{\overset{900}{\rightleftarrows}} \overset{2}{C4} \underset{20}{\overset{400}{\rightleftarrows}} \overset{(40)}{C5}$$
with $O1$ labeled 1.

MaxiK:

$150\,mM\ K^+:$
$$O1 \underset{52000}{\overset{3400}{\rightleftarrows}} \overset{0.04}{O2} \underset{88000}{\overset{25000}{\rightleftarrows}} \overset{0.01}{C3} \underset{6900}{\overset{10700}{\rightleftarrows}} \overset{0.02}{C4} \underset{200}{\overset{400}{\rightleftarrows}} \overset{(0.06)}{C5}$$
with $O1$ labeled 1.

$100\,mM\ K + 50mM\ Tl^+:$
$$O1 \underset{46000}{\overset{14000}{\rightleftarrows}} \overset{0.35}{O2} \underset{40000}{\overset{8700}{\rightleftarrows}} \overset{0.06}{C3} \underset{3300}{\overset{1200}{\rightleftarrows}} \overset{0.02}{C4} \underset{60}{\overset{200}{\rightleftarrows}} \overset{(0.34)}{C5}$$
with $O1$ labeled 1.

Fig. 8.3. Comparison of fit results at +100mV. Average rate constants (in s^{-1}) were obtained from a HMM fit for *Chara* and MaxiK. The occupation probabilities normalized to that of O1 are shown above the state symbols. Normalizing to O1 reveals similar Tl^+-induced shifts in both types of channel, favoring O2 and C3. (Occupation probabilities of C5 are falsified by the process of cleaning the time series. This does not disturb the rest of the Markov model, Colqhoun and Hawkes, 1982).

In *Chara* and in MaxiK, the most dramatic Tl^+-induced changes were found in the transitions between O1 and O2 and between C3 and C4. Because of the high scatter of this kind of analysis (see e.g., Fig. 6.5A), it is difficult to find out which changes of the rate constants are significant. However, the ratio of rate constants and thus the occupation probabilities are more reliable. The normalized occupation probabilities are shown above the state symbols.

Normalizing occupation probabilities to O1 reveals similar Tl^+-induced shifts in both types of channel, favoring O2 and C3. The Tl^+ influence on the O1-O2 transition changes the ratio of the occupation probabilities of O2 vs. O1 by a factor of 5 (*Chara*) or 9 (MaxiK) whereas the change in the C3-C4 transitions increase the relative occupation probability of C3 by a factor of 19 (*Chara*) or 6 (MaxiK), respectively.

The voltage dependence of the four rate constants belonging to the two Tl^+-influenced transitions O1-O2 and C3-C4 is shown in Fig. 8.4 and Fig. 8.5. The influence of cytosolic Tl^+ gets significant at potentials more positive than 60mV. It becomes obvious, that mainly the rate constants k_{O1O2} and k_{C3C4} are influenced by Tl^+, whereas k_{O2O1} and k_{C4C3} are more or less unchanged. By changing these rate constants independently in simulations (data not shown), it is easy to prove that the change in k_{O1O2} is the source for the altered open dwell-time histograms (Fig. 8.4) and k_{C3C4} for the change in the closed dwell-time histograms (Fig. 8.5).

Fig. 8.4. Dependence of the rate constants of the O1-O2 transitions on membrane potential in the absence and presence of 50 mM cytosolic Tl^+ with $[K^+] + [Tl^+] = 150$ mM.
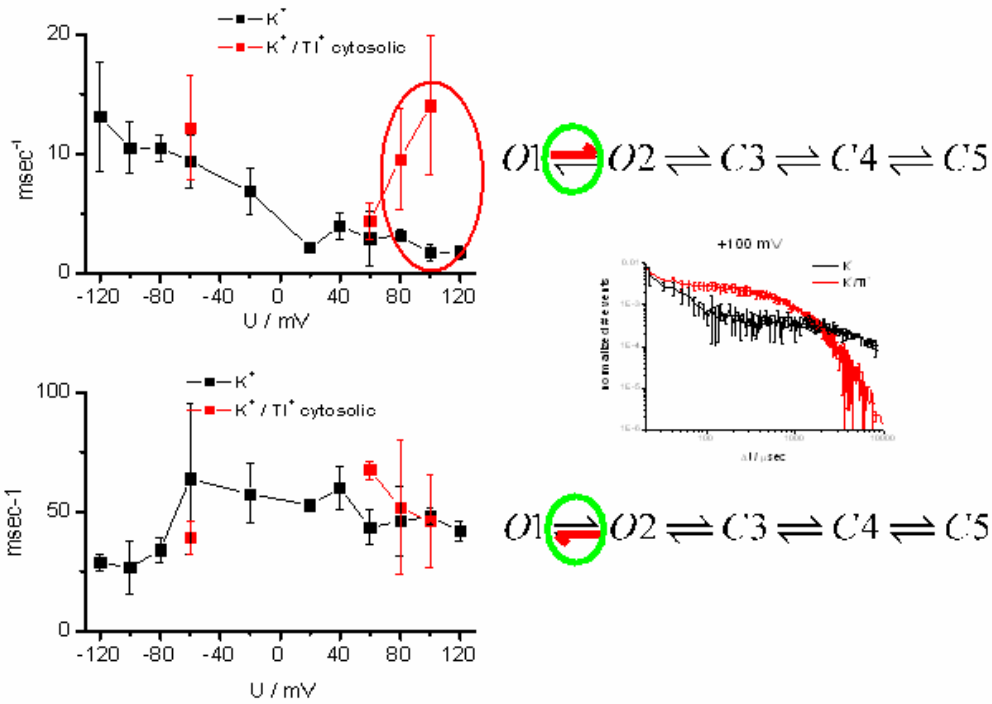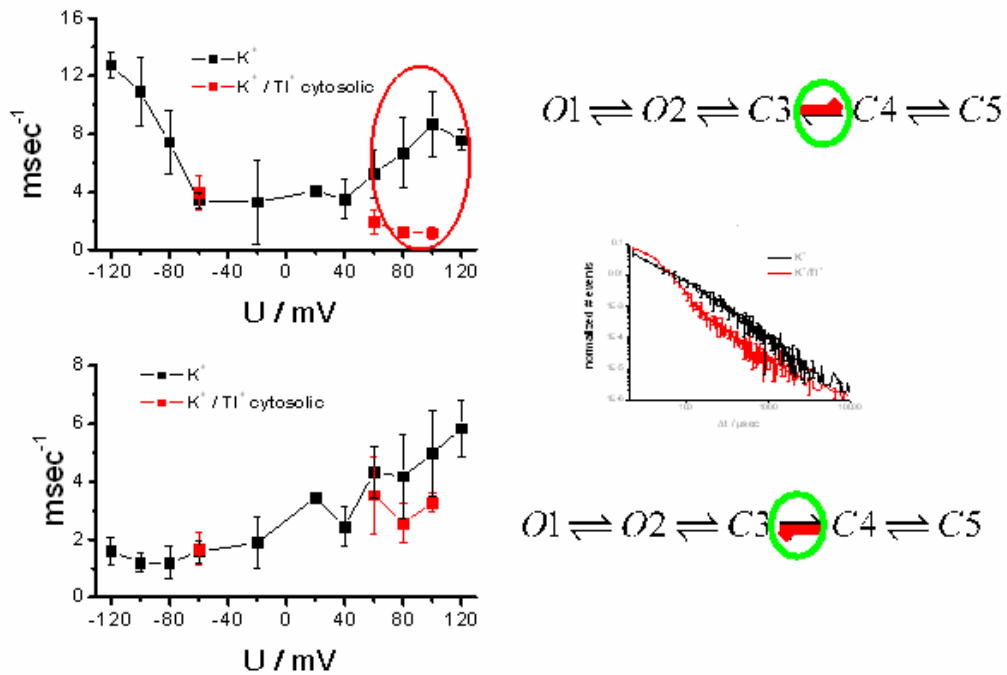

Fig. 8.5. Dependence of the rate constants of the C3-C4 transitions on membrane potential in the absence and presence of 50 mM cytosolic Tl^+ with $[K^+] + [Tl^+] = 150$ mM.

165

Measurement for luminal Tl^+ concentrations have also been done, but only the dwell-time histograms of the measurements obtained at -100 mV and +100 mV are displayed in Fig. 8.2. The reason is that during the course of this thesis it became more and more obvious that the temporal resolution of the HMM fit is not sufficient.

Thus, it may be questioned of whether the dwell-time histograms (Fig. 8.1 and Fig. 8.2) and the results of the HMM fits (Fig. 8.3, Fig. 8.4 and Fig. 8.5) have to be considered to be "wrong". The answer of this question requires the analysis on the basis of the "Great Markov Model" which is hindered by the problems discussed in the next section. In spite of these uncertainties, some conclusions can be drawn from the analysis:

1. The HMM fits were done with the apparent current. This would merge the bursts into an apparent open state. Because of this, the following interpretation of the results seems to be likely: The rate constants obtained from the HMM fit apply to a Markov model where the fast gating bursts are represented by the two apparent open states. In that case, the transitions between the closed states C3 and C4 (Fig. 8.5) may be taken as real results. The transitions between O1 and O2 however, are expected to be modified by an analysis based on the "true" Markov model.

2. Tl^+ affects the transitions between closed states when dragged into the pore (Fig. 8.2). This is further illustrated in Fig. 8.6. This conclusion will probably survive a more sophisticated analysis with better temporal resolution and the true current. Even though the rate constants of the Markov model probably are wrongly determined here because of insufficient temporal resolution (see above), the dwell-time histograms are measured quantities reflecting (although contorted) the gating behavior of the channel.

3. The finding related to the transitions between O1 and O2 will be modified by an analysis with higher temporal resolution. Actually, this has already occurred, because the findings in chapter 7 lead to a strong distinction between the effects of cytosolic and luminal Tl^+ which was not found in the results obtained from the dwell-time distributions (Fig. 8.2, Fig. 8.6) with a temporal resolution which was not high enough.
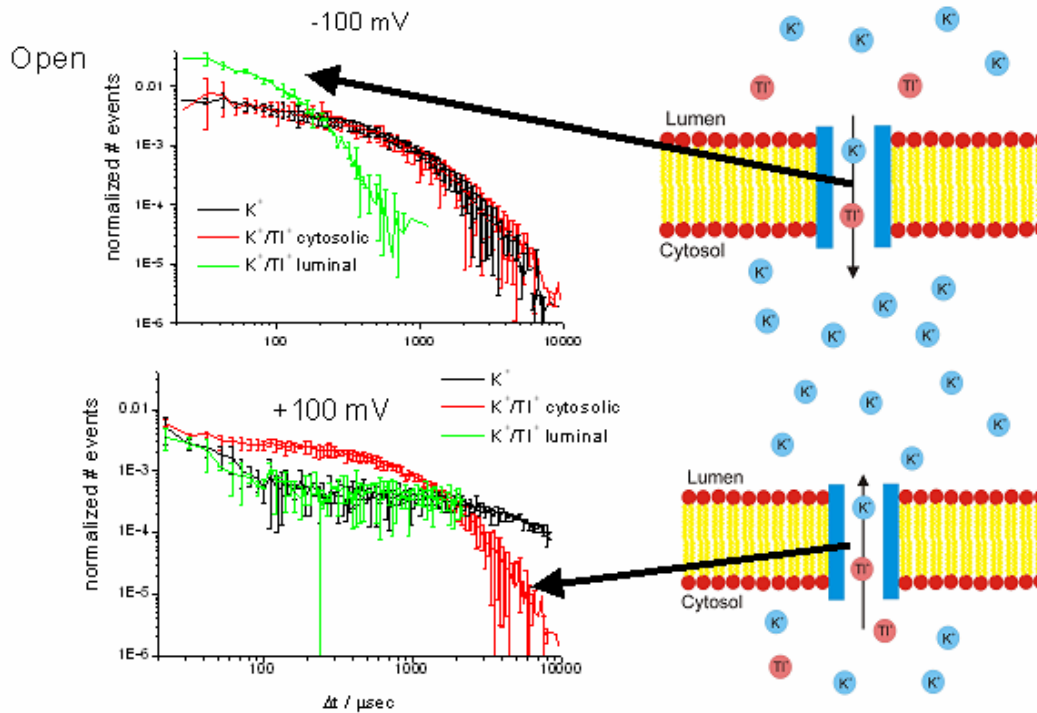
Fig. 8.6. Open dwell-time histograms obtained in pure K^+ (black) and K^+/Tl^+ mixture on the cytosolic (red) or luminal side (green). Shifts in the dwell-time distributions are only observed, if the mixture is pulled into the pore. This indicates that forces between the ions and residues of the pore and not binding sites at the channel mouth mediate the effect of Tl^+ on gating.

8.2. A pessimistic view of the chances of finding of the adequate model by mathematical analysis: SQ fit

After finishing the HMM analysis, it was tried to fit amplitude histograms from four time series measured at different voltage (+-20, +40 and +160 mV) by means of the SQ fit. In order to obtain a good signal-to-noise ratio, measurements in 400 mM KCl with 2.5 mM Ca^{2+} and 2.5 mM Mg^{2+} were selected (Fig. 6.2). As in the case of the HMM fit above, the number of the states of the Markov model was derived from the inspection of the dwell-time histograms (each Markov state causes one time constant in the dwell-time histograms). Two open and three closed states were indicated (for MaxiK and *Chara*), even though it always has to be kept in mind that there may be additional states whose occurrence is so rare that they do not have a significant effect on the measured time series or that they are too fast to be detected in the dwell-time histograms.

The SQ fit is described in section 5.2. It comprises two subsequent fits. First, the time series was fitted with a HMM fit. Then, the beta fit follows. It uses some of the slow rate constants delivered by the HMM fit as constant values and varies the fast rate constants. The knowledge of the true current required for the SQ fit was provided by the beta fit (section 5.3). Fig. 8.7 shows the results of some SQ fits obtained with the O-O-C-C-C model (5lin1 in Table 8.1). It is obvious that a good fit is only achieved when the form of the amplitude histograms is quite simple (Fig. 8.7C). However, Fig. 8.7A and B show severe deviations.

167
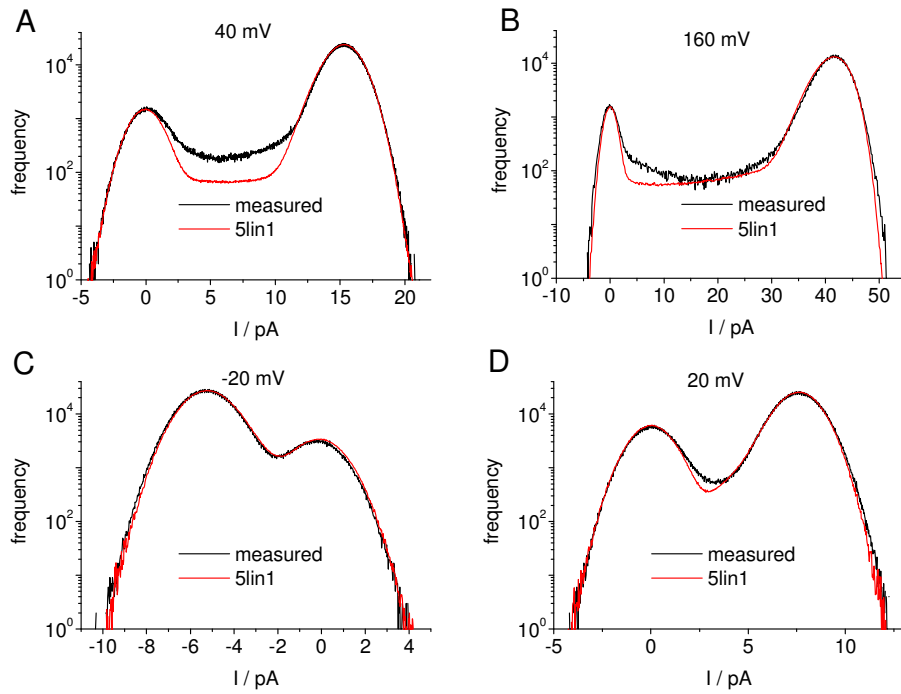
Fig. 8.7. Fitting time series recorded in 400 mM K$^+$ with Ca^{2+} and Mg^{2+} at 40 mV (A), 160 mV (B), -20 mV (C) and 20 mV (D) by means of the O-O-C-C-C model (5lin1 in Table 8.1).

The failure of the fits in Fig. 8.7 indicates that the wrong Markov model is used for the fits. Because of this, alternative models were tested as listed in Table 8.1.

Table 8.1. 5-state Markov models used for the fit presented in Fig. 8.7 and Fig. 8.8.

5lin1	$O1 \rightleftharpoons O2 \rightleftharpoons C3 \rightleftharpoons C4 \rightleftharpoons C5$
5branch1	$O1 \rightleftharpoons O2 \rightleftharpoons C4 \rightleftharpoons C5$ $\updownarrow$ $C3$
5branch2	$C1 \rightleftharpoons O2 \rightleftharpoons O3 \rightleftharpoons C4$ $\updownarrow$ $C5$
5branch3	$C3$ $\updownarrow$ $O1 \rightleftharpoons O2 \rightleftharpoons C4$ $\updownarrow$ $C5$
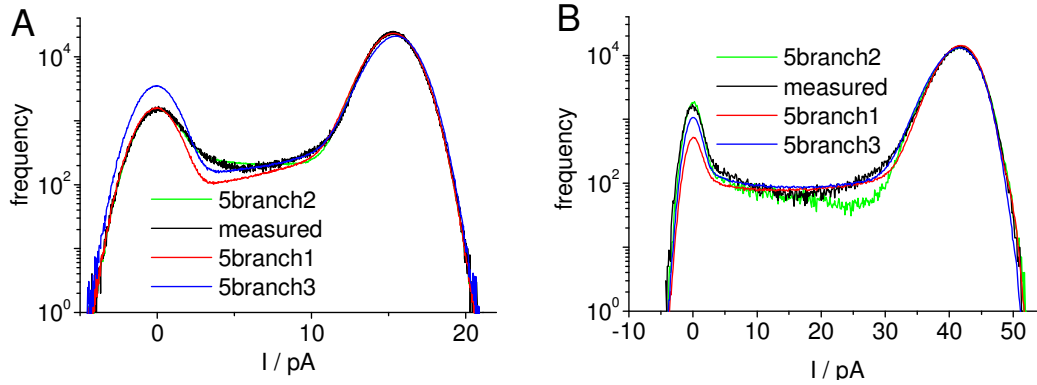
Fig. 8.8. Fitting the full amplitude histograms of time series obtained at +40 mV (A) and +160 mV (B) with the branched models shown in Table 8.1.

Fig. 8.7 and Fig. 8.8 show that none of the models in Table 8.1 were successful in fitting the full amplitude histograms. Although the peaks are fitted quite well in most cases, there are deviations in the middle region, indicating that the kinetics of the channel gating could not be properly reproduced. There are three possible explanations for the miserable performance of the models.

1. The number of states (two open- and three closed-states) is correct, but the small sample of only five models does not include the right one.
2. Bad fit performance; the algorithms have not found the best solution.
3. Five states are not enough.

The reliability of the above explanations is considered as follows.

1. There is some truth in the first argument as shown in the next section.
2. The fits were repeated at least 30 times each with different starting values. According to our experience, this should be enough to find the global minimum.
3. Generally, Markov models with much more than just five states are used for MaxiK (e.g., Magleby, 2001), their number mostly derived from theoretical considerations rather than dwell-time histograms as done here. Often, not all states can be seen in a certain experiment. Rothberg and Magleby (1999) for instance found that the number of observable states depends on the Ca^{2+} concentration or even more scaring, on the length of the time series (McManus and Magleby, 1988).

To test hypothesis 3 or just 1, countless SQ fits over the whole voltage range with at least dozens of different models would be necessary. The fitting attempts have shown that finding the correct Markov model is an approach with endless branching due to a plethora of different arrangements of states and of the inclusion of additional states. Each step has to be based on time consuming fitting routines. The interpretation of the arrangements which are not in contradiction to the experimental finding (a stronger statement is not possible) becomes very speculative.

Furthermore, there is the problem of equivalent Markov models, i.e., different arrangements of states yield identical kinetic behavior (Kienker, 1989). As described in section 4.3, Markov models are equivalent when a transformation matrix S exists which transforms the matrix of rate constants (K) of one model into that of the other model (K') with $SKS^{-1} = K'$. Finding S requires the solution of higher order non-linear equations by

fitting routines. If this very time-consuming procedure has been done, equivalent models may be separated by studying the effects of voltage or other parameters on the values of the rate constants seeking to find out which scheme yields the most convincing dependence on these parameters. The experimental and computational effort doing this may become unlimited without any warranty to get scientifically meaningful results.

All this leads to serious doubts of whether the mathematical approach alone is suitable for the search of the "Great Markov Model". Less time consuming, less brain-twisting, but by far more efficient seems to be the usage of mutants. They can provide a much more direct assignment of certain components of gating in the measured time series to certain moieties in the protein.

Thus, the outcome of these considerations is the recommendation to do experiments with channel mutants first. Knowing which part of the channel influences which part of the gating process in the time series strongly decreases the number of possible models. A Markov model is still necessary to provide a numerical basis for the bridge between physiological observation and protein dynamics. However, after having done the mutant studies, the chance of selecting a Markov model that directly maps the gating effects on conformational moieties of the channel protein should be strongly increased. Such a model extracts numerical key parameters from the experimental data which can be used to test MD simulations.

8.3. Partial approaches to the "Great Markov Model": An unexpected benefit of beta distributions with respect to the distinction between models

8.3.1. Fitting a gap in the beta distributions

In spite of the pessimistic view described above, there are some successful approaches dealing with submodels of the putative "Great Markov Model". The 2-state models which were used for beta fits in the analysis of fast gating in Schroeder and Hansen (2007; 2008) can be considered as extreme submodels which can be used only for the open-level distribution, see section 5.1 and Schroeder et al. (2004). Here it will be shown that at least information about the submodels generating the fast gating can be obtained from fitting the complete amplitude histogram by means of an SQ fit.

The models in Table 8.1 which led to the bad fits in Fig. 8.7 and Fig. 8.8 still keep the configuration of connected O1-O2 states, because it seemed to be convincing that the two O-states should be neighbors. The finding of a new model starts from an inspection of Fig. 8.9A.

Fortunately, it is not necessary to completely rely on the results which emerge out of the dark tunnel of mathematics and curve-fitting routines (which always include the possibility that the fitting routine has not found the global minimum of the least square function). A visual inspection of the deviations between measured and theoretical amplitude histograms can be employed to understand the reasons for the failure of the other models.

In Fig. 8.9A, the largest deviation (around 4 pA) is in the neighborhood of the C-peak (0 pA). It can be imagined that this gap can be filled by small spikes coming out of the closed state.

These spikes can be generated by sojourns from the long-living closed states C4 or C5 into an additional open state O6 with a short lifetime. Such an open state is introduced into the model 5branch1 in Table 8.1 converting it to 6branch1 in Table 8.2.
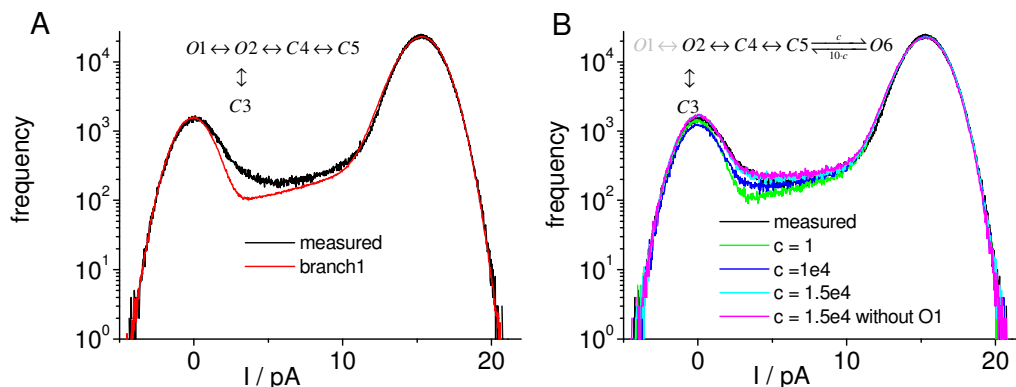
Fig. 8.9. Separation of the open states. (A) Failure of the branched model 5branch1 in Table 8.1 already shown in Fig. 8.8A. (B) Model 5branch1 with an additional open state O6 connected to C5. Fitting was done manually by simulating time series with the rate constants taken from (A) plus a guess for the rate constants k_{56} and k_{65} as given in the legend. The violet curve is obtained after omission of state O1.

Table 8.2. Markov models with separated open states used for the fit presented in Fig. 8.9B.

5lin2	$C3 \rightleftharpoons O2 \rightleftharpoons C4 \rightleftharpoons C5 \rightleftharpoons O6$
6branch1	$O1 \rightleftharpoons O2 \rightleftharpoons C4 \rightleftharpoons C5 \rightleftharpoons O6$ $\updownarrow$ $C3$

Indeed, the simulated curves in Fig. 8.9B show that a good match between measured and simulated amplitude histogram can be obtained when the transitions between C5 and O6 are introduced. The occupation probability of O1 is very low, and the violet curve shows that it probably can be omitted, effectively transforming the model into "5lin2" (Table 8.2) which indeed fits the data better than the models in Table 8.1.

8.3.2. Conclusions about the Markov model suggested by the fits in Fig. 8.9B

The good fit of the model 5lin2 in Fig. 8.9B in comparison to 5lin1 (Fig. 8.7) is unexpected, because the a priori assumption is that the open state is given when all gates are open, and that all transitions to closed states start from this open state (or an aggregated open state comprising two different conformations O1 and O2). Fig. 8.9 implies that there are kinetically different open states depending on the preceding sojourn in a certain closed state. The occurrence of separated open states leads to some interesting thoughts about the molecular mechanism of gating as discussed in section 8.3.3.
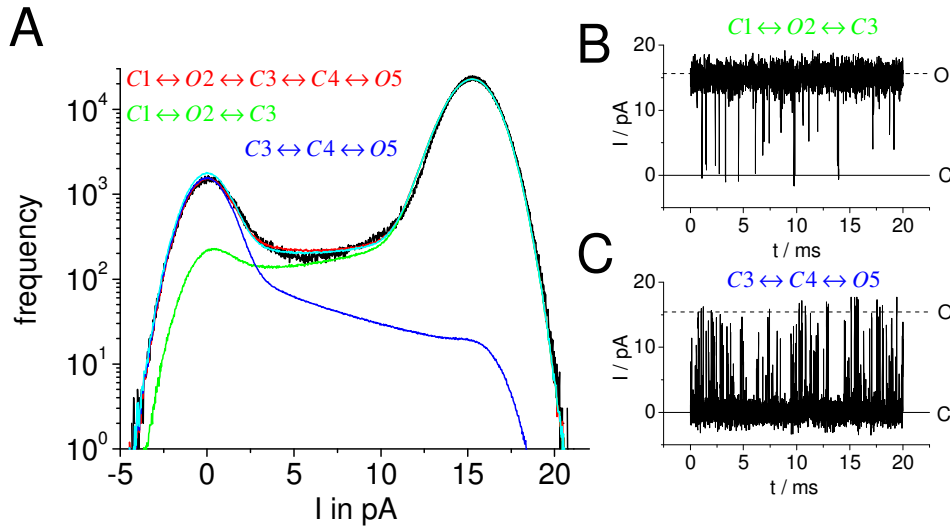
Fig. 8.10. Filling the gaps. The amplitude histogram of the successful fit in Fig. 8.9B is compared with the amplitude histograms of the submodels as indicated in the figure. (B,C) Surrogate time series generated by the submodels causing the submodel amplitude histograms in (A).

The mechanism of filling the gap of the amplitude histogram of the O-O-C-C-C model in Fig. 8.9A is illustrated in Fig. 8.10. The overall amplitude histogram of the model 5lin2 (red in Fig. 8.9B) is split into individual histograms resulting from the submodels shown in Fig. 8.10. In addition, the related surrogate time series are shown (Fig. 8.10B and C). The time series demonstrate what was anticipated when constructing the model 6branch1 which an additional open state O6 or its reduced version 5lin2 (Table 8.1). In order to fill the gaps near the C- and the O-peak additional transitions are required which generate short peaks out of the O-state (improvement by 5branch1, Fig. 8.8, or by the C1-O2 arrangement in 5lin2) and out of the C-state (improvement in Fig. 8.9B by adding the transition C5-O6).

The rate constants of these transitions have to be chosen in such a way that the generated jumps fill the gap at the C-slope: The current spikes have to start from the closed level and must not reach the O-level or even better not even the middle between O- and C-level (blue curve in Fig. 8.10A The rate constant k_{O6C5} of the C5-O6 transition of the models in Table 8.2 has to have a value greater than the corner frequency of the anti-aliasing filter allowing measured current spikes to reach about 30% of the O-level (Fig. 8.10A). The rate constant k_{C5O6} is determined by the number of points required to fill the gap. The related surrogate time series is shown in Fig. 8.10C.

The gating described above cannot be provided by the O-O-C-C-C model. It yields only the fast gating process which is required to generate the flickering causing the apparent open state. This process contributes to the width of the O-peak (Fig. 8.7A). The transitions O-C-C and O-C-C-C add no additional degrees of freedom for the right-hand slope of the C-level. These slower transitions fill the horizontal middle range between O and C (Fig. 8.7A). Thus, more than one C-O transition has to be implemented as done in the models in Table 8.2 (Fig. 8.9).

This requirement seems to be met by the branched models in Table 8.1 with at least two C-states communicating with the aggregated O-state O-O. However, also these models fail (Fig. 8.8). Obviously, there are not enough degrees of freedom. The model C-O-C-C-O yields 5 C-O transitions: C-O, O-C, O-C-C, C-C-O and C-O. It has to be

mentioned that C-C-O and C-O produce different contributions to the amplitude histogram.

O6 has not necessarily to be connected to C5. Alternatively it could be connected also to C4. In that case, the rate constant k_{O6C4} has to be equal to the rate constant k_{O6C5} because they both determine the lifetime of O6, and thus the magnitude of the spikes from the C-level (Fig. 8.10C). The rate constant k_{C4O6} has to account for the different occupancies of C3 and C4 leading to

$$k_{C4O6} = k_{C5O6} \frac{[C5]}{[C4]} \qquad (8.1)$$

in order to enable the same number of transitions into O6 in both models.

8.3.3. The rattly channel

In the investigations described above, very good fits were obtained with a model I intuitively did not like. However, the computer was persistent that the C-O-C-C-O model (5lin2) was better than the models in Table 8.1 with adjacent open states. The feature I disliked was the separation of the two open states by closed states. This was intuitively unexpected. An open state can occur only if all gates of the channel are open. Thus, one would expect that all closed states or chains of closed states would start from the same open state, representing the closure of one of the involved gates with one or more configurations. From dwell-time analysis it is known that there are two open states. Accepting this, it was expected that they were neighbors as in the models in Table 8.1. The meaning of such an aggregated open state would be that the protein can adopt two conducting confirmations and that closing the channel always has to start from this aggregated open state.

Separated open states may occur if the closing of the channel has influenced the backbone of the channel (e.g., induced by movements of the glycine hinge on S6) thus altering the kinetics of the open state (see section 2.5.2.4).

Alternatively the picture of a "rattly channel" comes to mind. Considering the role of incorrect gating in many diseases (Lehmann-Horn and Jurkat-Rott, 1999; Ashcroft, 2000; Shieh et al., 2000) it seems that all gating is "done on purpose", i.e., evolution has optimized gating to provide optimum performance in the organism. On the other hand we know that nature has a different policy as compared to human workshops. In a car, each part is manufactured in such a way that it is expected not to fail. If one part like a single transistor in the electronics fails, the whole car breaks down. Nature in contrast does not live up to the ambition that all individual parts have to work properly. Instead it provides many repair mechanisms which prevent that the organism drops dead if one part fails. This obviously makes living systems quite stable.

In the case of the successful models 5lin2 and 6branch1 in Table 8.2, there are two unstable configurations. The fast gating between C3 and O2/O1 is probably related to the reorientation of the amid plane between GYG and V in the selectivity filter (Berneche and Roux, 2005; Schroeder and Hansen, 2007). Considering the necessity of introducing the C5-O6 transition suggests the hypothesis that nature has not only failed to construct a perfectly open open state, but also a perfectly closed closed state. However, nature does not seem to care about perfect mechanisms.

9. Conclusion and Outlook

9.1. Usefulness of the analysis of fast gating.

Chapter 5 describes tremendous efforts to improve the temporal resolution of the analysis of gating in single-channel currents: the question arises of whether the results are worth this effort. I think so. Chapters 6 and 7 indicate that the improved fast gating analysis opens the access to the study of putative molecular mechanisms which are involved in ion conduction and gating. The two models in chapters 6 and 7 deal with the following effects of ion/channel interaction:

1. The stability of the **selectivity filter** is determined by interaction of ions with carbonyl groups of the P-loop.
2. Ions in the **cavity** may act directly on the ions in the selectivity filter or via binding sites in the cavity probably mediated by bridges between the P-loops and the supporting helices. In the case of Tl^+, we have to assume a second interaction site modulating the sensitivity to luminal ion depletion depending on the presence of Tl^+.
3. Diffusion limitation may occur at the **channel entrances** determined by the absence or presence of negative charges or by diffusion limitation in the inner pore. However, it also may be related to the energy barrier of leaving or entering the selectivity filter, e.g., determined by the exchange of the water shell for the channel environment.

The above three points indicate that the approach of this thesis addresses questions directly related to the molecular dynamics of the channel protein. In chapters 6 and 7 models of putative mechanisms are proposed. They are supported by some findings like the MD simulations of Bernèche and Roux (2000; 2005) dealing with the reorientation of the G-V amid plane next to the GYG motif induced by K^+ depletion. However, there are also contradicting results like the finding in a student's course that diffusion limitation by sugars (as found by Brelidze and Magleby, 2005) does not influence the gating behavior as would be expected from the model in appendix 6.5. The putative second binding side to explain the Tl^+ experiments in chapter 7 is completely arbitrary and was suggested in order to gain a working hypothesis.

Considering the growing amount of papers in this field, it cannot be expected that all these problems are solved within one thesis. However, this thesis has opened the way to address these questions by the direct measurement of the rate constants of gating. In the next section suggestions are made for further research.

9.2. Continuing the research

Both reviewers of the paper of Schroeder and Hansen (2007, chapter 6) stated that this approach can contribute to the closure of the gap between physiology and structural analysis. The ultimate goal of such an approach is providing experimental data which can be used to understand on a molecular level the functions determining conductivity and gating behavior of ion channels. Starting from the knowledge of channel structure, the influence of mutations on the physiological behavior is evaluated by means of MD simulations. If these calculations predict the observed physiological behavior correctly, then the probability is increased that the molecular mechanisms are understood. This approach becomes more convincing if not only static experimental results are predicted like conductivity or selectivity, but also dynamic properties like gating behavior. The investigations of this thesis have provided the most promising candidate for such an approach, i.e., fast gating in the range of less than 1 µs. The next task will be to find out which mode of gating observed in a measured time series of single-channel current is related to which movement of residues in the channel protein.

At the moment there is still a gap between the temporal domains of gating analysis and MD simulations. In the case of gating, there are some possibilities of increasing temporal resolution. Higher K^+ concentrations can be used. Brelidze and Magleby (2005) performed measurements in 2 M KCl. This would improve the signal-to-noise ratio considerably. Thus, a temporal range down to 0.1 µs seems to be accessible. However, it has to be considered that at a current of 64 pA the average number of ion passing during an open event of 0.1 µs is 40. There is not much numerical freedom for a further increase in temporal resolution of patch clamp data without merging the effects of gating and permeation (section 4.1.1).

On the other side of the gap, the group of Stefan Kast at the Dept. of Physical Chemistry of the TU-Darmstadt has reached the range of 30 ns in MD simulations for the viral Kcv channel (Tayefeh et al., 2007). Faster computers (probably using parallel processors) and improved heuristic algorithms will certainly allow much longer simulation times in the next few years. For instance, the "coarse grain" method (Bond et al., 2007), which leads to a tremendous reduction of the number of involved atoms by concentrating on the essential moieties of the protein, is one of these approaches which give hope that the necessary expansion of the time scale will be reached soon.

Nevertheless, already now these MD simulations are useful to provide a molecular fundament for an understanding of K^+ transport through Kcv and finally also for the analysis of fast gating. The simulations show spontaneous single file movement of K^+ ions through the pore (Tayefeh et al., 2007) and can explain K^+/Na^+ selectivity (Kast et al., 2008). Other results are discussed below.

In chapters 6 and 7, the reorientation of the amid plane between the G of GYG and the neighboring valine is mentioned. This picture arose from MD simulations of Bernèche and Roux (2000; 2005). Furthermore, there are MD simulations dealing with the occupation of the sites inside the selectivity filter or with the ion/filter interaction during the passage of an ion (Khalili-Araghi et al., 2006).

For the continuation of the investigation of the relationship between sub-µs gating and molecular dynamics started in this thesis, the viral Kcv channel (Pagliuca et al., 2007) may be a better choice than MaxiK. It is found in different species of *Chlorella* viruses and has the advantage of being truly minimal. Kcv is a tetramer of two transmembrane helices and a pore loop with minimal N and C termini and small

extracellular loops (Plugge et al., 2000; Gazzarrini et al., 2004; Kang et al., 2004; Pagliuca et al., 2007).

First, Kcv shares many useful characteristics with MaxiK, e.g., high single-channel current as related to a single-conductance of 200 pS (Pagliuca et al., 2007; Shim et al., 2007), and negative slopes as found in whole-cell experiments (Gazzarrini et al., 2006) and in single-channel recordings (Shim et al, 2007; Abenavoli and Moroni, University of Mailand, personal communication), the basis for the analysis in chapter 6. Second, Kcv has several advantages over MaxiK:

A. Kcv is much simpler than MaxiK because of its short sequence (only 94 amino acids compared with about 1200 for MaxiK). In chapter 7 (Schroeder and Hansen, 2008) there was some uncertainty of whether it is legitimate to ignore the voltage-driven movement of the S4 helix. A channel without S4 helix may hopefully decrease the problems of assigning physiological observations to the mutations of key residues, even though this hope is not always realistic.
B. A plethora of mutants is available. Different virus strains already offer several (Kang et al, 2004; Gazzarrini et al. 2004) functional variations, which are a good starting point for mutational analysis. Furthermore, new mutants can easily be manufactured (Thiel, TU Darmstadt, personal communication). Several of the already available mutants can be used directly to address the questions related to the models in chapter 6 and 7.
C. As mentioned above, the group of S. Kast, Darmstadt, has established Molecular Dynamics (MD) calculations for Kcv. Actually, at the moment, this model is only based on a homology model between the crystal structure of KirBac1.1 and Kcv. The goodness of the model will for sure be soon improved because the laboratory of Dr. Moroni in Milano is successfully growing crystals of the Kcv protein (A. Moroni, personal communication). This will lead in the foreseeable future to a high resolution structure of Kcv thus improving the quality of the MD model.

The usefulness of Kcv mutants for the continuation of the investigations of this thesis may be illustrated by some examples (G. Thiel, Darmstadt, personal communication):
The mutation KcvT63S is localized at the 4th binding site in the selectivity filter and decreases the affinity for the Ba^{2+} block by several orders of magnitude. According to Lu et al., (2001b), the Ba^{2+} block is an indicator of the filter structure or flexibility. Furthermore, this mutation also causes a high number of subconductance levels. Subconductance levels arise from averaging over fast gating bursts if recorded with insufficient temporal resolution. Because of these findings, this mutant is a promising candidate for studying the origin of fast gating, but also of luminal diffusion limitation.
Mutations in the Kvc turret (Fig. 2.2) reduce the conductivity of Kcv. This is useful for testing the relationships between fast gating and rate limitation by the loading reaction for inward current (see chapter 7) as postulated by Schroeder and Hansen (2008).
The mutant D45N influences the enrichment of K^+ at the luminal pore mouth as indicated by the calculated distributions of K^+ at the luminal pore mouth which are shown for WT and the mutant D45N in Fig. 2.7 (Rosenmund, 2006). This enrichment of ions at the entrances of the channel plays an important role in the diffusion limitation which causes ion depletion and gating according to Schroeder and Hansen (2007; 2008).

A putative interaction between inner gate and selectivity filter (section 2.5.2.4) can be studied by the following mutants:

Mutant KcvP13A on TM1 close to the slide helix leads to a „gain of function", i. e. an increased selectivity. This should also change fast gating. So far, only a slow component of gating is found at negative potentials which does not occur in wild-type (Hertel et al., 2006).

Mutations affecting the salt bridges between TM1 and TM2 at the cytosolic side of Kcv support the results obtained from MD simulation (Tayefeh et al., 2007; Kast et al., 2008) which indicate that the formation of salt bridges on the cytosolic side between TM1 and TM2 is important for the operation of the cytosolic gate. (B. Hertel, Darmstadt, unpublished results).

The above considerations show that there is a plethora of experiments which now can be done after the tools for the analysis of fast gating have been developed and their usefulness has been demonstrated in this thesis.

9.3. Applicability of the present software

In spite of the quite interesting scientific results obtained with the methods of fast gating analysis developed here, in this last section the question is considered of whether there will be a wide spread application of these methods in the scientific community. I have to confess that the analysis is quite time consuming. Dr. Cao in the faculty of Life Science of the University of Manchester, whom we met on a meeting of the European Biophysical society in Leeds this summer, wanted to apply our algorithms in order to find the true single-channel current in his data from various mutants of the P2X channel (Dr. Lishuang Cao, personal communication). Analyzing his time series on my laptop in Manchester revealed that the true-single-channel current was three times as high as the apparent current estimated directly from the records. Thus, the necessity of the analysis by means of our software was clearly indicated. However, it turned out that the effort for doing this analysis was very high.

There are many time consuming steps in the present software. Part of them cannot be avoided; part of them can if the software would be improved. Cleaning the time series from artifacts like baseline drift or noisy sections belongs to the first category. Replacing the human being by a computer would require really sophisticated algorithms for the inspection of the time series. These algorithms may exist; however, their implication would take probably more time than would be saved by the automatic processing of the time series.

What can be improved is the transfer of results from the program *Kiel-Patch* which generates the distributions–per-level to *downhill* doing the fits. Part of this work already has been done after our return from Manchester. Having done this earlier would have saved a lot of time in this thesis. Even more important would be the generation of graphs like those in Fig. 6.3. At the present time, figures still have to be made manually by loading the data into Origin®.

This is the old problem: Good software would accelerate the solutions of the scientific questions. However, during the time of developing the software you cannot do science. Murphy's Law takes care that you always make the wrong choice between these two options. Nevertheless, the strategy in this thesis was probably not so bad. The effort for the software was intense enough for providing the tools which could do the job, and left enough time for getting scientific results.

10. Summary

This thesis aims at the analysis of fast gating events in ion channels. Experiments were done on single MaxiK channels expressed in HEK cells using the patch clamp technique in voltage clamp mode. Crucial for high temporal resolution was the signal-to-noise ratio which was improved by optimizing the set-up and pipette treatment.

Furthermore, temporal resolution was increased by sharpening the mathematical tools employed in the analysis of the kinetic behavior of single-channel currents. This was done along four lines. 1. Splitting amplitude histograms into distributions-per-level and investigating their properties with respect to model discrimination, determination of the rate constants of fast gating and the detection of failures of jump detection. 2. Creating the SQ fit, a two-step fit algorithm consisting of a direct fit of patch clamp time series, by means of a 1-step prediction algorithm and a fit of the distribution-per-open-level by means of beta distributions. 3. Finding and testing the ability of the beta fit to determine the true single-channel current in time series where the apparent current was attenuated by averaging over undetected fast gating. 4. Comparing the SQ fit with the 2-dimensional dwell-time fit as improved by T. Huth.

After having developed the new tools, they were applied to the analysis of fast gating events. Two phenomena could gain the outmost benefit from the new analytical tools: 1. The negative slope in the current-voltage curve occurring at positive potentials in symmetrical solutions with K^+ as the only monovalent cation. 2. The negative slope occurring at negative potentials in luminal K^+/Tl^+ solution when the current dragged Tl^+ into the channel. Both kinds of measurement resulted in insights about ion/protein interaction.

The key for the creation of molecular models of ion/channel interactions was found in the experiments with K^+ as the sole monovalent cation. In the range of the negative slope, saturation of the true single-channel current and onset of fast gating occurred in the same voltage range. This finding suggested a mechanistic model: On the cytosolic side, diffusion limitation produced saturation of outward-current. This caused ion depletion in the selectivity filter. The idea that gating occurred when permeant ions did no longer compensate the repulsive forces of the carbonyl groups was supported by MD simulations reported in the literature. The model correctly predicted the effect of different K^+ concentrations. For explaining the negative slope induced by negative membrane potentials when luminal Tl^+ was dragged into the channel, the basic model had to be extended. Here, the effect of luminal diffusion limitation on voltage-induced gating was not sufficient for explaining the experimental findings. This effect had to be modulated by additional Tl^+ binding sites in the cavity or at the inner side of the selectivity filter.

Describing the full set of gating phenomena induced by Tl^+ would require the analysis of the "Great Markov Model" of the MaxiK channel. It is shown by preliminary approaches with classical tools what kind of insights would be obtained from this kind of analysis and what kind of problems keep the ratio "scientific output/time" at a very low level. Nevertheless, examples are given that the analysis of beta distributions can be helpful for the extension of the Markov model. Especially the picture of a rattly channel has arisen, implying that open states are not really open and closed states are not really closed. Finally, it is discussed that using the viral channel Kcv instead of MaxiK offers better chances to continue the building of a bridge between electrophysiology and structural biology as has been initiated in this thesis.

11. Zusammenfassung

Die vorliegende Arbeit befasst sich mit der Analyse schneller Schaltprozesse in einzelnen Ionenkanälen. Die Patch-Clamp Experimente wurden an mit humanen MaxiK-Kanälen stabil transfizierten HEK-Zellen vorgenommen. Wichtig zur Erzielung einer guten Zeitauflösung ist das Signal-Rausch-Verhältnis. Dazu diente die Verbesserung des Messaufbaus und der Patchpipetten.

Entscheidender für die Verbesserung der Zeitauflösung war hier jedoch die Weiterentwicklung der Programme zur kinetischen Analyse von Einzelkanalaufzeichnungen. Die vier Kernpunkte hierbei waren folgende: 1. Aufspaltung der Amplitudenhistogramme in Einzelhistogramme. Diese so genannten „distributions-per-level" erwiesen sich als nützlich in den Bereichen der Modellunterscheidung, der Bestimmung schneller Ratenkonstanten und der Erkennung von Fehlern in der Sprungdetektion. 2. Die Entwicklung eines Programms, das zwei Fitverfahren miteinander kombiniert (SQ-Fit): Den direkten Fit der Zeitreihe mit Einschrittprädiktion und den Fit der Amplitudenhistogramme mit Betaverteilungen. 3. Entwicklung und Erprobung einer neuen Anwendung für Betaverteilungen zur Rekonstruktion des wahren Einzelkanalstroms in Aufzeichnungen, in denen der scheinbare Strom durch nicht aufgelöstes schnelles Schalten stark reduziert ist. 4. Vergleich der Leistungsfähigkeit des SQ-Fits mit dem von Tobias Huth weiterentwickelten Fit der zweidimensionalen Dwell-Time-Histogramme.

Die neuen Werkzeuge wurden zur Analyse schneller Schaltereignisse eingesetzt. Zwei Phänomene waren dabei besonders interessant, weil sie wichtige Hinweise zur Ionen-Protein-Interaktion gaben: 1. Die negative Kennlinie bei positiven Membranpotentialen in der Stromspannungskurve in symmetrischen Messlösungen mit K^+ als einzigem einwertigen Kation. 2. Die negative Kennlinie bei negativen Membranpotentialen wenn eine K^+/Tl^+- Mischung von der luminalen Seite in die Pore gezogen wird.

Der Schlüssel zur Modellbildung für die Ionen-Protein-Interaktion fand sich in den Kalium-Experimenten: Im Bereich der negativen Kennlinie setzten das schnelle Schalten und die Sättigung des wahren Einzelkanalstroms ungefähr gleichzeitig ein. Dies führte zu folgendem Modell: Eine Diffusionslimitierung am cytosolischen Porenmund bewirkt eine Sättigung des Auswärtsstromes und eine Verarmung an Kaliumionen im Selektivitätsfilter. Letzteres destabilisiert das Filter und führt zu Schließungen, weil die abstoßenden Kräfte der sich gegenüberliegenden Karbonylgruppen nicht mehr kompensiert werden. MD-Simulationen in der Literatur unterstützen diese Annahme. Das Modell war in der Lage, die Spannungs- und Konzentrationsabhängigkeit der beobachteten Effekte vorherzusagen. Zur Erklärung der Tl^+-induzierten negativen Kennlinie bei negativen Spannungen musste das Modell erweitert werden, da die Annahme ähnlicher Diffusionslimitierungen am luminalen Porenmund nicht ausreichend war, um die Messergebnisse zu erklären. Es wurde vermutet, dass es in der Cavity oder am inneren Ende des Selektivitätsfilters Tl^+- Bindungsstellen gibt, die das Schalten zusätzlich modulieren.

Das gesamte Schaltverhalten der Kanäle mit und ohne Tl$^+$ zu beschreiben, erfordert ein wesentlich größeres Markov-Modell als jenes mit nur zwei Zuständen, das zur Analyse des schnellen Schalten in den Bursts benutzt wurde. Ein rein mathematisches Vorgehen, um dieses Modell zu finden, würde unverhältnismäßig viel Zeit erfordern. Darum wurde die Analyse nur kurz angerissen, um aufzuzeigen, in welche Richtung es gehen kann. Dabei zeigte sich, dass die Analyse von Betaverteilungen wichtige Beiträge zur Modellentwicklung liefern kann: So entstand das Bild des „klapprigen" Kanals, bei dem die Offenzustände nicht richtig offen und die Geschlossenzustände nicht richtig geschlossen sind. Zum Schluss wird noch diskutiert, dass ein Wechsel des Untersuchungsobjektes vom MaxiK zum wesentlich einfacheren viralen Kcv in zukünftigen Arbeiten vermutlich die hier begonnene Brückenbildung zwischen Elektrophysiologie und Strukturbiologie besser fördern wird.

12. References

Abramson, J., I. Smirnova, V. Kasho, G. Verner, H.R. Kaback and S. Iwata. 2003. Structure and mechanism of the lactose permease of Escherichia coli. *Science*. 301:610-615.

Adam, G., P. Läuger and G. Stark. 1988. Physikalische Chemie und Biophysik. 2nd edition. Springer-Verlag, Berlin and Heidelberg.

Ahern, C.A., A.L. Eastwood, H.A. Lester, D.A. Dougherty and R. Horn. 2006. A cation-pi interaction between extracellular TEA and an aromatic residue in potassium channels. *J Gen Physiol*. 128:649-657.

Aiyar, J., J.M. Withka, J.P. Rizzi, D.H. Singleton, G.C. Andrews, W. Lin, J. Boyd, D.C. Hanson, M. Simon, B. Dethlefs et al. 1995. Topology of the pore-region of a K^+ channel revealed by the NMR-derived structures of scorpion toxins. *Neuron*. 15:1169-1181.

Alagem, N., M. Dvir and E. Reuveny. 2001. Mechanism of Ba^{2+} block of a mouse inwardly rectifying K^+ channel: differential contribution by two discrete residues. *J Physiol*. 534:381-393.

Albertsen, A. 1992. Erfassung und Auswertung schneller Schaltvorgänge bei Patch-Clamp Untersuchungen. Diploma thesis, Christian Albrechts Universität, Kiel.

Albertsen, A. 1994. Fast Patch-Clamp Data Acquisition and Kinetic Analysis of Multi-Channel Records. PhD thesis, Christian Albrechts University, Kiel.

Albertsen, A. and U.P. Hansen. 1994. Estimation of kinetic rate constants from multi-channel recordings by a direct fit of the time series. *Biophys J*. 67:1393-1403.

Allen, T.W., O.S. Andersen and B. Roux. 2004. On the importance of atomic fluctuations, protein flexibility, and solvent in ion permeation. *J Gen Physiol*. 124:679-690.

Almers, W. and C.M. Armstrong. 1980. Survival of K^+ permeability and gating currents in squid axons perfused with K^+-free media. *J Gen Physiol*. 75:61-78.

Ambriz-Rivas, M., L.D. Islas and F. Gomez-Lagunas. 2005. K^+-dependent stability and ion conduction of *Shab* K^+ channels: a comparison with *Shaker* channels. *Pflugers Arch*. 450:255-261.

Andersen, O.S. and S.W. Feldberg. 1996. The heterogeneous collision velocity for hydrated ions in aqueous solutions is ~ 10^4 cm/s. *J Phys Chem*. 100:4622-4629.

Apell, H.J. 2003. Toward an understanding of ion transport through the Na,K-ATPase. *Ann N Y Acad Sci*. 986:133-140.

Armstrong, C.M. 2003. Voltage-gated K channels. *Sci STKE*. 2003:re10.

Armstrong, C.M., F. Bezanilla and E. Rojas. 1973. Destruction of sodium conductance inactivation in squid axons perfused with pronase. *J Gen Physiol*. 62:375-391.

Armstrong, C.M., F.M. Bezanilla and P. Horowicz. 1972. Twitches in the presence of ethylene glycol bis(-aminoethyl ether)-N,N'-tetracetic acid. *Biochim Biophys Acta*. 267:605-608.

Ashcroft, F.M. 2000. Ion channels and disease. Academic Press, 481 pp.

Bahring, R., L.M. Boland, A. Varghese, M. Gebauer and O. Pongs. 2001. Kinetic analysis of open- and closed-state inactivation transitions in human Kv4.2 A-type potassium channels. *J Physiol*. 535:65-81.

Baker. 1978. Proton Co-Transport of Organic Solutes by Plant Cells. *New Phytologist*. 81:485-497.

Ball, F.G. and J.A. Rice. 1992. Stochastic models for ion channels: introduction and bibliography. *Math. Biosci*. 112:189-206.

Ball, F.G., G.F. Yeo, R.K. Milne, R.O. Edeson, B.W. Madsen and M.S. Sansom. 1993. Single ion channel models incorporating aggregation and time interval omission. *Biophys J*. 64:357-374.

Ban, F., P. Kusalik and D.F. Weaver. 2004. Density functional theory investigations on the chemical basis of the selectivity filter in the K^+ channel protein. *J Am Chem Soc*. 126:4711-4716.

Baukrowitz, T. and G. Yellen. 1996. Use-dependent blockers and exit rate of the last ion from the multi-ion pore of a K^+ channel. *Science*. 271:653-656.

Baum, L.E., T. Petrie, G. Soules and N. Weiss. 1970. A maximization technique occurring in the statistical analysis of probabilistic functions of Markov chains. *Ann Math Statist*. 41:164-171.

Beckstein, O., P.C. Biggin, P. Bond, J.N. Bright, C. Domene, A. Grottesi, J. Holyoake and M.S. Sansom. 2003. Ion channel gating: insights via molecular simulations. *FEBS Lett*. 555:85-90.

Beilby, M.J. 1985. Potassium channels at *Chara* plasmalemma. *J Exp Bot*. 36:228-239.

Beimgraben, C. 2007. Assemblierung und Pharmakologie von spannungsabhängigen KCNQ (Kv7) K^+ Kanälen. PhD thesis, Christian Albrechts University, Kiel.

Bentrop, D., M. Beyermann, R. Wissmann and B. Fakler. 2001. NMR structure of the "ball-and-chain" domain of KCNMB2, the beta 2-subunit of large conductance Ca^{2+}- and voltage-activated potassium channels. *J Biol Chem*. 276:42116-42121.

Bernèche, S. and B. Roux. 2000. Molecular dynamics of the KcsA K^+ channel in a bilayer membrane. *Biophys J*. 78:2900-2917.

Bernèche, S. and B. Roux. 2005. A gate in the selectivity filter of potassium channels. *Structure*. 13:591-600.

Bertl, A., C.L. Slayman and D. Gradmann. 1993. Gating and conductance in an outward-rectifying K^+ channel from the plasma membrane of Saccharomyces cerevisiae. *J Membr Biol*. 132:183-199.

Bezanilla, F. 2000. The voltage sensor in voltage-dependent ion channels. *Physiol Rev*. 80:555-592.

Bezanilla, F. and C.M. Armstrong. 1972. Negative conductance caused by entry of sodium and cesium ions into the potassium channels of squid axons. *J Gen Physiol*. 60:588-608.

Bharucha Reid, A.T. 1960. Elements of the Theory of Markov Processes and their Applications. McGraw Hill, New York. 468 pp.

Bichet, D., M. Grabe, Y.N. Jan and L.Y. Jan. 2006. Electrostatic interactions in the channel cavity as an important determinant of potassium channel selectivity. *Proc Natl Acad Sci U S A*. 103:14355-14360.

Blatz, A.L. and K.L. Magleby. 1984. Ion conductance and selectivity of single calcium-activated potassium channels in cultured rat muscle. *J Gen Physiol*. 84:1-23.

Blatz, A.L. and K.L. Magleby. 1986. Correcting single channel data for missed events. *Biophys J*. 49:967-980.

Blunck, R., J.F. Cordero-Morales, L.G. Cuello, E. Perozo and F. Bezanilla. 2006. Detection of the opening of the bundle crossing in KcsA with fluorescence lifetime spectroscopy reveals the existence of two gates for ion conduction. *J Gen Physiol*. 128:569-581.

Blunck, R., U. Kirst, T. Riessner and U. Hansen. 1998. How powerful is the dwell-time analysis of multichannel records? *J Membr Biol*. 165:19-35.

Blunck, R., D.M. Starace, A.M. Correa and F. Bezanilla. 2004. Detecting rearrangements of *Shaker* and NaChBac in real-time with fluorescence spectroscopy in patch-clamped mammalian cells. *Biophys J*. 86:3966-3980.

Boels, H.D. and U.-P. Hansen. 1982. Light and electrical current stimulate the same feed-back system in *Nitella*. *Plant & Cell Physiol*. 23:343-346.

Bond, P.J., J. Holyoake, A. Ivetac, S. Khalid and M.S. Sansom. 2007. Coarse-grained molecular dynamics simulations of membrane proteins and peptides. *J Struct Biol*. 157:593-605.

Brelidze, T.I. and K.L. Magleby. 2005. Probing the geometry of the inner vestibule of BK channels with sugars. *J Gen Physiol*. 126:105-121.

Brelidze, T.I., X. Niu and K.L. Magleby. 2003. A ring of eight conserved negatively charged amino acids doubles the conductance of BK channels and prevents inward rectification. *Proc Natl Acad Sci U S A*. 100:9017-9022.

Caceci, M.S. and W.P. Cacheris. 1984. Fitting curves to data - the simplex algorithm is the answer. *BYTE*. 5:340-362.

Caliebe, A., U. Rosler and U.P. Hansen. 2002. A chi^2 test for model determination and sublevel detection in ion channel analysis. *J Membr Biol*. 185:25-41.

Calvacanti, S. and F. Fontanazzi. 1999. Deterministic model of ion channel flipping with fractal scaling of kinetic rates. *Ann Biomed Eng*. 165:682-695.

Camproux, A.C., R. Gautier and P. Tuffery. 2004. A hidden markov model derived structural alphabet for proteins. *J Mol Biol*. 339:591-605.

Camproux, A.C. and P. Tuffery. 2005. Hidden Markov model-derived structural alphabet for proteins: the learning of protein local shapes captures sequence specificity. *Biochim Biophys Acta*. 1724:394-403.

Capener, C.E., P. Proks, F.M. Ashcroft and M.S. Sansom. 2003. Filter flexibility in a mammalian K channel: models and simulations of Kir6.2 mutants. *Biophys J*. 84:2345-2356.

Catterall, W.A. 2000. From ionic currents to molecular mechanisms: the structure and function of voltage-gated sodium channels. *Neuron*. 26:13-25.

Chang, G. and C.B. Roth. 2001. Structure of MsbA from E. coli: a homolog of the multidrug resistance ATP binding cassette (ABC) transporters. *Science*. 293:1793-1800.

Choi, K.L., R.W. Aldrich and G. Yellen. 1991. Tetraethylammonium blockade distinguishes two inactivation mechanisms in voltage-activated K^+ channels. *Proc Natl Acad Sci U S A*. 88:5092-5095.

Claydon, T.W., S.Y. Makary, K.M. Dibb and M.R. Boyett. 2003. The selectivity filter may act as the agonist-activated gate in the G protein-activated Kir3.1/Kir3.4 K^+ channel. *J Biol Chem*. 278:50654-50663.

Cole, K.S. 1968. Membranes, Ions and Impulses. Univ. Calif. Press., Berkeley and Los Angeles.

Cole, K.S. and H.J. Curtis. 1938. Electric impedance of nitella during activity. *J Gen Physiol*. 22:

Cole, K.S. and H.J. Curtis. 1939. Electrical impedance of squid giant axon during activity. *J Gen Physiol*. 22:649-670.

Cole, K.S. and J.W. Moore. 1960. Potassium ion current in the squid giant axon: dynamic characteristica. *Biophys J*. 1:1-14.

Collander, R. and H. Barlund. 1933. Permeabilitätsstudien an *Chara* ceratophylla. *Acto Botanica Fennica*. 11:1-131.

Colquhoun, D., C.J. Hatton and A.G. Hawkes. 2003. The quality of maximum likelihood estimates of ion channel rate constants. *J Physiol*. 547:699-728.

Colquhoun, D. and A.G. Hawkes. 1977. Relaxation and fluctuations of membrane currents that flow through drug-operated channels. *Proc R Soc Lond B Biol Sci*. 199:231-262.

Colquhoun, D. and A.G. Hawkes. 1982. On the stochastic properties of bursts of single ion channel openings and of clusters of bursts. *Philos Trans R Soc Lond B Biol Sci*. 300:1-59.

Colquhoun, D. and A.G. Hawkes. 1990. Stochastic properties of ion channel openings and bursts in a membrane patch that contains two channels: evidence concerning the number of channels present when a record containing only single openings is observed. *Proc R Soc Lond B Biol Sci*. 240:453-477.

Colquhoun, D., A.G. Hawkes and K. Srodzinski. 1996. Joint distributions of apparent open times and shut times of single ion channels and the maximum likelihood fitting of mechanisms. *Phil. Trans. R. Soc. Lond. A*. 354:2555-2590.

Compoint, M., P. Carloni, C. Ramseyer and C. Girardet. 2004. Molecular dynamics study of the KcsA channel at 2.0-A resolution: stability and concerted motions within the pore. *Biochim Biophys Acta*. 1661:26-39.

Cordero-Morales, J.F., L.G. Cuello and E. Perozo. 2006. Voltage-dependent gating at the KcsA selectivity filter. *Nat Struct Mol Biol*. 13:319-322.

Cordero-Morales, J.F., L.G. Cuello, Y. Zhao, V. Jogini, D.M. Cortes, B. Roux and E. Perozo. 2006. Molecular determinants of gating at the potassium-channel selectivity filter. *Nat Struct Mol Biol*. 13:311-318.

Corey, D.P. and C.F. Stevens. 1983. Science and Technology of patch-recording electrodes. In Single Channel Recording. B. Sakmann, and E. Neher, editors. Plenum Press, New York and London. 53-68.

Cox, D.H., J. Cui and R.W. Aldrich. 1997. Separation of gating properties from permeation and block in mslo large conductance Ca-activated K^+ channels. *J Gen Physiol*. 109:633-646.

Crouzy, S.C. and F.J. Sigworth. 1990. Yet another approach to the dwell-time omission problem of single-channel analysis. *Biophys J*. 58:731-743.

Csanady, L. 2000. Rapid kinetic analysis of multichannel records by a simultaneous fit to all dwell-time histograms. *Biophys J*. 78:785-799.

DeCoursey, T.E., S.Y. Kim, M.R. Silver and F.N. Quandt. 1996. Ion channel expression in PMA-differentiated human THP-1 macrophages. *J Membr Biol*. 152:141-157.

del Camino, D., M. Holmgren, Y. Liu and G. Yellen. 2000. Blocker protection in the pore of a voltage-gated K^+ channel and its structural implications. *Nature*. 403:321-325.

del Camino, D. and G. Yellen. 2001. Tight steric closure at the intracellular activation gate of a voltage-gated K^+ channel. *Neuron*. 32:649-656.

Demo, S.D. and G. Yellen. 1992. Ion effects on gating of the Ca^{2+}-activated K^+ channel correlate with occupancy of the pore. *Biophys J*. 61:639-648.

Doyle, D.A. 2004. Structural changes during ion channel gating. *Trends Neurosci*. 27:298-302.

Doyle, D.A., J. Morais Cabral, R.A. Pfuetzner, A. Kuo, J.M. Gulbis, S.L. Cohen, B.T. Chait and R. MacKinnon. 1998. The structure of the potassium channel: molecular basis of K^+ conduction and selectivity. *Science*. 280:69-77.

Draber, S. 1994. Methods for Analyzing Fast Single-Channel Data and Results on the K^+-Channel under Cs^+-Blockade and under control Conditions. PhD thesis, Christian Albrechts University, Kiel.

Draber, S. and U.P. Hansen. 1994. Fast single-channel measurements resolve the blocking effect of Cs^+ on the K^+ channel. *Biophys J*. 67:120-129.

Draber, S. and R. Schultze. 1994. Correction for missed events based on a realistic model of a detector. *Biophys J*. 66:191-201.

Draber, S. and R. Schultze. 1994. Detection of jumps in single-channel data containing subconductance levels. *Biophys J*. 67:1404-1413.

Draber, S., R. Schultze and U.P. Hansen. 1991. Patch-clamp studies on the anomalous mole fraction effect of the K^+ channel in cytoplasmic droplets of Nitella: an attempt to distinguish between a multi-ion single-file pore and an enzyme kinetic model with lazy state. *J Membr Biol*. 123:183-190.

Durell, S.R. and H.R. Guy. 2001. A family of putative Kir potassium channels in prokaryotes. *BMC Evol Biol*. 1:14.

Eisenman, G. 1962. Cation selective glass electrodes and their mode of operation. *Biophys J*. 2:259-323.

Eisenman, G. and R. Horn. 1983. Ionic selectivity revisited: The role of kinetic and equilibrium processes in ion permeation through channels. *J Membr Biol*. 76:197-225.

Eisenman, G. and S. Krasne. 1973. Further considerations on the ion selectivity of carrier molecules and membranes. In IV International Biophysics Congress Symposium on Membrane Structure and Function. Moscow.

Farokhi, A., M. Keunecke and U.P. Hansen. 2000. The anomalous mole fraction effect in Chara: gating at the edge of temporal resolution. *Biophys J*. 79:3072-3082.

Feller, W. 1968. An Introduction to Probability Theory and Its Applications, Vol. 1. John Wiley & Sons,

Ferguson, W.B. 1991. Competitive Mg^{2+} block of a large-conductance, Ca^{2+}-activated K^+ channel in rat skeletal muscle. Ca^{2+}, Sr^{2+}, and Ni^{2+} also block. *J Gen Physiol*. 98:163-181.

Ferrer, T., J. Rupp, D.R. Piper and M. Tristani-Firouzi. 2006. The S4-S5 linker directly couples voltage sensor movement to the activation gate in the human ether-a'-go-go-related gene (hERG) K^+ channel. *J Biol Chem*. 281:12858-12864.

Fisahn, J., U.P. Hansen and D. Gradmann. 1986. Determination of charge, stoichiometry and reaction constants from I-V curve studies on a K^+ transporter in *Nitella*. *J Membr Biol*. 94:245-252.

FitzHugh, R. 1983. Statistical properties of the asymmetric random telegraph signal with application to single channel analysis. *Mathematical Bioscience*. 64:75-89.

Fredkin, D.R. and J.A. Rice. 1992. Maximum likelihood estimation and identification directly from single-channel recordings. *Proc. Roy. Soc. Lond. B*. 249:125-132.

Fredkin, D.R. and J.A. Rice. 2001. Fast evaluation of the likelihood of an HMM: Ion channel currents with filtering and colored noise. *IEEE Trans Sig Proc*. 49:625–633.

Fujiwara, Y. and Y. Kubo. 2006. Functional roles of charged amino acid residues on the wall of the cytoplasmic pore of Kir2.1. *J Gen Physiol*. 127:401-419.

Garofoli, S. 2003. Modeling permeation energetics in the KcsA potassium channel. *Biophys J*. 84:2814-2830.

Gazzarrini, S., A. Abenavoli, D. Gradmann, G. Thiel and A. Moroni. 2006. Electrokinetics of miniature K^+ channel: open-state V sensitivity and inhibition by K^+ driving force. *J Membr Biol*. 214:9-17.

Gazzarrini, S., J.L. Etten, D. DiFrancesco, G. Thiel and A. Moroni. 2002. Voltage-dependence of virus-encoded miniature K^+ channel Kcv. *J Membr Biol*. 187:15-25.

Gazzarrini, S., M. Kang, J.L. Van Etten, S. Tayefeh, S.M. Kast, D. DiFrancesco, G. Thiel and A. Moroni. 2004. Long distance interactions within the potassium channel pore are revealed by molecular diversity of viral proteins. *J Biol Chem*. 279:28443-28449.

Gibor, G., D. Yakubovich, A. Rosenhouse-Dantsker, A. Peretz, H. Schottelndreier, G. Seebohm, N. Dascal, D. E. Logothetis, Y. Paas, and B. Attali. 2007. An inactivation gate in the selectiovity filter of KCNQ1 potassium channels. *Biophys. J*. 93:4159-4172.

Giraldez, T., T.E. Hughes and F.J. Sigworth. 2005. Generation of functional fluorescent BK channels by random insertion of GFP variants. *J Gen Physiol*. 126:429-438.

Golub, G.H. and C.F. Van Loan. 1983. The Matrix Exponential. In Matrix Computations. Johns Hopkins University Press, Baltimore. 396-403.

Gradmann, D., H.G. Klieber and U.P. Hansen. 1987. Reaction kinetic parameters for ion transport from steady-state current-voltage curves. *Biophys J*. 51:569-585.

Graham, F.L., J. Smiley, W.C. Russell and R. Nairn. 1977. Characteristics of a human cell line transformed by DNA from human adenovirus type 5. *J Gen Virol*. 36:59-74.

Green, W.N. and O.S. Andersen. 1991. Surface charges and ion channel function. *Annu Rev Physiol*. 53:341-359.

Guidoni, L., V. Torre and P. Carloni. 2000. Water and potassium dynamics inside the KcsA K^+ channel. *FEBS Lett*. 477:37-42.

Haak, T.J. 2000. Entwicklung und Erprobung einer neuartigen Methode der Einzelkanalstrommessung in bioogischen Membranen. Diploma thesis, Christian Albrechts University, Kiel.

Hamill, O.P., A. Marty, E. Neher, B. Sakmann and F.J. Sigworth. 1981. Improved patch-clamp techniques for high-resolution current recording from cells and cell-free membrane patches. *Pflugers Arch*. 391:85-100.

Hansen, U.P. 1969. Demonstrationsversuche an Algenzellen zur Signalleitung in der Nervenfaser. *Math Phys Semesterber NF*. 16:150-169.

Hansen, U.P. 1986. Reaction kinetic models of pumps, cotransporters and channels. In: Ion Channels and Electrogenic Pumps in Biomembranes. Abstracts of Lectures and Posters. In Osaka University. L13-L33.

Hansen, U.P. 1990. Implications of control theory for homeostasis and phosphorylation of transport molecules. *Bot Acta*. 103:15-23.

Hansen, U.P., A. Albertsen, C. Moldaenke, S. Draber and R. Schultze. 1995. Detecting Events in Signals from Sensors: the Hinkley Detector is the Answer *Sensors and Materials*. 7:289-300.

Hansen, U.P., O. Cakan, M. Abshagen-Keunecke and A. Farokhi. 2003. Gating models of the anomalous mole-fraction effect of single-channel current in Chara. *J Membr Biol*. 192:45-63.

Hansen, U.P. and J. Fisahn. 1987. I/V-curve studies of the control of a K^+-transporter in *Nitella* by temperature. *J Membr Biol*. 98:1-13.

Hansen, U.P., D. Gradmann, D. Sanders and C.L. Slayman. 1981. Interpretation of current-voltage relationships for "active" ion transport systems: I. Steady-state reaction-kinetic analysis of class-I mechanisms. *J Membr Biol*. 63:165-190.

Hansen, U.P., M. Keunecke and R. Blunck. 1997. Gating and permeation models of plant channels. . *J Exp Bot*. 48:365-382.

Hansen, U.P., J. Tittor and D. Gradmann. 1983. Interpretation of current-voltage relationships for "active" ion transport systems: II. Nonsteady-state reaction kinetic analysis of class I mechanisms with one slow time-constant. *J Membr Biol*. 75:141-169.

Harlfinger, P. 2000. Bestimmung sehr schneller Übergangsraten in Markov-Prozessen durch verbesserte Berücksichtigung der Amplitudenverteilung im direkten Zeitreihenfit. Diploma thesis, Christian Albrechts University, Kiel.

Harlfinger, P. 2003. Detektion schneller Übergangsraten in Markov-Prozessen durch kombinierte Auswertung von Amplitudenhistogramm und Zeitreihe. PhD thesis, Christian Albrechts University, Kiel.

Haug, T., D. Sigg, S. Ciani, L. Toro, E. Stefani and R. Olcese. 2004. Regulation of K^+ flow by a ring of negative charges in the outer pore of BK_{Ca} channels. Part I: Aspartate 292 modulates K^+ conduction by external surface charge effect. *J Gen Physiol*. 124:173-184.

Heinemann, S.H. and F.J. Sigworth. 1991. Open channel noise. VI. Analysis of amplitude histograms to determine rapid kinetic parameters. *Biophys J*. 60:577-587.

Hertel, B., S. Tayefeh, M. Mehmel, S.M. Kast, J. Van Etten, A. Moroni and G. Thiel. 2006. Elongation of outer transmembrane domain alters function of miniature K^+ channel Kcv. *J Membr Biol*. 210:21-29.

Hille, B. 1973. Potassium channels in myelinated nerve: Selective permeability to small cations. *J Gen Physiol*. 61:669-686.

Hille, B. 1992. Ionic Channels of Excitable Membranes. 2nd edition. Sinauer Associates Inc., Sunderland, MA. 607 pp.

Hille, B., C.M. Armstrong and R. MacKinnon. 1999. Ion channels: from idea to reality. *Nat Med*. 5:1105-1109.

Hille, B. and W. Schwarz. 1978. Potassium channels as multi-ion single-file pores. *J Gen Physiol*. 72:409-442.

Hinkley, D.V. 1971. Interference about the change-point from cumulative-sum-tests. *Biometrika*. 57:1-17.

Hodgkin, A.L. and A.F. Huxley. 1952. A quantitative description of membrane current and its application to conduction and excitation in nerve. *J Physiol*. 117:500-544.

Hodgkin, A.L. and R.D. Keynes. 1955. The potassium permeability of a giant nerve fibre. *J Physiol*. 128:61-88.

Holland, I.B. and M.A. Blight. 1999. ABC-ATPases, adaptable energy generators fuelling transmembrane movement of a variety of molecules in organisms from bacteria to humans. *J Mol Biol*. 193:381-399.

Hope, A.B. 1961. Ionic relations of cells of *Chara australis*. V. The action potential. *Austr J Exp Biol*. 14:313-322.

Hoshi, T., W.N. Zagotta and R.W. Aldrich. 1990. Biophysical and molecular mechanisms of *Shaker* potassium channel inactivation. *Science*. 250:533-538.

Huang, X.D., Y. Ariki and M.A. Jack. 1990. Markov Models for Speech Recognition. Edinburgh University Press, Edinburgh.

Huang, Y., M.J. Lemieux, J. Song, M. Auer and D.N. Wang. 2003. Structure and mechanism of the glycerol-3-phosphate transporter from *Escherichia coli*. *Science*. 301:616-620.

Huth, T. 2005. 4-Mode-Gating-Modell; Modellierung der Inaktivierung des Natriumkanals. PhD thesis, Christian Albrecht University, Kiel.

Huth, T., I. Schroeder and U.P. Hansen. 2006. The power of two-dimensional dwell-time analysis for model discrimination, temporal resolution, multichannel analysis and level detection. *J Membr Biol*. 214:19-32.

Ilan, N. and S.A. Goldstein. 2001. Kcnko: single, cloned potassium leak channels are multi-ion pores. *Biophys J*. 80:241-253.

Immke, D., M. Wood, L. Kiss and S.J. Korn. 1999. Potassium-dependent changes in the conformation of the Kv2.1 potassium channel pore. *J Gen Physiol*. 113:819-836.

Isacoff, E.Y., Y.N. Jan and L.Y. Jan. 1990. Evidence for the formation of heteromultimeric potassium channels in *Xenopus* oocytes. *Nature*. 345:530-534.

Jackson, M.B. 1997. Inversion of Markov processes to determine rate constants from single-channel data. *Biophys J*. 73:1382-1394.

Jagendorf, A.T. and E. Uribe. 1966. Photophosphorylation and the chemi-osmotic hypothesis. *Brookhaven Symp Biol*. 19:215-245.

Jerng, H.H. and M. Covarrubias. 1997. K^+ channel inactivation mediated by the concerted action of the cytoplasmic N- and C-terminal domains. *Biophys J*. 72:163-174.

Jerng, H.H., M. Shahidullah and M. Covarrubias. 1999. Inactivation gating of Kv4 potassium channels: molecular interactions involving the inner vestibule of the pore. *J Gen Physiol*. 113:641-660.

Jiang, Y., A. Lee, J. Chen, M. Cadene, B.T. Chait and R. MacKinnon. 2002. Crystal structure and mechanism of a calcium-gated potassium channel. *Nature*. 417:515-522.

Jiang, Y., A. Lee, J. Chen, M. Cadene, B.T. Chait and R. MacKinnon. 2002. The open pore conformation of potassium channels. *Nature*. 417:523-526.

Jiang, Y., A. Lee, J. Chen, V. Ruta, M. Cadene, B.T. Chait and R. MacKinnon. 2003. X-ray structure of a voltage-dependent K^+ channel. *Nature*. 423:33-41.

Jogini, V. and B. Roux. 2007. Dynamics of the Kv1.2 voltage-gated K^+ channel in a membrane environment. *Biophys J*. 93:3070-3082.

Junge, W., H. Lill and S. Engelbrecht. 1997. ATP synthase: an electrochemical transducer with rotatory mechanics. *Trends Biochem Sci*. 22:420-423.

Kang, M., A. Moroni, S. Gazzarrini, D. DiFrancesco, G. Thiel, M. Severino and J.L. Van Etten. 2004. Small potassium ion channel proteins encoded by *chlorella* viruses. *Proc Natl Acad Sci U S A*. 101:5318-5324.

Kast, S.M., T. Kloss, S. Tayefeh and G. Thiel. 2008. Potassium channel filters select K^+ over Na^+ by providing different binding sites. *Proc. Natl. Acad. Sci. U S A*. (submitted).

Kawahara, K., M. Hunter and G. Giebisch. 1990. Calcium-activated potassium channels in the luminal membrane of Amphiuma diluting segment: voltage-dependent block by intracellular Na^+ upon depolarisation. *Pflugers Arch*. 416:422-427.

Keunecke, M. 1995. Der anomale Molfraktionseffekt im K^+ Kanal bei *Chara*. Diploma thesis, Christian Albrechts University, Kiel.

Keunecke, M. 2000. Untersuchungen zum Ionentransport aus dem Xylem in den Symplasten des Maisblattes. PhD thesis, Christian Albrechts University, Kiel.

Khalili-Araghi, F., E. Tajkhorshid and K. Schulten. 2006. Dynamics of K^+ ion conduction through Kv1.2. *Biophys J*. 91:L72-74.

Kienker, P. 1989. Equivalence of aggregated Markov models of ion-channel gating. *Proc R Soc Lond Biol*. 236: 269-309.

Kijima, S. and H. Kijima. 1987. Statistical analysis of channel current from a membrane patch. I. Some stochastic properties of ion channels or molecular systems in equilibrium. *J Theor Biol*. 128:423-434.

Kijima, S. and H. Kijima. 1987. Statistical analysis of channel current from a membrane patch. II. A stochastic theory of a multi-channel system in the steady-state. *J Theor Biol*. 128:435-455.

Kiss, L., J. LoTurco and S.J. Korn. 1999. Contribution of the selectivity filter to inactivation in potassium channels. *Biophys J*. 76:253-263.

Kitasato, H. 1968. The influence of H^+ on the membrane potential and ion fluxes of Nitella. *J Gen Physiol*. 52:60-87.

Klein, S., J. Timmer and J. Honerkamp. 1997. Analysis of multichannel patch clamp recordings by hidden Markov models. *Biometrics*. 53:870-884.

Klieber, H.G. and D. Gradmann. 1993. Enzyme kinetics of the prime K^+ channel in the tonoplast of *Chara*: selectivity and inhibition. *J Membr Biol*. 132:253-265.

Konski, A., D. Watkins-Bruner, H. Brereton, S. Feigenberg and G. Hanks. 2006. Long-term hormone therapy and radiation is cost-effective for patients with locally advanced prostate carcinoma. *Cancer*. 106:51-57.

Korn, S.J. and R. Horn. 1988. Statistical discrimination of fractal and Markov models of single-channel gating. *Biophys J*. 54:871-877.

Koval, O.M., Y. Fan and B.S. Rothberg. 2007. A role for the S0 transmembrane segment in voltage-dependent gating of BK channels. *J Gen Physiol*. 129:209-220.

Kuo, A., J.M. Gulbis, J.F. Antcliff, T. Rahman, E.D. Lowe, J. Zimmer, J. Cuthbertson, F.M. Ashcroft, T. Ezaki and D.A. Doyle. 2003. Crystal structure of the potassium channel KirBac1.1 in the closed state. *Science*. 300:1922-1926.

Kurata, H.T. and D. Fedida. 2006. A structural interpretation of voltage-gated potassium channel inactivation. *Prog Biophys Mol Biol*. 92:185-208.

Lankat-Buttgereit, B. and R. Tampe. 2002. The transporter associated with antigen processing: function and implications in human diseases. *Physiol Rev*. 82:187-204.

Larsson, H.P. and F. Elinder. 2000. A conserved glutamate is important for slow inactivation in K^+ channels. *Neuron*. 27:573-583.

Latorre, R., A. Oberhauser, P. Labarca and O. Alvarez. 1989. Varieties of calcium-activated potassium channels. *Annu Rev Physiol*. 51:385-399.

Lauger, P. and G. Stark. 1970. Kinetics of carrier-mediated ion transport across lipid bilayer membranes. *Biochim Biophys Acta*. 211:458-466.

Lehmann-Horn, F. and K. Jurkat-Rott. 1999. Voltage-gated ion channels and hereditary disease. *Physiol Rev*. 79:1317-1372.

LeMasurier, M., L. Heginbotham and C. Miller. 2001. KcsA: it's a potassium channel. *J Gen Physiol*. 118:303-314.

Li, X., G.C. Bett, X. Jiang, V.E. Bondarenko, M.J. Morales and R.L. Rasmusson. 2003. Regulation of N- and C-type inactivation of Kv1.4 by pH_o and K^+: evidence for transmembrane communication. *Am J Physiol Heart Circ Physiol*. 284:H71-80.

Li, Y., I. Berke, L. Chen and Y. Jiang. 2007. Gating and inward rectifying properties of the MthK K^+ channel with and without the gating ring. *J Gen Physiol*. 129:109-120.

Liebovitch, L., J. Fischbarg and J. Koniarek. 1987. Ion channel kinetics: a model based on fractal scaling rather then multistate Markov processes. *Math. Biosci*. 84:37-68.

Liman, E.R., P. Hess, F. Weaver and G. Koren. 1991. Voltage-sensing residues in the S4 region of a mammalian K^+ channel. *Nature*. 353:752-756.

Liu, Y.S., P. Sompornpisut and E. Perozo. 2001. Structure of the KcsA channel intracellular gate in the open state. *Nat Struct Biol*. 8:883-887.

Long, S.B., E.B. Campbell and R. Mackinnon. 2005. Crystal structure of a mammalian voltage-dependent *Shaker* family K^+ channel. *Science*. 309:897-903.

Loots, E. and E.Y. Isacoff. 2000. Molecular coupling of S4 to a K^+ channel's slow inactivation gate. *J Gen Physiol*. 116:623-636.

Lopez-Barneo, J., T. Hoshi, S.H. Heinemann and R.W. Aldrich. 1993. Effects of external cations and mutations in the pore region on C-type inactivation of *Shaker* potassium channels. *Receptors Channels*. 1:61-71.

Löptien, U. 1999. Modellidentifikation bei der Untersuchung von Ionenkanälen. Diploma thesis, Christian Albrechts University, Kiel.

Loussouarn, G., E.N. Makhina, T. Rose and C.G. Nichols. 2000. Structure and Dynamics of the Pore of Inwardly Rectifying K_{ATP} Channels. *J Biol Chem*. 275:1137–1144.

Lu, R., A. Alioua, Y. Kumar, M. Eghbali, E. Stefani and L. Toro. 2006. MaxiK channel partners: physiological impact. *J Physiol*. 570:65-72.

Lu, T., A.Y. Ting, J. Mainland, Y.G. Jan, P.G. Schultz and J. Yang. 2001. Probing ion permeation and gating in a K^+ channel with backbone mutations in the selectivity filter. *Nat Neurosci*. 4:239-246.

Lu, T., L. Wu, J. Xiao and J. Yang. 2001. Permeant ion-dependent changes in gating of Kir2.1 inward rectifier potassium channels. *J Gen Physiol*. 118:509-522.

Lu, Z. and R. MacKinnon. 1994. A conductance maximum observed in an inward-rectifier potassium channel. *J Gen Physiol*. 104:477-486.

Luhring, H. 1999. pH-sensitive gating kinetics of the maxi-K channel in the tonoplast of *Chara australis*. *J Membr Biol*. 168:47-61.

Lühring, H.E. 1986. Recording of single K^+ channels in the membrane of cytoplasmic droplets of *Chara australis*. *Protoplasma*. 133:

Maathuis, F.J. and D. Sanders. 1992. Plant membrane transport. *Curr Opin Cell Biol*. 4:661-669.

Magleby, K.L. 2001. Kinetic gating mechanisms for BK channels: when complexity leads to simplicity. *J Gen Physiol*. 118:583-587.

Magleby, K.L. and L. Song. 1992. Dependency plots suggest the kinetic structure of ion channels. *Proc Biol Sci*. 249:133-142.

Magleby, K.L. and D.S. Weiss. 1990. Estimating kinetic parameters for single channels with simulation. A general method that resolves the missed event problem and accounts for noise. *Biophys J*. 58:1411-1426.

Magleby, K.L. and D.S. Weiss. 1990. Identifying kinetic gating mechanisms for ion channels by using two-dimensional distributions of simulated dwell times. *Proc Biol Sci*. 241:220-228.

Mann, G.E., D.L. Yudilevich and L. Sobrevia. 2003. Regulation of amino acid and glucose transporters in endothelial and smooth muscle cells. *Physiol Rev*. 83:183-252.

Marmont, G. 1949. Studies on the axon membrane; a new method. *J Cell Physiol*. 34:351-382.

Marty, A. 1983. Blocking of large unitary calcium-dependent potassium currents by internal sodium ions. *Pflugers Arch*. 396:179-181.

Matteson, D.R. and R.P. Swenson, Jr. 1986. External monovalent cations that impede the closing of K channels. *J Gen Physiol*. 87:795-816.

McManus, O.B. and K.L. Magleby. 1988. Kinetic states and modes of single large-conductance calcium-activated potassium channels in cultured rat skeletal muscle. *J Physiol*. 402:79-120.

Meera, P., M. Wallner, M. Song and L. Toro. 1997. Large conductance voltage- and calcium-dependent K^+ channel, a distinct member of voltage-dependent ion channels with seven N-terminal transmembrane segments (S0-S6), an extracellular N terminus, and an intracellular (S9-S10) C terminus. *Proc Natl Acad Sci U S A*. 94:14066-14071.

Melishchuk, A., A. Loboda and C.M. Armstrong. 1998. Loss of S*haker* K channel conductance in 0 K^+ solutions: role of the voltage sensor. *Biophys J*. 75:1828-1835.

Michalek, S., M. Wagner and J. Timmer. 2000. A new approximate likelihood estimator for ARMA-filtered hidden Markov-models. *IEEE Trans Sig Proc*. 48:1537–1547.

Miller, C. 1991. 1990: annus mirabilis of potassium channels. *Science*. 252:1092-1096.

Milne, R.K., G.F. Yeo, B.W. Madsen and R.O. Edeson. 1989. Estimation of single channel kinetic parameters from data subject to limited time resolution. *Biophys J*. 55:673-676.

Mitchell, P. 1966. Chemiosmotic coupling in oxidative and photosynthetic phosphorylation. *Biol Ren*. 41:455-502.

Miyazawa, A., Y. Fujiyoshi and N. Unwin. 2003. Structure and gating mechanism of the acetylcholine receptor pore. *Nature*. 423:949-955.

Mlynarski, W., A.I. Tarasov, A. Gach, C.A. Girard, I. Pietrzak, L. Zubcevic, J. Kusmierek, T. Klupa, M.T. Malecki and F.M. Ashcroft. 2007. Sulfonylurea improves CNS function in a case of intermediate DEND syndrome caused by a mutation in KCNJ11. *Nat Clin Pract Neurol*. 3:640-645.

Morais-Cabral, J.H., Y. Zhou and R. MacKinnon. 2001. Energetic optimization of ion conduction rate by the K^+ selectivity filter. *Nature*. 414:37-42.

Moss, B.L. and K.L. Magleby. 2001. Gating and conductance properties of BK channels are modulated by the S9-S10 tail domain of the alpha subunit. A study of mSlo1 and mSlo3 wild-type and chimeric channels. *J Gen Physiol*. 118:711-734.

Moss, G.W. and E. Moczydlowski. 1996. Rectifying conductance substates in a large conductance Ca^{2+}-activated K^+ channel: evidence for a fluctuating barrier mechanism. *J Gen Physiol*. 107:47-68.

Mullins, L.J. 1959. The penetration of some cations into muscle. *J Gen Physiol*. 42:817-829.

Mullins, L.J. 1962. Efflux of chloride ions during the action potential of Nitella. *Nature*. 196:986-987.

Murata, Y., Y. Fujiwara and Y. Kubo. 2002. Identification of a site involved in the block by extracellular Mg^{2+} and Ba^{2+} as well as permeation of K^+ in the Kir2.1 K^+ channel. *J Physiol*. 544:665-677.

Murata, Y., H. Iwasaki, M. Sasaki, K. Inaba and Y. Okamura. 2005. Phosphoinositide phosphatase activity coupled to an intrinsic voltage sensor. *Nature*. 435:1239-1243.

Neher, E. and B. Sakmann. 1976. Single-channel currents recorded from membrane of denervated frog muscle fibres. *Nature*. 260:799-802.

Nelson, P.H. 2002. A permeation theory for single-file ion channels: corresponding occupancy states produce Michaelis-Menton behaviour. *J. Chem. Phys*. 117:11396-11403.

Nimigean, C.M., J.S. Chappie and C. Miller. 2003. Electrostatic tuning of ion conductance in potassium channels. *Biochemistry*. 42:9263-9268.

Nimigean, C.M. and C. Miller. 2002. Na^+ block and permeation in a K^+ channel of known structure. *J Gen Physiol*. 120:323-335.

Niu, X., X. Qian and K.L. Magleby. 2004. Linker-gating ring complex as passive spring and Ca^{2+}-dependent machine for a voltage- and Ca^{2+}-activated potassium channel. *Neuron*. 42:745-756.

Noskov, S.Y., S. Bernèche and B. Roux. 2004. Control of ion selectivity in potassium channels by electrostatic and dynamic properties of carbonyl ligands. *Nature*. 431:830-834.

Noskov, S.Y. and B. Roux. 2006. Ion selectivity in potassium channels. *Biophys Chem*. 124:279-291.

Numberger, M. and A. Draguhn. 1996. Patch-Clamp-Technik. Spektrum Akademischer Verlag GmbH, Heidelberg, Berlin, Oxford.

Ogielska, E.M. and R.W. Aldrich. 1998. A mutation in S6 of Shaker potassium channels decreases the K$^+$ affinity of an ion binding site revealing ion-ion interactions in the pore. *J Gen Physiol*. 112:243-257.

Ogielska, E.M. and R.W. Aldrich. 1999. Functional consequences of a decreased potassium affinity in a potassium channel pore. Ion interactions and C-type inactivation. *J Gen Physiol*. 113:347-358.

Opsahl, L.R. and W.W. Webb. 1994. Lipid-glass adhesion in giga-sealed patch-clamped membranes. *Biophys J*. 66:75-79.

Orio, P., P. Rojas, G. Ferreira and R. Latorre. 2002. New disguises for an old channel: MaxiK channel beta-subunits. *News Physiol Sci*. 17:156-161.

Pagliuca, C., T.A. Goetze, R. Wagner, G. Thiel, A. Moroni and D. Parcej. 2007. Molecular properties of Kcv, a virus encoded K$^+$ channel. *Biochemistry*. 46:1079-1090.

Papazian, D.M. 2004. BK channels: the spring between sensor and gate. *Neuron*. 42:699-701.

Partridge, C.J., D.J. Beech and A. Sivaprasadarao. 2001. Identification and pharmacological correction of a membrane trafficking defect associated with a mutation in the sulfonylurea receptor causing familial hyperinsulinism. *J Biol Chem*. 276:35947-35952.

Parzefall, F., R. Wilhelm, M. Heckmann and J. Dudel. 1998. Single channel currents at six microsecond resolution elicited by acetylcholine in mouse myoballs. *J Physiol*. 512 (Pt 1):181-188.

Pauling, L. 1960. Nature of the chemical bond and structure of molecules and crystals. 3rd edition. Cornell University Press, Ithaka.

Pavlov, E., C. Bladen, R. Winkfein, C. Diao, P. Dhaliwal and R.J. French. 2005. The pore, not cytoplasmic domains, underlies inactivation in a prokaryotic sodium channel. *Biophys J*. 89:232-242.

Pawula, R. 1970. The transition probability density function of the low-pass filtered random telegraph signal. *Internat J Control*. 12:25-32.

Perozo, E., D.M. Cortes and L.G. Cuello. 1999. Structural rearrangements underlying K$^+$-channel activation gating. *Science*. 285:73-78.

Perozo, E., D.M. Cortes, P. Sompornpisut, A. Kloda and B. Martinac. 2002. Open channel structure of MscL and the gating mechanism of mechanosensitive channels. *Nature*. 418:942-948.

Perozo, E., A. Kloda, D.M. Cortes and B. Martinac. 2001. Site-directed spin-labeling analysis of reconstituted Mscl in the closed state. *J Gen Physiol*. 118:193-206.

Piskorowski, R. and R.W. Aldrich. 2002. Calcium activation of BK$_{Ca}$ potassium channels lacking the calcium bowl and RCK domains. *Nature*. 420:499-502.

Piskorowski, R.A. and R.W. Aldrich. 2006. Relationship between pore occupancy and gating in BK potassium channels. *J Gen Physiol*. 127:557-576.

Plieth, C. 1996. Untersuchungen zur Bestimmung von Ionenkanälen und ihrer Änderung in grünen pflanzlichen Zellen und Geweben mit Hilfe bildverarbeitender radiometrischer Fluoreszenz-Mikroskopie und der Laser-Doppler-Anemometrie. PhD thesis, Christian Albrecht University, Kiel.

Plugge, B., S. Gazzarrini, M. Nelson, R. Cerana, J.L. Van Etten, C. Derst, D. DiFrancesco, A. Moroni and G. Thiel. 2000. A potassium channel protein encoded by chlorella virus PBCV-1. *Science*. 287:1641-1644.

Press, W.H., B.P. Flannery, S.A. Teukolsky and W.T. Vetterling. 1987. Numerical Recipes. The Art of Scientific Computing. Vol. Cambridge University Press, Cambridge, New York, New Rochelle, Melbourne, Sidney.

Priest, B.T., A.M. Swensen and O.B. McManus. 2007. Automated electrophysiology in drug discovery. *Curr Pharm Des*. 13:2325-2337.

Proks, P., C.E. Capener, P. Jones and F.M. Ashcroft. 2001. Mutations within the P-loop of Kir6.2 modulate the intraburst kinetics of the ATP-sensitive potassium channel. *J Gen Physiol*. 118:341-353.

Proks, P., C. Girard, S. Haider, A.L. Gloyn, A.T. Hattersley, M.S.P. Sansum and F.M. Ashcroft. 2005. A gating mutation at the internal mouth of the Kir6.2 pore is associated with the DEND syndrome. *EMBO reports*. 6:470-475.

Qin, F., A. Auerbach and F. Sachs. 2000. Hidden Markov modeling for single channel kinetics with filtering and correlated noise. *Biophys J*. 79:1928-1944.

Ransom, C.B. and H. Sontheimer. 2001. BK channels in human glioma cells. *J Neurophysiol*. 85:790-803.

Renart, M.L., F.N. Barrera, M.L. Molina, J.A. Encinar, J.A. Poveda, A.M. Fernandez, J. Gomez and J.M. Gonzalez-Ros. 2006. Effects of Conducting and Blocking Ions on the Structure and Stability of the Potassium Channel KcsA. 281:29905-29915.

Riessner, T. 1994. Statistische Analyse von schnellen Schaltereignissen in Patch-Clamp Daten mit Hilfe von erweiterten Beta-Verteilungen. Diploma thesis, Christian Albrechts University, Kiel.

Riessner, T. 1998. Level Detection and Extended Beta Distributions for the Analysis of Fast Rate Constants of Markov Processes in Sampled Data. Shaker-Verlag, Aachen, Germany. 74 pp.

Riessner, T., F. Woelk, M. Abshagen-Keunecke, A. Caliebe and U.P. Hansen. 2002. A new level detector for ion channel analysis. *J Membr Biol*. 189:105-118.

Rose, R.C. and B.H. Juang. 1996. Hidden Markov models for speech and signal recognition. . *Electroencephalogr Clin Neurophysiol Suppl*. 45:137-152.

Rosenberg, H.H. 2006. Funktionelle Rolle von Oberflächenladungen in der Turret-Domäne des viralen Miniatur-Kaliumkanals Kcv. PhD thesis, Technische Universität Darmstadt, Darmstadt.

Rosenmund, C., Y. Stern-Bach and C.F. Stevens. 1998. The tetrameric structure of a glutamate receptor channel. *Science*. 280:1596-1599.

Rothberg, B.S. and K.L. Magleby. 1999. Gating kinetics of single large-conductance Ca^{2+}-activated K^+ channels in high Ca^{2+} suggest a two-tiered allosteric gating mechanism. *J Gen Physiol*. 114:93-124.

Roux, B. 2006. Extracellular blockade of potassium channels by TEA^+: the tip of the iceberg? *J Gen Physiol*. 128:635-636.

Ruppersberg, J.P., K.H. Schroter, B. Sakmann, M. Stocker, S. Sewing and O. Pongs. 1990. Heteromultimeric channels formed by rat brain potassium-channel proteins. *Nature*. 345:535-537.

Sakano, K. and M. Tazawa. 1986. Tonoplast origin of the envelope membrane of cytoplasmic droplets prepared from *Chara* internodal cells. *Protoplasma*. 131:247-249.

Sakmann, B. and E. Neher. 1995. Single-Channel Recording. 2nd edition. Plenum Press, New York and London. 700 pp.

Sakmann, B. and G. Trube. 1984. Voltage-dependent inactivation of inward-rectifying single-channel currents in the guinea-pig heart cell membrane. *J Physiol*. 347:659-683.

Sala, S., R.V. Parsey, A.S. Cohen and D.R. Matteson. 1991. Analysis and use of the perforated patch technique for recording ionic currents in pancreatic beta-cells. *J Membr Biol*. 122:177-187.

Sambongi, Y., Y. Iko, M. Tanabe, H. Omote, A. Iwamoto-Kihara, I. Ueda, T. Yanagida, Y. Wada and M. Futai. 1999. Mechanical rotation of the c subunit oligomer in ATP synthase (F0F1): direct observation. *Science*. 286:1722-1724.

Sanders, D. 1990. Kinetic modeling of plant and fungal membrane transport systems. *Annu Rev Plant Physiol Plant Mol Biol*. 41:77-107.

Sanders, D. and U.P. Hansen. 1981. Mechanism of Cl^- transport at the plasma membrane of *Chara corallina*: II. Transinhibition and the determination of H^+/Cl^- binding order from a reaction kinetic model. *J Membr Biol*. 58:139-153.

Sanders, D., U.P. Hansen and C.L. Slayman. 1981. Role of the plasma membrane proton pump in pH regulation in non-animal cells. *Proc Natl Acad Sci U S A*. 78:5903-5907.

Sands, Z.A. and M.S. Sansom. 2007. How does a voltage sensor interact with a lipid bilayer? Simulations of a potassium channel domain. *Structure*. 15:235-244.

Sato, C. and G. Matsumoto. 1995. Sodium channel functioning based on an octagonal structure model. *J Membr Biol*. 147:45-70.

Schrempf, H., O. Schmidt, R. Kummerlen, S. Hinnah, D. Muller, M. Betzler, T. Steinkamp and R. Wagner. 1995. A prokaryotic potassium ion channel with two predicted transmembrane segments from Streptomyces lividans. *Embo J*. 14:5170-5178.

Schröder, I., P. Harlfinger, T. Huth and U.P. Hansen. 2005. A subsequent fit of time series and amplitude histogram of patch-clamp records reveals rate constants up to 1 per microsecond. *J Membr Biol*. 203:83-99.

Schröder, I., T. Huth, V. Suitchmezian, J. Jarosik, S. Schnell and U.P. Hansen. 2004. Distributions-per-level: a means of testing level detectors and models of patch-clamp data. *J Membr Biol*. 197:49-58.

Schroeder, I. 2003. Überprüfung von Vorhersagen und Ergänzungen zum Markov-Modell des Anomalen Molfraktionseffektes in *Chara*. Diploma thesis, Christian Albrechts University, Kiel.

Schroeder, I. and U.P. Hansen. 2006. Strengths and limits of Beta distributions as a means of reconstructing the true single-channel current in patch clamp time series with fast gating. *J Membr Biol*. 210:199-212.

Schroeder, I. and U.P. Hansen. 2007. Saturation and microsecond gating of current indicate depletion-induced instability of the MaxiK selectivity filter. *J Gen Physiol*. 130:83-97.

Schroeder, I. and U.P. Hansen. 2008. Tl^+-induced μs-gating of current indicates instability of the MaxiK selectivity filter as caused by ion/protein interaction. *J Gen Physiol*. submitted.

Schultze, R. and S. Draber. 1993. A nonlinear filter algorithm for the detection of jumps in patch-clamp data. *J Membr Biol*. 132:41-52.

Sheppard, D.N. and M.J. Welsh. 1999. Structure and function of the CFTR chloride channel. *Physiol Rev*. 79:S23-45.

Shieh, C.C., M. Coghlan, J.P. Sullivan and M. Gopalakrishnan. 2000. Potassium channels: molecular defects, diseases, and therapeutic opportunities. *Pharmacol Rev*. 52:557-594.

Shim, J.W., M. Yang and L.Q. Gu. 2007. In vitro synthesis, tetramerization and single channel characterization of virus-encoded potassium channel Kcv. *FEBS Lett*. 581:1027-1034.

Shrivastava, I.H., D.P. Tieleman, P.C. Biggin and M.S. Sansom. 2002. K^+ versus Na^+ ions in a K channel selectivity filter: a simulation study. *Biophys J*. 83:633-645.

Siedow, J.N. and A.L. Umbach. 1995. Plant Mitochondrial Electron Transfer and Molecular Biology. *Plant Cell*. 7:821-831.

Siepel, A. and D. Haussler. 2004. Combining phylogenetic and hidden Markov models in biosequence analysis. *J Comput Biol*. 11:413-428.

Skou, J.C. 1965. Enzymatic Basis for Active Transport of Na^+ and K^+ across Cell Membrane. *Physiol Rev*. 45:596-617.

Somodi, S., Z. Varga, P. Hajdu, J.G. Starkus, D.I. Levy, R. Gaspar and G. Panyi. 2004. pH-dependent modulation of Kv1.3 inactivation: role of His399. *Am J Physiol Cell Physiol*. 287:C1067-1076.

Sorensen, J.B., M.S. Nielsen, C.N. Gudme, E.H. Larsen and R. Nielsen. 2001. Maxi K^+ channels co-localised with CFTR in the apical membrane of an exocrine gland acinus: possible involvement in secretion. *Pflugers Arch*. 442:1-11.

Spruce, A.E., N.B. Standen and P.R. Stanfield. 1989. Rubidium ions and the gating of delayed rectifier potassium channels of frog skeletal muscle. *J Physiol*. 411:597-610.

Starkus, J.G., L. Kuschel, M.D. Rayner and S.H. Heinemann. 1997. Ion conduction through C-type inactivated *Shaker* channels. *J Gen Physiol*. 110:539-550.

Stocker, A., S. Keis, J. Vonck, G.M. Cook and P. Dimroth. 2007. The structural basis for unidirectional rotation of thermoalkaliphilic F1-ATPase. *Structure*. 15:904-914.

Sukharev, S., S.R. Durell and H.R. Guy. 2001. Structural models of the MscL gating mechanism. *Biophys J*. 81:917-936.

Swenson, R.P., Jr. and C.M. Armstrong. 1981. K^+ channels close more slowly in the presence of external K^+ and Rb^+. *Nature*. 291:427-429.

Tabcharani, J.A., J.M. Rommens, Y.X. Hou, X.B. Chang, L.C. Tsui, J.R. Riordan and J.W. Hanrahan. 1993. Multi-ion pore behaviour in the CFTR chloride channel. *Nature*. 366:79-82.

Tamargo, J., R. Caballero, R. Gomez, C. Valenzuela and E. Delpon. 2004. Pharmacology of cardiac potassium channels. *Cardiovasc Res*. 62:9-33.

Tayefeh, S., T. Kloss, G. Thiel, B. Hertel, A. Moroni and S.M. Kast. 2007. Molecular dynamics simulation of the cytosolic mouth in Kcv-type potassium channels. *Biochemistry*. 46:4826-4839.

Tester, M. 1988. Blockade of potassium channels in the plasmalemma of *Chara corallina* by Tetraethylammonium, Ba^{2+}, Na^+ and Cs^+. *J Membr Biol*. 105:77-85.

Thiel, G. 1995. Dynamics of chloride and potassium currents during the action potential in *Chara* studied with action potential clamp. *Eur Biophys J*. 24:85-92.

Tittor, J. and U.-P. Hansen. 1983. Impedance of the electrogenic Cl^--pump in *Acetabularia*: Electrical frequency entrainments, voltage-sensitivity and reaction-kinetic interpretation. *J Membr Biol*. 75:129-139.

Townsend, C. and R. Horn. 1999. Interaction between the pore and a fast gate of the cardiac sodium channel. *J Gen Physiol*. 113:321-332.

Trapp, S., P. Proks, S.J. Tucker and F.M. Ashcroft. 1998. Molecular analysis of ATP-sensitive K channel gating and implications for channel inhibition by ATP. *J Gen Physiol*. 112:333-349.

Tsushima, R.G., J.E. Kelly and J.A. Wasserstrom. 1996. Characteristics of cocaine block of purified cardiac sarcoplasmic reticulum calcium release channels. *Biophys J*. 70:1263-1274.

Tupper, J.T. and H. Tedeschi. 1969. Microelectrode studies on the membrane properties of isolated mitochondria. *Proc Natl Acad Sci U S A*. 63:370-377.

Umrath, K. 1930. Untersuchungen über Plasma und Plasmaströmung an Characeen. IV. Potentialmessungen an *Nitella mucronata* mit besonderer Berücksichtigung der Erregungserscheinungen *Protoplasma*. 9:576-597.

Unwin, N. 1995. Acetylcholine receptor channel imaged in the open state. *Nature*. 373:37-43.

Varma, S. and S.B. Rempe. 2007. Tuning ion coordination architectures to enable selective partitioning. *Biophys J*. 93:1093-1099.

Venkataramanan, L., R. Kuc and F.J. Sigworth. 1998. Identification of

hidden Markov models for ion channel currents - Part II: State dependent excess noise. *IEEE Trans Sig Proc*. 46:1916–1929.

Venkataramanan, L., R. Kuc and F.J. Sigworth. 2000. Identification of hidden Markov models for ion channel currents - Part III: Bandlimited sampled data. *IEEE Trans Sig Proc*. 48:376–385.

Venkataramanan, L. and F.J. Sigworth. 2002. Applying hidden Markov models to the analysis of single ion channel activity. *Biophys J*. 82:1930-1942.

Venkataramanan, L., J.L. Walsh, R. Kuc and F.J. Sigworth. 1998. Identification of hidden Markov models for ion channel currents - Part I: Colored background noise. *IEEE Trans Sig Proc*. 46:1901–1915.

Verrey, F., D.L. Jack, I.T. Paulsen, M.H. Saier, Jr. and R. Pfeiffer. 1999. New glycoprotein-associated amino acid transporters. *J Membr Biol*. 172:181-192.

Wacke, M., G. Thiel and M.T. Hutt. 2003. Ca^{2+} dynamics during membrane excitation of green alga *Chara*: model simulations and experimental data. *J Membr Biol*. 191:179-192.

Wang, Z., X. Zhang and D. Fedida. 2000. Regulation of transient Na^+ conductance by intra- and extracellular K^+ in the human delayed rectifier K^+ channel Kv1.5. *J Physiol*. 523 Pt 3:575-591.

Wedler, G. 1985. Lehrbuch der Physikalischen Chemie. 2nd edition. VCH, Weinheim. 924 pp.

Weise, R. and D. Gradmann. 2000. Effects of Na^+ on the predominant K^+ channel in the tonoplast of *Chara*: decrease of conductance by blocks in 100 nanosecond range and induction of oligo- or poly-subconductance gating modes. *J Membr Biol*. 175:87-93.

Weiss, D.S. and K.L. Magleby. 1989. Gating scheme for single GABA-activated Cl^- channels determined from stability plots, dwell-time distributions, and adjacent-interval durations. *J Neurosci*. 9:1314-1324.

White, P.J. and M.S. Ridout. 1998. The estimation of rapid rate constants from current-amplitude frequency distributions of single-channel recordings. *J Membr Biol*. 161:115-129.

Witt, H.T. 1979. Energy conversion in the functional membrane of photosynthesis. Analysis by light pulse and electric pulse methods. The central role of the electric field. *Biochim Biophys Acta*. 505:355-427.

Woelk, F. 2000. Signal Detection in Noisy Markov-Processes. Diploma thesis, Christian Albrechts University, Kiel.

Wood, M.J. and S.J. Korn. 2000. Two mechanisms of K^+-dependent potentiation in Kv2.1 potassium channels. *Biophys J*. 79:2535-2546.

Woodhull, A.M. 1973. Ionic blockage of sodium channels in nerve. *J Gen Physiol*. 61:687-708.

Wu, J. 1991. Microscopic model for selective permeation in ion channels. *Biophys J*. 60:238-251.

Xie, L.H., S.A. John, B. Ribalet and J.N. Weiss. 2004. Regulation of gating by negative charges in the cytoplasmic pore in the Kir2.1 channel. *J Physiol*. 561:159-168.

Yang, J., M. Yu, Y.N. Jan and L.Y. Jan. 1997. Stabilization of ion selectivity filter by pore loop ion pairs in an inwardly rectifying potassium channel. *Proc Natl Acad Sci U S A*. 94:1568-1572.

Yeh, J.Z. and C.M. Armstrong. 1978. Immobilisation of gating charge by a substance that simulates inactivation. *Nature*. 273:387-389.

Yeh, S.H., H.K. Chang and R.C. Shieh. 2005. Electrostatics in the cytoplasmic pore produce intrinsic inward rectification in kir2.1 channels. *J Gen Physiol*. 126:551-562.

Yellen, G. 1984. Ionic permeation and blockade in Ca^{2+}-activated K^+ channels of bovine chromaffin cells. *J Gen Physiol*. 84:157-186.

Yellen, G. 1998. Premonitions of ion channel gating. *Nat Struct Biol*. 5:421.

Yellen, G. 2002. The voltage-gated potassium channels and their relatives. *Nature*. 419:35-42.

Yellen, G., D. Sodickson, T.Y. Chen and M.E. Jurman. 1994. An engineered cysteine in the external mouth of a K^+ channel allows inactivation to be modulated by metal binding. *Biophys J*. 66:1068-1075.

Yeo, G.F., R.K. Milne, R.O. Edeson and B.W. Madsen. 1988. Statistical inference from single channel records: two-state Markov model with limited time resolution. *Proc R Soc Lond B Biol Sci*. 235:63-94.

Yi, B.A., Y.F. Lin, Y.N. Jan and L.Y. Jan. 2001. Yeast screen for constitutively active mutant G protein-activated potassium channels. *Neuron*. 29:657-667.

Zhang, Y., X. Niu, T.I. Brelidze and K.L. Magleby. 2006. Ring of negative charge in BK channels facilitates block by intracellular Mg^{2+} and polyamines through electrostatics. *J Gen Physiol*. 128:185-202.

Zhao, Y., V. Yarov-Yarovoy, T. Scheuer and W.A. Catterall. 2004. A gating hinge in Na^+ channels; a molecular switch for electrical signaling. *Neuron*. 41:859-865.

Zheng, J. and F.J. Sigworth. 1997. Selectivity changes during activation of mutant *Shaker* potassium channels. *J Gen Physiol*. 110:101-117.

Zheng, J. and F.J. Sigworth. 1998. Intermediate conductances during deactivation of heteromultimeric *Shaker* potassium channels. *J Gen Physiol*. 112:457-474.

Zheng, J., L. Vankataramanan and F.J. Sigworth. 2001. Hidden Markov model analysis of intermediate gating steps associated with the pore gate of *Shaker* potassium channels. *J Gen Physiol*. 118:547-564.

Zhou, M., J.H. Morais-Cabral, S. Mann and R. MacKinnon. 2001. Potassium channel receptor site for the inactivation gate and quaternary amine inhibitors. *Nature*. 411:657-661.

Zhou, Y. and R. MacKinnon. 2003. The occupancy of ions in the K^+ selectivity filter: charge balance and coupling of ion binding to a protein conformational change underlie high conduction rates. *J Mol Biol*. 333:965-975.

Zhou, Y. and R. MacKinnon. 2004. Ion binding affinity in the cavity of the KcsA potassium channel. *Biochemistry*. 43:4978-4982.

Zhou, Y., J.H. Morais-Cabral, A. Kaufman and R. MacKinnon. 2001. Chemistry of ion coordination and hydration revealed by a K^+ channel-Fab complex at 2.0 A resolution. *Nature*. 414:43-48.

13. Erklärung

Hiermit erkläre ich an Eides statt, dass ich die vorliegende Doktorarbeit selbstständig unter Anleitung meiner akademischen Lehrer angefertigt habe und keine anderen als die angegebenen Hilfsmittel benutzt habe.

Teilergebnisse sind nach Absprache mit meinen akademischen Betreuern zur Veröffentlichung eingereicht worden.

Die Doktorarbeit selbst hat aber noch nicht im Rahmen einer Prüfung vorgelegen.

Des weiteren bestätige ich hiermit, dass ich noch keinen Promotionsversuch, weder an der Christian-Albrechts-Universität zu Kiel noch an anderen Universitäten, unternommen habe.

Kiel, 14. Dezember 2007

_____

(Indra Schröder)

14. Lebenslauf

Name:	Indra Schröder
Geburtsdatum:	01.02.1978
Geburtsort:	Hamburg
Staatsangehörigkeit:	deutsch
Eltern:	Elke Schröder, geb. Marquardsen,
	Jürgen Schröder
Familienstand:	ledig
Wohnungsanschrift:	Jungmannstr. 54, 24105 Kiel

Schulbildung: 1984 – 1988: Grundschule Kellinghusen
                  1988 – 1997: Jürgen-Fuhlendorf-Gymnasium,
                               Bad Bramstedt
Schulabschluss: Mai 1997: Abitur

Studium: 1997 – 2003: Physikstudium an der CAU Kiel
                  November 1999: Vordiplom mit Nebenfach Chemie,
                  Note: „Sehr gut“.

Hochschulabschluss: September 2003: Diplom in Physik. Note:
                  "Mit Auszeichnung“.
                  Thema der Diplomarbeit: Überprüfung von Vorhersagen
                  und Ergänzungen zum Markov-Modell des Anomalen
                  Molfraktionseffektes in *Chara.*
                  Die Arbeiten wurden durchgeführt in der Arbeitsgruppe
                  von Prof. U.-P. Hansen im Zentrum für Biochemie und
                  Molekularbiologie der Christian-Albrechts-Universität zu
                  Kiel.

Tätigkeiten: Seit Oktober 2003:, Doktorarbeit im Zentrum für
                  Biochemie und Molekularbiologie unter der Betreuung
                  von Prof. U.-P. Hansen. Thema der Arbeit: Improved
                  sub-µs gating analysis indicates conformational changes
                  as caused by ion/pore interactions in the MaxiK channel.
                  2 Jahre auf einer Landesstelle mit Lehrverpflichtung:
                  gemeinsame Vorlesung mit U.-P. Hansen
                  (Zeitreihenanalyse) und Praktikumsbetreuung im
                  Biochemischen Grundpraktikum und FP II Biophysik
                  2 Jahre auf dem DFG Projekt HA712/14-2

24105 Kiel, 14. Dezember 2007

15. Danksagung

Mein Dank gilt allen aktuellen und ehemaligen Mitgliedern der Arbeitsgruppen Biophysik und Strukturbiologie im ZBM für die gleichzeitig gemütliche und anregende Arbeitsatmosphäre. Insbesondere:

Ulf-Peter Hansen für die in jeder Hinsicht außergewöhnliche Betreuung. ;-)

Sonja, Kerstin und Christin für das liebevolle Handling der Zellen.

Christoph, Sonja und den beiden Simones und Stefanie für die Hilfe am FRET-Projekt, das dann leider doch in die Hose ging…

Unserem Hiwi Immke, die viele schöne Messungen beisteuerte.

Den FPII Praktikanten, die geduldig die unmöglichsten Messbedingungen ausprobierten.

Außerdem danke ich den Borstlern, die mich mit den stabil transfizierten HEK-Zellen versorgten.

Zu guter Letzt, aber nicht als Letzten, danke ich meinen Eltern, die immer hinter mir stehen.